

**Investigation of Contrast-Enhanced Dual Energy Mammography  
(CEDEM) on a Breast CT Platform**

by

Shih-ying Huang

B. S. (University of California, San Diego) 2004

A dissertation submitted in partial satisfaction of the  
requirements for the degree of  
Doctor of Philosophy

in

Biomedical Engineering

in the

OFFICE OF GRADUATE STUDIES  
of the  
UNIVERSITY OF CALIFORNIA, DAVIS

Approved:

---

John M. Boone, Chair

---

Anthony J. Seibert

---

Ramsey D. Badawi

Committee in Charge

2011

Copyright © 2011 Shih-ying Huang  
All Rights Reserved

Shih-ying Huang  
Fall 2011  
Biomedical Engineering

## Investigation of Contrast-Enhanced Dual Energy Mammography (CEDEM) on a Breast CT Platform

### **Abstract**

X-ray computed tomography of the breast (breast CT) has been developed at UC Davis in the hope to improve the detection and diagnosis of breast cancer. A recent clinical trial of contrast-enhanced breast CT (CE-bCT) has shown promising potential in distinguishing benign breast lesions and malignant breast lesions with an increase in signal enhancement. Currently, the temporal characteristics of contrast kinetics in a clinical setting remain unclear. It is essential to design optimal CE-bCT protocols to acquire bCT images with the best signal enhancement of breast lesions. In order to quantify the kinetic characteristics of suspicious breast lesions, contrast-enhanced dual energy mammography (CEDEM) was developed as a low-dose and fast projection imaging technique to complement the anatomical details provided by the dedicated breast CT system.

This dissertation presents a comprehensive investigation of the implementation of CEDEM using the breast CT system in a pre-clinical setting. The objectives of this study were (1) to characterize breast morphology, such as skin thickness, breast dimension, and breast glandular fraction, using the clinical breast CT data

sets to construct realistic breast models, and (2) to determine the x-ray technique factors (kV, filters, mAs, and dose allocation between the two images) to acquire high-quality CEDEM images for a given mean glandular dose. Computer simulation and experimental acquisitions were performed to guide and validate the static CEDEM optimizations. CEDEM acquisitions were designed to deliver the mean glandular dose equivalent to that of two-view mammogram. Adhering to the radiation dose limitation, practical x-ray technique factors with optimal filter materials were studied for a number of breast thickness and breast glandular composition. With the optimal x-ray technique factors in acquiring static CEDEM, the dynamic CEDEM imaging was shown feasible with a dynamic breast phantom in capturing contrast time density curves. This research provides the scientific underpinning and guidance in terms of methodology for the future clinical implementation of contrast-enhanced dual energy mammography.

# Contents

<b>Abstract</b>	<b>-ii-</b>
<b>Table of Contents</b>	<b>-iv-</b>
<b>List of Figures</b>	<b>-viii-</b>
<b>List of Tables</b>	<b>-xiv-</b>
<b>Acknowledgments</b>	<b>-xv-</b>
<b>1 Introduction</b>	<b>1</b>
1.1 Breast Cancer . . . . .	2
1.2 Breast Imaging Modalities . . . . .	2
1.2.1 Mammography . . . . .	2
1.2.2 The Dedicated Breast Computed Tomography (bCT) . .	3
1.2.3 Breast Magnetic Resonance Imaging (MRI) . . . . .	5
1.3 Breast Imaging with Injected Contrast Agents . . . . .	8
1.3.1 The Physiology of Contrast Media . . . . .	8
1.3.2 Contrast-Enhanced Mammography (CEM) . . . . .	9
1.3.3 Contrast-Enhanced Breast CT (CE-bCT) . . . . .	10
1.4 Dual Energy Imaging . . . . .	11
1.4.1 Contrast-Enhanced Dual Energy Mammography (CE-DEM) . . . . .	12
1.5 Dissertation Overview . . . . .	14
1.6 References . . . . .	15
<b>2 The Characterization of Breast Morphology</b>	<b>19</b>
2.1 Breast Skin Thickness . . . . .	20
2.1.1 Motivation . . . . .	20
2.1.2 Patient Population . . . . .	20
2.1.3 Image Spatial Resolution . . . . .	21

2.1.4	The Three-Dimensional Skin Thickness Algorithm . . . . .	23
2.1.5	Algorithm Validation . . . . .	26
2.1.6	The Breast Skin Thickness Using BCT . . . . .	28
2.1.7	Breast dosimetry in mammography with Monte Carlo simulation . . . . .	33
2.1.8	Discussion and Conclusions . . . . .	33
2.2	Breast Size, Shape, and Fibroglandular Tissue Distribution . .	38
2.2.1	Motivation . . . . .	38
2.2.2	Image Acquisition and Patient Population . . . . .	39
2.2.3	Defining Breast Metrics . . . . .	40
2.2.3.1	Breast Effective Diameter . . . . .	40
2.2.3.2	Breast Volume (3D) and Areal (2D) Glandular Fraction . . . . .	42
2.2.3.3	Radial Distribution of Breast Glandular Fraction	43
2.2.3.4	Breast Projection Areal Glandular Fraction . .	43
2.2.4	Data Analysis . . . . .	45
2.2.4.1	3D (Volumetric) Breast Assessment . . . . .	45
2.2.4.2	2D (Projection and bCT Images) Breast Assessment . . . . .	51
2.2.4.3	Breast Shape and Size Assessment . . . . .	53
2.2.4.4	3D Breast Modeling . . . . .	58
2.2.5	Discussion and Conclusions . . . . .	62
2.3	References . . . . .	66
<b>3</b>	<b>The Simulation of CEDEM Images</b>	<b>70</b>
3.1	Motivation . . . . .	71
3.2	The Semi-Empirical Linear Model of Indirect, Flat-panel X-ray Detectors . . . . .	71
3.2.1	Theory . . . . .	72
3.2.2	Breast CT Data Acquisition and Processing . . . . .	76
3.2.3	X-ray Spectrum Model . . . . .	76
3.2.4	Detector Signal Statistics Parameters . . . . .	79
3.2.5	Detector Signal Correlation . . . . .	82
3.2.6	Noise Components in the Noise Power Spectrum (NPS)	84
3.3	Validation of the Semi-Empirical Linear Detector Model . . . . .	86

3.3.1	Images of Air Scans . . . . .	86
3.3.2	Images of Objects . . . . .	90
3.4	Discussion . . . . .	93
3.5	Conclusions . . . . .	97
3.6	References . . . . .	97
<b>4</b>	<b>The Optimization of CEDEM Using Breast CT</b>	<b>101</b>
4.1	Motivation . . . . .	102
4.2	The Static Breast Phantom . . . . .	102
4.3	The Concentration of Iodine in Clinical Setting . . . . .	106
4.4	Dose Calculation . . . . .	109
4.5	The Dynamic Filter Changer . . . . .	113
4.6	Initial Static CEDEM Optimization . . . . .	113
4.6.1	Computer Simulation Method . . . . .	114
4.6.2	Image Simulation and Acquisition . . . . .	117
4.6.3	Optimization Methods and Results . . . . .	118
4.6.4	Optimization Conclusions . . . . .	120
4.7	Comprehensive Static CEDEM Optimization . . . . .	121
4.7.1	Image Simulation and Acquisition . . . . .	122
4.7.2	Optimization Methods . . . . .	124
4.7.3	kV Optimization . . . . .	129
4.7.3.1	Mean Glandular Dose . . . . .	132
4.7.3.2	Breast Thickness . . . . .	133
4.7.3.3	Iodine Concentration . . . . .	135
4.7.3.4	Breast Composition . . . . .	135
4.7.3.5	Dose Allocation . . . . .	139
4.7.4	Optimization Conclusions . . . . .	141
4.8	The Dynamic CEDEM Imaging . . . . .	145
4.8.1	The Breast Tumor Flow Chamber . . . . .	145
4.8.2	The Kinetic Parameters of the Flow Chamber . . . . .	146
4.8.3	The Dynamic X-ray CEDEM Acquisition . . . . .	155
4.9	The optimized Dynamic CEDEM protocol . . . . .	158
4.10	References . . . . .	161

<b>5 Summary and Future Work</b>	<b>164</b>
5.1 Imaging System Components . . . . .	167
5.2 The CEDEM Clinical Study . . . . .	168
5.3 Coda . . . . .	169
5.4 References . . . . .	169
<b>Production Notes</b>	<b>170</b>
<b>Appendices</b>	<b>171</b>
<b>A Breast CT Forward Projection</b>	<b>172</b>
A.1 Motivation . . . . .	173
A.2 Methods and Materials . . . . .	173
A.3 Results . . . . .	175
A.4 Discussion and Summary . . . . .	175
<b>B Normalization of the Image Filter</b>	<b>177</b>

# List of Figures

1.1	The dedicated breast CT systems . . . . .	4
1.2	The normal vs. tumor capillary . . . . .	8
1.3	The illustration of dual energy imaging . . . . .	13
1.4	The illustration of the signal enhancement vs. time with the dynamic CEDEM acquisition . . . . .	15
2.1	The spatial accuracy phantom: side view and top view . . . . .	22
2.2	The distance validation of the reconstructed bCT images . . . . .	23
2.3	Skin-thickness assessment: the 360-degree radial scan profile	25
2.4	Skin thickness assessment: the three-dimensional, patch-by-patch plane-fitting method . . . . .	27
2.5	A histogram of the estimated wall thickness of the physical phantom . . . . .	28
2.6	A histogram of the breast skin thickness among 51 women using the three-dimensional surface fit approach . . . . .	29
2.7	A histogram of the breast skin thickness of one single bCT volume using the three-dimensional surface fit approach . . . . .	30
2.8	The breast skin thickness as a function of anterior-posterior position (women of five bra cup sizes) . . . . .	31
2.9	The breast skin thickness: right breast vs. left breast among 49 women . . . . .	32
2.10	The normalized glandular dose ( $D_{gN}$ ) coefficients as a function of kVp for a 4-cm and 6-cm 50% glandular breast . . . . .	34
2.11	The $D_{gN}$ increase (%) over that of a breast with 4-mm skin thickness as a function of kVp for a 4-cm and 6-cm 50% glandular breast . . . . .	35

2.12 A coronal bCT image of a recent bCT participant with skin thickening . . . . .	37
2.13 An example illustrating how the radial glandular fraction is calculated using a segmented coronal-reconstructed bCT image . . . . .	44
2.14 The definition of the three breast regions considered in calculating radial glandular fraction . . . . .	44
2.15 Breast volume as function of patient age . . . . .	47
2.16 Breast volume as function of bra cup size . . . . .	48
2.17 VGF of the affected and unaffected breasts . . . . .	49
2.18 VGF as function of bra cup size . . . . .	50
2.19 VGF as function of BIRADS breast density . . . . .	51
2.20 VGF as function of $D_{chestwall}$ and patient age . . . . .	52
2.21 $AGF_{T2}$ and VGF as function of BIRADS breast density . . . . .	54
2.22 VGF as function of $AGF_{Ti}, i = 1, 2, \dots, 8$ . . . . .	55
2.23 $RGF_n(r)$ for the three breast regions . . . . .	56
2.24 $GF_{coronal}$ as function of the posterior-to-anterior direction z . . . . .	57
2.25 $GF_{sagittal}$ as a function of the superior-to-inferior direction y . . . . .	58
2.26 $D_{eff}$ as a function of the posterior-to-anterior direction z . . . . .	59
2.27 Histograms of $D_{chestwall}$ for four bra cup size categories . . . . .	60
2.28 Histograms of breast length for four bra cup size categories . . . . .	61
2.29 Three-dimensional description of breast glandular distribution for bra cup size B . . . . .	63
2.30 Three-dimensional description of breast glandular distribution for bra cup size D . . . . .	64
 3.1 80-kVp TASMIP spectra . . . . .	78
3.2 Air-kerma-rate-to-mA factors . . . . .	79
3.3 The detector mean and variance factors . . . . .	81
3.4 The quantum detection efficiency and fraction of energy absorption in 0.6-mm CsI scintillator . . . . .	81
3.5 The illustration of compiling a 2D digital MTF filter . . . . .	83
3.6 The presampling and digital modulation transfer function of the breast CT system . . . . .	85

3.7	The noise component, $v_2$ , as a function of mean $m_{emp}$ and kVp for four filter materials . . . . .	87
3.8	The $m_{ROI}$ as a function of air kerma for 4 x-ray spectra . . . . .	89
3.9	The $v_{ROI}$ as a function of air kerma for 4 x-ray spectra . . . . .	90
3.10	The radially-averaged NPS of the simulated and measured air scan images acquired with 4 x-ray spectra . . . . .	91
3.11	The contour of absolute percent error in the radially-averaged NPS of the simulated air scan images compared to that of the measured air scan images . . . . .	92
3.12	The comparison of the signal mean and variance maps between the simulated and experimental images . . . . .	94
4.1	The CEDEM optimization flow chart . . . . .	102
4.2	The x-ray mass attenuation coefficients of water and polyethylene vs. glandular and adipose tissues. . . . .	104
4.3	The custom-made polyethylene slabs . . . . .	105
4.4	The anatomical ROI example from a mammography image and a breast CT projection image of the static breast phantom . .	106
4.5	The anatomical noise power spectrum of the 8-cm, 40% glandular breast phantom . . . . .	107
4.6	The relationship of iodine concentration as a function of the mean signal in Hounsfield unit . . . . .	108
4.7	A histogram of the signal enhancement in the clinical CE-bCT data sets among 52 breast lesions. . . . .	109
4.8	A histogram of the iodine concentration estimated from the clinical CE-bCT data sets among 52 breast lesions. . . . .	110
4.9	The glandular dose per million photons $F(E)$ of 10-cm, 14-cm, and 18-cm breast thickness (glandular fraction of 0%, 50%, and 100%) . . . . .	112
4.10	The mean glandular dose (MGD, in the unit of mGy) as a function of compressed breast thickness (cm) . . . . .	113
4.11	The mechanical drawing of the filter changer . . . . .	114
4.12	The pictures of the filter changer on the breast CT system . .	115
4.13	An illustration of the imaging geometry and setup in the initial computer simulation method . . . . .	117

4.14 An illustration of the imaging setup with the 8-cm breast phantom using the breast CT system . . . . .	118
4.15 The computer-simulated and experimental images of a 8-cm breast phantom using 40 kVp / 1.5-mm Al . . . . .	119
4.16 An illustration of log-weighted subtraction . . . . .	120
4.17 The kV-optimization results using simulation and experiments . . . . .	121
4.18 The 8-cm, 10-cm, and 13-cm physical breast phantoms . . . . .	123
4.19 The flat-fielded simulated and experimentally-acquired projection images of a 8-cm, 10-cm, and 13-cm breast phantom with 17% volume glandular fraction . . . . .	125
4.20 $SDNR$ or $\sigma_{bg}^2$ as a function of the DE weighting factor $w_t$ . . . . .	126
4.21 The CEDEM images of a breast phantom with 8-cm thick and 17% volume glandular fraction using two different $w_t$ 's . . . . .	127
4.22 A demonstration of calculating GLCM . . . . .	128
4.23 The $\bar{H}$ and $\bar{C}$ are shown as a function $w_t$ for GLCM analysis . .	130
4.24 The CEDEM images of a breast phantom with 8-cm thick and 17% volume glandular fraction using $w_t^2$ , $w_t^3$ , and $\bar{w}_t$ . . . . .	130
4.25 The mean glandular dose delivered per frame as a function of kV using 0.1-mm Sn and 0.2-mm Cu for 8-cm, 10-cm, and 13-cm breast thickness (glandular fraction of 5%, 17%, and 25%) . . . . .	134
4.26 The $\bar{w}_t$ as a function of kV for 8-cm, 10-cm, and 13-cm breast phantoms (VGF of 25%) . . . . .	136
4.27 The $\frac{SDNR}{\sqrt{MGD}}$ (iodine concentration of 21.6 mg/ml) and the number of allowable CEDEM images given $MGD_{mammo}$ as a function of kV for 8-cm, 10-cm, and 13-cm breast phantoms (VGF of 25%) . . . . .	137
4.28 The $\frac{SDNR}{\sqrt{MGD}}$ evaluated for iodine concentration of 10.8 mg/ml, 5.4 mg/ml, and 2.7 mg/ml as a function of kV for 8-cm, 10-cm, and 13-cm breast phantoms (VGF of 25%) . . . . .	138
4.29 The $\frac{SDNR}{\sqrt{MGD}}$ as a function of kV for 8-cm breast phantom with VGF of 5% and 17% . . . . .	139
4.30 The $\frac{SDNR}{\sqrt{MGD}}$ as a function of kV for 10-cm breast phantom with VGF of 5% and 17% . . . . .	140
4.31 The $\frac{SDNR}{\sqrt{MGD}}$ as a function of kV for 13-cm breast phantom with VGF of 5% and 17% . . . . .	140

4.32 The $\frac{SDNR}{\sqrt{MGD}}$ (iodine concentration of 21.6 mg/ml) and the number of allowable CEDEM images given $MGD_{mammo}$ as a function of dose ratio for 8-cm breast phantoms (VGF of 5%, 17%, and 25%)	142
4.33 The $\frac{SDNR}{\sqrt{MGD}}$ (iodine concentration of 21.6 mg/ml) and the number of allowable CEDEM images given $MGD_{mammo}$ as a function of dose ratio for 8-cm breast phantoms (VGF of 5%, 17%, and 25%)	143
4.34 The $\frac{SDNR}{\sqrt{MGD}}$ (iodine concentration of 21.6 mg/ml) and the number of allowable CEDEM images given $MGD_{mammo}$ as a function of dose ratio for 8-cm breast phantoms (VGF of 5%, 17%, and 25%)	144
4.35 The mechanical design of the flow chamber and the fabricated chamber . . . . .	147
4.36 The marked flow rate as a function of flow rate measured from <i>Manostat®</i> peristaltic pumps and <i>Buchler®</i> polystaltic pumps	148
4.37 The CED-MRI contrast kinetic curves from patients with malignant and benign cancers . . . . .	150
4.38 The wiring diagram of controlling the flow chamber . . . . .	151
4.39 Examples of the RGB frame and the segmented RGB frames from the flow chamber video . . . . .	152
4.40 The diagram defining the flow parameter within the flow chamber	153
4.41 A timing diagram of the flow chamber parameters during a 8-minute acquisition . . . . .	155
4.42 The signal enhancement over time for low-enhancement and high-enhancement contrast kinetic profiles using the videos of the flow chamber . . . . .	156
4.43 The photos of the dynamic breast phantom with and without breast slabs . . . . .	157
4.44 The Sn-image, Cu-image, and CEDEM image of the dynamic breast phantom using 55 kV . . . . .	157
4.45 The contrast kinetic curves generated from the dynamic CEDEM acquisition of the dynamic breast phantom using kinetic profiles of four types of malignant breast cancer . . . . .	159
4.46 The contrast kinetic curves generated from the dynamic CEDEM acquisition of the dynamic breast phantom using the kinetic profile of the benign breast cancer . . . . .	160
4.47 An example of the dynamic CEDEM protocol with the high-dose and low-dose CEDEM acquisition . . . . .	161

A.1 Forward projection images of a bCT data set . . . . . 176

# List of Tables

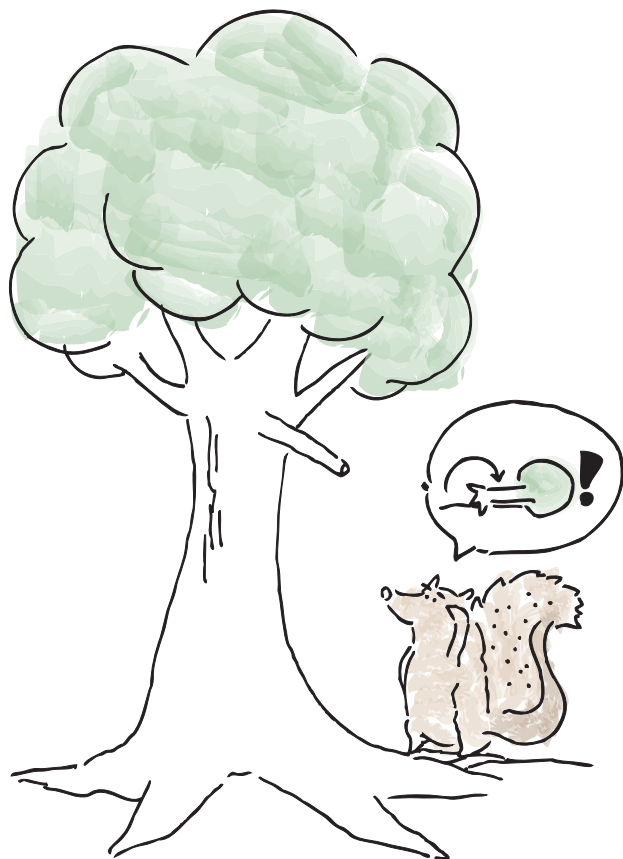
1.1	Dedicated breast cone-beam CT scanner specifications . . . . .	6
2.1	A list of mean breast skin thickness for five different breasts (bra cup size A, B, C, D, DD) . . . . .	31
2.2	Patient population of the comprehensive breast metrics study	41
2.3	The power-function coefficients describing $AGF_{Ti}$ as a function of VGF . . . . .	54
3.1	The half-value-layer of the x-ray spectrum . . . . .	77
4.1	The x-ray technique factors as function of kV to acquire low- energy and high-energy images . . . . .	123
4.2	The number of averaged frames (both Sn-images and Cu-images) used for the high-dose CEDEM acquisition for 8-cm, 10-cm, and 13-cm breast thickness and volume glandular fraction of 5%, 17%, and 25% . . . . .	132
4.3	The list of flow parameters used to generate high-enhancement and low-enhancement kinetic profiles . . . . .	154

## Acknowledgments

1. Dr. Boone, Seibert, Ramsey (my phd committee)
2. Dr. Karen Lindfors and the radiologists and tech crew
3. Dr. Craig abbey for long but helpful conversation on working on the detector paper
4. conversation with Gerhard Roo and his team from Varian Medical System on the detector information
5. conversation with Dr. Bruce Whiting on detector stats
6. conversation with Dr. Jeff Seiwerdsen and Dr. Samuel Richard for insights of cascaded system analysis
7. collaboration on manuscript preparation with Dr. Martin Yaffe
8. awesome boone lab members (Kai Yang, Orlando Valesquez, Alex Kwan, George Burkett Jr, Shonket Ray, Nathan Packard, Dandan Zhang, Katie Metheny, Sarah McKenney, Anita Nosratieh, Nicolas Prionas, Lin Chen, Peymon Pezi)
9. other BME and other department Phd students members (Ramsey's lab, Charles Caskey for showing me equipments to build my phantoms, Jiro, Cathy, Bevin Lin for all the support; big help from Julia Choi for how to start writing and awesome help in learning how to use  $\text{\LaTeX}$ )
10. UCDMC admin people (Laurie Finch, Desiree, Linda, John Brook for supplying the contrast solution to use for experiments, Clara and Naomi for keeping up with the patient data
11. BME admin people (Christal Wintersmith and the track advisors and Dr. Insana to encourage me to pursue a PhD degree)
12. close friends who support my constantly during PhD (Acacia fellowship and DCCC) and my family member
13. GOD!!!!!!

# Chapter 1

## Introduction



## **1.1 Breast Cancer**

Breast cancer is one of the most common non-skin related malignancies and is the second leading cause of cancer mortality among women in the United States. About 1 in 8 women in the United States (12%) will develop invasive breast cancer over the course of her lifetime ([Altekruse et al., 2010](#)). Breast cancer is a disease characterized by abnormal proliferation of the epithelial or glandular cells in the breast. A malignant tumor is a group of cancer cells that may grow into surrounding tissues or spread to distant areas of the body. With the cause of most breast cancer uncertain, it is most effective to detect breast cancer in its early development stage. Studies have found that early detection of breast cancer improves patient survival rate significantly ([Michaelson et al., 2002](#)). Therefore, the development of breast imaging technology is useful to improve early detection and reduce mortality due to breast cancer.

## **1.2 Breast Imaging Modalities**

### **1.2.1 Mammography**

Mammography (screen film or digital) has been used throughout North America for breast cancer screening in asymptomatic patients. Mammography is a low-cost, low-radiation-dose procedure used to detect breast cancer. The principle of mammography is to image a compressed breast by acquiring x-ray projection images using x-ray detection technologies, such as screen-film detectors, computed radiography (CR) plates, and flat-panel detectors. Mammographic x-ray tubes typically consist of molybdenum anode and molybdenum (Mo) or Rhodium (Rh) target. The x-ray peak potential ranges from 24 kVp to 35 kVp to generate x-ray spectra optimal in creating contrast between the adipose and fibroglandular tissues in a mammogram. The pixel size of the detectors used for mammography is typically 100  $\mu\text{m}$  or less. Thus, mammography is excellent at detecting microcalcifications with diameters rang-

ing between 100 to 150  $\mu\text{m}$  (Rong et al., 2002). Although mammography can produce high-contrast images and detect small objects very well, it is not without limitation. Due to the superposition of overlapping breast tissue, the visualization of breast masses is often limited and obscured in dense breasts. Thus, mammography is not sensitive to detect larger breast tumors embedded in a heterogeneously dense or extremely dense breast (Kopans, 2007). In addition, breast compression during mammography procedure is likely to cause patient discomfort and in some cases discourages women from having a mammogram. While mammography produces high-quality two-dimensional (2D) images of the breast, the move toward the three-dimensional (3D) imaging modalities have been actively explored to overcome the limitations of 2D imaging.

### 1.2.2 The Dedicated Breast Computed Tomography (bCT)

The dedicated breast CT system has been developed as part of the Breast Tomography Project at UC Davis Medical Center. The prototype 1 breast CT scanner, named Albion (Figure 1.1a), was fabricated and is currently acquiring patient scans off site through a collaboration with University of Pittsburgh. A prototype 2 scanner, named Bodega (Figure 1.1b), was constructed and is currently acquiring patient scans at the Ambulatory Care Center, UC Davis Medical Center. The prototype 2 breast CT scanner employs a PaxScan 4030CB (Varian Medical Systems, Palo Alto, CA, USA). The flat-panel detector with CsI-amorphous-silicon has a  $40 \times 30 \text{ cm}^2$  detector active area with a  $2048 \times 1536$  image matrix of  $194 \mu\text{m}$  detector elements. The Varian detector can currently acquire  $1 \times 1$  pixel-binning images at a frame rate up to 7.5 frames per second (fps) ( $194 \mu\text{m}^2$  pixels at the detector), and 30 frame-per-second (fps) is feasible using  $2 \times 2$  pixels binned ( $388-\mu\text{m}^2$  pixels at the detector). The scanner software also allows image acquisition at the desired frame rate up to 60 fps in  $2 \times 4$  binning mode. The Bodega breast CT system makes use of a Comet x-ray tube (Comet AG, Flamatt, Switzerland) with a  $0.4 \text{ mm} \times 0.4 \text{ mm}$  focal spot and kVp range of 40 - 120 kVp. The x-ray tube has a

tungsten anode and beryllium window. The x-ray generator can run from 0.1 to 20.0 mA, depending upon kVp and given the limitation of the x-ray tube rating. The detector and x-ray tube are installed onto the rotating gantry, driven by a servo motor. An additional stepping motor was incorporated to drive the x-ray tube vertically, which allows helical and saddle trajectories in the breast CT acquisition.

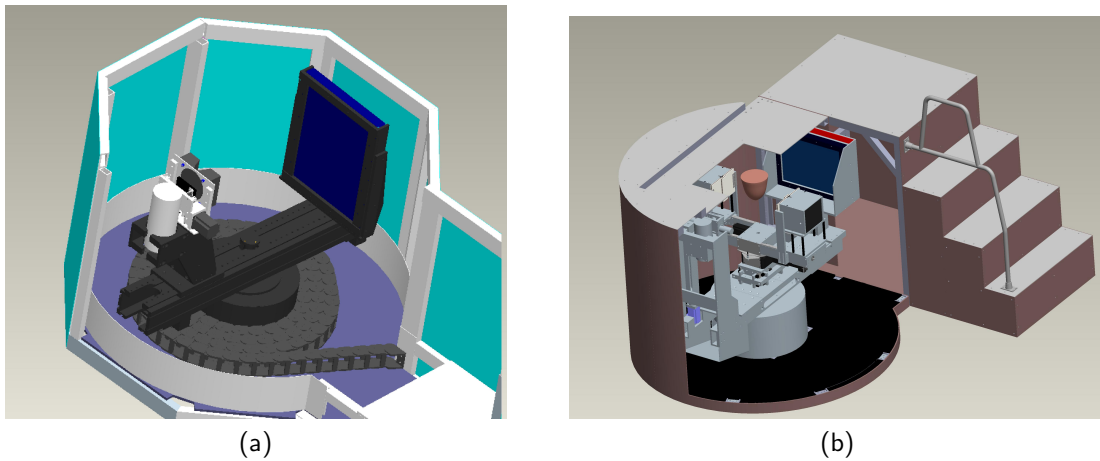


Figure 1.1. The dedicated breast CT systems **(a)** Albion **(b)** Bodega

The breast CT scanner operates at 80 kVp, and the technique factors (mAs) were selected based on the self-reported bra cup size of the patient. The mAs was selected such that the mean glandular dose from the bCT scan was virtually identical to two-view mammography for each woman (2 - 10 mGy) ([Boone et al., 2005](#)). The CT scan was performed in the coronal plane, imaging only a single breast in pendant geometry with the woman prone on the scanner tabletop with the breast hanging through a circular hole in the table. The x-ray tube and the detector system rotate around the pendant breast in the horizontal plane. The current cone-beam CT reconstruction generates bCT images in Hounsfield Unit (HU), and it also corrects for beam hardening and scatter using a numerical normalization method ([Yang et al.](#)). The cone-beam CT reconstruction typically produces 200 - 512 breast CT images per breast. The  $512 \times 512$  reconstructed CT images have pixel

dimensions ranging between  $194 \mu\text{m}$  and  $407 \mu\text{m}$  (depending on the size of the breast), and the slice thickness is approximately  $0.21 \text{ mm}$ . The technical components, imaging geometry, and image processing of the two prototype breast CT systems are summarized in Table 1.1.

Overall, breast CT can resolve masses in dense breasts while improving patient comfort (no breast compression). Studies have shown that breast CT was equal to mammography for visualization of breast lesions ([Lindfors et al., 2008](#)). Breast CT was significantly better than mammography in visualizing masses ( $p = 0.002$ ) while mammography excelled at visualizing microcalcifications ( $p = 0.006$ ). Therefore, breast CT may someday be used in addition to mammography, depending on the breast cancer type and tissue composition.

### 1.2.3 Breast Magnetic Resonance Imaging (MRI)

Magnetic resonance imaging of the breast is particularly useful in evaluating women whose breast tissues are mammographically dense and who are at high risk of breast cancer due to familial disposition in screening. MR imaging uses a powerful magnetic field of protons, excited by a radiofrequency (RF) pulse ( $90^\circ$  flip angle), and the MR signal of tissues in 3D are acquired which produce detailed images of body structures and tissues. The longitudinal ( $T_1$ ) and transverse ( $T_2$ ) relaxation times measured after the radiofrequency pulse is used to distinguish different tissues based on the macromolecular environment (or the magnetic dipole moments) of the hydrogen nuclei. Breast MRI is performed on a standard whole body magnet at a field strength of  $0.5 \text{ Tesla}$  to  $1.5 \text{ Tesla}$ . Breast RF receiver coils are tuned to the magnetic strength to measure the signal emitted from excited tissues. Magnetic gradients applied in three orthogonal directions are used to localize the source of the signal to reconstruct MR images. With current-state-of-art MR systems, the inplane pixel size is on the order of  $0.5 \times 0.5$  to  $0.8 \times 0.8 \text{ mm}$  and the through-plane pixel size (slice thickness) ranges from  $1$  to  $3 \text{ mm}$ .

Breast MRI is routinely acquired with the injection of gadolinium chelates (a  $T_1$ -shortening contrast agent) due to the low specificity of breast cancer tis-

Table 1.1. Dedicated Breast Cone-Beam CT Scanner Specifications.

Scanner	1 <sup>st</sup> Generation (Albion)	2 <sup>nd</sup> Generation (Bodega)
<b>X-ray Tube</b>	640 Watt, water-cooled, tungsten anode (Comet, Flamatt, Switzerland)	1000 Watt, water-cooled, tungsten anode (Comet, Flamatt, Switzerland)
<b>Focal Spot &amp; Filtration</b>	0.40 × 0.40 mm, 0.30 mm Cu Filtration	0.40 × 0.40 mm, 0.20 mm Cu Filtration
<b>X-ray Detector</b>	CsI TFT array (Paxscan 4030CB, Varian Imaging Systems, Palo Alto, CA), 40 cm × 30 cm	Same as Albion
<b>Acquisition Parameters</b>	30 fps, 1024 × 768 pixels, 388 $\mu$ m pixel pitch (with 2 × 2 binning)	Same as Albion
<b>Gantry</b>	Horizontal plane rotation, powered by integrated bearing-motor-encoder system, 13 ft-lbs of continuous torque (Kollmorgen, Radford, VA)	Horizontal plane rotation, powered by integrated bearing-motor-encoder system, 100 ft-lbs of continuous torque (Kollmorgen, Radford, VA)
<b>Scan Field of View</b>	19.7 cm diameter (average)	19.7 cm diameter (average)
<b>Scan Parameters</b>	500 cone-beam projections over 360 degrees in 16.6 sec	500 cone-beam projections over 360 degrees in 16.6 sec
<b>kVp</b>	80 kVp	80 kVp
<b>mAs</b>	~ 50 – 120 mAs (depending on breast size)	~ 40 – 192 mAs (depending on breast size)
<b>Reconstruction</b>	Filtered back-projection using Shepp-Logan filter, 512 × 512 × (300-500) pixel (x,y,z) volume data set	Filtered back-projection using Shepp-Logan filter, 512 × 512 × (300-500) pixel (x,y,z) volume data set

sue in MR images.  $T_1$ -weighted gradient-echo imaging is typically performed for contrast-enhanced breast MRI. Dynamic contrast-enhanced MRI (DCE-MRI) has been shown to be useful for detection and diagnosis of breast cancer. A temporal series of three-dimensional  $T_1$ -weighted MR images is typically acquired during the uptake of a gadolinium-based contrast agent. These images allow the radiologists to visualize suspicious tissues and to evaluate the likelihood of malignancy by the tissue morphology and kinetic characteristics. Static  $T_2$ -weighted MR images provide complementary information for distinguishing benign fibroadenoma from malignant cancer since both have similar enhancement patterns in DCE  $T_1$ -weighted images. Bilateral breast imaging is typically suggested with efficient protocols in injecting contrast agents. The temporal resolution of a DCE-MRI acquisition ranges from 60 to 120 seconds, with each MRI takes 2 to 15 minutes to complete.

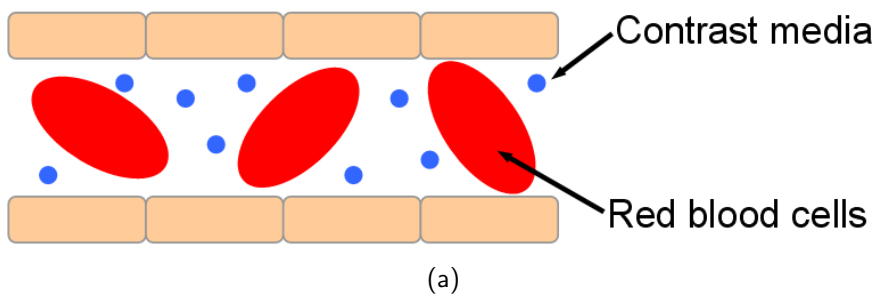
Breast MRI can produce tomographic images with image resolution slightly poorer than that of breast CT. Although MRI introduces no ionizing radiation to the patient, the imaging time is longer and likely to affect image quality due to motion artifacts. In addition, a study reported in the *New England Journal of Medicine* (Kriege et al., 2004) found higher sensitivity using breast MRI with contrast than mammography (79.5 % vs. 33.3 %) in detecting breast carcinoma among women at-risk for breast cancer. DCE-MR data also demonstrates that invasive breast cancers tend to exhibit more rapid and more focal uptake of contrast agent than normal fibroglandular tissue or benign breast lesions. After uptake, invasive breast cancers tend to exhibit irregular margins and some have washout of contrast agent, which is not typical of benign lesions and is largely due to the vascular development around the tumor cite (Section 1.3.1). In addition to the 3D tomographic nature of the MRI images, the use of contrast is the key factor in improving the detection of breast cancer based on its signal enhancement and contrast kinetics profile.

## 1.3 Breast Imaging with Injected Contrast Agents

### 1.3.1 The Physiology of Contrast Media

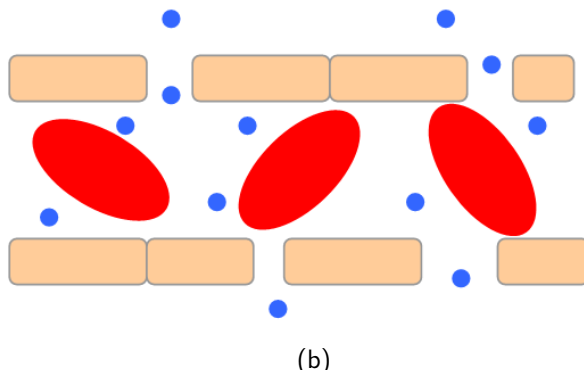
Tumor growth is characterized in many cases by the abnormal angiogenesis where new capillaries are developed to obtain nutrition from diffusion from surrounding vessels. New vessels develop from preexisting ones through sprouting rather than normal vascular development. Figure 1.2 demonstrates the process of vasculature development around the tumor region compared to that around the normal tissues. Tumor angiogenesis is active continuously, which leads to a high fraction of immature blood vessels. Therefore, tumor vessels are usually structurally and functionally immature, or “leaky” ([van Vliet et al., 2005](#)).

#### Normal capillary



(a)

#### Tumor capillary



(b)

Figure 1.2. (a) The normal capillary and (b) the tumor capillary with the injected contrast agent are illustrated. The red ovals represent the red blood cells. The blue circles represent the contrast medium

The incorporation of contrast agents with imaging has been shown valuable in breast MRI. The mechanism for enhancement of invasive breast cancers depends largely on the accumulation of the contrast agent in the extracellular space through angiogenic vessels. The relatively small molecule of the contrast media can easily diffuse from the intravascular space to the interstitium or extravascular space. It is the amount of the accumulation in the interstitium or extracellular space that give rise to signal enhancement when imaging. The accumulation of contrast media is likely due to higher densities of microvessels to support tumor growth found in invasive breast cancer (Barbareschi et al., 1995; Miles, 1999). In addition, more protein-like molecules may permeate between the intercellular bed and the extracellular space due the “leaky” blood vessels. Vascular endothelial growth factor (VEGF) is known to affect vascular permeability, and VEGF has been known to be higher in invasive breast cancers than in normal fibroglandular tissues and most benign breast lesions (Hendrick, 2008; Knopp et al., 1999). These factors have been shown to give rise to a remarkable degree of enhancement due to the accumulation of contrast agents around the malignant tumors.

### 1.3.2 Contrast-Enhanced Mammography (CEM)

Knowing the promising results of radiographic imaging with contrast agents, it is natural to acquire mammogram with intravenous contrast agents. Iodine-base contrast media are typically used in radiology. As discussed in Section 1.2.1, Mo-Mo or Mo-Rh is the optimal x-ray anode-target combination used in mammography at lower kVp. The lower x-ray energies used increase the soft tissue contrast in mammography. However, in order to maximize the visualization of iodine-based agents, higher x-ray energies beyond the K-edge of iodine at 33.2 keV is typically used in contrast-enhanced mammography. Most studies of CEM use x-ray spectra up to 50 kVp with digital mammography units. The higher x-ray energies used in CEM allow higher contrast-to-noise ratio in iodine but sacrifice the visualization of microcalcifications. Studies show that CEM can potentially improve the identification of breast

lesions in the the mammographically dense breasts ([Diekmann et al., 2011](#); [Jong et al., 2003](#)).

Temporal subtraction is one CEM protocol which can characterize the time sensitive property of contrast agents. For temporal subtraction, a pre-contrast image is acquired first. Then, the iodine-base contrast agent is administered. A number of post-contrast images are acquired after the contrast agent injection with a 1-minute interval. The pre-contrast image is subtracted from the post-contrast images to evaluate the temporal profile of the contrast enhancement. as an Alternative to DCE-MRI, studies found that multiple CEM is a cost-effective approach to depict the contrast kinetics, which may differentiate benign and malignant breast tumors. While the temporal subtraction can locate breast tumors with contrast agents, the visualization of breast tumors is often affected by motion artifact during the long acquisition time and poor subtraction due to the overlapping iodine signal. The use of compression can also affect the contrast kinetics profile. Therefore, the interpretation of the kinetic information from CEM needs further investigation.

### 1.3.3 Contrast-Enhanced Breast CT (CE-bCT)

With the promising indication of CEM and DCE-MRI, contrast-enhanced breast CT may overcome some of the limitations of CEM. Analogous to other contrast-enhanced imaging modalities, a pre-contrast bCT is acquired prior to the post-contrast bCT with 70 - 90 seconds of delay. Initial clinical studies ([Prionas et al., 2010](#)) at UCDMC found that the Hounsfield unit (HU) of malignant lesions was enhanced much higher than that of benign lesions ( $55.9 \text{ HU} \pm 4.0$  vs.  $17.5 \text{ HU} \pm 6.1$ ) in CE-bCT images. Furthermore, the tomographic nature of breast CT (see Section [1.2.2](#)) can resolve the overlapping tissues with contrast agents for better visualization of breast tumors. Along with other contrast-enhanced imaging, this exciting finding confirms the benefit of contrast agents for better detection of malignant breast tumors. The optimal delay time to acquire CE-bCT still remains unknown,

which requires low-dose projection imaging techniques to describe the contrast kinetics among women of different sizes. Limitations of CE-bCT include the invasive nature of the contrast injection, potential allergic reaction to the contrast agent in patients, and the likelihood of false positive in enhancing non-tumor regions in the breast.

## 1.4 Dual Energy Imaging

Dual-energy imaging was first developed for dual-energy x-ray absorptiometry (DEXA). The technique images bones with two different energy x-ray beams. The two x-ray images can estimate the soft-tissue absorption, and bone mineral density can then be determined by subtracting the soft-tissue absorption. The concept of DEXA were easily translated to other imaging protocols, such as chest, cardiac, and breast imaging. Dual-energy imaging may be a good candidate for a low-dose projection imaging to optimize bolus timing during the contrast-enhanced breast CT.

The dual energy technique exploits the energy dependence of the x-ray attenuation through materials of different compositions in the breast, specifically iodine and breast tissues. A pair of low and high-energy images is obtained after the administration of an iodinated contrast agent. The dual-energy subtracted image  $I_{DE}(x, y)$  is typically obtained using log-weighted subtraction combining the low-energy image  $I_L(x, y)$  and the high-energy image  $I_H(x, y)$  as

$$I_{DE}(x, y) = w_t \ln I_L(x, y) - \ln I_H(x, y) \quad (1.1)$$

where  $w_t$  is the weighting factor and  $I_0(x, y)$  is the image acquired with no object in the field of view. Log-weighted subtraction is implemented in order to enhance the visibility of the contrast uptake area in the image. The shaping of the x-ray spectrum to acquire the low and high-energy images is crucial. Typically, an x-ray spectrum is shaped by filtering with different materials, by changing the x-ray spectrum peak voltage, or the combination of the two schemes. Depending on the object of interest, the two spectra may be shaped

such that one spectrum has x-ray energies above the K-edge of the material of interest and the other below. Figure 1.3 illustrates the advantage of x-ray spectrum separation to achieve signal enhancement in the material of interest, which is iodine in this case. The combination of images acquired with the two spectra takes advantage of the dramatic differences between the x-ray transmission properties of the two materials of interest (e.g. iodine and breast tissues). Log-weighted subtraction (Lewin et al., 2003) and basis decomposition (Alvarez and Macovski, 1976) are typically used to process the contrast-enhanced dual energy image.

### 1.4.1 Contrast-Enhanced Dual Energy Mammography (CE-DEM)

Contrast-enhanced dual energy mammography is the dual energy projection imaging of the breast with iodine-based contrast agents. The idea of contrast-enhanced dual energy mammography was pioneered a decade ago (Lewin et al., 2001), but the detector technology, such as x-ray image screens and image intensifiers, was the limiting factor in producing high-quality images. Current state-of-art x-ray detectors have been developed to be highly sensitive to detect signal from x-ray photons. X-ray peak voltages ranging between 45 and 49 kVp are typically used in acquiring dual-energy mammography. The dual-energy technique was implemented with several technologies including flat-panel thin-film-transistor detectors (Richard et al., 2005), scanned multislit system (Bornefalk et al., 2006), and photon-counting detectors (Carton et al., 2007). Encouraging technical and clinical results have been published for the last several years on contrast enhanced dual-energy mammography as a potentially useful adjunct to mammography. Johns et al. (1985) was the first groups to pioneer this imaging technique in breast imaging to demonstrate that dual-energy imaging can indeed enhance the detectability of calcification in a breast in a phantom study. Lewin et al. (2003) was first to implement dual-energy contrast-enhanced digital subtraction

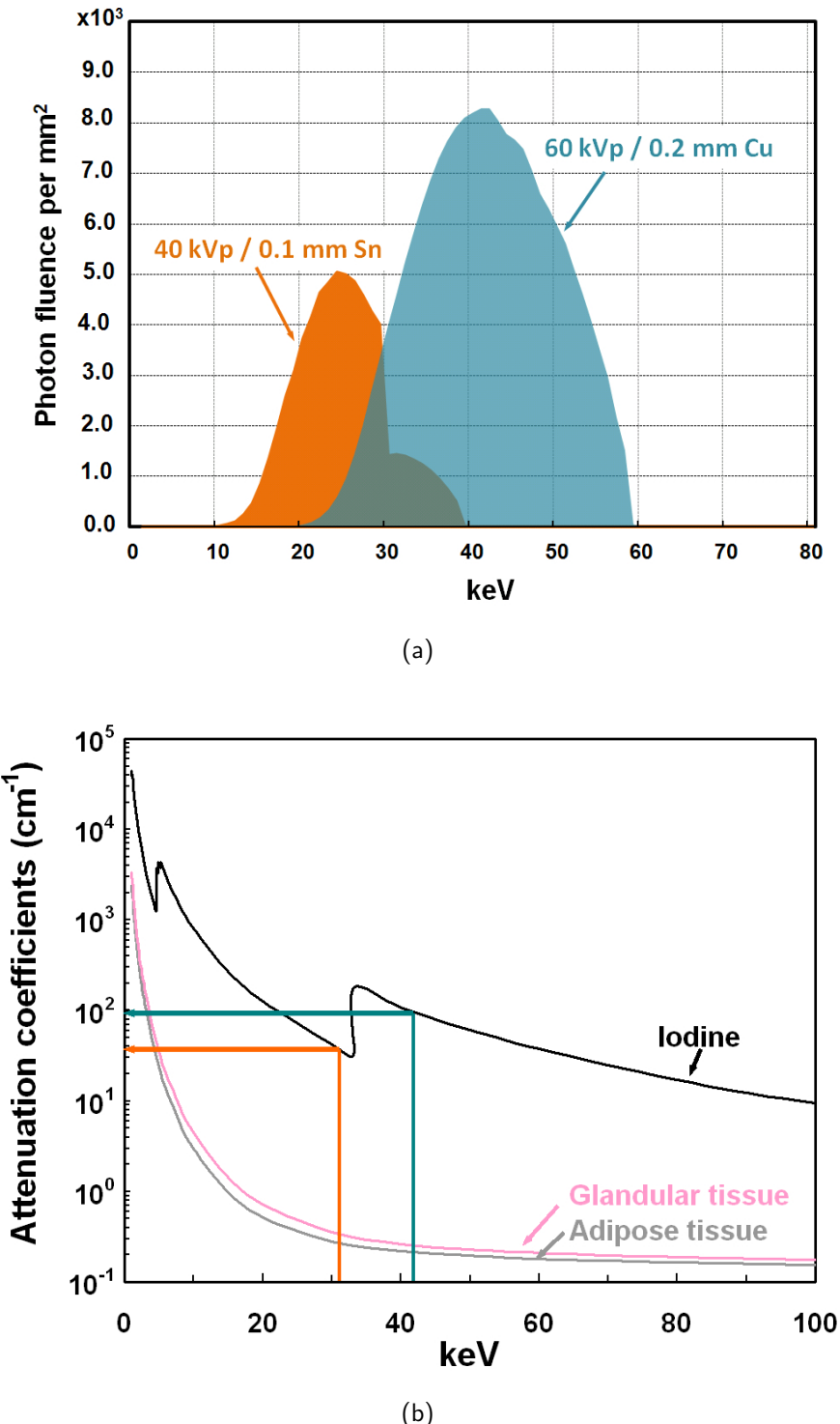


Figure 1.3. **(a)** The separation of two x-ray spectra (40 kVp filtered with 0.1-mm Sn and 60 kVp filtered with 0.2-mm Cu) in dual energy imaging is illustrated. **(b)** The difference in x-ray attenuation coefficients of iodine (the signal of interest in this example) is shown. The effective energy of the x-ray spectrum with 40 kVp/0.1 mm Sn is 31.1 keV, whereas that of the x-ray spectrum with 60 kVp/0.2 mm Cu is 43.8 keV.

mammography in a clinical trial where 85% of the invasive cancers showed strong enhancement.

Despite the limitations of projection breast imaging such as tissue superposition, promising lesion enhancement with contrast agents in CEDEM likely improve the sensitivity to breast cancer. In addition to visualization of breast tumor, the kinetic profile of contrast agents was found to provide addition information for diagnosis. The two energy images from the dual-energy mammography can be acquired in a short period of time (sub-second), and can reduce the amount of motion artifact with relatively low patient dose. Our laboratory is currently engaged in a phase II breast CT clinical trial, including non-contrast and contrast-enhanced breast CT acquisition. The ability to quantify the kinetic properties of tumor enhancement on per patient basis would benefit the imaging protocol design and the ability to detect breast cancer. Since dynamic breast CT will deliver much higher radiation dose to patients, we propose the use of contrast-enhanced dual-energy mammography (CEDEM) as a cost-effective, low-dose technique adjunct to breast CT system to depict the kinetic curve in breast cancer shown in Figure 1.4. CEDEM could also be used in concert with a contrast-enhanced breast CT acquisition.

## 1.5 Dissertation Overview

The dissertation will investigate the implementation of contrast-enhance dual energy mammography using breast CT platform. Before implementing any imaging technique, it is important to thoroughly understand the object of interest. Therefore, Chapter 2 will describe the extensive characterization of breast morphology using the breast CT data sets available from the breast CT clinical trial at UC Davis Medical Center. In addition to understand the object of interest, it is important to characterize the imaging system. Chapter 3 will describe the model and methods to simulate projection images using breast CT system in hope to guide the optimization of CEDEM. Chapter 4 will

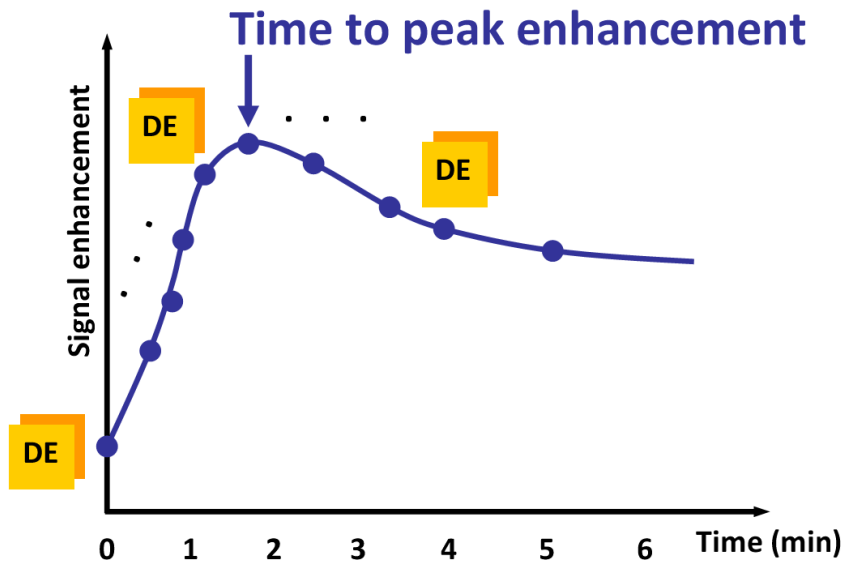


Figure 1.4. The characterization of signal enhancement from the contrast agent is illustrated as a function of time using the dynamic CEDEM acquisition.

focus on the methods and results of several CEDEM optimization tasks in the hope to implement CEDEM clinically. Finally, Chapter 5 will conclude the dissertation with summaries and future directions of CEDEM. Appendices are included with additional work on generating forward projection images of a breast CT volume rotated with the desired angles.

## 1.6 References

- S.F. Altekruse, C.L. Kosary, and M. Krapcho. Seer cancer statistics review, 1975-2007. Technical report, National Cancer Institute, 2010. [1.1](#)
- R. E. Alvarez and A. Macovski. Energy-selective reconstructions in x-ray computerized tomography. *Phys Med Biol*, 21(5):733–44, 1976. [1.4](#)
- M. Barbareschi, N. Weidner, G. Gasparini, L. Morelli, S. Forti, C. Eccher, P. Fina, O. Caffo, E. Leonardi, F. Mauri, P. Bevilacqua, and P. D. Palma. Microvessel density quantification in breast carcinomas - assessment by

- light-microscopy vs a computer-aided image-analysis system. *Applied Immunohistochemistry*, 3(2):75–84, 1995. [1.3.1](#)
- J. M. Boone, A. L. Kwan, J. A. Seibert, N. Shah, K. K. Lindfors, and T. R. Nelson. Technique factors and their relationship to radiation dose in pendant geometry breast ct. *Medical physics*, 32(12):3767–76, 2005. [1.2.2](#)
- H. Bornefalk, J. M. Lewin, M. Danielsson, and M. Lundqvist. Single-shot dual-energy subtraction mammography with electronic spectrum splitting: feasibility. *Eur J Radiol*, 60(2):275–8, 2006. [1.4.1](#)
- A. K. Carton, K. Lindman, C. Ullberg, T. Francke, and A. D. A. Maidment. Dual-energy subtraction for contrast-enhanced digital breast tomosynthesis. *Proceedings of SPIE*, 6510:651007, 2007. [1.4.1](#)
- F. Diekmann, M. Freyer, S. Diekmann, E. M. Fallenberg, T. Fischer, U. Bick, and A. Pollinger. Evaluation of contrast-enhanced digital mammography. *Eur J Radiol*, 78(1):112–21, 2011. [1.3.2](#)
- R. E. Hendrick. *Breast MRI Fundamentals and Technical Aspects*. Springer Science + Business Media, LLC, 2008. [1.3.1](#)
- P. C. Johns, D. J. Drost, M. J. Yaffe, and A. Fenster. Dual-energy mammography: initial experimental results. *Med Phys*, 12(3):297–304, 1985. [1.4.1](#)
- R. A. Jong, M. J. Yaffe, M. Skarpathiotakis, R. S. Shumak, N. M. Danjoux, A. Gunesekara, and D. B. Plewes. Contrast-enhanced digital mammography: initial clinical experience. *Radiology*, 228(3):842–50, 2003. [1.3.2](#)
- M. V. Knopp, E. Weiss, H. P. Sinn, J. Mattern, H. Junkermann, J. Radeleff, A. Magener, G. Brix, S. Delorme, I. Zuna, and G. van Kaick. Pathophysiologic basis of contrast enhancement in breast tumors. *Jmri-Journal of Magnetic Resonance Imaging*, 10(3):260–266, 1999. [1.3.1](#)
- D. B. Kopans. *Breast Imaging*. Lippincott Willimans & Wilkins Kluwer Business, Philadelphia, PA, 3rd edition, 2007. [1.2.1](#)

M. Kriege, C. T. Brekelmans, C. Boetes, P. E. Besnard, H. M. Zonderland, I. M. Obdeijn, R. A. Manoliu, T. Kok, H. Peterse, M. M. Tilanus-Linthorst, S. H. Muller, S. Meijer, J. C. Oosterwijk, L. V. Beex, R. A. Tollenaar, H. J. de Koning, E. J. Rutgers, and J. G. Klijn. Efficacy of mri and mammography for breast-cancer screening in women with a familial or genetic predisposition. *N Engl J Med*, 351(5):427–37, 2004. [1.2.3](#)

J. M. Lewin, F. Larke, and R. E. Hendrick. Dual-energy contrast-enhanced digital subtraction mammography: Development and clinical results of a new technique for breast cancer detection. *Radiology*, 221:339–339, 2001. [1.4.1](#)

J. M. Lewin, P. K. Isaacs, V. Vance, and F. J. Larke. Dual-energy contrast-enhanced digital subtraction mammography: feasibility. *Radiology*, 229(1):261–8, 2003. [1.4](#), [1.4.1](#)

K. K. Lindfors, J. M. Boone, T. R. Nelson, K. Yang, A. L. Kwan, and D. F. Miller. Dedicated breast ct: initial clinical experience. *Radiology*, 246(3):725–33, 2008. [1.2.2](#)

J. S. Michaelson, M. Silverstein, J. Wyatt, G. Weber, R. Moore, E. Halpern, D. B. Kopans, and K. Hughes. Predicting the survival of patients with breast carcinoma using tumor size. *Cancer*, 95(4):713–23, 2002. [1.1](#)

K. A. Miles. Tumour angiogenesis and its relation to contrast enhancement on computed tomography: a review. *Eur J Radiol*, 30(3):198–205, 1999. [1.3.1](#)

N. D. Prionas, K. K. Lindfors, S. Ray, S. Y. Huang, L. A. Beckett, W. L. Monsky, and J. M. Boone. Contrast-enhanced dedicated breast ct: initial clinical experience. *Radiology*, 256(3):714–23, 2010. [1.3.3](#)

S. Richard, J. H. Siewerdsen, D. A. Jaffray, D. J. Moseley, and B. Bakhtiar. Generalized dqe analysis of radiographic and dual-energy imaging using flat-panel detectors. *Med Phys*, 32(5):1397–413, 2005. [1.4.1](#)

X. J. Rong, C. C. Shaw, D. A. Johnston, M. R. Lemacks, X. Liu, G. J. Whitman, M. J. Dryden, T. W. Stephens, S. K. Thompson, K. T. Krugh, and C. J. Lai. Microcalcification detectability for four mammographic detectors: flat-panel, ccd, cr, and screen/film). *Med Phys*, 29(9):2052–61, 2002. [1.2.1](#)

M. van Vliet, C. F. van Dijke, P. A. Wielopolski, T. L. ten Hagen, J. F. Veenland, A. Preda, A. J. Loeve, A. M. Eggermont, and G. P. Krestin. Mr angiography of tumor-related vasculature: from the clinic to the micro-environment. *Radiographics*, 25 Suppl 1:S85–97; discussion S97–8, 2005.

[1.3.1](#)

K. Yang, A. Kwan, G. Burkett, and J. M. Boone. Hounsfield units calibration with adaptive compensation of beam hardening for a dose limited breast ct system, July 30 - Aug 3, 2006 . [1.2.2](#)

## Chapter 2

# The Characterization of Breast Morphology



## 2.1 Breast Skin Thickness

### 2.1.1 Motivation

Dosimetry for both screen-film and digital mammography relies directly on the normalized glandular dose (DgN) coefficients which are determined using Monte Carlo computations (Boone and V. N. Cooper, 2000; Boone et al., 2000). For most DgN coefficients that are used in the United Kingdom and the United States, the skin thickness surrounding the breast was assumed to be 4 mm (Boone, 1999; Dance, 1980, 1990; Rosenstein et al., 1985; Wu et al., 1991, 1994). While skin thickness is a relatively minor consideration in breast dosimetry in regards to mammography, the skin surrounding the breast tissue does act much like an x-ray beam filter, preferentially removing low-energy x-ray photons which contribute primarily to radiation dose to the breast. In addition to the slight beam filtration effect, the skin layer on the x-ray entrant side of the breast experiences the full incident x-ray beam, and tissues at greater depth receive exponentially less of the x-ray beam intensity.

Recent investigations in our laboratory have focused on the engineering development and clinical implementation of breast computed tomography (CT) (Boone et al., 2005). Access to the high-resolution breast CT (bCT) images from 51 women has allowed the assessment of skin thickness for the screening population. Based upon the observation of these images, and because the skin thickness is known to play at least a minor role in breast dosimetry, an analysis of the skin thickness on bCT images was performed to develop a more accurate understanding of the range of skin thickness encountered in the clinical screening population.

### 2.1.2 Patient Population

A prototype breast CT scanner Section 1.2.2 was used to conduct phase I and II clinical trial studies under several IRB-approved protocols. In the phase

In trial, breast CT images were acquired from 10 healthy women volunteers. During phase II testing, women who may have breast cancer (BIRADS 4 & 5) were imaged in order to evaluate the efficacy of breast CT for the early detection of breast cancer. BCT images were acquired prior to the breast biopsy. A total of 100 single breast volume data sets from 51 women were used to analyze the breast skin thickness (bilateral bCT volume sets from 49 women; unilateral bCT volume data from 2 women). Fifty-eight breast volume sets were the healthy breasts of normal volunteers and the contralateral breasts of those with benign findings and breast cancer. Two breast volume sets were the breasts with benign findings, while the remaining forty breast volume sets were diagnosed with breast cancer. The bra cup size was used as a parameter in x-ray technique selection, and the 51 women examined in this investigation had the following distribution: A cup: 1, B: 12, C: 20, D: 14, and DD: 4.

### 2.1.3 Image Spatial Resolution

To ensure the accuracy of the skin thickness analysis, the measured and actual voxel positions in the x, y, and z directions from a reference phantom were compared. A phantom was designed and constructed as shown in Figure 2.1. It was composed of two foam boards crossed and secured on a platform. On each board, a number of 6-mm, round, plastic pellets (BBs) were securely placed in several columns that were 25 mm apart. Six or more BBs were placed 1.0 or 2.0 cm apart in each column. The true physical distance between the BBs in x and y direction was measured with a standard ruler. The orientation of the boards was designed such that distances between BBs in the x and y plane could be directly measured from the reconstructed images in the coronal view. Distances in the z direction were determined by examining the slice position (z) embedded in the header of the reconstructed images. The true distance between the BBs in the image data sets along the z direction was independently computed using custom software ([Yang et al., 2006](#)). This software individually tracked the projection position of all BBs

relative to the detector plane in one column from 500 acquired projection images to compute the true physical distance between each BB in the z direction. CT scan data sets were acquired in order to precisely locate columns of steel BBs at eleven different positions. Linear regression was used to fit the distances determined from the images against the physically measured distances. The orientation of the reconstructed bCT images was also verified from the design of this phantom, as the top corners of the foam boards were labeled with different numbers of BBs representing the four orientations within a bCT image. The correct orientation of the reconstructed bCT images, however, was not crucial in this analysis.

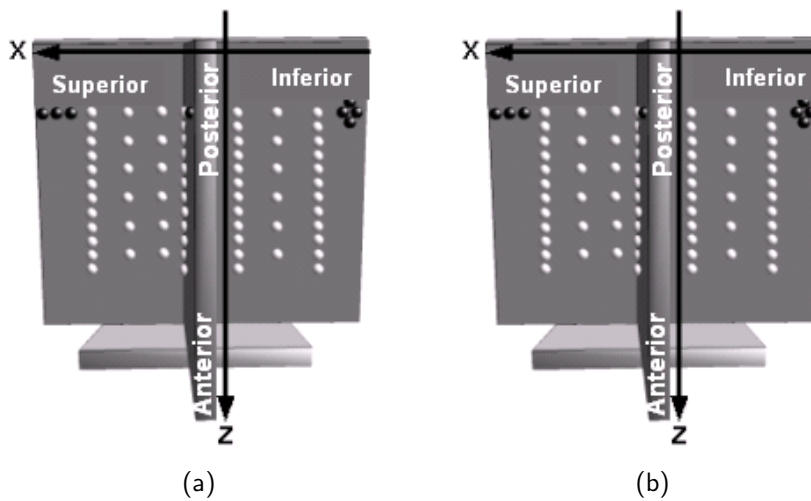


Figure 2.1. The spatial accuracy phantom was constructed with two foam boards, as shown in (a) side view and (b) top view. The corresponding x, y, and z dimensions in a reconstructed volume set are illustrated as well.

Figure 2.2a, Figure 2.2b, Figure 2.2c show the relationship between distances measured using the bCT image data as a function of physical measurements, for the x, y, and z dimensions, respectively. Each of these curves is seen to lie very close to the line of identity. Linear regression was also used, and the best-fit lines fall closely to the slope (1.0) and intercept (0.0) of the line of identity, with some bias at small values.

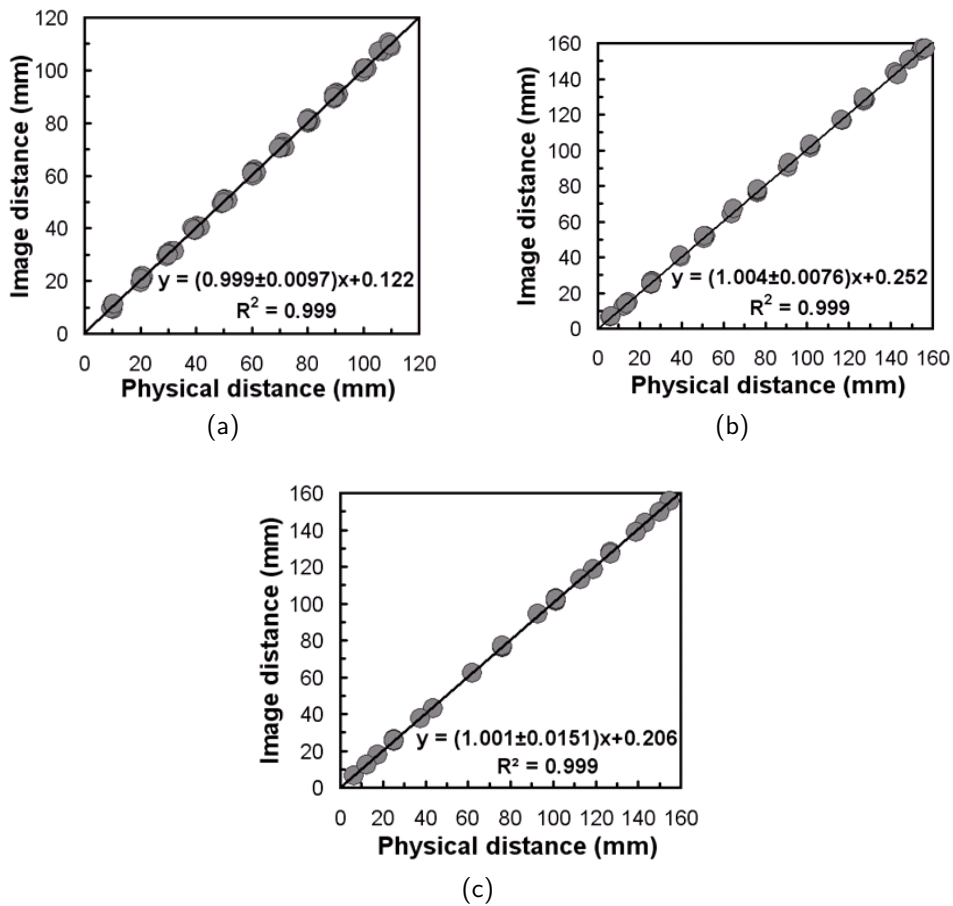


Figure 2.2. The relative physical distances are shown for the **(a)** x-dimension, **(b)** y-dimension, and **(c)** z-dimension of a reconstructed volume as a function of the relative distances measured from the reconstructed image.

#### 2.1.4 The Three-Dimensional Skin Thickness Algorithm

The image data sets of 51 women (100 breasts) were downloaded to a workstation, and breast skin thickness was evaluated. For the coronal bCT images, the breast silhouette was segmented from the air surround using a threshold value computed by a histogram-based iterative algorithm ([Gonzalez and Woods, 2002](#)). The iterative algorithm computed an optimal threshold by recursively searching for the best image intensity which distinguishes between the breast tissue and background (air) gray scale. The image histogram was separated into two regions based on the average of the gray scale

values within two user-defined regions. With this approach, the portion of bCT image corresponding to air was suppressed to a gray scale value of zero.

Segmentation of the breast skin layer was implemented with a simple derivative filter in a circular-ray tracing fashion. Skin segmentation was performed on the coronal images. The center of mass was determined for the breast in each image. From the center of mass, a line was projected outward at 0.5-degree intervals for a 360-degree radial evaluation of the image (Figure 2.3a). Each line continued to the edge of the breast, or one pixel inward from where the surrounding air was previously segmented. In order to rectify any under or over estimation of skin exterior, the Euclidean distance between the center of mass and the skin edge (skin exterior length) was evaluated. The skin exterior length as a function of angle was replaced with the mean skin exterior length (determined over 360 degrees) of the adjacent skin exteriors if it significantly deviated from the mean skin exterior length. This procedure had the effect of smoothing the skin contour. Each profile was evaluated from the breast edge inward, in the direction towards the center of mass. To account for the ambiguity between glandular tissue and skin (which have very similar gray scale values), the search range was restricted to 5 mm. Based on simulations and performance on the bCT images, it was found that this resulted in robust detection of the inner skin layer. The actual number of pixels evaluated in this process varied, since each breast volume set had slightly different pixel dimensions. A first-order derivative filter was applied along each profile to differentiate the gray-level intensity between a pixel and its outward adjacent pixel. The inner skin layer was positioned one pixel inward (towards the center of mass) from the pixel transition having the minimum gradient (Figure 2.3b).

The position of the inner and outer skin layers located by the preliminary radial evaluation did not reflect the best estimate of the border locations due to the presence of noise. With the 720 locations of inner and outer skin layers initially determined at 0.5-degree increments around the breast, the Euclidean distance between the inner and outer skin layer positions was

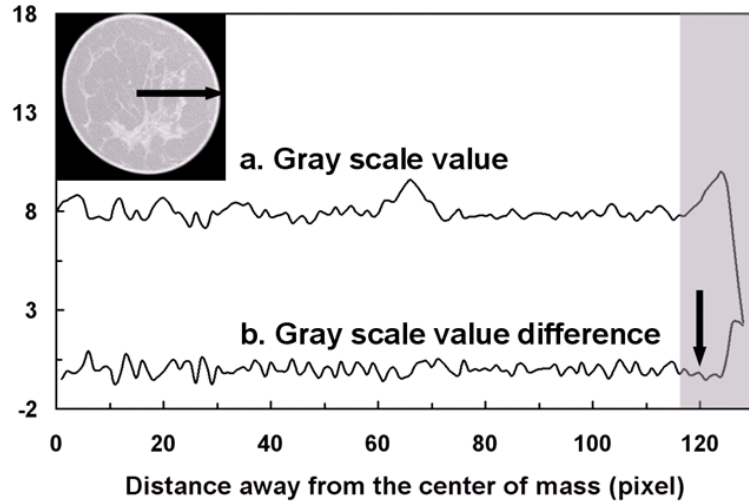


Figure 2.3. (a) A profile acquired from the 360-degree radial scan illustrating the gray value distribution of a breast from the center of mass towards the skin edge for the 0-degree profile. (b) This curve illustrates the gray value difference determined by applying a first-order derivative filter to the profile in (a). The gray region designates the region of interest in locating the inner skin layer.

computed as the preliminary skin thickness, as a function of angle. The computed thickness was spatially filtered with a  $1 \times 5$  average kernel to reduce the level of noise in the preliminary skin thickness evaluation. The average kernel used is defined in Equation (2.1):

$$g(x) = \sum_{k=1}^M s(x+k)h(k) \quad (2.1)$$

$$h(x) = \frac{1}{M}, \text{ where } x = \frac{-M}{2}, \dots, \frac{M}{2}$$

where  $s(x)$  is the non-smoothed skin thickness,  $h(x)$  is the average kernel of size  $M$ , and  $g(x)$  is the smoothed skin thickness. The noise-reduced, finely sampled inner and outer breast skin boundaries were determined for each bCT coronal image (at a specific position along the breast anterior-posterior direction). The collection of inner and outer two-dimensional skin boundaries for all of the coronal bCT images represented a three-dimensional (3D) description of the breast boundaries, i.e. a set of 3D point clouds. The 3D

breast boundaries were used to determine the actual skin thickness, taking into consideration the curvature of the breast in the anterior-posterior direction (this procedure is described in the next paragraph).

The most accurate estimate of breast skin thickness was to measure the distance between the inner and outer skin layers with respect to the 3D normal to the surface of the breast. To realistically fit the 3D surface, a set of small surface patches which spanned the breast surface in 3D was used (Figure 2.4a). At a radial location of a specific z position, 36 surrounding sampled points were used to fit a plane in a least-square fashion (using an opened source plane fitting routine ([Kovesi](#))). Two planes corresponding to the inner and outer skin layers were fit to the surface patches. The breast skin thickness was measured by determining the distance from the 3D normal of the inner skin plane to the outer skin plane (Figure 2.4b). Forty-eight radial locations were used at each z position (the number of z positions depends on the breast length) to determine the skin thickness of a given breast. To eliminate obvious outliers among the skin thickness estimate from the least-square approach, the 10% trimmed mean among the skin thickness estimate across the fitted breast surface was computed as the single “skin thickness” for each breast. The mean, standard deviation, and range of the measured skin thickness were evaluated for 100 breasts corresponding to 51 women. In addition, distributions of the skin thickness estimate among different breast metrics (bra cup size A, B, C, D, and DD; right vs. left breast) were determined.

### 2.1.5 Algorithm Validation

In order to validate the accuracy of the skin-thickness algorithm, a physical phantom was constructed using a water-filled plastic bowl. A CT scan of the bowl was acquired using the breast CT scanner. The wall thickness around the bowl was physically measured with a micrometer (Starrett N. 436-1IN, 0.001-inch precision) at several locations around the surface of the bowl. The average value among the wall thickness of the physical phantom was consid-

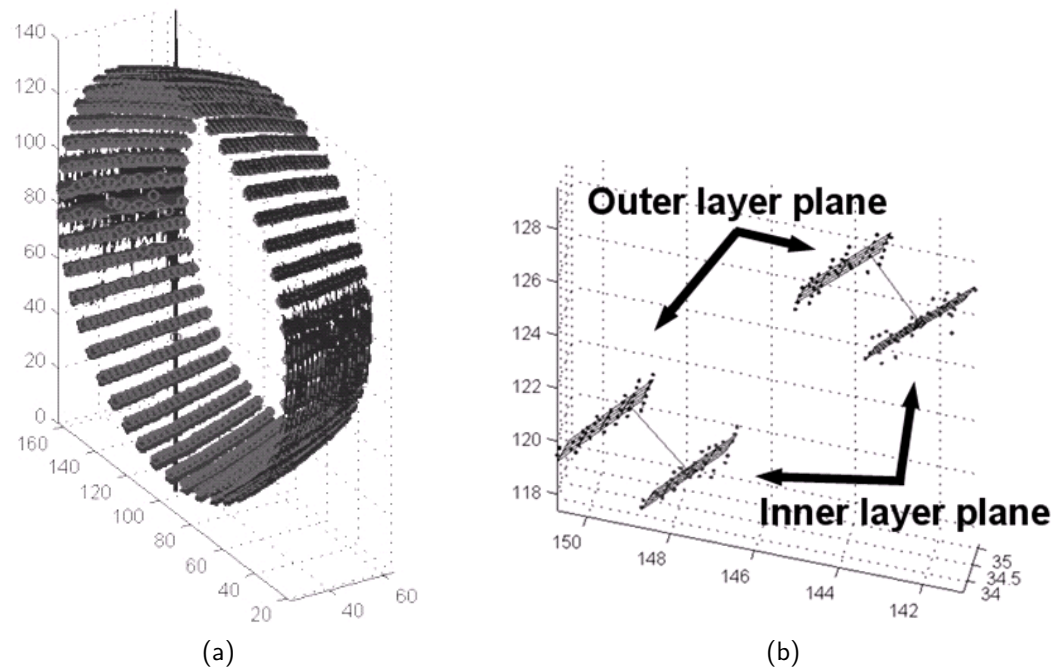


Figure 2.4. The three-dimensional, patch-by-patch plane-fitting method to measure the breast skin thickness is illustrated. The fitted planes of the inner and outer wall layers are shown from the CT images of the physical phantom. (a) This graph illustrates the three-dimensional planes (least-square fitted) to the inner and outer layers over the entire surface. (b) The thickness was measured with the distance originating from a point on the fitted inner layer plane along its normal to the outer layer plane.

ered as “truth” to compare with the algorithmically-determined wall thickness of the corresponding portion of the physical phantom. The histogram of the estimated wall thickness of the physical phantom was evaluated to examine the accuracy of the thickness measurements.

Among 61 manual thickness measurements of the physical phantom, the mean wall thickness ( $\pm$  standard deviation) was  $2.58 \pm 0.17$  mm. This measurement was considered as the “truth” to validate the accuracy of the algorithm. From the CT images of the physical phantom, the mean algorithm-measured thickness was  $2.30 \pm 0.21$  mm. Although the estimated thickness was significantly different from the truth by approximately 0.2 mm ( $p < 0.001$ , Mann-Whitney rank sum test), the range of the “truth” thickness overlapped

largely with that of the algorithm-measured thickness. Figure 2.5 illustrates the distribution of the estimated wall thickness of the physical phantom using 461 surface patches. The histogram displays a fairly concentrated profile close to the estimated wall thickness. This assessment suggests that the skin-thickness algorithm is accurate to within approximately  $200\text{ }\mu\text{m}$ . Thus, the algorithm can be adapted to the clinical bCT data with the same degree of accuracy.

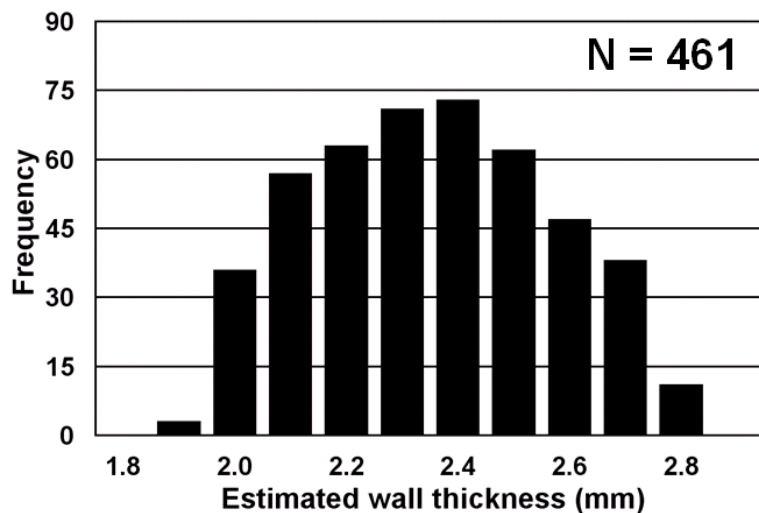


Figure 2.5. A histogram shows the distribution of wall thickness using the three-dimensional, patch-by-patch approach on the surface sampled from the CT images of the physical phantom. Among 461 surface patches, the average wall thickness ( $\pm$  intra-measurement standard deviation) was  $2.30 \pm 0.21$  mm, with the range from 1.9 to 2.7 mm.

### 2.1.6 The Breast Skin Thickness Using BCT

A histogram of breast skin thickness estimated by the 3D skin thickness algorithm among the entire patient population is shown in Figure 2.6. Among 51 women, the mean breast skin thickness ( $\pm$  inter-breast standard deviation) was found to be  $1.45 \pm 0.30$  mm (ranging from 0.9 to 2.3 mm). The mean breast skin thickness among the cancer-free breasts was found to be

$1.45 \pm 0.29$  mm (ranged from 1.0 to 2.2 mm), while the average skin thickness among those with benign findings was  $1.53 \pm 0.54$  mm (ranged from 1.2 to 1.9 mm). The mean skin thickness among breasts with biopsy-confirmed breast cancer was found to be  $1.46 \pm 0.32$  mm (ranged from 0.9 to 2.3 mm). There was no significant difference between these three groups: benign vs. cancer-free ( $p = 0.918$ , Mann-Whitney rank sum test), cancer-free vs. breast cancer ( $p = 0.712$ , t-test), and benign vs. breast cancer ( $p = 0.769$ , t-test). Among the three populations, most women (i.e. the 50% range) have breast skin thickness spanning between 1.2 and 1.6 mm.

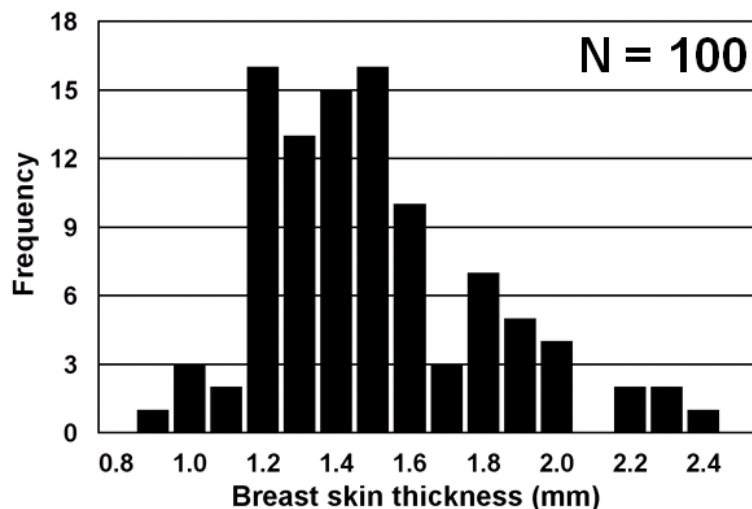


Figure 2.6. A histogram showing the distribution of breast skin thickness using the three-dimensional, patch-by-patch approach on the breast surface sampled from the clinical bCT volumes. Among 100 breasts (51 women), the average breast skin thickness ( $\pm$  inter-breast standard deviation) was  $1.45 \pm 0.30$  mm, ranged from 0.9 to 2.3 mm.

The histogram of the breast skin thickness estimated from the 3D approach of one single breast was shown in Figure 2.7. The skin thickness measurements from 692 breast surface patches demonstrated good precision with a mean skin thickness of 1.51 mm. Thus, the 3D surface fitting approach demonstrates the potential in reducing the bias from the non-normal crossing at the skin line.

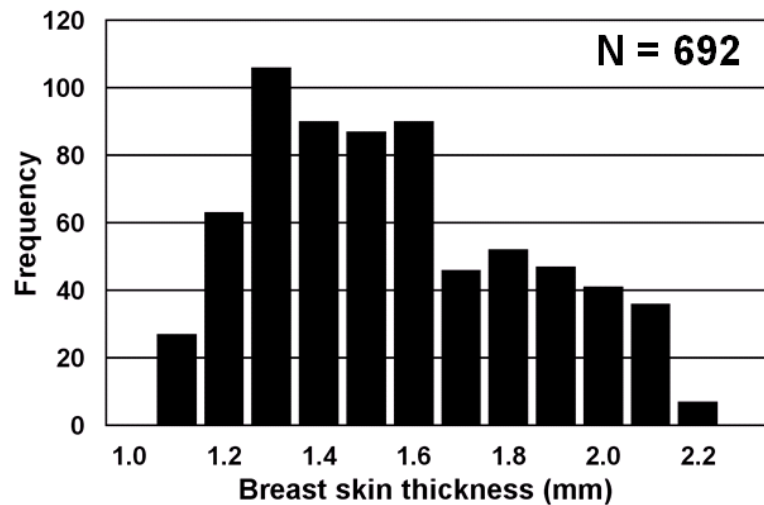


Figure 2.7. A histogram of breast skin thickness using the three-dimensional surface-fit approach with one single bCT volume data set. Among the skin thickness measured from 692 breast surface patches, the mean skin thickness ( $\pm$  intra-breast standard deviation) was  $1.51 \pm 0.28$  mm, with a range of 1.1 to 2.1 mm.

The skin thickness was determined as a function of the anterior-posterior position in the breast. Figure 2.8 shows the skin thickness as a function of relative position (in percent) between the most posterior slice and the most anterior slice of the bCT volume set, for a representative woman in each of five bra cup size categories (A, B, C, D, and DD). Each breast image data set used in Figure 2.8 represented the median breast volume for each bra cup size. Additionally, Table 2.1 lists the skin thickness distributions in Figure 2.8 numerically to better demonstrate the intra-breast standard deviation due to the algorithm. The breast skin profiles along the breast length of five different women show fairly uniform skin thickness across the entire breast surface. The fairly non-fluctuating trend seen in the profiles demonstrated the effectiveness of the 3D surface fitting approach to accurately measure the breast skin thickness at any 3D location on a breast skin surface.

Figure 2.9 shows the skin thickness of the left breast as a function of the skin thickness of the same woman's right breast. Linear regression was used

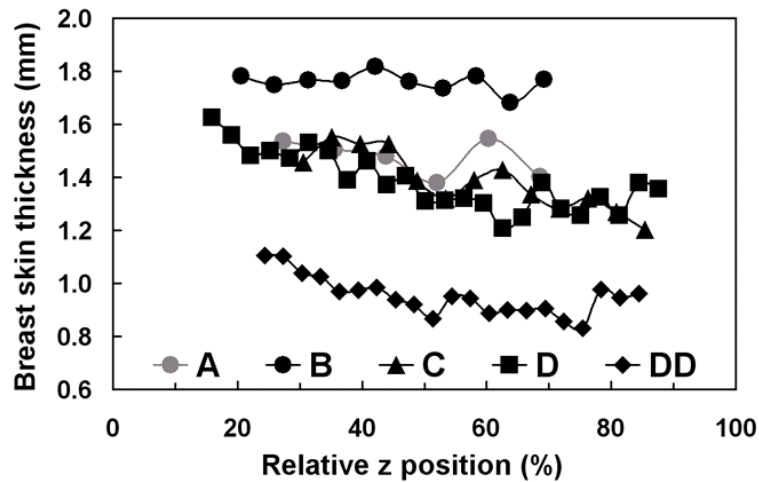


Figure 2.8. The breast skin thickness as a function of anterior-posterior position in breasts of 5 women representative of each bra cup size category (A, B, C, D, and DD). The graph illustrates the profile of skin thickness along the anterior-posterior direction of each breast.

Table 2.1. A list of mean breast skin thickness ( $\pm$  intra-breast standard deviation) and the corresponding range for five different breasts (bra cup size A, B, C, D, and DD). The data represent the same volume sets whose profile distributions were shown in Figure 2.8.

Bra cup size	Number of slice positions per breast volume set	Mean breast skin thickness $\pm$ intra-breast standard deviation (mm)	Breast skin thickness range (mm)
A	6	1.47 $\pm$ 0.07	1.4 - 1.5
B	10	1.76 $\pm$ 0.04	1.7 - 1.8
C	13	1.38 $\pm$ 0.10	1.2 - 1.6
D	24	1.38 $\pm$ 0.10	1.2 - 1.6
DD	21	0.95 $\pm$ 0.07	0.8 - 1.1

to fit the left versus right breast skin thickness. The linear regression equation suggests that left breast skin thickness correlates with right breast skin thickness (slope  $\pm$  slope variation of  $0.96 \pm 0.55$ ,  $r^2 = 0.8542$ ), as expected. Among 49 women, slightly thicker skin was observed in the left breast ( $p = 0.003$ , paired t-test). The thicker skin thickness in the left breast is likely due to the fact that left breasts were found to be slightly larger than right breasts in women (Manning et al., 1997; Scutt et al., 2006). The figure indicates some degree of uniform skin thickness between both breasts of a woman, which is an expected observation since skin thickness does not generally fluctuate largely over the both breasts (Witten, 1969).

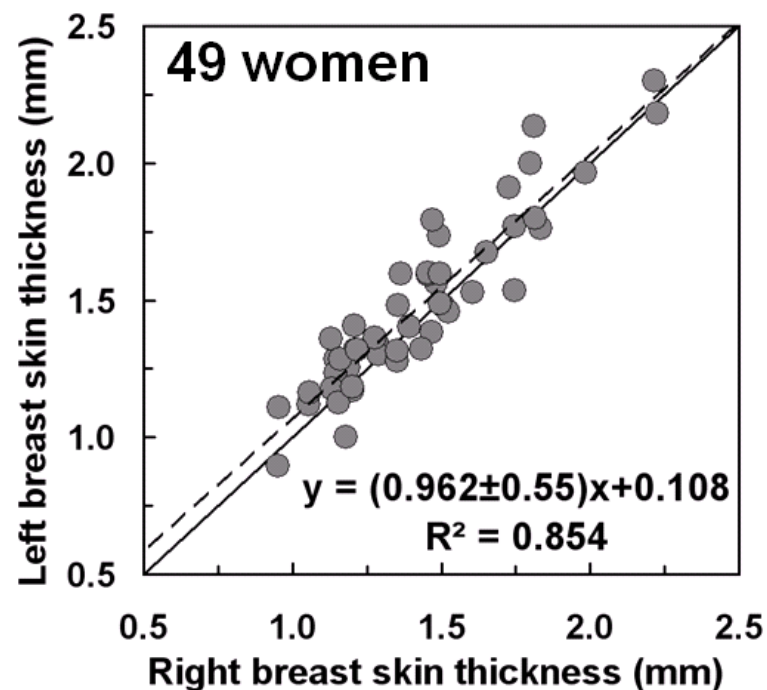


Figure 2.9. The relationship between the right breast skin thickness and the left breast skin thickness of the same woman (49 women is shown; two women had data for only one breast). The solid line is the line of identity. The fitted slope is significantly different from 1.0 ( $p = 0.003$ , paired t-test).

### 2.1.7 Breast dosimetry in mammography with Monte Carlo simulation

Previously validated Monte Carlo techniques (Boone, 1999; Boone and V. N. Cooper, 2000; Boone et al., 2000) were used to assess the normalized glandular dose coefficients ( $D_{gN}$ ) in mammography over a range of breast thickness (2 - 8 cm), x-ray energies (4-35 keV), and skin thickness (1.0 - 4.0 mm). The simulation was implemented based on the x-ray spectrum with molybdenum anode-molybdenum filter (Mo-Mo).  $D_{gN}$  values were determined using one million photons in a monoenergetic simulation, and a spectral model was used to convert the monoenergetic data to the polyenergetic  $D_{gN}$  values (Boone, 1999).

The Monte Carlo results of the normalized glandular dose ( $D_{gN}$ ) coefficients for 4-cm and 6-cm 50% glandular breasts with different skin thickness (1.0 - 4.0 mm) are illustrated in Figure 2.10. The curves show the  $D_{gN}$  values expressed in mean glandular dose per incident air kerma ( $\text{mGy} \times \text{mGy}^{-1}$ ) over a range of x-ray spectra. Figure 2.11 demonstrates the influence of breast skin thickness in terms of the percentage increase in  $D_{gN}$  values relative to the assumption of a 4-mm skin thickness. Averaged over different x-ray spectra (24 - 35 kVp),  $D_{gN}$  values of a 4-cm 50% glandular breast increase by  $9.0\% \pm 1.1\%$  (standard deviation) for a 2.5-mm skin thickness and by  $16.0\% \pm 2.0\%$  for a 1.5-mm skin thickness. For a 6-cm 50% glandular breast, the  $D_{gN}$  values increases on average by  $11.0\% \pm 1.3\%$  for a 2.5-mm skin thickness and by  $19\% \pm 2.3\%$  for a 1.5-mm skin thickness.

### 2.1.8 Discussion and Conclusions

A comprehensive evaluation of breast skin thickness was performed across breast CT image data sets from 51 women. In the early era of screen-film mammography, the thickness of the normal skin was widely quoted to be in the range from 0.5 to 1.5 mm (Witten, 1969). In more recent studies, the normal skin thickness of the breast was found to be slightly thicker, ranging from 0.7 to 3.0 mm (T. L. Pope et al., 1984; Willson et al., 1982). Another

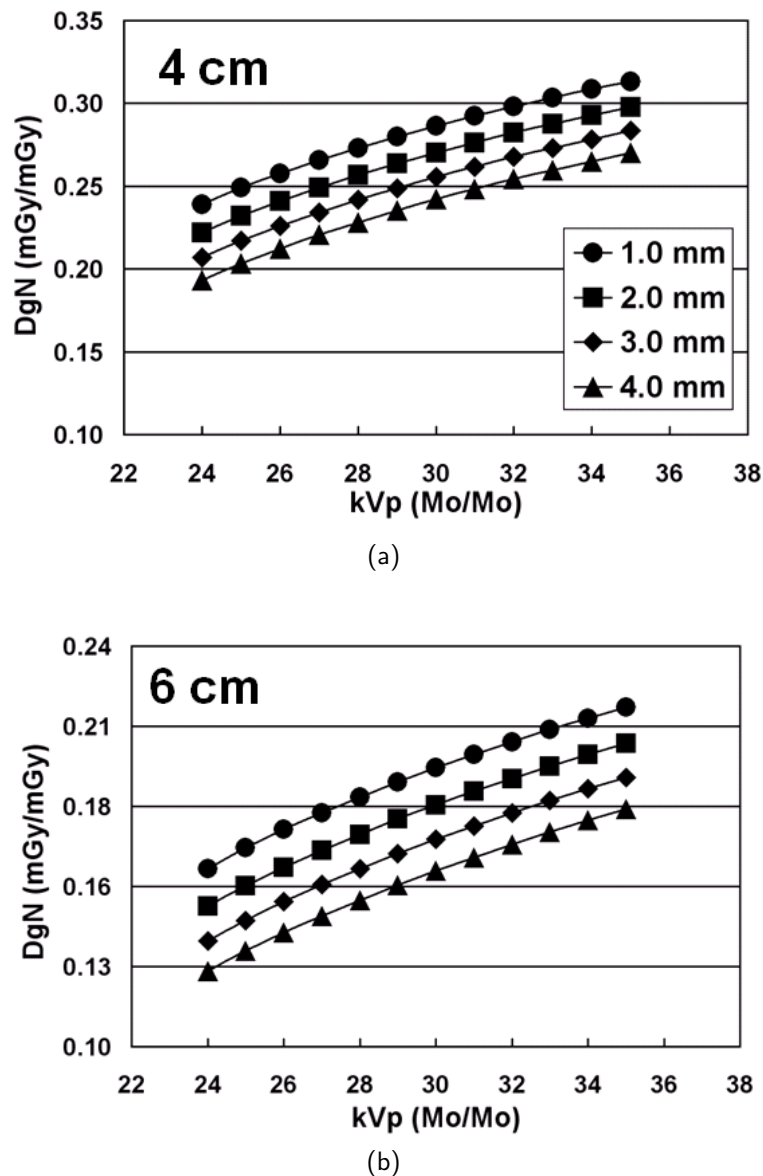


Figure 2.10. The normalized glandular dose ( $D_{gN}$ ) coefficients as a function of  $kVp$  for (a) a 4-cm 50% glandular breast and (b) a 6-cm 50% glandular breast with 1.0, 2.0, 3.0, and 4.0-mm skin thickness.

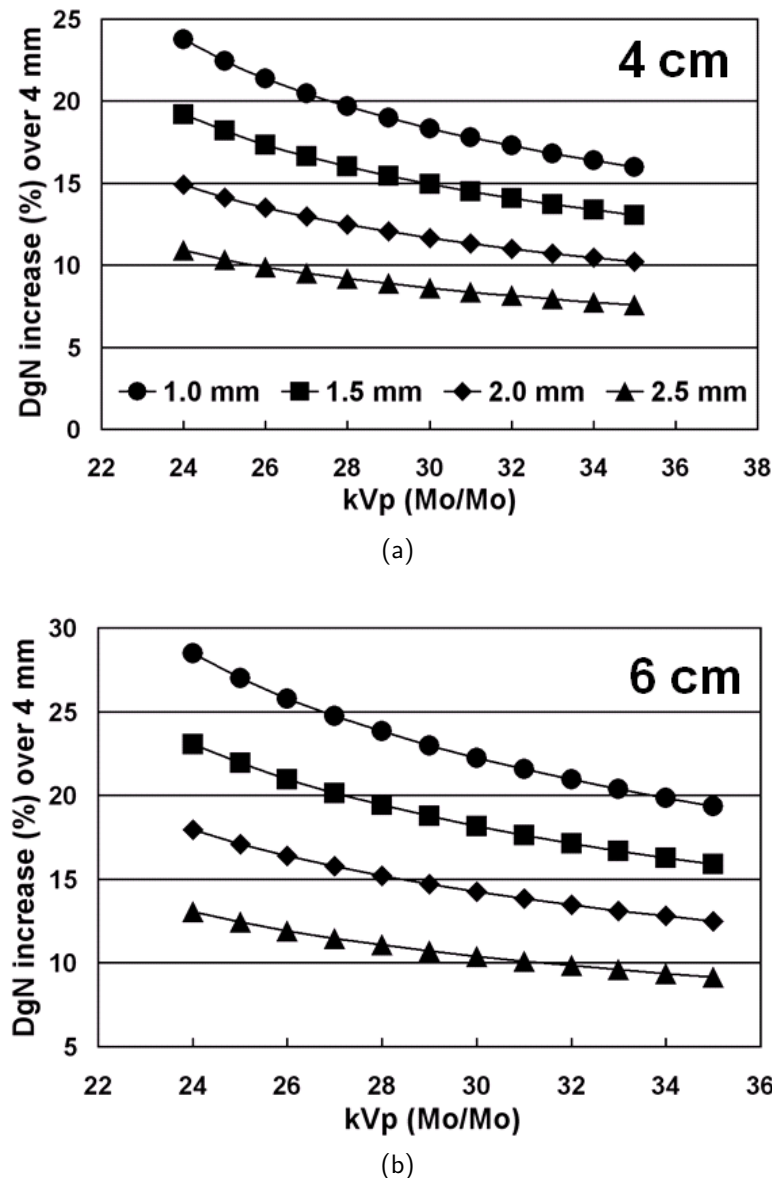


Figure 2.11. The  $D_{gN}$  increase (%) over that of a breast with 4-mm skin thickness as a function of kVp for (a) a 4-cm 50% glandular breast and (b) a 6-cm 50% glandular breast with 1.0, 1.5, 2.0, and 2.5-mm skin thickness.

recent study found that mammographic skin thickness ranged from 0.5 to 3.1 mm ([Ulger et al., 2003](#)). Our study has found a similar skin range (1.0 to 2.2 mm) among cancer-free breasts compared to the skin thickness range determined in previous studies. Skin thickness is one of the parameters considered in assessing the radiation dose in mammography. The skin thickness was assumed to be 4 - 5 mm for most Monte-Carlo based studies of  $D_{gN}$  values performed in the past ([Boone, 1999](#); [Dance, 1980, 1990](#); [Rosenstein et al., 1985](#); [Wu et al., 1991, 1994](#)). The smaller average skin thickness (1.45 mm) found in this study will result in slightly higher  $D_{gN}$  coefficients than those computed using greater skin thicknesses in the Monte Carlo computations. Figure [2.10](#) and Figure [2.11](#) demonstrate that a non-negligible increase in  $D_{gN}$  values occurs for typical mammographic spectra (24 - 35 kVp) when a thinner skin layer was used.

Normal human skin is comprised of three main layers: the epidermis, dermis, and subcutaneous fat tissues. The epidermis layer has a quoted range between 0.07 - 1.4 mm ([Farlex](#)); and the dermis layer is quoted to range between 1.0 - 2.0 mm ([Slomianka](#)). The average skin depth, including only the epidermis and dermis layers, was then approximately 2.24 mm. If indeed the subcutaneous fat layer of the skin (which is probably not resolved with breast CT) is distinct and isolated from the adipose tissue of the breast parenchyma, the thicker skin layer would act to shield the breast and existing  $D_{gN}$  values would likely to be accurate. If, however, glandular tissue filaments (which is the tissue at risk for breast cancer) can extend into the subcutaneous fat layer as anecdotal evidence from the breast CT images suggests, the thinner skin layers would imply that a slight increase in  $D_{gN}$  values would be warranted.

Although our study has shown that there is no significant difference among the skin thickness of three breast populations (cancer-free, benign, and cancer), Figure [2.12](#) demonstrates local skin thickening in a recent bCT data of a woman with biopsy-confirmed breast cancer. Previous studies have shown the prognostic significance of the mammographically demonstrated skin thickening among noninflammatory breast cancer ([Shukla et al., 1979, 1984](#)).

However, the correlation between breast cancer development and skin thickening is out of the scope of this study.

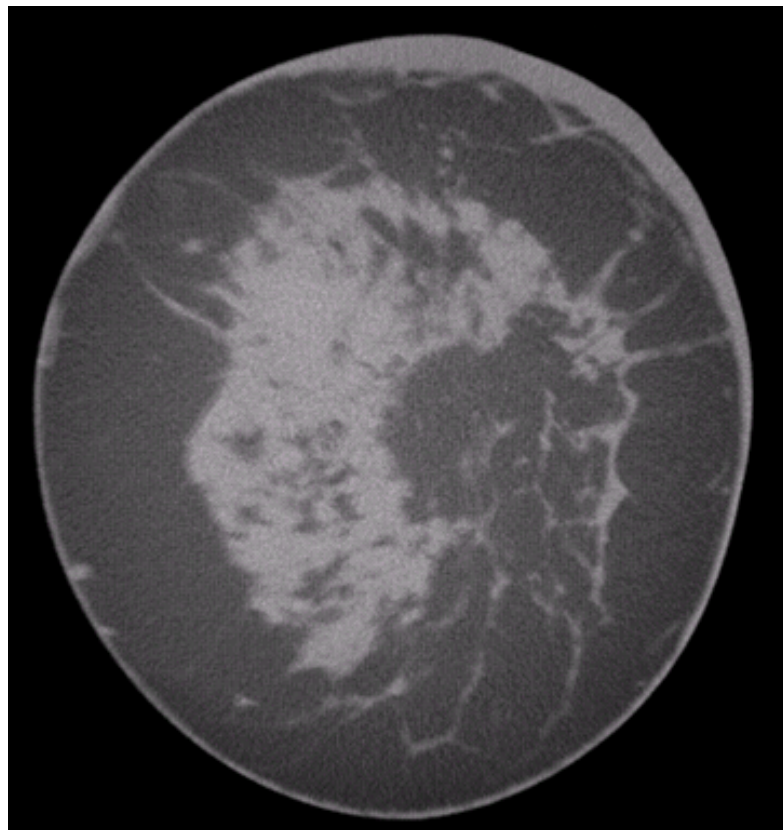


Figure 2.12. A coronal bCT image of a recent bCT participant displays local skin thickening in the breast with biopsy-confirmed breast cancer.

Breast CT images were used to assess skin thickness using an automated algorithm. The algorithm's accuracy was assessed against physical measurements of a breast-shaped phantom and found to be within 0.20 mm. The overall breast skin thickness from the 51 women assessed in this study was found to average  $1.45 \text{ mm} \pm 0.30 \text{ mm}$ . Most Monte Carlo derived dose conversion coefficients ( $D_{gN}$  coefficients) used for dosimetry in mammography assume a 4.0-mm breast skin thickness, and the thinner skin thickness found in this study would imply that a slight increase of 10 - 20% in  $D_{gN}$  coefficients may be warranted.

## 2.2 Breast Size, Shape, and Fibroglandular Tissue Distribution

### 2.2.1 Motivation

Understanding the characteristics of breast anatomy is the first step to modeling the interaction between the breast and a proposed or existing imaging system. Sophisticated physical phantoms and computer models of the breast have been useful for various research purposes including optimization of breast imaging systems and x-ray dosimetry using Monte Carlo simulation. Two-dimensional (2D) (Bochud et al., 1999; Kallergi et al., 1998; Lado et al., 1997; Lefebvre et al., 1994; Nappi and Dean, 1997) and three-dimensional (3D) (Bakic et al., 2002; Bliznakova et al., 2003) breast models have been developed. The complexity of breast tissues such as ductal lobular units, Cooper's ligaments, ductal networks, pectoralis muscles, and various types of breast cancer have been analyzed and simulated using well-established mathematical models based on 2D mammographic images. This advancement in characterizing breast morphology of a compressed breast is largely due to the fact that mammography, which images only compressed breasts, is the standard technology of breast cancer screening. With the advent of breast x-ray tomosynthesis, there is a growing need in the medical imaging community to correlate the information from 2D mammographic images with that of 3D breast images. This need is driven by a quest by radiologists specializing in breast imaging to better understand the topology of the 3D breast, as well as by researchers who focus on optimizing image content and reducing radiation dose in breast imaging.

The objectives of this work were to characterize the metrics of breast anatomy using 3D reconstructed data sets from a clinical trial of breast CT (bCT) and to compare the information available from the bCT data sets with that from 2D projection images of the breast. The data reported herein may be useful to researchers interested in developing breast imaging systems.

### 2.2.2 Image Acquisition and Patient Population

Two dedicated breast CT scanners (“Albion” and “Bodega”, see Section 1.2.2) were used to acquire the bCT images used in this investigation. For all available reconstructed bCT data set, a three dimensional segmentation method (Packard and Boone, 2007; Yaffe et al., 2009) used a combination of iterative thresholding, a connected-component algorithm, and a 3D median filter to segment each bCT volume data set into five components: air, adipose tissue, fibroglandular tissue, chest wall, and skin. For all the bCT volume data considered in this study, the segmentation result of the middle-breast coronal bCT image was visually inspected by one observer. The rating of “poor” indicates that less than 25% of the true fibroglandular tissue was segmented correctly as fibroglandular tissue by this method. A rating of “fair” indicates that approximately 50% of the true fibroglandular tissue was segmented, and a rating of “good” indicates that more than 75% of the true fibroglandular tissue was segmented. d The prototype breast CT scanners were used to conduct phase I and II clinical trial studies under several IRB-approved protocols. Informed, written consent was acquired from all participating women. In the phase I trial, breast CT images were acquired from 10 healthy women volunteers. During phase II testing, women who were at high degree of suspicion for breast cancer after their conventional imaging (BIRADS 4 & 5) were scanned in order to evaluate breast CT imaging. bCT images were acquired immediately prior to breast biopsy. Among 240 women, bCT images of 30 women with bilateral breast cancer, breast implants, poor segmentation results, or unavailable bCT images of the unaffected breast were excluded from this study. Pectoralis muscle was seen in bCT images in 85 out of 210 (40%) women in this study. A total of 208 women with bilateral bCT data sets (including those with benign, malignant, or no findings) were included in the comparison of volume glandular fraction between the affected (that breast containing the suspicious lesion) and unaffected breast. For all other analyses discussed herein, 219 single bCT data sets from 210 women (bilateral bCT data sets from 9 women) were used to analyze breast shape and

composition. Among the 219 bCT data sets, 22 bCT data sets were breasts with no biopsy (healthy volunteer) or no finding, 93 bCT data sets were from the unaffected breasts of women with benign findings, and 104 bCT data sets were from the unaffected breasts of women diagnosed with breast cancer. Bra cup size was used as a parameter in x-ray technique selection, and 216 out of 219 bCT data sets examined in this investigation had the following distribution; 9.7% (21) were A or AA cup, 25.5% (55) were B cup, 36.1% (78) were C cup, 28.7% (62) were D or DD cup. Experienced radiologists characterized breast density at mammography according to BIRADS criteria as fatty (< 25% fibroglandular tissue), scattered fibroglandular density (25% - 50% fibroglandular tissue), heterogeneously dense (51% - 75% fibroglandular tissue), or extremely dense (> 75% fibroglandular tissue). Since the mammograms of the 10 healthy women in this study were not available, the BIRADS breast density of 200 women was known; 9.0% (18) were fatty, 28.5% (57) were scattered, 39.0% (78) were heterogeneous, 23.5% (47) were extremely dense. The ages of the women in this study ranged between 35 and 82 years, with a median age of 54. Table 2.2 includes a summary of patient population distribution described above.

Among 219 bCT data sets, the visual assessment of the segmented bCT images demonstrated that 93.1% of the total bCT data sets were rated as “good” segmentation, 4.1% rated as “fair” segmentation, and 2.7% as “poor” segmentation.

### **2.2.3 Defining Breast Metrics**

#### **2.2.3.1 Breast Effective Diameter**

For a given coronal-reconstructed bCT image, the breast effective diameter was computed by equating the total pixels marked as “tissue” to the area of a circle  $A = \pi(\frac{D}{2})^2$ . For a bCT segmented image, any pixel marked as skin, chest wall, fibroglandular tissue, or adipose tissue was considered as “tissue” to compute the total pixel count (A) for each bCT image. The breast effective

Table 2.2. The breakdown of patient population for this study

<b>Categories</b>	<b>The comparison of VGF between the affected and unaffected breasts</b>		<b>All other studies</b>
	<b>Breast cancer diagnosis</b>	<b># of women (out of 208 women)</b>	<b># of bCT data sets (out of 219 bCT data sets)</b>
Healthy	12	22	
Benign findings	92	93	
Malignant	104	104	
<b>Bra cup size</b>		<b># of bCT data sets (out of 216 bCT data sets)</b>	
A or AA		21	
B		55	
C		78	
D or DD		62	
<b>BIRADS breast density</b>		<b># of bCT data sets (out of 200 bCT data sets)</b>	
Fatty		18	
Scattered		57	
Heterogeneous		78	
Dense		47	

diameter (cm) of a coronal bCT image position z was calculated as

$$D_{eff}(z) = 2 \cdot x_{pix} \cdot \sqrt{\frac{A}{\pi}} \quad (2.2)$$

where A is the total pixel count of breast area for a coronal bCT image and  $x_{pix}$  is the pixel dimension (cm) in a coronal bCT image.

For a given bCT data set, the first ( $s_{start}$ ) and last ( $s_{end}$ ) good coronal bCT images were manually determined and recorded. The first coronal image was visually determined as the most posterior image that was free of significant artifacts. The last coronal image was the most anterior image that did not

contain artifact or nipple. The breast diameter (cm),  $D_{chestwall}$ , was determined by averaging the breast effective diameter of the coronal bCT images close to the women's chest wall as

$$D_{chestwall} = \frac{1}{5} \sum_{z=s_d-2}^{s_d+2} D_{eff}(z) \quad (2.3)$$

where  $s_d$  is the coronal bCT image position that is 5% of the number of available coronal bCT images ( $s_{start} - s_{end} + 1$ ) from the  $s_{start}$ .

### 2.2.3.2 Breast Volume (3D) and Areal (2D) Glandular Fraction

For all glandular volumetric assessments, the volume glandular fraction (3D) was computed within the defined region of the bCT segmented images (bounded by the first and last good coronal bCT images) using Equation (2.4),

$$VGF = \frac{V_{glandular}}{V_{glandular} + V_{adipose}} \cdot 100\% \quad (2.4)$$

where  $V_{glandular}$  is the number of voxels marked as “fibroglandular tissue” and is  $V_{adipose}$  the number of voxels marked as “adipose tissue” in a bCT data set. In addition, sagittal bCT images were generated by projecting the segmented bCT data set in a sagittal orientation. The coronal and sagittal areal glandular fractions ( $GF_{coronal}$  and  $GF_{sagittal}$ ) were calculated using Equation (2.5) for all available 2D images in a bCT data set.

$$GF_p(s) = \frac{A_{glandular}(s)}{A_{glandular}(s) + A_{adipose}(s)} \cdot 100\% \quad (2.5)$$

where  $A_{glandular}(s)$  is the number of pixels marked as “fibroglandular tissue” and  $A_{adipose}(s)$  is the number of pixels marked as “adipose tissue” in a bCT image position  $s$  in the coronal or sagittal plane, where  $s = z$  or  $y$  and  $p =$  coronal or sagittal, respectively.

### 2.2.3.3 Radial Distribution of Breast Glandular Fraction

To better understand the fibroglandular distribution within the breast, the distribution of fibroglandular tissue in a coronal bCT image was determined radially. Among the pixels around the circle with a radius  $r$  (relative radial distance) originating from the image center of mass, the radial glandular fraction,  $RGF_{s_i}(r)$ , of a coronal bCT image,  $s_i$ , was computed as the fraction of pixels marked as “fibroglandular tissue” (see Figure 2.13). The relative radial distance was determined by normalizing the absolute radial distance with the breast radius of the bCT image of interest. One-hundred relative radial distances were considered for each bCT image in this analysis. To obtain a thorough glandular fraction analysis, an entire bCT data set was evenly divided into three regions. Region 1 was the posterior breast section, region 2 was the middle breast section, and region 3 was the anterior breast section (see Figure 2.14). The radial glandular fraction,  $RGF_n(r)$ , of a breast region,  $n$  (1, 2, or 3), was determined by averaging the over five images centered about  $s_n$  as in Equation (2.6),

$$RGF_n(r) = \frac{1}{5} \sum_{s_i=s_n-2}^{s_n+2} RGF_{s_i}(r) \quad (2.6)$$

### 2.2.3.4 Breast Projection Areal Glandular Fraction

The volume glandular fraction was compared with the areal glandular fraction expected from mammography. To properly estimate the areal glandular fraction determined at mammography, a segmented bCT data set was projected in the sagittal orientation to simulate the process of creating a mammographic image. Two steps of projecting through the segmented bCT data set were implemented. A projection of the entire segmented bCT data set was used to delineate the breast border. Secondarily, the number of voxels segmented as “fibroglandular tissue” along a projection ray through a bCT data set were recorded onto a glandular projection image,  $I_{glandproj}(x, y)$ . To

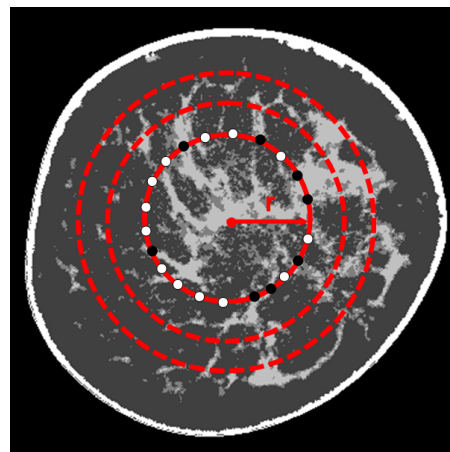


Figure 2.13. The method in calculating the radial glandular fraction  $RGF_{s_i}(r)$  is demonstrated using a segmented coronal bCT image. For a radial distance,  $r$ ,  $RGF_{s_i}(r)$  is the percentage of the number of pixels marked as “fibroglandular tissue” (●) out of the number of pixels marked as “fibroglandular tissue” or “adipose tissue” (○).

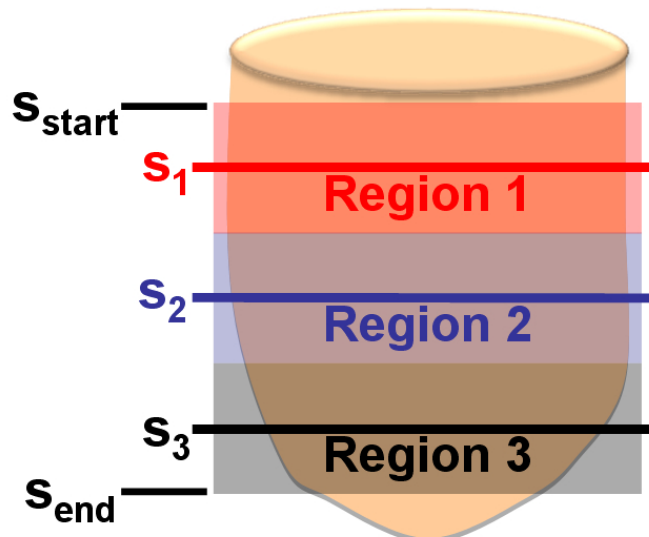


Figure 2.14. The location of three breast regions of a bCT volume bounded by the first good coronal bCT slice ( $s_{start}$ ) and the last good coronal bCT slice ( $s_{end}$ ) is illustrated for evaluating  $RGF_n(r)$ . Region 1 is the posterior section, region 2 is the middle section, and region 3 is the anterior section. The middle slices of the three breast regions are  $s_1$ ,  $s_2$ , and  $s_3$ , respectively.

simulate the effect of a wide range of radiologists' visual inspection of breast density at mammography,  $I_{glandproj}(x, y)$  of each bCT data set was then segmented by 8 global thresholds ( $T = 0, 15.75, 31.5, \dots, 110.25$ , in gray scale value). The breast areal glandular fraction ( $AGF_{T_i}$ ) of each bCT data set using a threshold,  $T_i$ , was determined using Equation (2.7),

$$AGF_{T_i} = \frac{A_{gland,T_i}}{A_{gland,T_i} + A_{adipose,T_i}} \cdot 100\% \quad (2.7)$$

where  $A_{gland,T_i}$  is the number of pixels where  $I_{glandproj}(x, y) > T_i$  and  $A_{adipose,T_i}$  is the number of pixels where  $I_{glandproj}(x, y) \leq T_i$ .

## 2.2.4 Data Analysis

### 2.2.4.1 3D (Volumetric) Breast Assessment

The volumes of adipose tissue and fibroglandular tissue were examined as a function of age. The volume data was binned into 16 age groups (35 - 37, 38 - 41, ...,  $\geq 81$  years). The mean volume of the respective tissue types (adipose and fibroglandular tissues) and the mean total breast volume were presented as a function of the averaged age for the 16 age groups. The relationship between the volume glandular fraction and age was found using the same age grouping. Similarly, the volume glandular fraction data was categorized into 10 breast diameter ( $D_{chestwall}$ ) groups according to the 10<sup>th</sup>-percentile  $D_{chestwall}$  ( $0 \leq D_{chestwall} < 9.9$  cm), the 20<sup>th</sup>-percentile  $D_{chestwall}$  ( $9.9 \leq D_{chestwall} < 10.9$  cm), ..., and  $> 90^{\text{th}}\text{-percentile } D_{chestwall}$  ( $D_{chestwall} \geq 15.2$  cm). The mean volume glandular fractions of 10  $D_{chestwall}$  groups were found as a function of the averaged  $D_{chestwall}$  for each group. In addition, the relationship between the volume glandular fraction between the affected and unaffected breasts was evaluated for women with no finding, benign and malignant findings. The distributions of total breast volume and volume glandular fraction for each of the four bra cup sizes (A, B, C, D) were examined. The relationship between VGF and bra cup size was presented using a box-and-whisker plot

(whisker =  $1.5 \cdot$  interquartile range), where the solid dot is the mean VGF with standard error and crosses represent outliers among the VGF of each bra cup size. Box-whisker plots were used in similar fashion to present other data in this study. In addition, analysis of variance (ANOVA) and post-hoc multiple comparisons with Bonferroni correction were used to identify significant differences among data groups when applicable. Linear regression was used when appropriate. For all the analyses in this study, we considered statistical significance at a two-sided p-value  $< 0.05$ .

Figure 2.15 shows the volume of adipose tissue, fibroglandular tissue, and total breast tissues as a function of age. The volume of adipose tissue increases steadily while the volume of fibroglandular tissue decreases gradually as women age. Figure 2.16 shows that the total breast volume increases as the self-reported bra cup size goes from A to D among 219 women. The mean total breast volumes ( $\pm$  standard error) for bra cup size A, B, C, and D were  $324.7 \pm 44.2$  ml,  $467.9 \pm 36.2$  ml,  $803.1 \pm 33.0$  ml,  $1203.7 \pm 68.7$  ml, respectively.

Figure 2.17 demonstrates the relationship between the VGF of the affected and unaffected breasts among women with no finding, benign or malignant findings. The VGF of the affected breasts appeared to be slightly higher than that of the unaffected breasts for women with benign or malignant findings while the women with no finding exhibited almost identical VGF for both breasts. However, the VGF of the affected breasts and unaffected breasts were not significantly different for the women with benign findings ( $p = 0.40$ ) and malignant findings ( $p = 0.09$ ). Since there might be bias in segmenting bCT data sets with breast cancer, the VGF of the unaffected breast was thought to be a better representation of fibroglandular composition of a woman.

Figure 2.18 presents the distributions of VGF among women with bra cup size A, B, C, and D. The mean VGF's ( $\pm$  standard error) for bra cup size A, B, C, and D were  $17.7 \pm 3.7\%$ ,  $19.2 \pm 1.7\%$ ,  $13.2 \pm 1.2\%$ , and  $13.2 \pm 1.3\%$ . The VGF of women with bra cup size A and B appears to be slightly larger

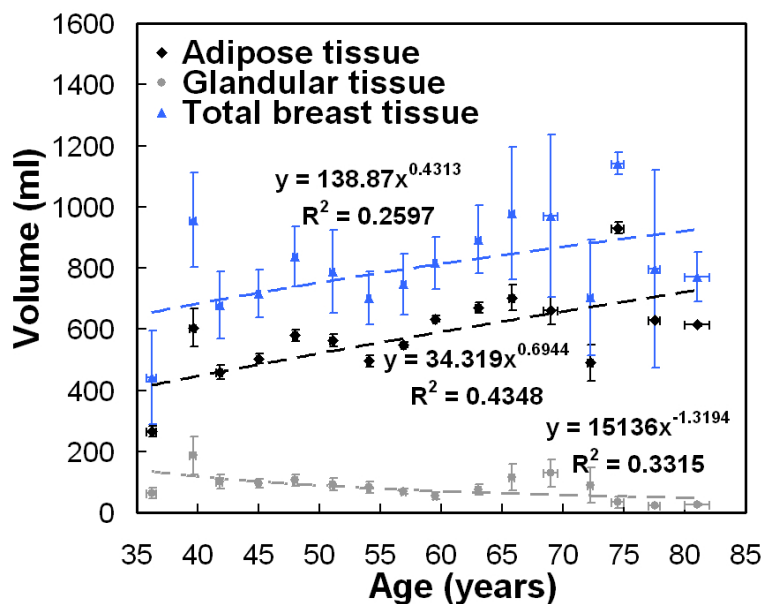


Figure 2.15. The relationship between breast tissue volume and age is illustrated. The dashed line is the line of best fit using a power function. A breast is likely to be composed of more adipose tissue and less fibroglandular tissue as a woman ages. Standard error bars are shown.

than that of the women with bra cup size C and D. Overall, the mean VGF's of at least two bra cup sizes were significantly different between each other ( $p = 0.01$ , ANOVA). Post-hoc multiple comparisons with Bonferroni correction suggested that only VGF of bra cup size B was found to be significantly different from that of bra cup size C ( $p = 0.0042$ ) and D ( $p = 0.0054$ ). The mean VGF's ( $\pm$  standard error) for the BIRADS categories of fatty, scatter, heterogeneous, and extremely dense were found to be  $6.5 \pm 1.4\%$ ,  $8.8 \pm 1.0\%$ ,  $15.8 \pm 1.1\%$ , and  $25.2 \pm 2.2\%$ , respectively. As shown in Figure 2.19, the box-and-whisker plot shows that breasts with higher BIRADS breast density are likely to have higher VGF as well. With each increasing BIRADS category, VGF increased by 5.62% ( $p < 0.001$ ).

A linear function ( $r^2 = 0.93$ ) was fit to VGF as a function of breast diameter of the chest wall in Figure 2.20a. Breasts with larger diameter close to the chest wall were found to have a higher fraction of adipose tissue content. Figure 2.20b suggests that VGF decrease as women age.

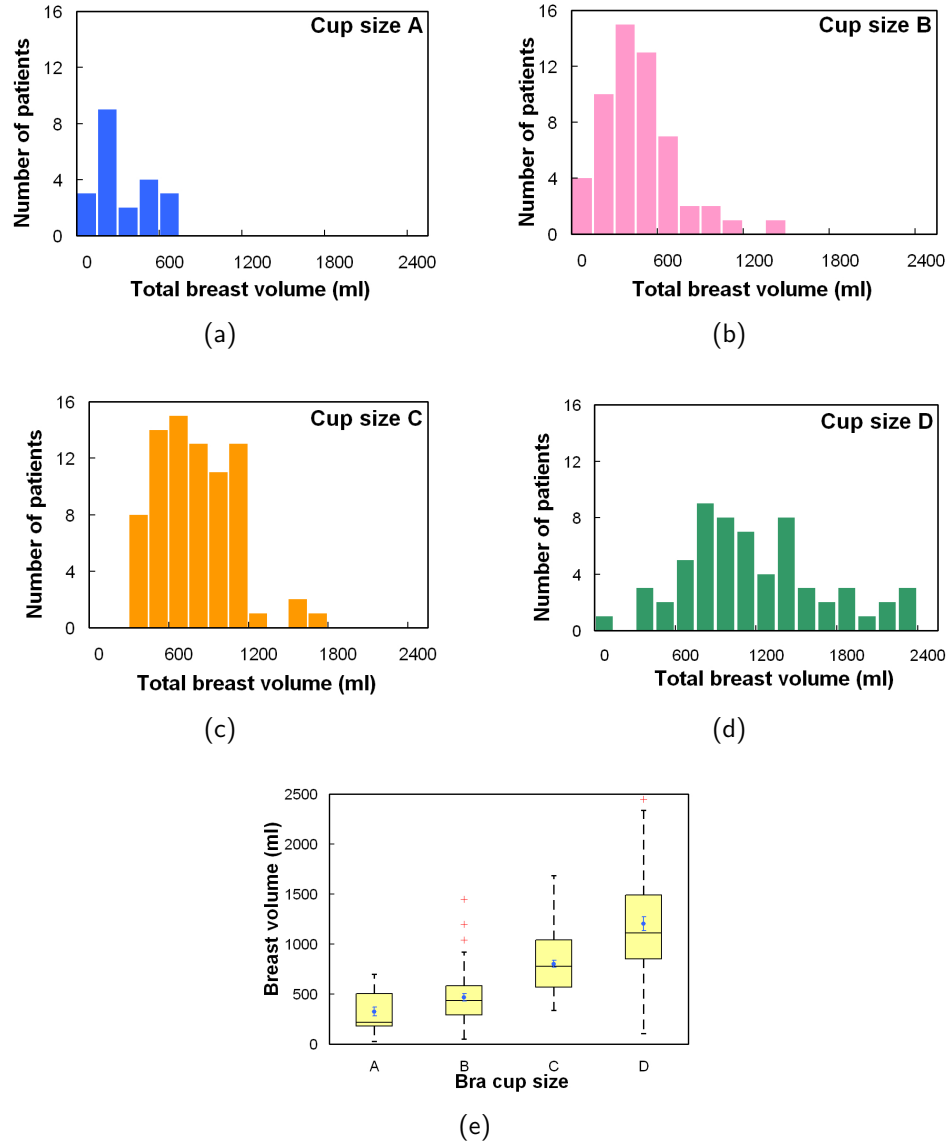


Figure 2.16. Histogram distributions of the total breast volume (ml) for bra cup size **(a)** A, **(b)** B, **(c)** C, and **(d)** D are shown. **(e)** A box-and-whisker plot of breast volume as a function of bra cup size is illustrated.

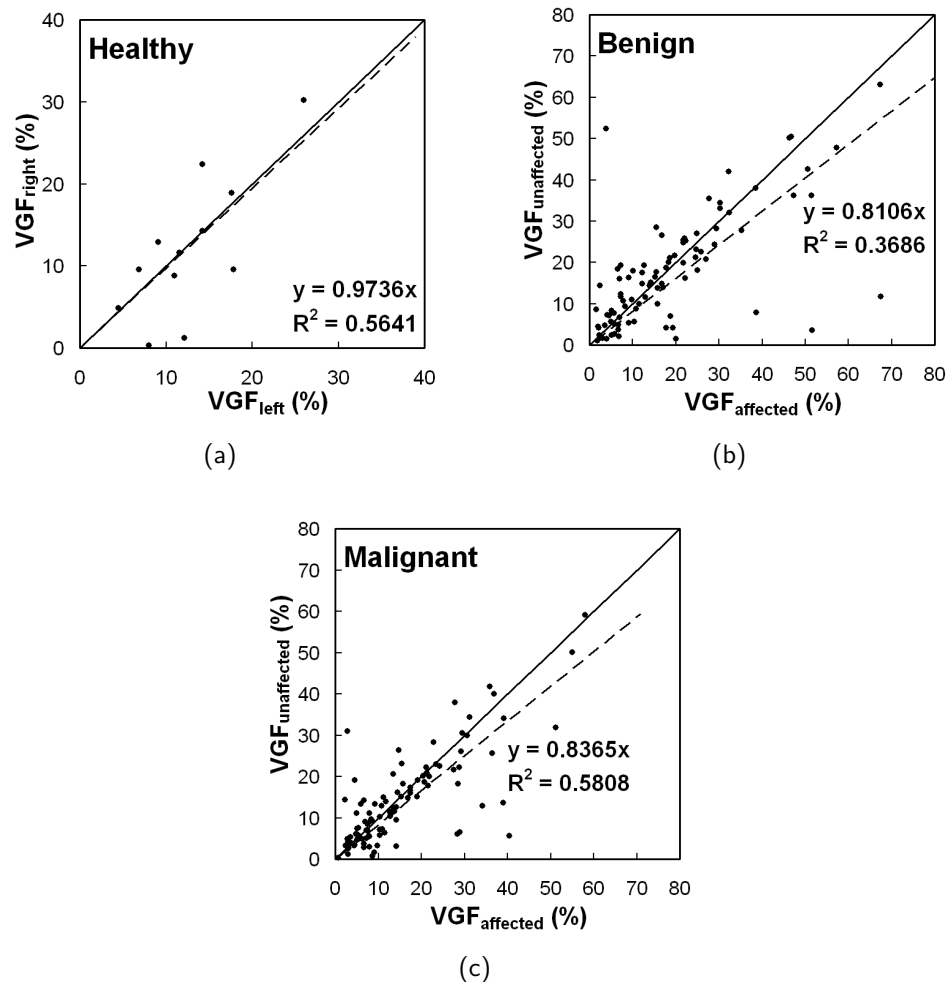


Figure 2.17. The correlation of the VGF between the left and right breasts of women is shown for women with (a) no findings. The relationship of the VGF between the affected and unaffected breasts of women with (b) benign findings and (c) malignant findings is shown. The solid line is the line of identity; the dashed line is the fitted linear regression.

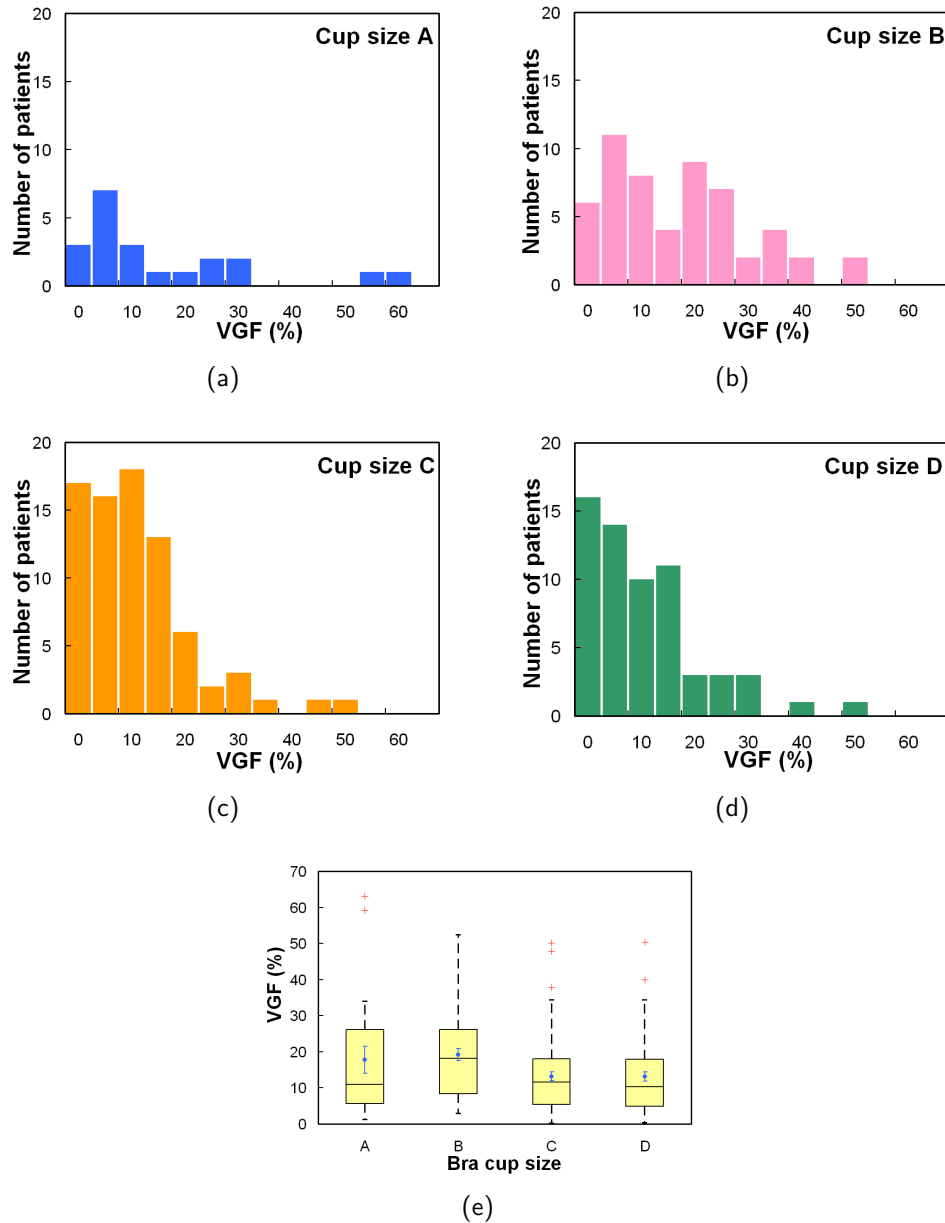


Figure 2.18. Histogram distributions of the VGF (%) for bra cup size (a) A, (b) B, (c) C, and (d) D are shown. (e) A box-and-whisker plot of VGF as a function of bra cup size is shown.

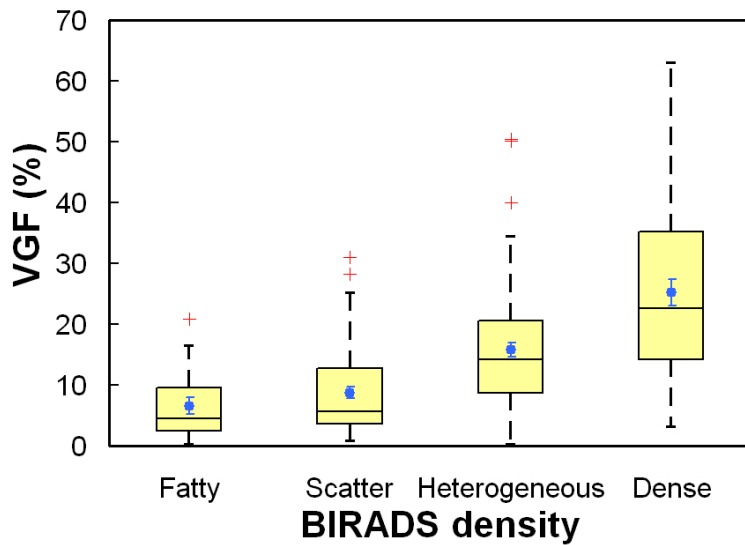


Figure 2.19. The graph shows a box-and-whisker plot of volume glandular fraction (VGF) versus BIRADS density.

#### 2.2.4.2 2D (Projection and bCT Images) Breast Assessment

The relationship between the breast volume glandular fraction (VGF) and the areal glandular fraction ( $AGF_{T_i}$ ) was determined using 8 global thresholds for all bCT data sets. To characterize the breast composition relative to location in the breast, the of three breast regions, where  $n = 1$  (posterior), 2 (middle), and 3 (anterior), was determined for women with four bra cup size categories (A, B, C, D). The mean, median, 25<sup>th</sup> percentile, 75<sup>th</sup> percentile, and the standard error were reported for all four bra cup sizes. In addition, the areal glandular fraction of coronal bCT images,  $GF_{coronal}(z)$ , and sagittal bCT images,  $GF_{sagittal}(y)$ , were computed using Equation (2.5). Due to the range in breast sizes, the image position (coronal: z direction; sagittal: y direction) was normalized relative to the maximum diameter or length of a bCT data set. Because different slice thicknesses were used in the bCT data sets, cubic spline interpolation (Matlab<sup>©</sup>) was applied to the distributions, and , for all bCT data sets to evaluate the areal glandular fraction as a function of relative image position (0, 0.005, 0.01, . . . , 1.0). For each relative image position, the

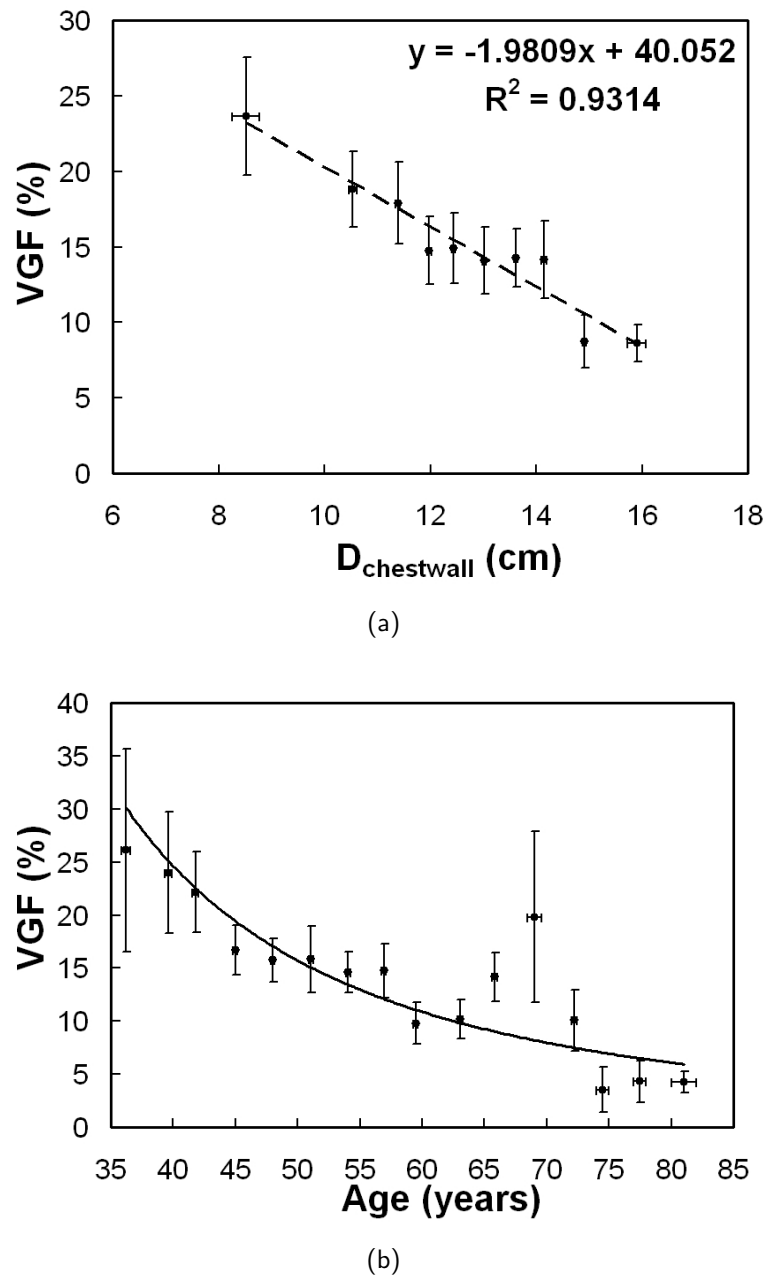


Figure 2.20. The volume glandular fraction (VGF) is illustrated as a function of (a) breast diameter near the chest wall ( $D_{chestwall}$ ) and (b) age. Standard error bars are shown.

mean, median, 25<sup>th</sup> and 75<sup>th</sup> percentiles, and standard error were computed for bCT data sets of four bra cup sizes.

Figure 2.21 illustrates the capability of the metrics  $AGF_{Ti}$  in characterizing the range of VGF for each BIRADS density category. It is shown that  $AGF_{Ti}$  increases more than  $VGF$  for each increasing BIRADS category. It also shows that  $AGF_{Ti}$ , a 2D-image based metrics, reveals different glandular fraction distribution than  $VGF$ , a 3D-image based metrics. To relate  $AGF_{Ti}$  with  $VGF$ , Figure 2.22 shows that VGF increases with AGF (using 8 global thresholds) in a power-law trend. The AGF as a function of VGF using each global threshold was fit using a power function ( $y = ax^b + c$ ). The coefficients of the power function fit are recorded in Table 2.3. Figure 2.23 shows the distribution of radial glandular fraction for three breast regions. For women with bra cup sizes A and B, fibroglandular tissue tends to locate in the center portion of the breast evenly throughout the three breast regions. For women with cup sizes C and D, fibroglandular tissue is concentrated more in the breast center toward the breast anterior regions. Figure 2.24 and Figure 2.25 display the distributions of  $GF_{coronal}(z)$  and  $GF_{sagittal}(y)$  for each bra cup size. The dashed line is the mean  $GF_p$ , and the solid line is the median  $GF_p$ . The darker shade covers the range of 25<sup>th</sup> percentile below and 75<sup>th</sup> percentile above the median. The lighter shade covers the range of standard error above and below the mean. Across all four bra cup sizes,  $GF_{coronal}(z)$  was found to be relatively homogeneously distributed but increased dramatically toward the nipple, as shown in Figure 2.24. Figure 2.25 shows that  $GF_{sagittal}(y)$  is concentrated heavily in the middle of the breast, with a slight offset ( 10%) inferiorly.

#### 2.2.4.3 Breast Shape and Size Assessment

The breast effective diameter as a function of relative posterior-anterior position was computed to characterize the breast shape for each bra cup size. The same cubic interpolation scheme (Section 2.2.4.2) was applied to the distribution, , at the desired relative position. The mean, median, 25<sup>th</sup> and 75<sup>th</sup>

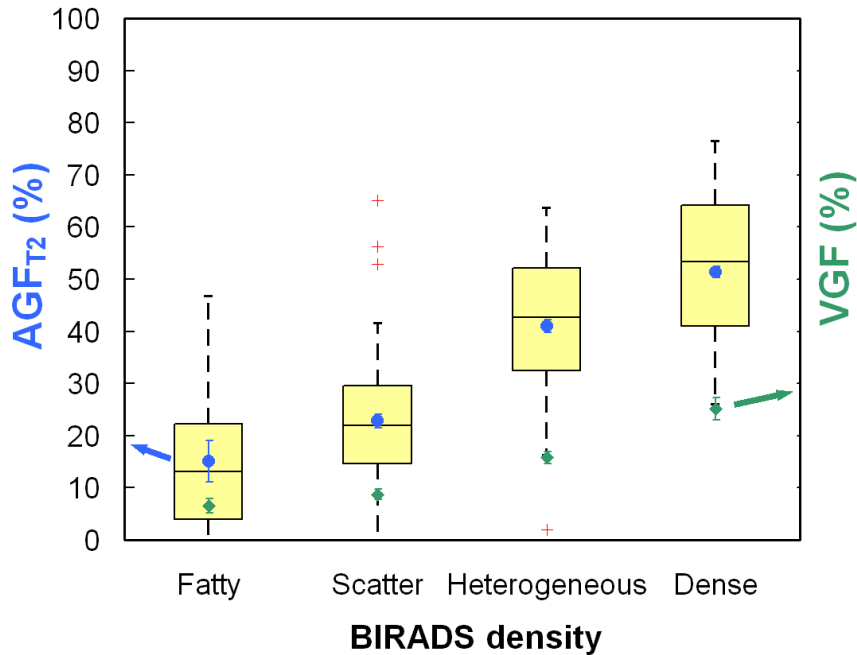


Figure 2.21. A box-and-whisker plot of areal glandular fraction using threshold T2 ( $AGF_{T2}$ ) as a function of BIRADS density is shown. The mean VGF ( $\pm$  standard error) is shown as comparison for each BIRADS density category.

Table 2.3. The coefficients of the power function ( $y = ax^b + c$ ) fit to AGF as a function VGF using 8 global thresholds in Figure 2.22.

Global threshold ( $T_i$ )	<b>a</b>	<b>b</b>	<b>c</b>	$r^2$
0.00	-52.0122	-0.3221	88.3594	0.5619
15.75	34.4143	0.2744	-31.7009	0.6931
31.50	8.3916	0.5645	-10.9426	0.7312
47.25	2.6417	0.8236	-5.6304	0.7447
63.00	0.9318	1.0571	-3.6154	0.7545
78.75	0.3509	1.2709	-2.5259	0.7462
94.50	0.1210	1.4953	-1.7542	0.7208
110.25	0.0384	1.7281	-1.1792	0.6715

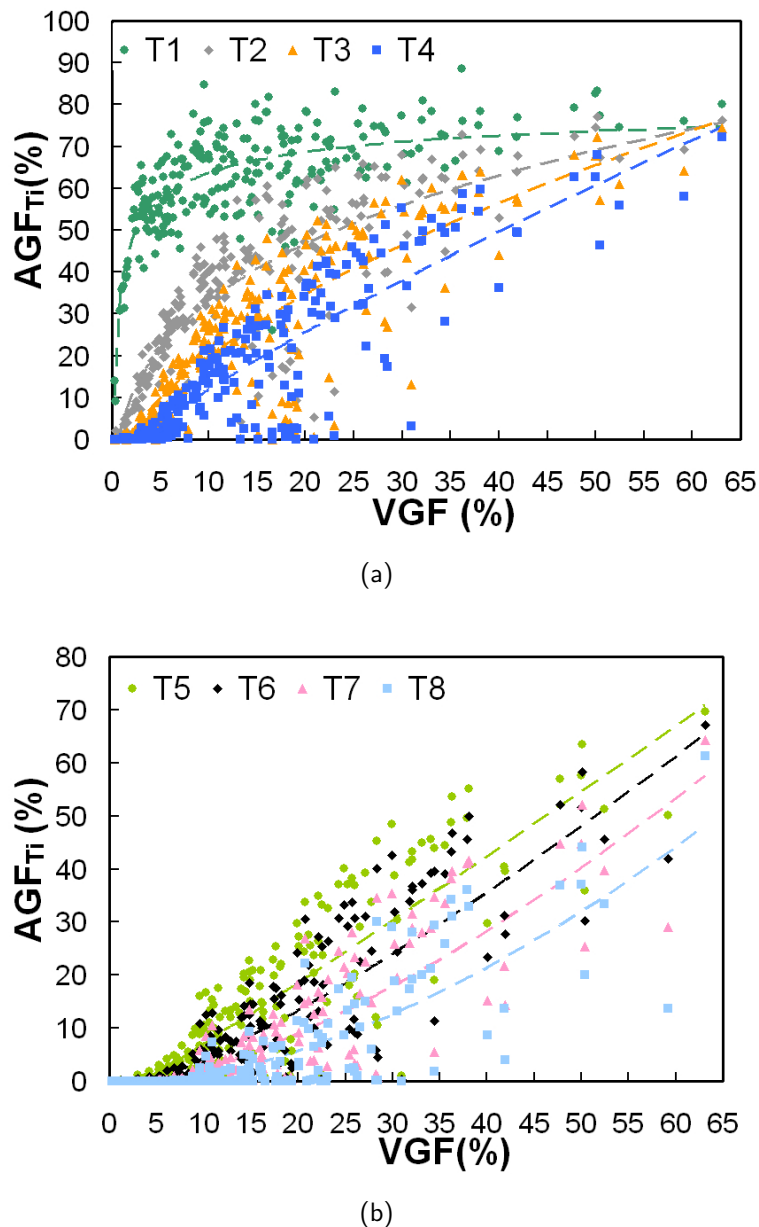


Figure 2.22. The areal glandular fraction is shown versus the volume glandular fraction using a threshold level (gray scale value) where (a)  $T1 = 0$ ,  $T2 = 15.75$ ,  $T3 = 31.50$ ,  $T4 = 47.25$  and (b)  $T5 = 63$ ,  $T6 = 78.75$ ,  $T7 = 94.50$ ,  $T8 = 110.25$

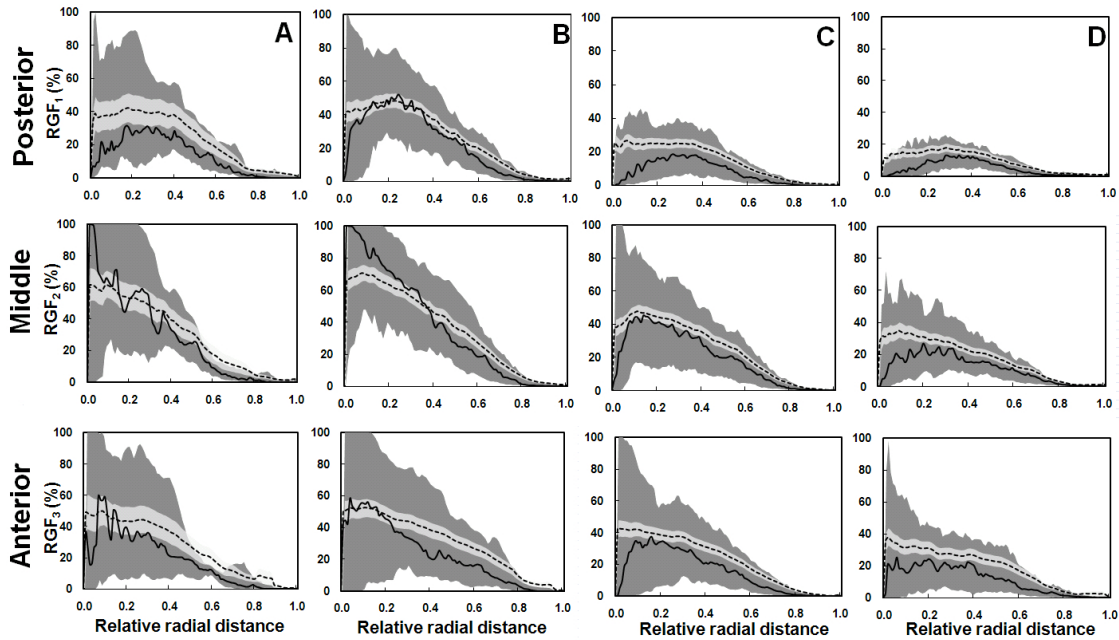


Figure 2.23. The radial glandular fraction is plotted as a function of relative radial distance for women with bra cup size A, B, C, and D for three breast regions (posterior, middle, and anterior). The dashed line is the mean  $RGF_n$ , and the solid line is the median  $RGF_n$ . The darker shade covers the range of 25<sup>th</sup> percentile below and 75<sup>th</sup> percentile above the median. The lighter shade covers the range of standard error above and below the mean.

percentiles, and standard error were determined. A 3<sup>rd</sup>-order polynomial was fit to the mean for women with each bra cup size. The breast length (cm) was determined by the length, in z location, covered by the first good coronal bCT image and the last good coronal bCT image. In addition, the distributions of breast diameter and breast length for 4 bra cup sizes were evaluated. The total breast volume of the right and left breasts was also compared.

Across all 4 bra cup sizes, Figure 2.26 shows that the breast shape can be generally characterized by the breast effective diameter, which gradually decreases from posterior to anterior. A 3<sup>rd</sup>-order polynomial described those trends well ( $r^2 > 0.9993$ ). The starting of a breast increased as a function of bra cup sizes. In more detail, Figure 2.27 shows that the mean breast diameter ( $D_{chestwall}$ ) slightly increased with bra cup sizes, where  $D_{chestwall}$  was measured at the relative z location indicated by the dashed line in Figure 2.26a.

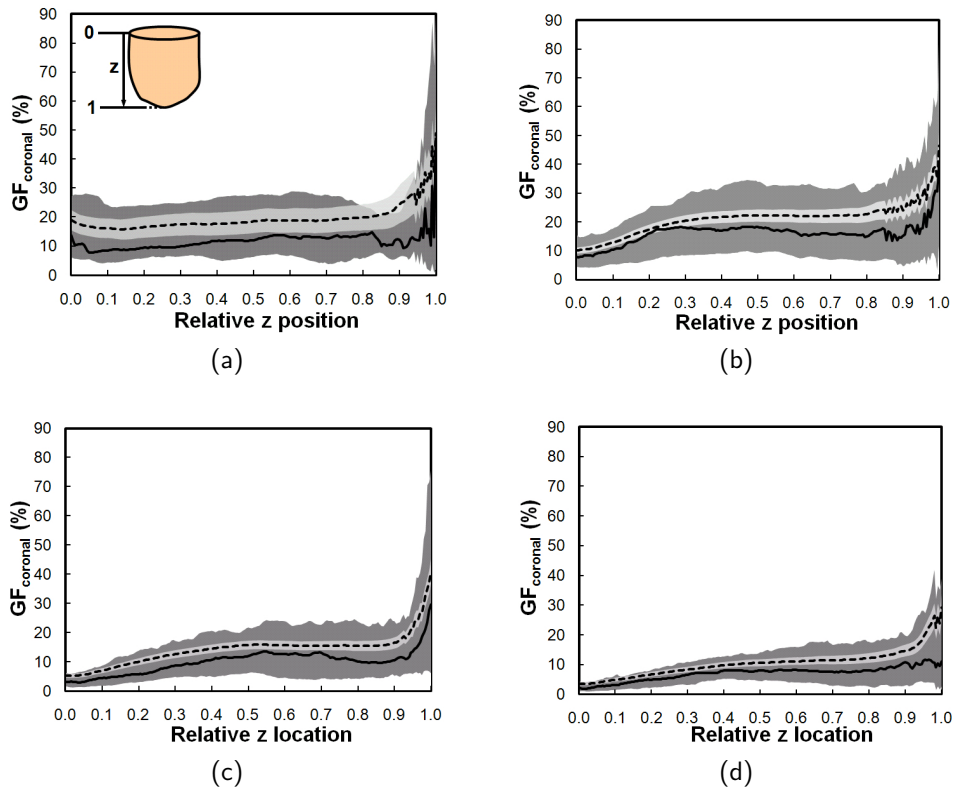


Figure 2.24. The glandular fraction of coronal bCT slices  $GF_{coronal}$  is shown versus the relative z position for women with bra cup size (a) A, (b) B, (c) C, and (d) D. The direction of z position relative to a bCT volume data set is illustrated in A, where 0 is posterior and 1 is anterior. The dashed line is the mean  $GF_{coronal}$ , and the solid line is the median  $GF_{coronal}$ . The darker shade covers the range of 25<sup>th</sup> percentile below and 75<sup>th</sup> percentile above the median. The lighter shade covers the range of standard error above and below the mean.

The mean breast diameters ( $\pm$  standard error) for bra cup size A, B, C, and D were  $11.1 \pm 0.5$  cm,  $11.4 \pm 0.3$  cm,  $13.0 \pm 0.2$  cm, and  $13.7 \pm 0.2$  cm, respectively. Figure 2.27 suggests that breasts with larger diameter corresponded to larger bra cup sizes. In addition, Figure 2.28 illustrates that breast length appears to increase slightly with bra cup size. The mean breast lengths ( $\pm$  standard error) for bra cup sizes A, B, C, and D were  $5.7 \pm 0.5$  cm,  $7.1 \pm 0.3$  cm,  $9.4 \pm 0.2$  cm, and  $9.7 \pm 0.2$  cm, respectively. The box-and-whisker plot in Figure 2.28e confirmed that women with larger bra cup size tend to have longer breast length. Lastly, the right breast volume was found to be com-

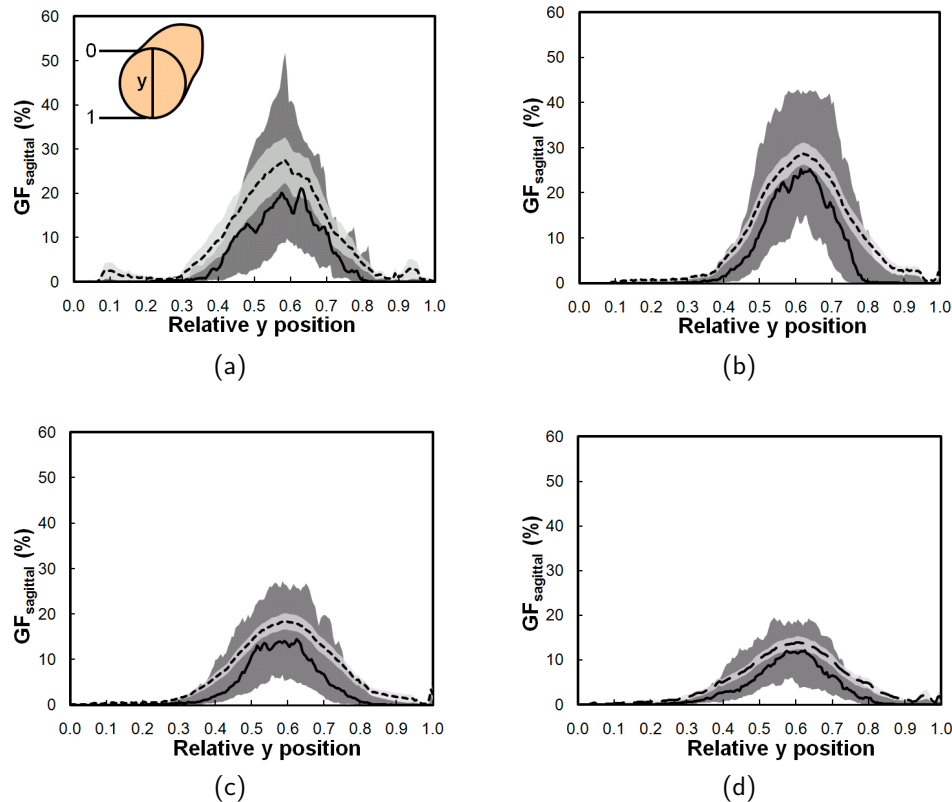


Figure 2.25. The glandular fraction of sagittal bCT slices  $GF_{sagittal}$  versus the relative y position for women is shown for breasts with bra cup size (a) A, (b) B, (c) C, and (d) D. The direction of y position relative to a bCT volume data set is illustrated in A, where 0 is superior and 1 is inferior. The dashed line is the mean  $GF_{sagittal}$ , and the solid line is the median  $GF_{sagittal}$ . The darker shade covers the range of 25<sup>th</sup> percentile below and 75<sup>th</sup> percentile above the median. The lighter shade covers the range of standard error above and below the mean.

parable to the left breast volume (slope = 0.995). A paired student's t test confirmed that the right breast volume was not significantly different from the left breast volume ( $p = 0.17$ ). A total of 48.7% of all the breasts in this analysis were ones with the benign or malignant findings.

#### 2.2.4.4 3D Breast Modeling

For a woman with a given bra cup size and VGF, one can use the data found in Section 2.2.4.1, Section 2.2.4.2, and Section 2.2.4.3 to simulate a breast of

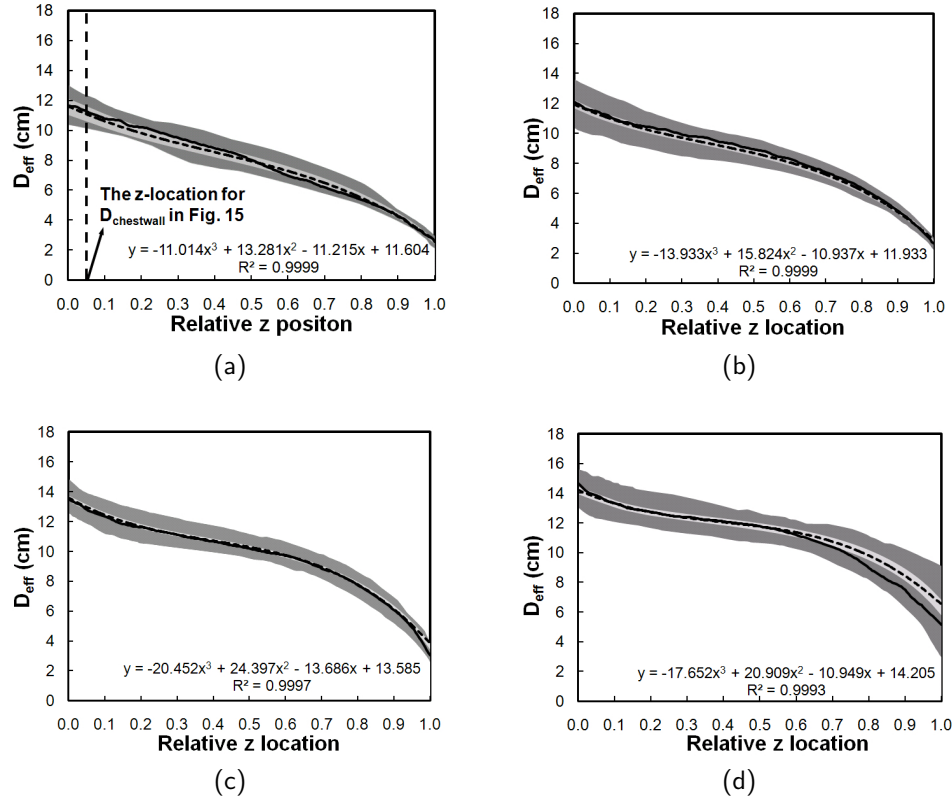


Figure 2.26. The breast effective diameter versus the relative z position is shown for women with bra cup size (a) A, (b) B, (c) C, and (d) D. The dashed line is the mean  $D_{eff}$ , and the solid line is the median  $D_{eff}$ . The darker shade covers the range of 25<sup>th</sup> percentile below and 75<sup>th</sup> percentile above the median. The lighter shade covers the range of standard error above and below the mean. A 3<sup>rd</sup>-order polynomial was fit to the mean breast diameter profile for each bra cup size.

such specification. The images were simulated using a voxel dimension of  $200 \times 200 \times 200 \mu\text{m}^3$ . The breast volume dimension was determined by the mean  $D_{chestwall}$  and the mean breast length among women of a specific bra cup size. For a coronal bCT image, pixels within a circle with the effective diameter originated from the image center at a z position were assigned as breast tissue. A skin thickness of 1.5 mm (Huang et al., 2008) was included within the breast circle. The coronal areal glandular fraction for a relative z location was determined by  $GF_{coronal}$ , characterized by a 3<sup>rd</sup>-order polynomial found among women with the specific bra cup size. The profile of  $RGF_n(r)$  at each z

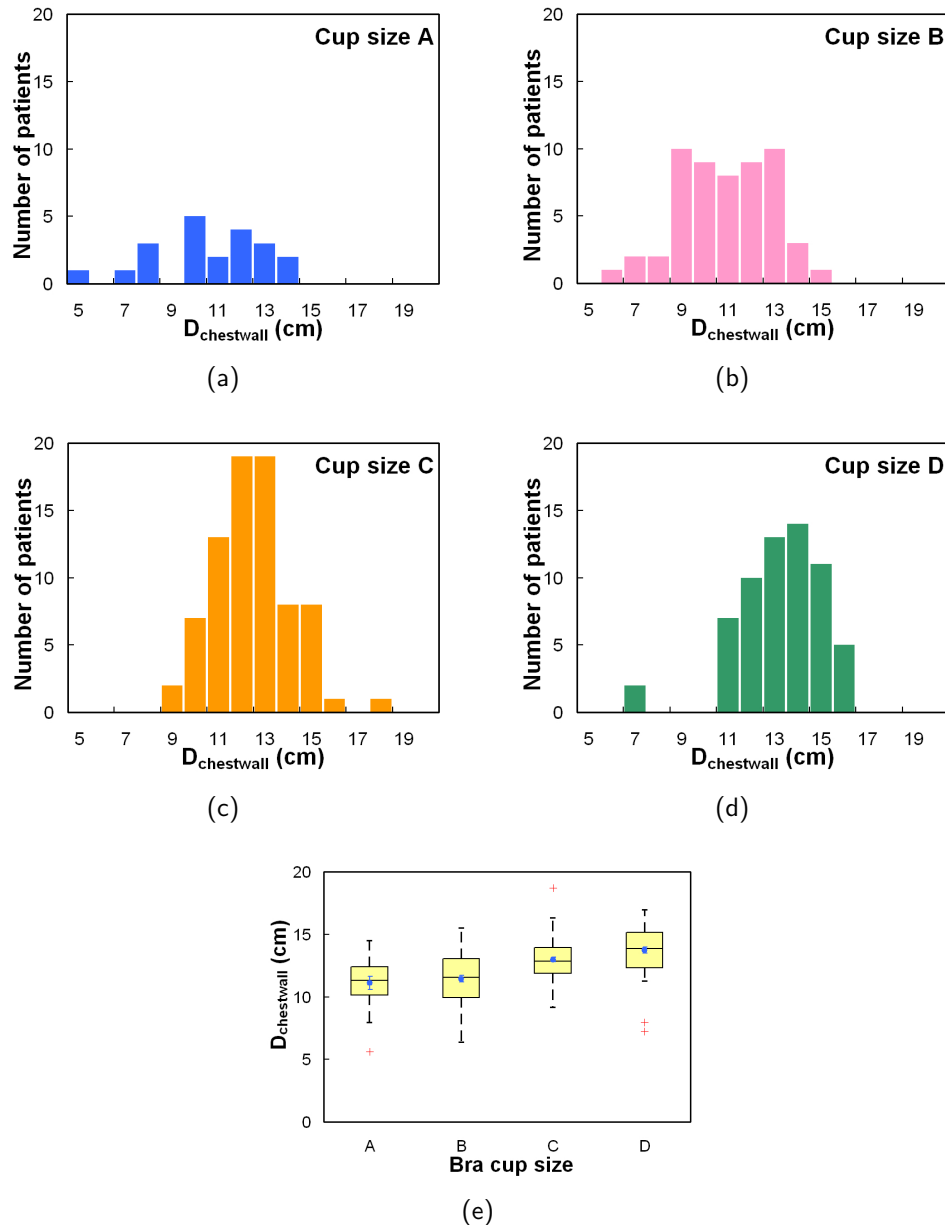


Figure 2.27. Histogram distributions of the breast diameter ( $D_{\text{chestwall}}$ ) near the chest wall is shown for women of bra cup sizes (a) A, (b) B, (c) C, and (d) D. (e) A box-and-whisker plot of  $D_{\text{chestwall}}$  is shown as a function of bra cup size.

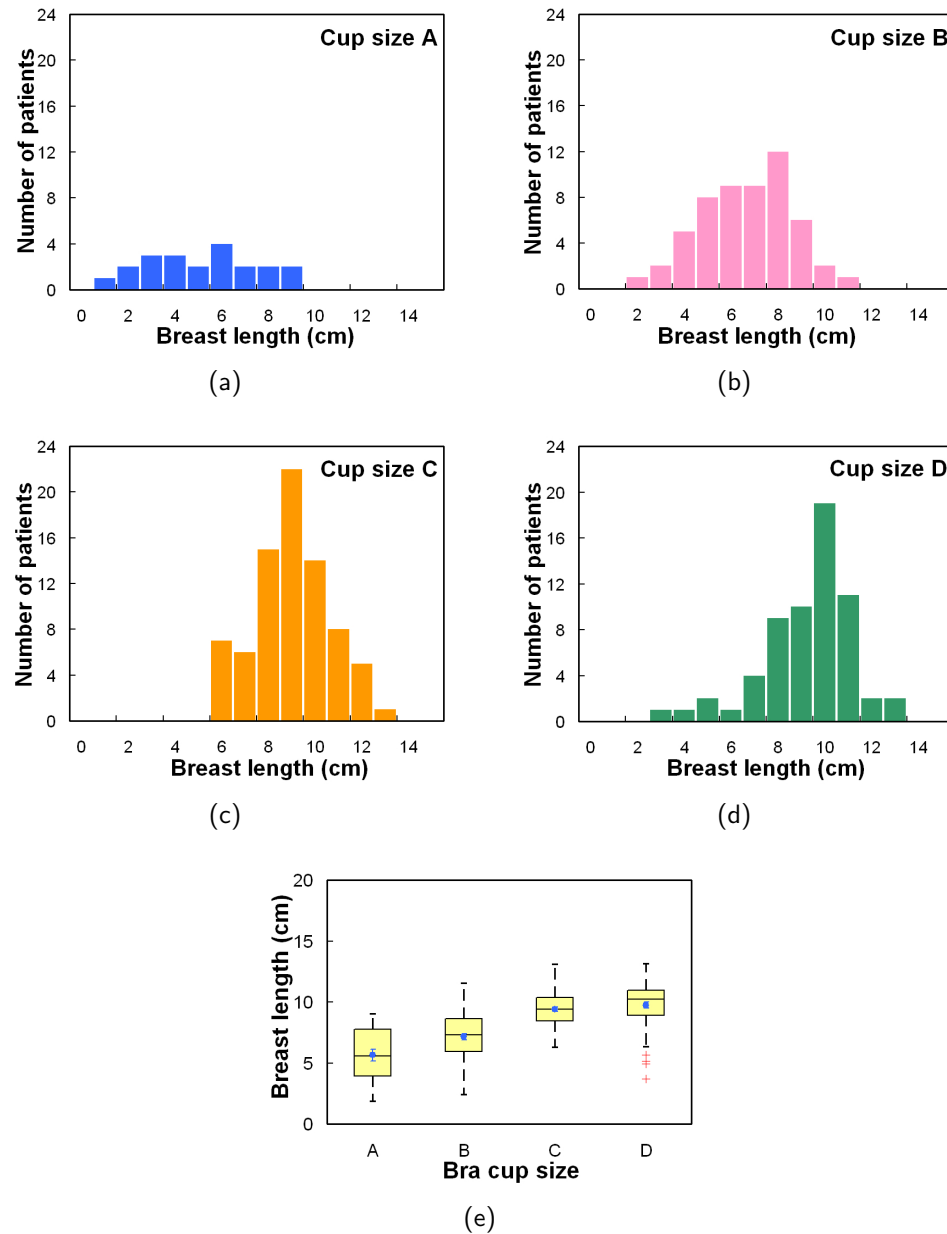


Figure 2.28. Histogram distributions of the breast length (cm) are shown for bra cup size (a) A, (b) B, (c) C, and (d) D. (e) A box-and-whisker plot of breast length as a function of bra cup size is illustrated.

location was determined using cubic spline interpolation (Matlab<sup>©</sup>) from the  $RGF_1(r)$ ,  $RGF_n(2)$ , and  $RGF_3(r)$  found in Section 2.2.4.2. The distribution of was normalized such that the resulting glandular distribution would sum up to  $GF_{coronal}(z)$  at a particular z location. For a coronal bCT image, the probability of a pixel being fibroglandular tissue was assigned radially. Among the pixels around the circle of a given radial distance, a number of pixels were randomly selected using a uniform distribution to achieve  $RGF_n(r)$  at the radial distance. The probability of being fibroglandular tissue (normally distributed between 0 and 1) was assigned for each randomly selected pixel. Since the fibroglandular tissue typically originates from the nipple, the coronal bCT images were simulated from breast anterior to breast posterior. The resulting images were compiled into a volume data set, which were rendered in 3D using ImageJ 3D viewer (ImageJ 1.44d).

Figure 2.29 and Figure 2.30 display the simulated bCT images for a woman with bra cup size B and D, respectively. The simulated 3D breast with bra cup size B has a  $D_{chestwall}$  of 11.6 cm and breast length of 7.3 cm. The simulated 3D breast with bra cup size D has a  $D_{chestwall}$  of 13.8 cm and breast length of 10.2 cm. The shape of the breasts with bra cup size B and D were determined using the distribution shown in Figure 2.27. The VGF of the simulated breast with bra cup size B was found to be 18.4% while that with bra cup size D was found to be 9.0%. Figure 2.29d and Figure 2.30d illustrate that the fibroglandular tissue was distributed in the central breast portion in two orthogonal views of the breast as found in Figure 2.23, Figure 2.24, and Figure 2.25.

## 2.2.5 Discussion and Conclusions

In this study, a comprehensive analysis of breast composition and breast shape was performed to characterize breast anatomy in women of different ages and with different breast sizes. The data presented provide anatomically grounded information to guide the construction of physical or simulated breast phantoms. In addition to the detailed description of breast geometry,

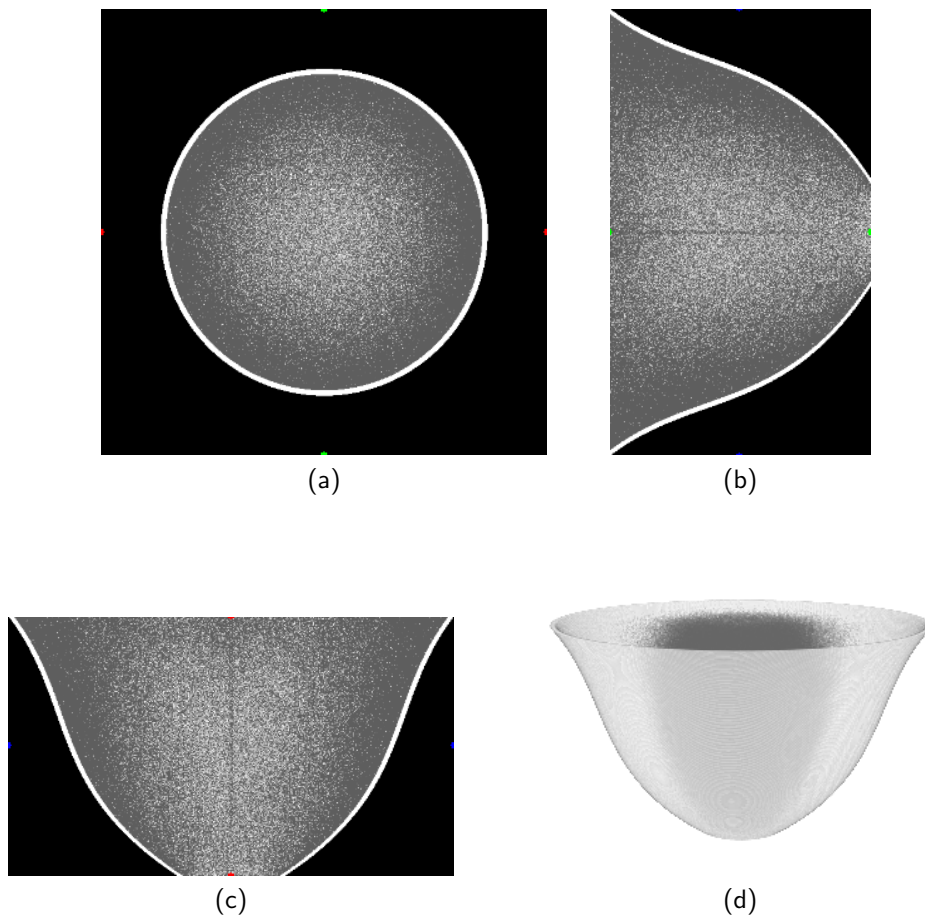


Figure 2.29. A 3D computer-simulated breast phantom using the found glandular fraction distribution of a woman with bra cup size B is illustrated in (a) the coronal plane, (b) the sagittal plane, (c) the axial plane, and (d) 3D rendered image.

the distribution of fibroglandular tissue in the breast was reported using both 2D and 3D metrics.

It is important to note that the BIRADS density determined at mammography tends to overestimate the glandular fraction due to the overlap of fibroglandular tissue distribution from breast compression and the projection imaging geometry. This study found that BIRADS densities overestimate the true volume glandular fraction by approximately 1.9-fold for fatty breasts, 4.2-fold for scattered breasts, 4.0-fold for heterogeneous breasts, and 3.5-fold for extremely dense breasts. The findings also confirm the overestimation

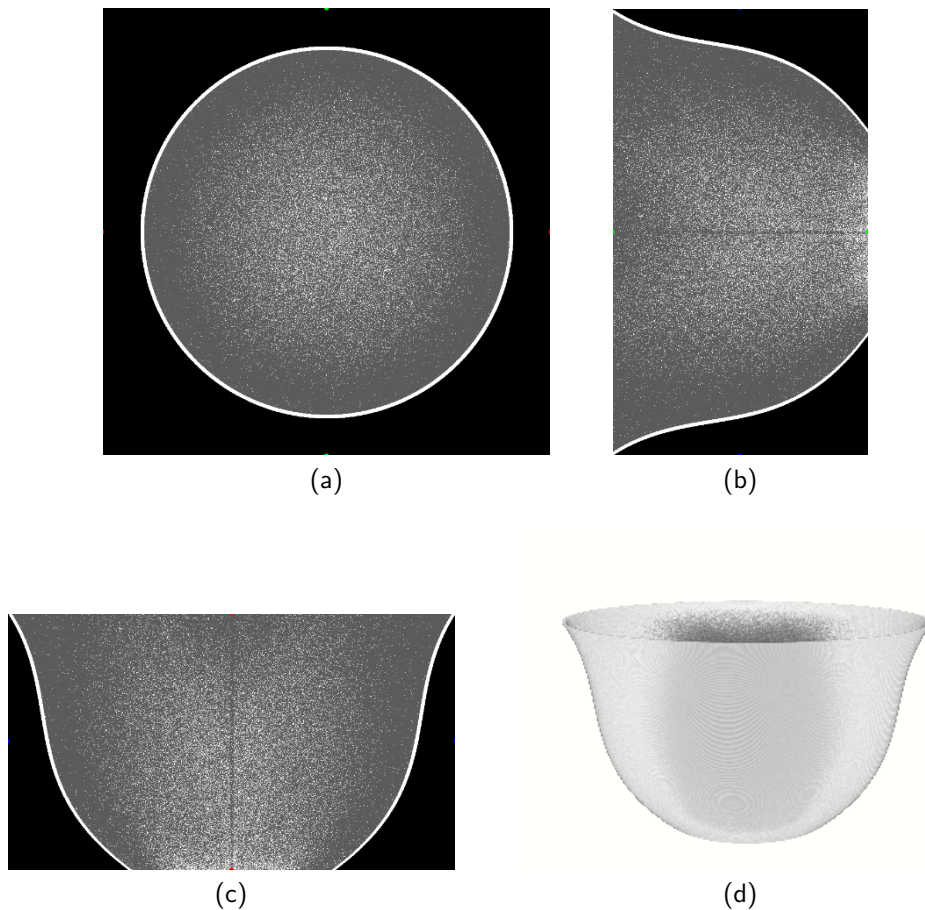


Figure 2.30. A 3D computer-simulated breast phantom using the found glandular fraction distribution of a woman with bra cup size D is illustrated in (a) the coronal plane, (b) the sagittal plane, (c) the axial plane, and (d) 3D rendered image.

of breast density at mammography for the “average” breast, which has been shown to be 19.3% but not the commonly assumed 50% (Yaffe et al., 2009). However, Figure 2.19 and Figure 2.22 can be used to estimate the VGF for a given mammographic BIRADS category or AGF (assuming no breast compression). Furthermore, the coefficients in Table 2.3 allow one to estimate VGF from AGF for a variety of segmentation thresholds. The global thresholding scheme (Section 2.2.3.4) used in estimating breast density at 2D projection images is crude but represents the subjective visual thresholding by a wide variety of observers. Further studies should establish where most ra-

diologists fall in this range of thresholds. The effect of breast compression on VGF-AGF relationship must also be explored.

The study results also guide the construction of a physical or simulated breast phantom, accounting for age and breast size (volume, breast diameter, and length). Previous studies ([Kopans, 2007](#); [Stomper et al., 1996](#)) have suggested that the breast density decreases steadily with increasing age. [Figure 2.15](#) and [Figure 2.20b](#) confirm this observation. Breast diameter, breast length, VGF, and fibroglandular tissue distribution appear to change with bra cup size. Bra cup size may be a rough classification of breast size with respect to these metrics. Moreover, [Figure 2.23](#), [Figure 2.24](#), and [Figure 2.25](#) suggest that fibroglandular tissue generally originates from the breast nipple and locate heavily in the center part of a breast in 3D. Based on mammographic images, a previous study ([Astley and Caulkin, 2002](#)) suggests that fibroglandular tissue is preferentially located in the center portion of a breast in both medial-lateral and cranial-caudal directions. The finding in this study suggests a similar trend in fibroglandular tissue distribution in 3D. Combining VGF,  $RGF_n$ ,  $GF_{coronal}$  and  $GF_{sagittal}$  from this study, a 3D probability map of fibroglandular tissue within a breast of a given breast size can be generated (demonstrated in [Figure 2.29](#) and [Figure 2.30](#)). At certain breast locations, the mean  $RGF_n$ ,  $GF_{coronal}$ , or  $GF_{sagittal}$  is larger than its 75<sup>th</sup> percentile due to outliers among the data. Breast phantoms calibrated to age, size, and fibroglandular tissue distribution may be useful for observer performance studies in breast imaging and Monte Carlo simulation of x-ray dosimetry.

Limitations of this study include the bCT protocol in scanning larger patients. For women with bra cup size D or larger, the breast is confined anteriorly to be within the field of view. In doing so, breast length may be slightly underestimated. The wide range of chest wall and axillary coverage in the bCT images may poorly characterize breast tissue distribution in these regions, leading to slight inaccuracy in VGF and AGF.

Despite these limitations, this work presents a description of the breast

using the largest available set of images acquired with breast CT, to our knowledge. This study describes the relationship between the 2D and 3D representations of fibroglandular fraction and the overestimation when using BIRADS density. A number of breast anatomical metrics were introduced and characterized in detail, describing breast shape, breast diameter and length, radial breast glandular fraction in three breast regions, and glandular fraction along two orthogonal planes of the breast as a function of patient age and bra cup size. Three-dimensional breast phantoms can be accurately generated using the breast anatomical metrics developed in this study.

## 2.3 References

- S. M. Astley and S. Caulkin. The generation of synthetic spiculated lesions in digital mammograms using statistical models. *Radiology*, 225:645–645, 2002. [2.2.5](#)
- P. R. Bakic, M. Albert, D. Brzakovic, and A. D. A. Maidment. Mammogram synthesis using a 3d simulation. 1. breast tissue model and image acquisition simulation. *Medical physics*, 29(9):2131–2139, 2002. [2.2.1](#)
- K. Bliznakova, Z. Bliznakov, V. Bravou, Z. Kolitsi, and N. Pallikarakis. A three-dimensional breast software phantom for mammography simulation. *Physics in Medicine and Biology*, 48(22):3699–3719, 2003. [2.2.1](#)
- F. O. Bochud, C. K. Abbey, and M. P. Eckstein. Statistical texture synthesis of mammographic images with clustered lumpy backgrounds. *Optics Express—Optics Express*, 4(1), 1999. [2.2.1](#)
- J. M. Boone. Glandular breast dose for monoenergetic and high-energy x-ray beams: Monte carlo assessment. *Radiology*, 213(1):23–37, 1999. [2.1.1](#), [2.1.7](#), [2.1.8](#)
- J. M. Boone and 3rd V. N. Cooper. Scatter/primary in mammography: Monte carlo validation. *Med Phys*, 27(8):1818–31, 2000. [2.1.1](#), [2.1.7](#)
- J. M. Boone, M. H. Buonocore, and 3rd V. N. Cooper. Monte carlo validation in diagnostic radiological imaging. *Med Phys*, 27(6):1294–304, 2000. [2.1.1](#), [2.1.7](#)

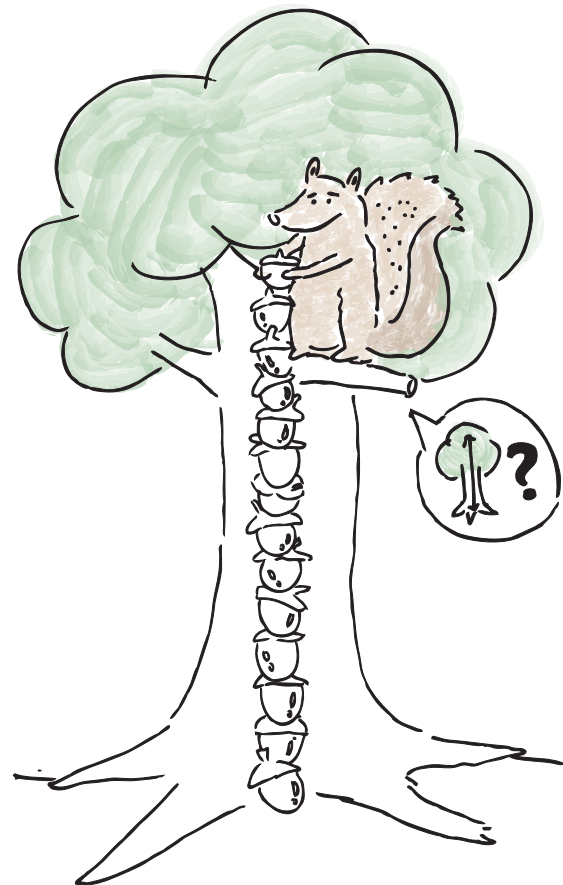
- J. M. Boone, A. L. Kwan, J. A. Seibert, N. Shah, K. K. Lindfors, and T. R. Nelson. Technique factors and their relationship to radiation dose in pendant geometry breast ct. *Medical physics*, 32(12):3767–76, 2005. **2.1.1**
- D. R. Dance. The monte carlo calculation of integral radiation dose in xero-mammography. *Physics in medicine and biology*, 25(1):25–37, 1980. **2.1.1**, **2.1.8**
- D. R. Dance. Monte carlo calculation of conversion factors for the estimation of mean glandular breast dose. *Phys Med Biol*, 35(9):1211–9, 1990. **2.1.1**, **2.1.8**
- Inc. Farlex. Epidermis. URL <http://medical-dictionary.thefreedictionary.com/epidermis>. **2.1.8**
- Rafael C. Gonzalez and Richard E. Woods. *Digital Image Processing*. Prentice Hall, Upper Saddle River, New Jersey 07458, 2nd edition, 2002. **2.1.4**
- S. Y. Huang, J. M. Boone, K. Yang, A. L. C. Kwan, and N. J. Packard. The effect of skin thickness determined using breast ct on mammographic dosimetry. *Medical physics*, 35(4):1199–1206, 2008. **2.2.4.4**
- M. Kallergi, M. A. Gavrielides, C. G. Berman, J. J. Kim, and R. A. Clark. Simulation model of mammographic calcifications based on the american college of radiology breast imaging reporting and data system, or birads. *Academic Radiology*, 5(10):670–679, 1998. **2.2.1**
- Daniel B. Kopans. *Breast Imaging*, p. 350-351. Linppincott-Raven Publishers, Philadelphia, Pennsylvania 19106-3780, third edition, 2007. **2.2.5**
- P. D. Kovesi. Matlab and octave functions for computer vision and image processing. URL <http://www.csse.uwa.edu.au/~pk/research/matlabfns/>. **2.1.4**
- M. J. Lado, P. G. Tahoces, M. Souto, A. J. Mendez, and J. J. Vidal. Real and simulated clustered microcalcifications in digital mammograms. roc study of observer performance. *Med Phys*, 24(9):1385–94, 1997. **2.2.1**
- F. Lefebvre, H. Benali, R. Gilles, and R. Di Paola. A simulation model of clustered breast microcalcifications. *Med Phys*, 21(12):1865–74, 1994. **2.2.1**
- J. T. Manning, D. Scutt, G. H. Whitehouse, and S. J. Leinster. Breast asymmetry and phenotypic quality in women. *Evolution and Human Behavior*, 18(4):223–236, 1997. **2.1.6**

- J. J. Nappi and P. B. Dean. Mammographic feature generator for evaluation of image analysis algorithms. *Image Processing - Medical Imaging 1997, Pts 1 and 2*, 3034:911–918, 1997. **2.2.1**
- N. Packard and J. M. Boone. Glandular segmentation of cone beam breast ct volume images. *Proc. of SPIE*, 6510(1):651038, 2007. **2.2.2**
- Marvin Rosenstein, Linda W. Andersen, and Gordon B. Warner. *Handbook of Glandular Tissue Doses in Mammography*. HHS publication FDA 85-8239. U.S. Dept. of Health and Human Services, Public Health Service, Food and Drug Administration, Center for Devices and Radiological Health, Rockville, Maryland 20857, 1985. **2.1.1, 2.1.8**
- D. Scutt, G. A. Lancaster, and J. T. Manning. Breast asymmetry and predisposition to breast cancer. *Breast Cancer Res*, 8(2):R14, 2006. **2.1.6**
- H. S. Shukla, L. E. Hughes, I. H. Gravelle, and A. Satir. The significance of mammary skin edema in noninflammatory breast cancer. *Ann Surg*, 189(1):53–7, 1979. **2.1.8**
- H. S. Shukla, I. H. Gravelle, L. E. Hughes, R. G. Newcombe, and S. Williams. Mammary skin oedema: a new prognostic indicator for breast cancer. *Br Med J (Clin Res Ed)*, 288(6427):1338–41, 1984. **2.1.8**
- L. Slomianka. Blue histology - integumentary system. URL <http://www.lab.anhb.uwa.edu.au/mb140/CorePages/Integumentary/Integum.htm#Dermis>. **2.1.8**
- P. C. Stomper, D. J. Dsouza, P. A. DiNitto, and M. A. Arredondo. Analysis of parenchymal density on mammograms in 1353 women 25-79 years old. *American Journal of Roentgenology*, 167(5):1261–1265, 1996. **2.2.5**
- Jr. T. L. Pope, M. E. Read, T. Medsker, A. J. Buschi, and A. N. Brenbridge. Breast skin thickness: normal range and causes of thickening shown on film-screen mammography. *J Can Assoc Radiol*, 35(4):365–8, 1984. **2.1.8**
- H. Ulger, N. Erdogan, S. Kumanlioglu, and E. Unur. Effect of age, breast size, menopausal and hormonal status on mammographic skin thickness. *Skin Res Technol*, 9(3):284–9, 2003. **2.1.8**
- S. A. Willson, E. J. Adam, and A. K. Tucker. Patterns of breast skin thickness in normal mammograms. *Clin Radiol*, 33(6):691–3, 1982. **2.1.8**
- David M. Witten. *The Breast, p. 15.* An Atlas of Tumor Radiology. Year Book Medical Publishers, Chicago, 1969. **2.1.6, 2.1.8**

- X. Wu, G. T. Barnes, and D. M. Tucker. Spectral dependence of glandular tissue dose in screen-film mammography. *Radiology*, 179(1):143–8, 1991. **2.1.1, 2.1.8**
- X. Wu, E. L. Gingold, G. T. Barnes, and D. M. Tucker. Normalized average glandular dose in molybdenum target-rhodium filter and rhodium target-rhodium filter mammography. *Radiology*, 193(1):83–9, 1994. **2.1.1, 2.1.8**
- M. J. Yaffe, J. M. Boone, N. Packard, O. Alonzo-Prouix, S. Y. Huang, C. L. Perssotti, A. Al-Mayah, and K. Brock. The myth of the 50-50 breast. *Medical physics*, 36(12):5437–5443, 2009. **2.2.2, 2.2.5**
- K. Yang, A. L. Kwan, D. F. Miller, and J. M. Boone. A geometric calibration method for cone beam ct systems. *Medical physics*, 33(6):1695–706, 2006. **2.1.3**

## Chapter 3

# The Simulation of CEDEM Images



### 3.1 Motivation

Optimization of any imaging task start with a thorough understanding of components within a x-ray imaging system, such as the x-ray source, detectors, and system geometry. Ways to simulate images of a given imaging system is helpful in guiding experimental setting and in confirming experimental results. Therefore, this chapter will describe an approach to simulate projection images closely calibrated to the breast CT system for various optimization purposes.

### 3.2 The Semi-Empirical Linear Model of Indirect, Flat-panel X-ray Detectors

Modeling x-ray detectors is a key step towards understanding the signal and noise propagation characteristics of the system. Flat-panel x-ray detectors with indirect detection have been used widely in medical imaging systems for generating superior-quality images. Converting the incident x-ray photons to a digital signal from an indirect, flat-panel detector involves several stages of signal transfer through the scintillator, photodiodes, and subsequent electronics. It is essential to understand how signal and noise behave in flat panel projection images, in order to optimize cone beam computed tomography (CT) reconstruction using these detectors.

For an indirect, flat-panel x-ray detector, the signal collection is based on energy deposition of the incident x-ray photons in the detector. This process of image formation is not trivial, as described in previous studies such as cascaded system analysis (CSA) ([Cunningham et al., 1994](#); [Siewerdsen et al., 1997, 1998](#)) and doubly stochastic Poisson processes ([Barrett et al., 1997](#)). Numerous signal transduction events related to the absorption of x-ray photons in the detector add to the complexity of modeling an energy-integrating detector. Moreover, the presence of inhomogeneous objects, such as anatomical structures, introduces variability in the signal and transfer process of the

detector. The cascaded system analysis elegantly describes the system signal and noise transfer when imaging with anatomical structures in the stochastic processes. The analytical approach provides essential understanding of signal and noise propagation, and it can be implemented when performing task-dependent analysis without physically generating images. In applications where generating images of a given heterogeneous-material object is useful for system optimization, such as dual-energy mammography or other imaging procedures, an approximation of the analytical approach would be useful in simulating images for a given set of imaging parameters. Therefore, it is the goal of this paper to introduce a semi-empirical linear model to simulate images with (or without) attenuating materials using x-ray energy-integrating detectors for a known x-ray spectrum.

### 3.2.1 Theory

X-ray energy-integrating detectors, such as indirect, flat-panel x-ray detectors, produce signal based on the energy that each x-ray quantum contributes. In x-ray imaging procedures, the x-ray spectrum characterizes the x-ray energy distribution that is incident upon the object and the detector. Once an x-ray spectrum characterized by a Poisson process interacts with an energy-integrating detector system, the probability distribution of the output signal is in general no longer a Poisson process, but rather becomes a Compound Poisson process ([Whiting et al., 2006](#)), due to the multi-stage process of x-ray energy-integration. [Yang et al. \(2010\)](#) has demonstrated that the Compound Poisson statistics was effective to model the first and second moments of a single detector element signal, i.e. mean and variance. In order to simulate images with accurate signal and noise, the characterization of signal correlation among all detector elements in addition to their 1<sup>st</sup>- and 2<sup>nd</sup>-moment statistics is also needed. In this study, we adopted some of the CSA theoretical steps ([Siewerdsen et al., 1997, 1998](#)) in modeling signal and noise transfer in an energy-integrating x-ray detector. Therefore, this section will focus on a summary of the CSA signal transfer steps and the approximation steps in

simulating images considering multi-pixel signal and noise relationships of an x-ray energy-integrating detector.

Let the distribution of the incident photon energy,  $E$ , with the x-ray incident air kerma,  $A$ , be described by the x-ray spectrum  $\Phi(E; A)$  in photons/mm<sup>2</sup>. The mean photon counts,  $\bar{S}_0(x, y, E)$ , at the face of the detector is

$$\bar{S}_0(x, y, E) = \frac{\Phi(E; A)}{(x - x^s)^2 + (y - y^s)^2 + (z - z^s)^2} \quad (3.1)$$

where  $(x_s, y_s, z_s)$  is the location of x-ray source. With an object in the field of view, the mean photon counts are attenuated according to Beer's law depending on the energy-dependent attenuation coefficient  $\mu_m(E)$  and the path length  $T_m(x, y)$  of each material  $m$  present in the x-ray path. Assuming that there are a total of  $M$  materials in the object, the attenuated photon counts is

$$\bar{S}_1(x, y, E) = \bar{S}_0(x, y, E) e^{-\sum_{m=1}^M \mu_m(E) T_m(x, y)} \quad (3.2)$$

The effect of scattered x-rays is not considered in this study. As the x-ray photons propagate through the detector scintillator, the mean photon counts are attenuated according to the x-ray attenuation properties given  $\mu_s(E)$  and thickness  $T_s$ . The scintillator then converts the x-ray energy deposited into light photons given the fractional energy absorbed in the scintillator per attenuated x-ray photon  $Q_s(E)$  and the number of light photons produced per attenuated x-ray photon  $G_s$ . The conversion of x-ray photons to optical photons depends on the energy of the absorbed x-ray photons. Below the K-edge of the scintillator material,  $Q_s(E)$  is close to unity considering the energy loss in the form of L-fluorescent x-rays and other x-ray interactions. Above the K-edge,  $Q_s(E) < 1$  due to the loss of energy in the form of K-fluorescent x-rays escaping the scintillator. The light photons are coupled with the photodiodes according to its optical coupling efficiency  $G_p$  to produce electron-hole pairs for signal readout. The signal readout is influenced by the point spread function of the scintillator blur  $PSF_{det}(x, y)$  due to multiple x-ray interaction within the scintillator layers. The digital signal readout from the photodi-

odes is then given by

$$\bar{S}_2(x, y, E) = \left[ G_s G_p Q_s(E) E \left( 1 - e^{-\mu_s(E) T_s} \right) \bar{S}_1(x, y, E) \right] * * PSF_{det}(x, y) \quad (3.3)$$

Let  $PSF_{det}(x, y) = 1$  for simplicity. The digital signal readout at the  $n^{th}$  pixel, locating at  $(x_n, y_n)$ , is obtained by integrating  $\bar{S}_2(x, y, E)$  over energy and over the area of the detector element specified by the detector element function  $P_n(x, y)$  defined as

$$P_n(x, y) = \begin{cases} 1, & \Delta_x(n-1) \leq x < \Delta_x n, \Delta_y(n-1) \leq y < \Delta_y n \\ 0, & \text{otherwise} \end{cases} \quad (3.4)$$

where  $\Delta_x$  and  $\Delta_y$  are the horizontal and vertical dimensions of the detector element, respectively. Assuming a linear detector gain  $G_{ADU}$ , the mean detector output signal  $\bar{S}_3(x_n, y_n)$  is given by

$$\bar{S}_3(x_n, y_n) = G_{ADU} \int_E \int_x \int_y \bar{S}_2(x, y, E) P_n(x, y) dx dy dE \quad (3.5)$$

The statistics of the detector output signal is thought to follow the Compound Poisson statistics (Whiting et al., 2006) suggesting a linear relationship between the signal mean and variance from an energy-integrating detector. For an incident x-ray spectrum, the mean  $m_{sim}(x_n, y_n)$  and variance  $v_{sim}(x_n, y_n)$  are predicted to linearly relate to  $\bar{S}_3(x_n, y_n)$  by some factors,  $f_{mean}$  and  $f_{var}$ ,

$$m_{sim}(x_n, y_n) = f_{mean} \bar{S}_3(x_n, y_n) \quad (3.6)$$

$$v_{sim}(x_n, y_n) = f_{var} m_{sim}(x_n, y_n) \quad (3.7)$$

$f_{mean}$  and  $f_{var}$  are factors relating  $\bar{S}_3(x_n, y_n)$  to the mean  $m_{emp}(x_n, y_n)$  and vari-

ance  $v_{emp}(x_n, y_n)$  empirically determined for a given incident x-ray spectrum,

$$f_{mean} = \frac{m_{emp}(x_n, y_n)}{\bar{S}_3(x_n, y_n)} \quad (3.8)$$

$$f_{var} = \frac{v_{emp}(x_n, y_n)}{f_{mean}\bar{S}_3(x_n, y_n)} \quad (3.9)$$

In addition to accurate prediction of the signal mean and variance, noise properties in the Fourier domain are useful in simulating images appropriately. Cascaded system analysis (Siewerdsen et al., 1997, 1998) can predict the noise power spectrum  $NPS_{sim}(u, v)$  of indirect-detection flat panel imagers for an incident x-ray spectrum in the form of

$$NPS_{sim}(u, v) = v_1 MTF_{d,sinc}^2 + v_2 MTF_{d,det}^2 + NPS_{add}(u, v) \quad (3.10)$$

where  $v_1$  and  $v_2$  are simplified as some portion of the signal variance ( $S_5(u, v)$ ) in eq. 7a in Siewerdsen et al. (1998)).  $MTF_{d,sinc}(u, v)$  and  $MTF_{d,det}(u, v)$  represent the digital modulation transfer function (MTF) of the detector pixel sampling and detector system, respectively.  $NPS_{add}(u, v)$  is the noise power spectrum of the detector electronic noise, characterized by variance,  $v_{add}$ . For a given incident x-ray spectrum,  $v_1$  and  $v_2$  are estimated from the measured NPS from the detector system. Simulated projection images of the detector system  $I_{sim}(x_n, y_n)$  are then generated by summing the estimated noise components with the predicted signal mean  $m_{sim}(x_n, y_n)$

$$I_{sim}(x_n, y_n) = m_{sim}(x_n, y_n) + \tilde{N}_1(x_n, y_n) + \tilde{N}_2(x_n, y_n) + \tilde{N}_{add}(x_n, y_n) \quad (3.11)$$

where

$$\tilde{N}_1(x_n, y_n) = DFT_{2D}^{-1} \left[ DFT_{2D} \left[ \tilde{N}_{0,v_1}(x_n, y_n) \right] \cdot MTF_{d,sinc}(u, v) \right] \quad (3.12)$$

$$\tilde{N}_2(x_n, y_n) = DFT_{2D}^{-1} \left[ DFT_{2D} \left[ \tilde{N}_{0,v_2}(x_n, y_n) \right] \cdot MTF_{d,det}(u, v) \right] \quad (3.13)$$

$$\tilde{N}_{add}(x_n, y_n) = \tilde{N}_{0,v_{add}} \quad (3.14)$$

where  $\tilde{N}_{0,v}$  is a normally-distributed random number with zero-mean and variance of v.

### 3.2.2 Breast CT Data Acquisition and Processing

The dedicated breast CT (bCT) scanner (Boone et al., 2001) was designed, assembled and integrated in our laboratory at UC Davis. The bCT scanner uses a Comet x-ray tube (Comet AG, Flamatt, Switzerland). The x-ray tube has a tungsten anode and a beryllium window, and the x-ray beam was attenuated with several filter materials for experimental purpose (discussed below). The x-ray focal spot was located 511 mm from the isocenter and 1037 mm from the detector panel. The breast CT scanner operates at x-ray tube potentials ranging from 10 to 160 kV. The x-ray generator (Gulmay CP160, United Kingdom) can deliver a range of mA levels depending on the kV given the limitation of the 1000 W x-ray tube rating. The x-ray beam was collimated such that cone-beam was projected onto the detector, with no primary radiation falling outside the extent of the detector and its bezel. The x-ray detector (PaxScan 4030CB, Varian Medical Systems, Palo Alto, CA) uses a layer of 600- m columnar CsI:TI scintillator over amorphous silicon thin film transistors (TFTs) arrays. The  $2 \times 2$  binning, fixed low-gain mode ( $1024 \times 768$  detector elements,  $388\text{-}\mu\text{m}$  pixel size, maximum 30 frames per second) was used in acquiring all the projection images in this study. The frame rate of the detector (the inverse of the integrating time of each projection image) was reduced in some cases to ensure sufficient photon fluence incident on the detector. In this study, each bCT projection image was dark-field (averaged over 300 frames) subtracted and dead-pixel corrected.

### 3.2.3 X-ray Spectrum Model

The TASMIP spectrum model (Boone and Seibert, 1997) was used to model the polyenergetic x-ray spectra used in this study. The beam quality of the bCT scanner was determined physically by measuring the half-value-layer

Table 3.1. The half-value-layer (HVL) of the x-ray spectrum from the bCT system

<b>kVp</b>	<b>HVL (mm Al)</b>			
	<b>0.1 mm Sn</b>	<b>0.2 mm Cu</b>	<b>1.5 mm Al</b>	<b>0.05 mm Ag</b>
50	1.024	3.113	1.337	0.750
60	1.133	3.845	1.526	0.888
70	1.307	4.501	1.749	1.024
80	1.490	5.058	2.016	1.160
90	1.675	5.760	2.171	1.287
100	2.017	6.294	2.473	1.402

(HVL). The HVL of the incident x-ray spectrum was measured with type 1100 aluminum and an ion chamber (RadCal Model 9010, Monrovia, CA). The measured HVL was used to calibrate the TASMIP spectrum to produce an x-ray spectrum which closely matches the x-ray beam quality of the bCT system. Each calibrated TASMIP spectrum was normalized to  $8.7 \mu\text{Gy}$  at the system isocenter. For a given kV and filter material, the air kerma rate at the system isocenter was measured as a function of x-ray tube current (mA). Linear regression was applied to the measured air kerma rate as a function of mA, where air kerma rate =  $f_k \cdot mA$ . The determined value of  $f_k$  for each kV and filter material was used to scale the modeled x-ray output to that of the calibrated TASMIP spectrum of the physical bCT system.

Figure 3.1 shows the TASMIP x-ray spectra calibrated to the half-value-layer of the bCT system operating at 80 kV filtered with 0.1-mm Sn, 0.2-mm Cu, 1.5-mm Al, and 0.05-mm Ag. Table I illustrates a list of the HVL's measured from the bCT system operating at all kV and filter combinations. The HVL's of the spectra filtered with 0.2 mm Cu are higher compared with those filtered with other filters, thus, these spectra deliver harder and more penetrating x-ray photons. Figure 3.2 shows the air-kerma-rate-to-mA factor  $f_k$  for all kV and filter combinations. The x-ray fluence increases with mA and kV for all filter materials. The  $f_k$  was found to be unique for each filter material.

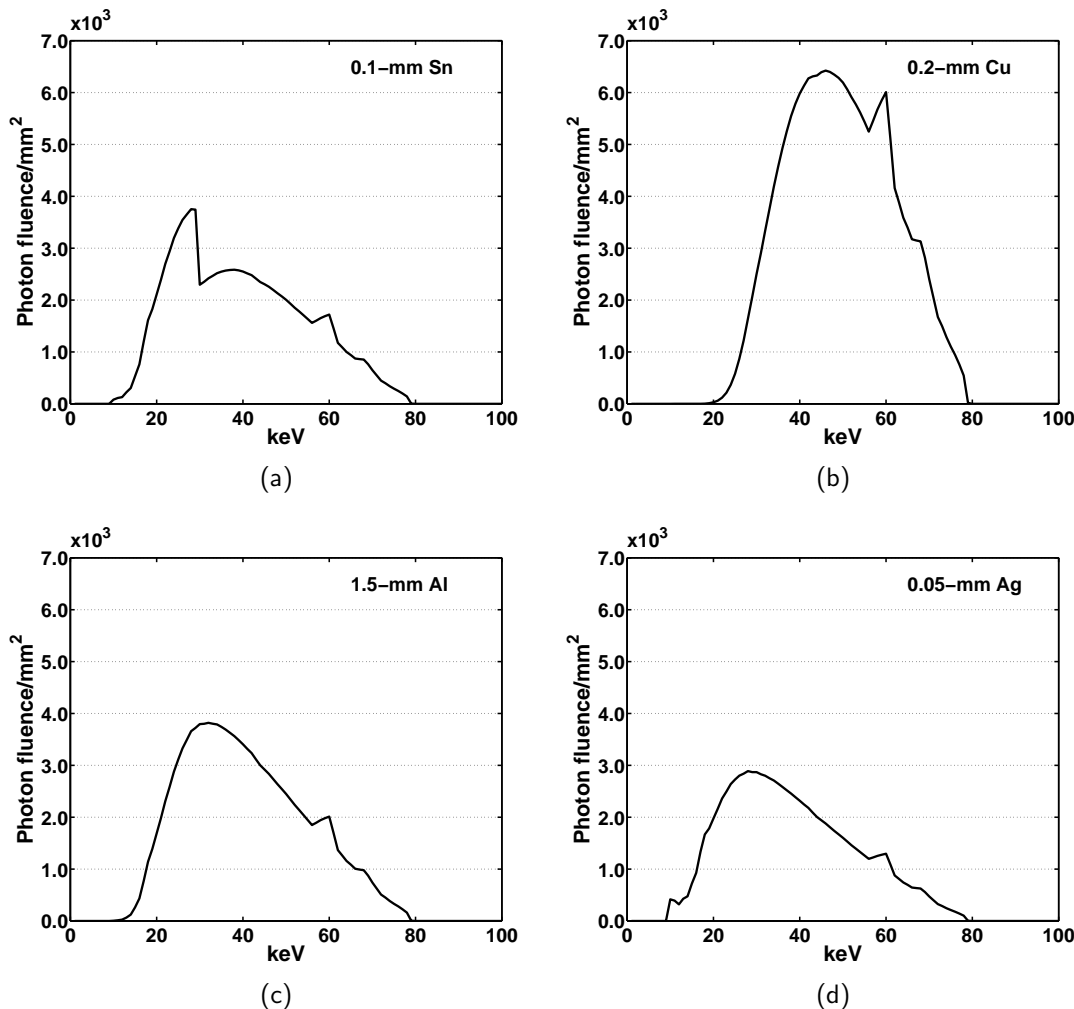


Figure 3.1. The TASMIP x-ray spectra calibrated to the bCT scanner at 80 kVp filtered with (a) 0.1 mm Sn, (b) 0.2 mm Cu, (c) 1.5 mm Al, and (d) 0.05 mm Ag. Each spectrum was normalized to 8.7  $\mu\text{Gy}$ .

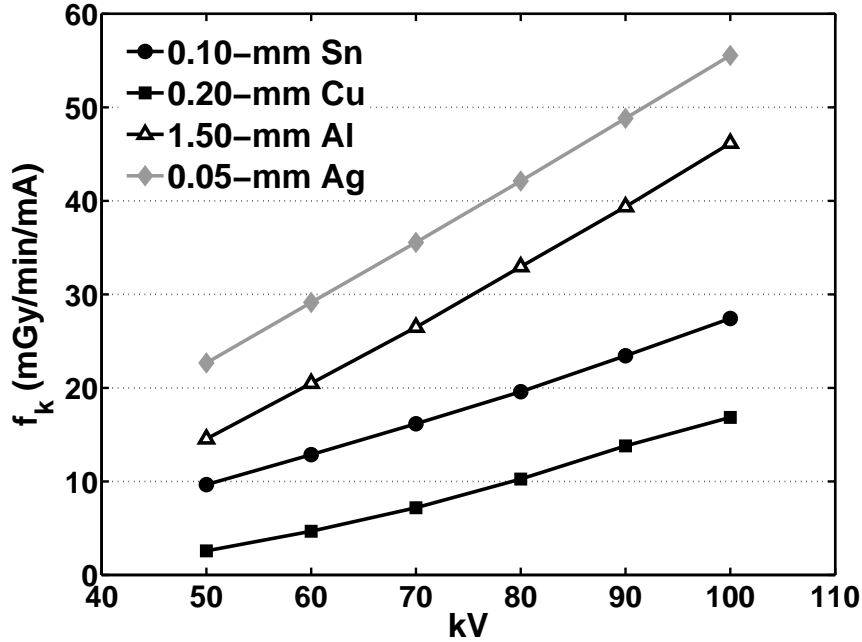


Figure 3.2. The mA-to-air-kerma-rate factor  $f_k$  is shown as a function of kV for four filters.

### 3.2.4 Detector Signal Statistics Parameters

For an indirect x-ray detector with CsI scintillator, 56 optical photons ( $G_s = 56$  in Equation (3.3)) are produced per keV energy absorbed in the scintillator (J.A. and Rowlands, 2000). 80% of the produced optical photons were assumed to be incident on the image array and 80% of the incident optical photons were assumed to convert to electron-hole pairs in a photodiode. Thus, optical coupling efficiency  $G_p$  was assumed to be 64% in Equation (3.3). In addition, the variance of the detector electronic noise,  $v_{add}$ , was found to be  $15.1 \pm 1.3 \text{ ADU}^2$  (Yang et al., 2010).  $G_{ADU}$  was found to be 1525 electrons per ADU in Equation (3.5) for projection images acquired with  $2 \times 2$  binning low-gain mode (Yang et al., 2010).

The factors relating the energy-integrated x-ray spectrum to signal statistics,  $f_{mean}$  and  $f_{var}$ , are essential in simulating bCT projection images for an incident x-ray spectrum. These factors were determined directly from the

measured signal statistics. For each filter material and thickness, 500 stationary bCT projection images with no object present were acquired over a range of kV (50, 60, 70, 80, 90, 100 kV) and x-ray tube current (mA) values in order to characterize the detector signal statistics. To reduce the influence of detector lag, the detector was exposed with x-rays for 18 seconds prior to image acquisition. The filter materials and filter thicknesses investigated in this study were 0.1-mm Tin (Sn), 0.2-mm copper (Cu), 1.5-mm aluminum (Al), and 0.05-mm silver (Ag). For an incident x-ray spectrum, the ensemble average  $m_{emp}(x_n, y_n)$  over 500 realizations was computed for each detector element at several air kerma levels. The variance,  $v_{emp}(x_n, y_n)$  was calculated using the detrended mean-subtracted value,  $I_{noise,k}(x_n, y_n)$ ,

$$I_{noise,k}(x_n, y_n) = I'_k(x_n, y_n) - S_k(x_n, y_n) \quad (3.15)$$

where  $I'_k(x_n, y_n)$  is the mean-subtracted bCT image and  $S_k(x_n, y_n)$  is the two-dimensional (2D) 2<sup>nd</sup>-order polynomial function fit to  $I_{noise,k}(x_n, y_n)$  for  $k = 1, 2, \dots, 500$ . With the determined  $m_{emp}(x_n, y_n)$  and  $v_{emp}(x_n, y_n)$ , the  $f_{mean}$  and  $f_{var}$  were obtained using Equation (3.8). For a given x-ray spectrum (the one not considered in the makeup of this model), the  $f_{mean}$  and  $f_{var}$  were estimated by interpolating across kV's using linear regression for a given filter material and thickness.

Figure 3.3 shows the mean and variance factors  $f_{mean}$  and  $f_{var}$  for all kV and filters used in this study. It suggests that  $f_{mean}$  and  $f_{var}$  increase linearly with kV ( $f_{mean}$ :  $R^2 = 0.91, 0.93, 0.86, 0.99$  for 0.1-mm Sn, 0.2-mm Cu, 1.5-mm Al, and 0.05-mm Ag respectively;  $f_{var}$ :  $R^2=0.99$  for all filters). It also indicates that there exist some unique mean and variance factors for each kV and filter combination. In addition to 1<sup>st</sup> and 2<sup>nd</sup>-order statistics of the detector signal, the quantum detection efficiency and the fraction of energy absorbed in a 0.6-mm Cesium Iodine (CsI) scintillator per attenuated x-ray photon are shown in Figure 3.4. X-ray quanta of higher energy are less likely to be detected within a 0.6-mm CsI scintillator. Above the iodine K-edge

(33.2 keV), the amount of incident x-ray energy absorbed by the 0.6-mm CsI scintillator reduced drastically due to the escape of K-fluorescence x-rays.

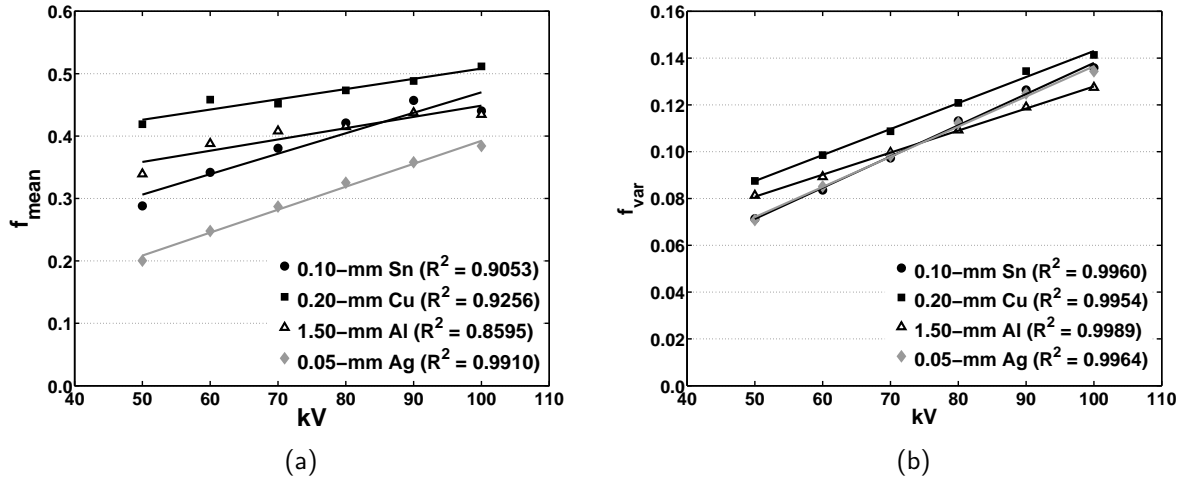


Figure 3.3. (a) The mean factors,  $f_{mean}$ , and (b) the variance factors,  $f_{var}$ , for all kVp and filter combinations.

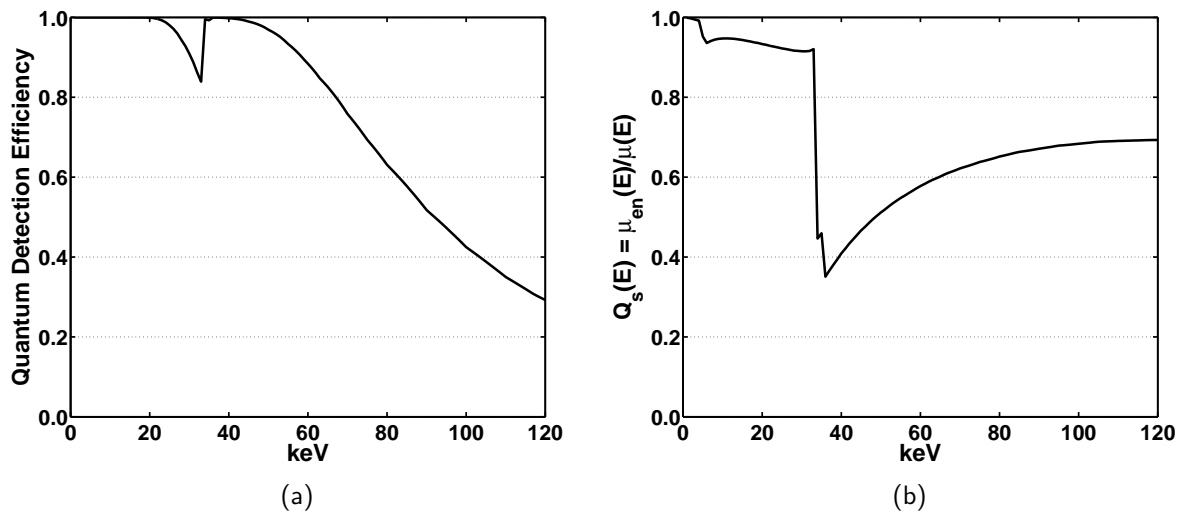


Figure 3.4. (a) The quantum detection efficiency of a 0.6-mm CsI scintillator is shown as a function of keV. (b) The fraction of energy absorbed in a 0.6-mm CsI scintillator per attenuated x-ray photon as a function of keV is illustrated.

### 3.2.5 Detector Signal Correlation

In addition to the first and second-order statistics of the detector signal, signal correlation among detector elements can be characterized by a mathematic filter. Depending on the detector element structure and signal readout, a detector will have a unique correlation structure typically described by the modulation transfer function (MTF) of the system. The detector MTF was measured using an edge phantom, which is the same one used in the ACRIN DMIST trial ([Bloomquist et al., 2006](#)). The edge consists of a 0.1-mm thick, 5 cm × 5 cm niobium foil on top of a 0.8-mm thick, 10 cm × 10 cm aluminum sheet. With the edge phantom placed at the surface of the detector, 300 stationary projection images were averaged for each measurement. The effect of focal spot blur was minimized by placing the edge phantom on the detector surface. Therefore, focal spot blur was not considered in this study. The presampling MTF ( $MTF_{pre}$ ) was then calculated using an over-sampling method ([Fujita et al., 1992](#)). The edge phantom was placed at three different locations on the detector, the final  $MTF_{pre}$  was computed by averaging over the vertical and horizontal  $MTF_{pre}$  measured at three detector locations.

$MTF_{pre}$  describes the system response of a continuously sampled system. However, the signal correlation between the detector elements is usually influenced due to the discretization of detector elements. Signal undersampling from a detector system introduces signal aliasing, which violates the presumed stationary property of the MTF. To rectify this effect of aliasing, the digital MTF  $MTF_{d,det}(u, v)$  of the detector system ([J. T. Dobbins, 1995](#)) was calculated as

$$MTF_{d,det}(u, v) = MTF_{pre}(u, v) * *III(u, v) \quad (3.16)$$

$$\text{where } III(u, v) = \sum_{j,k=-\infty}^{\infty} \delta(u - ju_s, v - kv_s) \quad (3.17)$$

where  $u_s$  and  $v_s$  are the sampling frequency in horizontal and vertical direction. In this study,  $MTF_{d,sinc}(u, v)$  is the digital MTF of the detector sampling

where

$$MTF_{d,sinc}(u, v) = \left[ \text{sinc}(a_x u) \text{sinc}(a_y v) \right] * * III(u, v) \quad (3.18)$$

where  $a_x$  and  $a_y$  are the dimension of the active area of a detector element. The digital MTF was thought to be a reasonable approximation of the detector system, albeit bounded by the Nyquist frequency. Figure 3.5 illustrates the compilation of 2D digital MTF's using Equation (3.16) and Equation (3.18). The 2D digital MTF filters were normalized prior to applying to the normally-distributed noise in Equation (3.12). Details of the

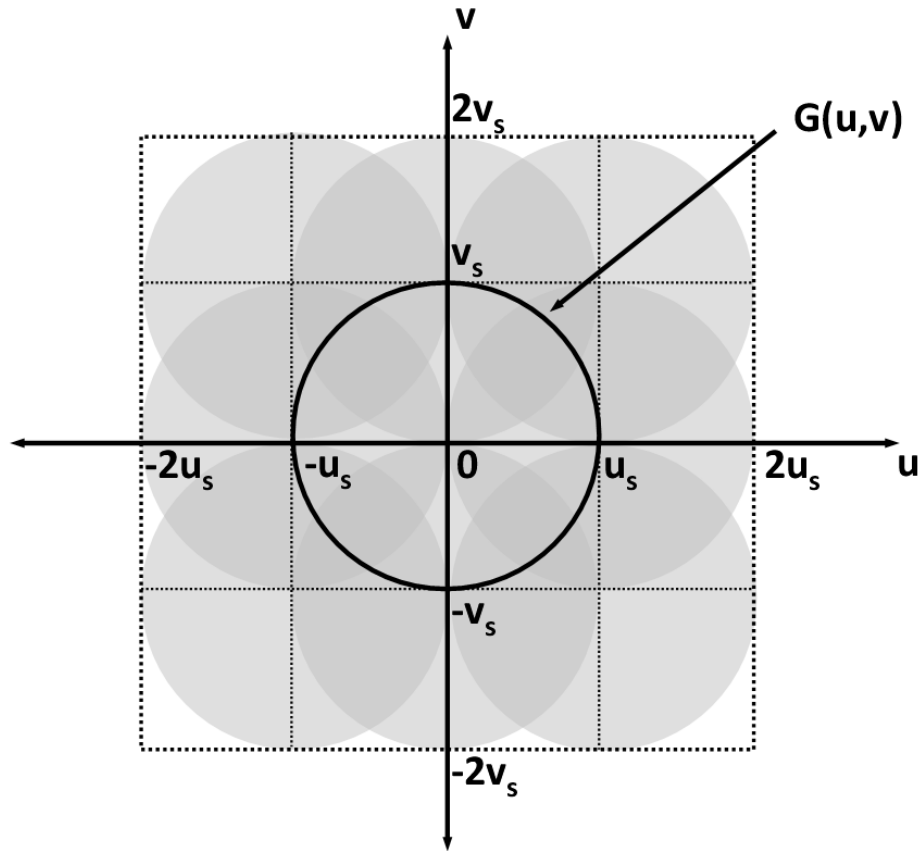


Figure 3.5. The implementation of 2D digital MTF's with the aliasing effect is illustrated in the Fourier domain. The 2D MTF is described as  $G(u, v)$  (black line). Aliasing is created by sampling the same function at the frequency  $-u_s \leq u < u_s$  and  $-v_s \leq v < v_s$ .

Figure 3.6a presents the detector modulation transfer function  $MTF_{d,det}$

of the bCT scanner at three different detector locations. The system response appears to be reasonably stationary across the three detector locations (center, bottom, and right). The MTF measured at the detector covered with larger cone angle was found to be slightly lower than that measured at other locations. The oblique interaction of x-rays through the DMIST edge phantom may likely project a thicker edge spread function, which suggests a larger degree of blur in the detector system response. Figure 3.6b shows the MTF of the detector sampling  $MTF_{d,sinc}$  calculated using a sinc function with  $a_x = a_y = 0.7 \cdot 0.388$  mm (the fill factor of a detector element is 70%). The figures also shows the digital MTF,  $MTF_{d,det}$  and  $MTF_{d,sinc}$ , where the effect of aliasing changes the shape of the filters describing the detector system response.

### 3.2.6 Noise Components in the Noise Power Spectrum (NPS)

The noise power spectrum (NPS) of the measured air scans was computed. For a given incident x-ray spectrum, 500 mean-subtracted, noise images  $I'_k(x_n, y_n)$  were generated for  $k = 1, 2, \dots, 500$ . Forty-eight regions of interest (ROIs) were used to compute the NPS for each  $I'_k(x_n, y_n)$ . The size of a ROI was 5 x 5 cm<sup>2</sup> (128 x 128 detector elements). The noise ROI, , was detrended by subtracting the ROI mean from each ROI. No windowing was applied since images were well flat-fielded and detrended. The two-dimensional discrete Fourier transform ( $DFT_{2D}$ ) of the zero-mean  $R'_m(x_n, y_n)$  was calculated for each ROI. The empirical NPS of a bCT projection image was defined as,

$$NPS_{emp}(u, v) = \frac{1}{M} \sum_{m=1}^M \left| DFT_{2D} [R'_m(x_n, y_n)] \right|^2 \frac{\Delta_x \Delta_y}{N_x N_y} \quad (3.19)$$

where M is the number of ROIs and  $N_x$  and  $N_y$  are the number of elements in the horizontal and vertical dimensions of the ROI. Knowing the analytical NPS defined in Equation (3.10), the noise components  $v_1$  and  $v_2$  were

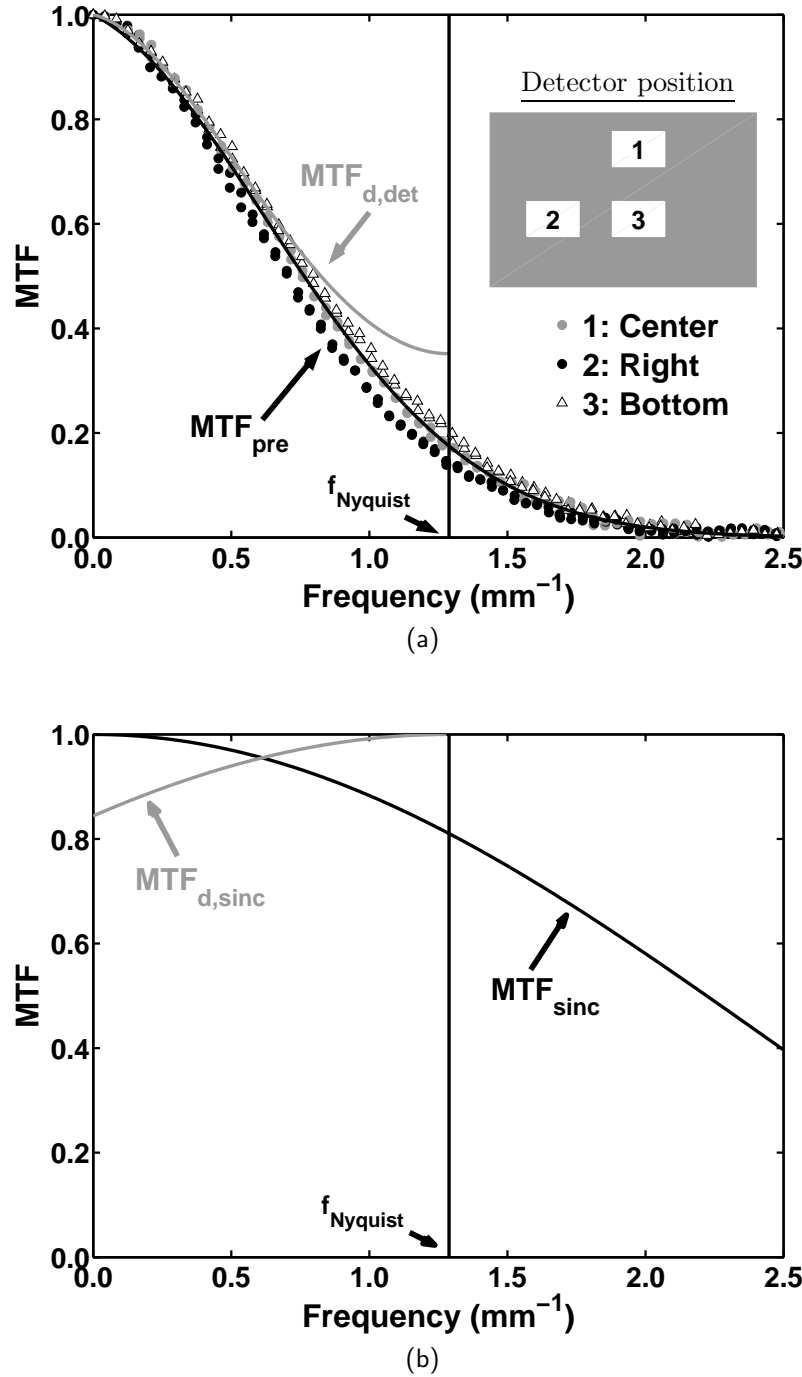


Figure 3.6. (a) The presampling MTF ( $MTF_{pre}$ ) of three detector locations are shown. Gray dots: center, black dots: right; triangle: bottom; black line: averaged  $MTF_{pre}$ . The digital MTF( $MTF_{d,det}$ ) of the detector system is shown in grey line. (b) The presampling MTF of detector sampling function ( $MTFsinc$ , black line) and the digital MTF of the detector sampling function ( $MTFd,sinc$ , gray line) are illustrated.

determined by minimizing the sum of squared difference (SSD) between the one-dimensional (1D) simulated NPS  $NPS_{sim}(u; v_1, v_2)$  and the 1D empirical NPS  $NPS_{emp}(u)$  for a given incident x-ray spectrum given by

$$SSD = \sum_u \left[ NPS_{sim}(u; ; v_1, v_2) - NPS_{emp}(u) \right]^2 \quad (3.20)$$

The SSD was minimized over the appropriate range of  $v_2$  by setting  $v_1 \equiv \bar{v}_{emp} - v_2 - v_{add}$  where  $\bar{v}_{emp}$  is the mean  $v_{emp}(x_n, y_n)$  averaged over all detector elements.  $v_2$  was characterized as a function of signal mean  $m_{emp}(x_n, y_n)$  for all kV and filter materials considered in this study. For a given incident x-ray spectrum (the one not considered in the makeup of this model),  $v_2$  was predicted by interpolating across kV's using 2<sup>nd</sup>-order polynomials for a given filter material and thickness.

Figure 3.7 shows the noise component  $v_2$  as a function of mean  $m_{emp}$  for all x-ray spectra considered in this model (50, 60, . . . , 100 kV filtered with 0.1-mm Sn, 0.2-mm Cu, 1.5-mm Al, and 0.05-mm Ag). The linear regression was used to fit  $v_2$  as a function of the mean  $m_{emp}$  for each kV and filter combinations.  $v_2$  was found to be linearly related to mean  $m_{emp}$  indicating both noise components  $v_1$  and  $v_2$  are linearly related with the energy-integrated detector signal.

### 3.3 Validation of the Semi-Empirical Linear Detector Model

#### 3.3.1 Images of Air Scans

For validation purposes, measured and simulated air scan images were produced using the following kV and filter combinations at 4 different air kerma levels: 40 kV/0.1-mm Sn, 65 kV/0.2-mm Cu, 85 kV/1.5-mm Al, and 95 kV/0.05-mm Ag. The noise power spectra of the simulated and measured air scans were computed to validate this model as described in section III.B.4. The

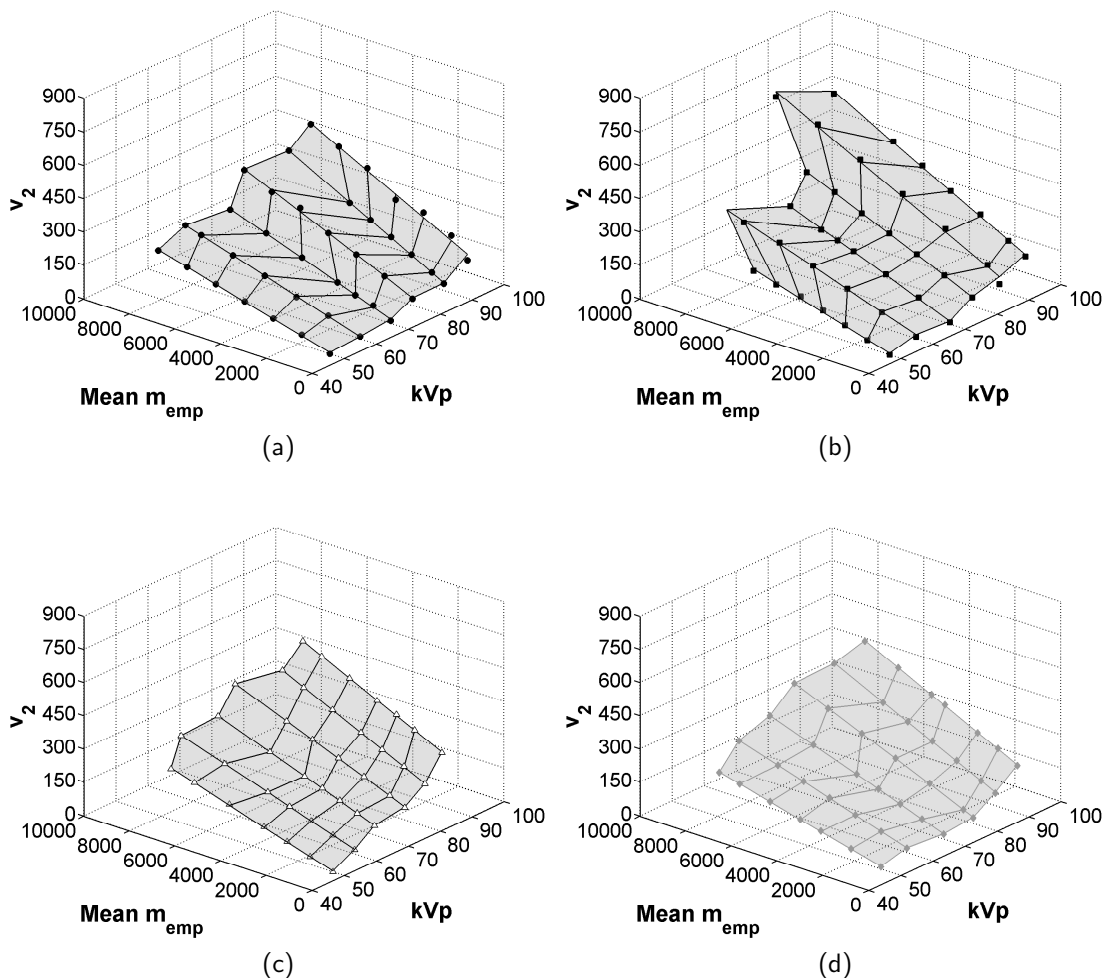


Figure 3.7. The noise component,  $v_2$ , in the noise power spectrum is shown as a function of ensemble signal mean,  $m_{emp}$ , and kVp for the incident x-ray spectra filtered with (a) 0.1-mm Sn, (b) 0.2-mm Cu, (c) 1.5-mm Al, and (d) 0.05-mm Ag.

radially-averaged NPS was used to illustrate the two-dimensional (2D) NPS in one-dimension (1D). The ensemble average of ROI mean  $m_{ROI}$  of the air scan images was evaluated. The ensemble average of the ROI variance  $v_{ROI}$  of the noise image was computed as

$$v_{ROI} = \int_{-\infty}^{\infty} \int_{-\infty}^{\infty} NPS(u, v) dudv \quad (3.21)$$

For a given kV and filter material, the ensemble average NPS of the measured air scans were compared with those of the simulated air scans. The ROI mean and variance of the measured and simulated projection images were compared as well.

Figure 3.8 and Figure 3.9 show the ROI mean  $m_{ROI}$  and variance  $v_{ROI}$  of the simulated and measured air scan images as a function of air kerma for the incident x-ray spectra of 40 kV/0.1-mm Sn, 65 kV/0.2-mm Cu, 85kV/1.5-mm Al, and 95 kV/0.05-mm Ag. The  $m_{ROI}$  and  $v_{ROI}$  were found to be linearly related to air kerma incident on the detector. The  $m_{ROI}$  or  $v_{ROI}$  relationship to air kerma was found to be characteristic of each incident x-ray spectrum in this study since each spectrum has a specific and (see Figure 3.3). The average absolute percent error (over 4 air kerma levels) between the simulated and measured ROI mean was 9.95%, 7.28%, 4.27%, and 1.83% for 40 kV/0.1-mm Sn, 65 kV/0.2-mm Cu, 85kV/1.5-mm Al, and 95 kV/0.05-mm Ag, respectively. The average absolute percent error (over 4 air kerma levels) between the simulated and measured ROI variance was 5.54%, 7.25%, 3.61%, and 4.10% for the four kV/filter combinations. Thus, the  $m_{ROI}$  and  $v_{ROI}$  demonstrate reasonable agreement between the measured and simulated air scan images of the four kV and filter combinations considered in this study.

Figure 3.10 shows the radially-averaged NPS computed of the measured and simulated air scan images with the incident x-ray spectra with 40 kV/0.1 mm Sn (36.45  $\mu$ Gy), 65 kV/0.2 mm Cu (27.20  $\mu$ Gy), 85 kV/1.5 mm Al (5.97  $\mu$ Gy), and 95 kV/0.05 mm Ag (10.57  $\mu$ Gy). Reasonable agreement between the NPS of simulated and measured air scan images was observed for these

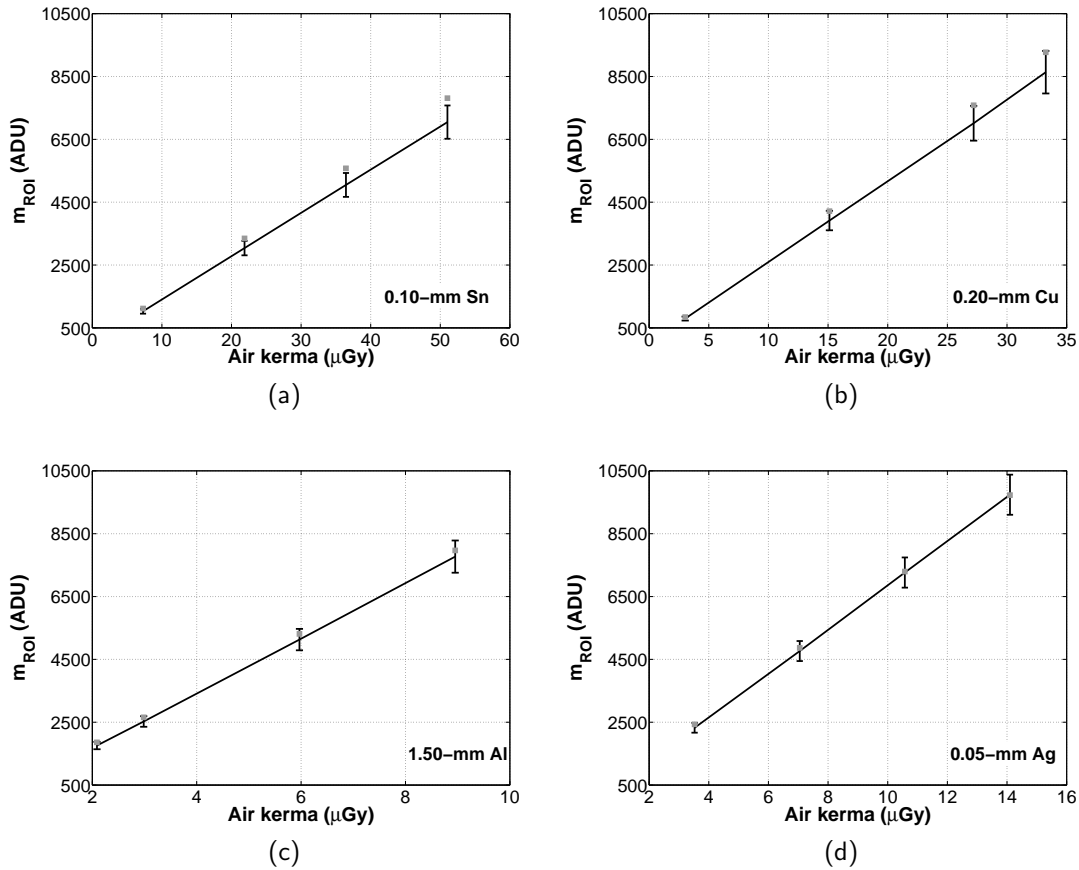


Figure 3.8. The ROI mean,  $m_{ROI}$ , of the simulated and measured air scan images is shown as a function of air kerma for the incident x-ray spectrum (a) 40 kVp/0.1 mm Sn, (b) 65 kVp/0.2 mm Cu, (c) 85 kVp/1.5 mm Al, and (d) 95 kVp/0.05 mm Ag. The gray dots represent the simulated data while the black lines (error bar of standard deviation) represent the measure data.

incident x-ray spectra. Figure 3.11 illustrates contour plots of the absolute percent error between the radially-averaged NPS of the simulated and measured air scan images with 40 kV/0.1 mm Sn, 65 kV/0.2 mm Cu, 85 kV/1.5 mm Al, and 95 kV/0.05 mm Ag at four air kermal levels. The absolute percent error between the measured and simulated NPS ranges from 0.083% to 47.128% (40 kV/0.1 mm Sn), 0.031% to 20.248% (65 kV/0.2 mm Cu), 0.008% to 16.593% (85 kV/1.5 mm Al), and 0.016% to 17.924% (95 kV/0.05 mm Ag). Figure 3.11 suggests that this model is fairly robust in predicting the NPS of

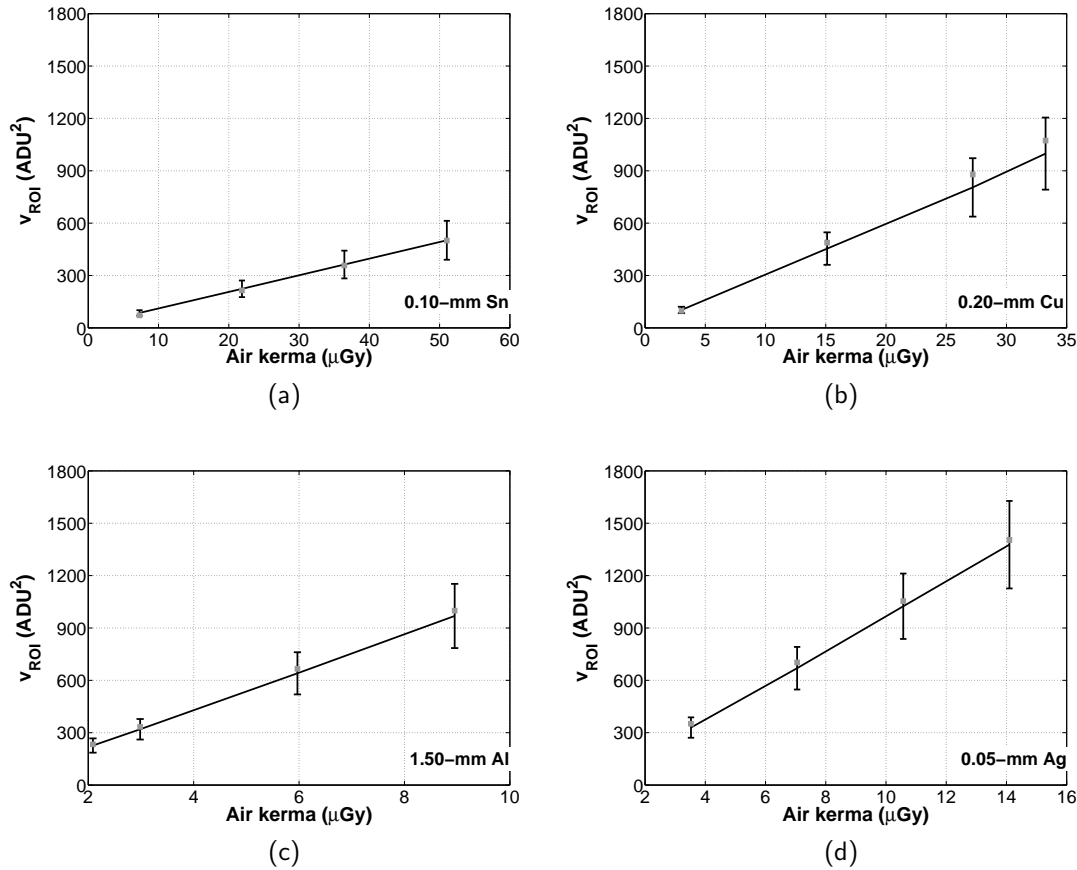


Figure 3.9. The ROI variance,  $v_{ROI}$ , of the simulated and measured air scan images is shown as a function of air kerma for the incident x-ray spectrum (a) 40 kVp/0.1 mm Sn, (b) 65 kVp/0.2 mm Cu, (c) 85 kVp/1.5 mm Al, and (d) 95 kVp/0.05 mm Ag. The gray dots represent the simulated data while the black lines (error bar of standard deviation) represent the measure data.

the breast CT system above electronic-noise dominated region of operation (x-ray spectra with lower kV and air kerma).

### 3.3.2 Images of Objects

In addition to air scan images, an 8-cm rectangular object filled with adipose tissue was simulated in three-dimensions (3D). Two cylinders of different diameters filled with water were simulated in the rectangular object. Four rectangular boxes filled with different iodine concentration (21.6 mg/ml, 10.8

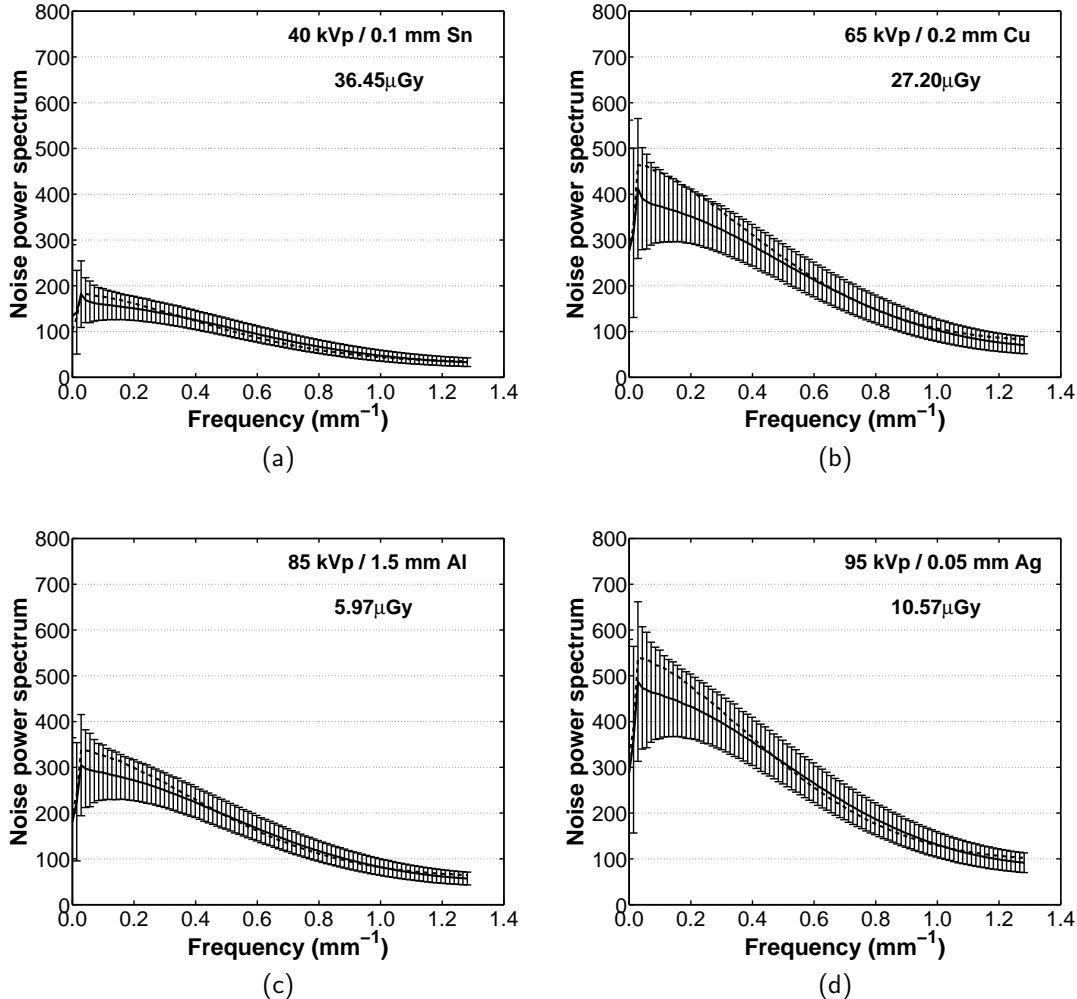


Figure 3.10. The radially-averaged noise power spectrum of the simulated and measured air scan images is compared for the incident x-ray spectrum **(a)** 40 kVp/0.1 mm Sn ( $36.45 \mu\text{Gy}$ ), **(b)** 65 kVp/0.2 mm Cu ( $27.20 \mu\text{Gy}$ ), **(c)** 85 kVp/1.5 mm Al ( $5.97 \mu\text{Gy}$ ), and **(d)** 95 kVp/0.05 mm Ag ( $10.57 \mu\text{Gy}$ ). The lines (with error bars of standard deviation) represent the measured data. The dotted lines represent the simulated data.

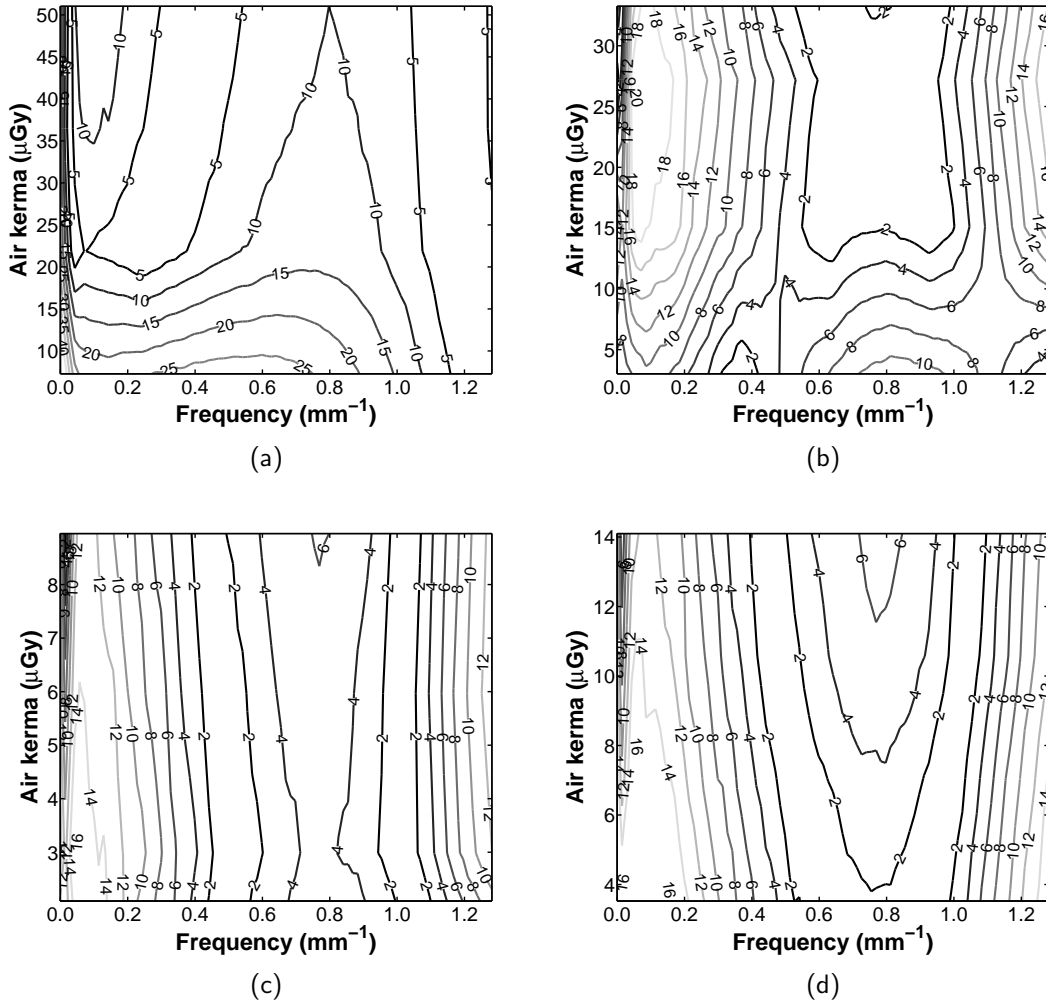


Figure 3.11. The contour of the absolute percent error (%) in the radially-averaged NPS of the simulated air scan images compared to that of the measured air scan images is illustrated for the incident x-ray spectrum (a) 40 kVp/0.1 mm Sn, (b) 65 kVp/0.2 mm Cu, (c) 85 kVp/1.5 mm Al , and (d) 95 kVp/0.05 mm Ag. The contour plot consists of the absolute percent error in NPS of four air kerma levels for x-ray spectrum with each kVp and filter combination.

mg/ml, 5.4 mg/ml, and 2.7 mg/ml) were also simulated within the 8-cm object. The x-ray path length of each material in the 3D object connecting the x-ray source to each detector element was calculated using Siddon's algorithm ([Jacobs et al., 1998](#); [Siddon, 1985](#)). A physical phantom was also constructed for validation purpose. Due to similar x-ray transmission properties, polyethylene and water were used as good surrogates of adipose tissue and glandular tissue respectively ([Prionas et al., 2011](#)). An 8-cm thick polyethylene slab was drilled with two holes of different diameters. The iodine solution (Visipaque<sup>TM</sup>, 270 mgI/ml) was diluted to the desired concentration and was filled in cuvettes. The 8-cm polyethylene slab with the cuvettes filled with iodine solution was immersed in water within a plastic container for imaging purposes. Two hundred measured and simulated images of the 8-cm rectangular object were generated using the following kV, filter material, and air kerma level: 40 kV/0.1-mm Sn (51.03  $\mu$ Gy), 65 kV/0.2-mm Cu (33.24  $\mu$ Gy), 85 kV/1.5-mm Al (8.95  $\mu$ Gy), and 95 kV/0.05-mm Ag (14.10  $\mu$ Gy). For each detector element, the signal mean and variance were computed among all 200 samples, giving rise to the mean and variance map. The mean and variance map of the measured and simulated images were compared for validation.

Figure [3.12](#) demonstrates the measured and simulated images of the 8-cm rectangular object for the incident x-ray spectra of 40 kV/0.1-mm Sn, 65 kV/0.2-mm Cu, 85 kV/1.5-mm Al, and 95 kV/0.05-mm Ag. The simulated images appeared to resolve the different shapes within the 8-cm object similarly to the measured images. Overall, the 1st- and 2nd-order statistics of the simulated images show agreement with that of the measure images. The mean and variance profiles of the simulated images were consistently lower than that of the measured data largely due to the absence of the scattered x-rays.

## 3.4 Discussion

In this study, a semi-empirical linear model was developed and validated for an indirect, flat-panel x-ray detector. The factors which characterize the sig-

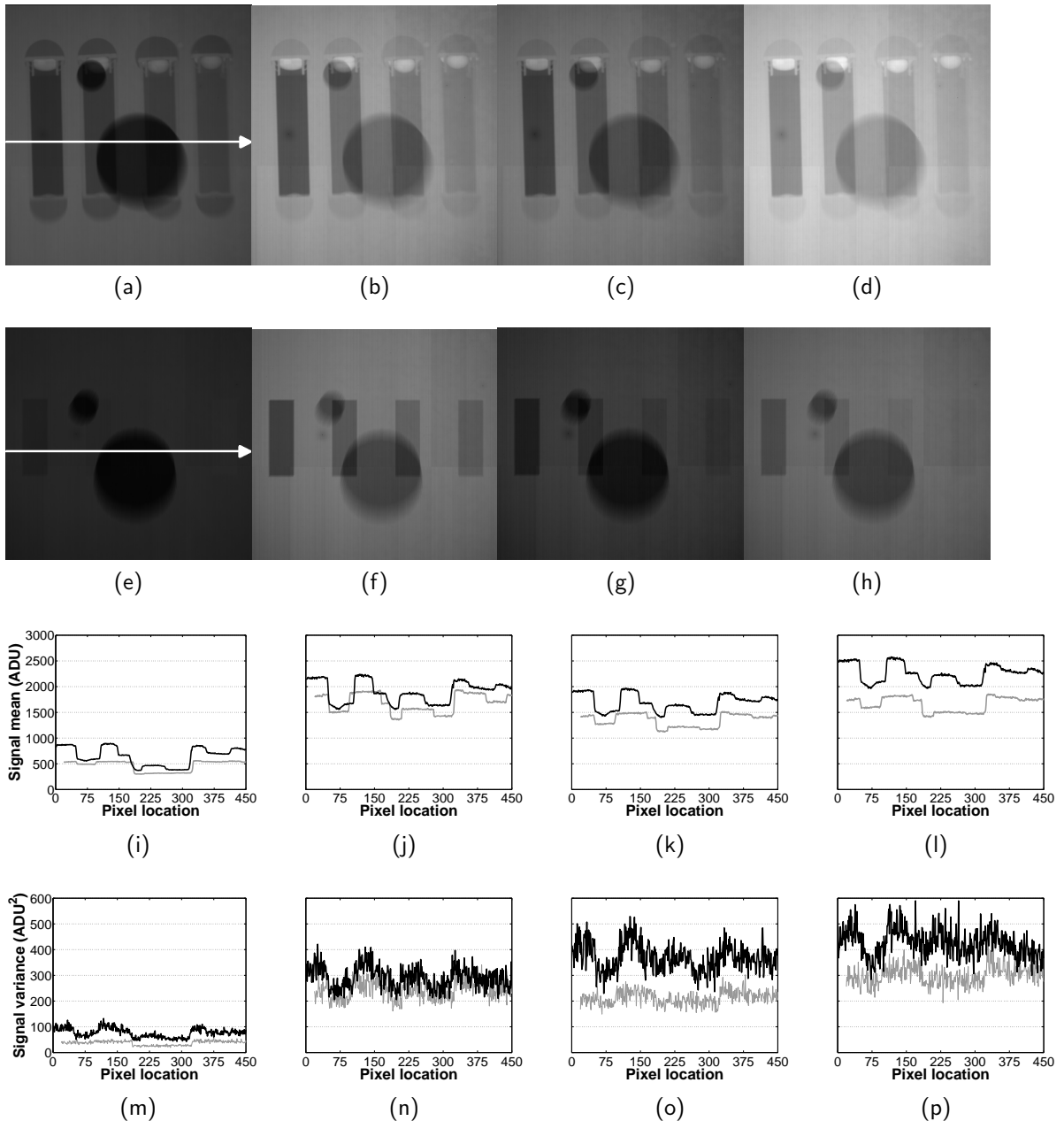


Figure 3.12. The signal mean map of the measured projection images of the 8-cm rectangular box phantom are shown for the following kV and filter combinations: (a) 40 kV/0.1-mm Sn, (b) 65 kV/0.2-mm Cu, (c) 85 kV/1.5-mm Al, and (d) 95 kV/0.05-mm Ag. The signal mean map of the simulated projection images for the four kV/filter combinations are shown in (e),(f),(g),(h). The line profiles of the mean maps are shown in (i),(j),(k),(l) for these incident x-ray spectra. The line profiles of the variance maps are shown in (m),(n),(o),(p). The black line is the profile for the measured data and the gray line is that of the simulated data.

nal mean and variance were found to be unique for a given incident x-ray spectrum and were empirically determined. For a given incident x-ray spectrum (kV, filter material, and filter thickness) and pixel dimension, images with (or without) objects can be generated using the steps described in Section 3.2.1.

The quest of understanding the signal and noise transfer in an x-ray energy-integrating detector started from the incident x-ray spectrum and progressed to detector readout in this study. Figure 3.8 and Figure 3.9 suggest that the signal variance of projection images (not reconstructed images) is linearly proportional to the signal mean since the signal mean and variance both demonstrate linear relationship with air kerma. This finding confirms the predicted relationship derived from the Compound Poisson statistics of an energy-integrating detector. In addition to the signal and noise relationship based on single-pixel analysis in Yang et al., this work extends the single-pixel relationship to multi-pixel relationships, where all detector elements and their correlation were considered. The mean factor  $f_{mean}$  in this study is thought to be proportional to what was referred as "detector sensitivity" or  $\Gamma$  defined in Siewerdsen et al. (2004). The theoretically derived detector sensitivity for a range of kV, filter materials, and filter thickness exhibit a complicated relationship that is specific to the incident x-ray spectrum and the detector type (Figure 5 and 7 in Siewerdsen et al. (2004)). This finding suggests that the factors describing the signal and noise are characteristic of a given detector type and incident x-ray spectrum. The wide range of the factors in Figure 3.3 confirms that and depend on the kV and filter material of the incident x-ray spectrum. For an accurate prediction of detector signal and noise, the empirically determined factors,  $f_{mean}$  and  $f_{var}$ , can be used to model the trend of signal and noise for a given incident x-ray spectrum and the type of x-ray scintillator. In addition to  $f_{mean}$  and  $f_{var}$ , the noise components in NPS were found to be essential in incorporating noise in simulating images. The noise components  $v_1$  and  $v_2$  consist of the Poisson excess of various gains during indirect detection of a given incident x-ray spectrum. The

compilation of Poisson excess from multiple signal and noise stages parallels the idea of the Compound Poisson statistic. These two approaches confirmed the linear relationship between  $v_{emp}$  or  $v_2$  and mean  $m_{emp}$  in Figure 3.3 and Figure 3.7.

With the known signal mean and variance (assuming no detector lag and no fluctuation in the x-ray source output), one can apply the correlation among the detector elements by filtering the normally-distributed random numbers with the digital MTF's ( $MTF_{d,det}$  and  $MTF_{d,sinc}$ ) while maintaining the magnitude of signal mean and variance. This step remains mathematically appropriate when assuming no pixel correlation prior to applying detector correlation and sampling. In addition, the digital MTF was used in this method because the acquired bCT projection images were constrained by the Nyquist limits of the detection system which essentially define the digital MTF and signal aliasing. Since a continuous description of the signal with no effect of detector sampling is impossible to measure from the detector,  $MTF_{d,det}$  and  $MTF_{d,sinc}$  were thought to appropriately describe the effect of scintillator blur and pixel sampling. As a result, this assumption is likely to give rise to the discrepancy seen in the NPS of the simulated air scan images. However, the degree of discrepancy in NPS of the air scan images appears to be reasonable for the purpose of this study.

Additionally, this semi-empirical model was validated with attenuating objects in the imaging system. While the signal mean and variance of the simulated images appeared to be comparable to that of the measured images, the absence of scattered x-rays resulted in the lower signal mean and variance in the simulated images. Since the breast CT system has a relatively large air gap (53 cm), the scattered radiation is reduced with a scatter-to-primary ratio (SPR) ranging from 20% (10-cm breast) to 50% (14-cm breast) (Kwan et al., 2005). For the purpose of generating images for additional processing, such as dual-energy processing, the absence of scattered radiation in this model can be justified since its effect can be potentially reduced by image processing.

There are several limitations in this study. The method of determining the signal noise in this study excludes the temporal components, such as x-ray source fluctuation and detector signal lag. The temporal components were not characterized and can have nontrivial effects on signal noise ([Friedman and Cunningham, 2010](#); [Siewerdsen and Jaffray, 1999](#)). In addition, the  $MTF_{pre}$  was measured with minimal effect of the x-ray focal spot blur. Moreover, the validation with attenuating objects suggests that the absence of scattered radiation was noticeable in the simulated images. Therefore, the characterization of x-ray focal spot and scatter radiation will need to be explored as additional simulation steps in future studies. Despite these limitations, the semi-empirical linear model can be useful in characterizing the signal and noise propagation necessary to simulate images in an indirect, flat-panel x-ray detector.

### 3.5 Conclusions

An approach to simulate x-ray projection images from an energy-integrating flat-panel detector was described in the spatial domain and the Fourier domain. The mean factors, variance factors, and the noise components for incident x-ray spectra ranging 50 to 100 kV filtered with 0.1-mm Sn, 0.2-mm Cu, 1.5-mm Al, and 0.05-mm Ag were empirically determined using a dedicated breast CT system. The signal and noise properties of the simulated images with and without objects show reasonable agreement with those of the measured images for any incident x-ray spectrum filtered with the 0.1-mm Sn, 0.2-mm Cu, 1.5-mm Al, or 0.05-mm Ag. This model can be used in addition to other simulation tools as a way to understand how signal and noise propagate in an imaging chain. It is a useful tool that closely calibrates to a given system for optimizing various imaging tasks.

### 3.6 References

H. H. Barrett, R. F. Wagner, and K. J. Myers. Correlated point processes in radiological imaging. *Proceedings of the SPIE - The International Society for Optical Engineering*, 3032:110–124, 1997. [3.2](#)

A. K. Bloomquist, M. J. Yaffe, E. D. Pisano, R. E. Hendrick, G. E. Mawdsley, S. Bright, S. Z. Shen, M. Mahesh, E. L. Nickoloff, R. C. Fleischman, M. B. Williams, A. D. Maidment, D. J. Beideck, J. Och, and J. A. Seibert. Quality control for digital mammography in the acrin dmist trial: part i. *Med Phys*, 33(3):719–36, 2006. [3.2.5](#)

J. M. Boone and J. A. Seibert. An accurate method for computer-generating tungsten anode x-ray spectra from 30 to 140 kv. *Med Phys*, 24(11):1661–70, 1997. [3.2.3](#)

J. M. Boone, T. R. Nelson, K. K. Lindfors, and J. A. Seibert. Dedicated breast ct: radiation dose and image quality evaluation. *Radiology*, 221(3):657–67, 2001. [3.2.2](#)

I. A. Cunningham, M. S. Westmore, and A. Fenster. A spatial-frequency dependent quantum accounting diagram and detective quantum efficiency model of signal and noise propagation in cascaded imaging systems. *Med Phys*, 21(3):417–27, 1994. [3.2](#)

S. N. Friedman and I. A. Cunningham. A spatio-temporal detective quantum efficiency and its application to fluoroscopic systems. *Med Phys*, 37(11):6061–9, 2010. [3.4](#)

H. Fujita, D. Y. Tsai, T. Itoh, K. Doi, J. Morishita, K. Ueda, and A. Ohtsuka. A simple method for determining the modulation transfer function in digital radiography. *IEEE Trans Med Imaging*, 11(1):34–9, 1992. [3.2.5](#)

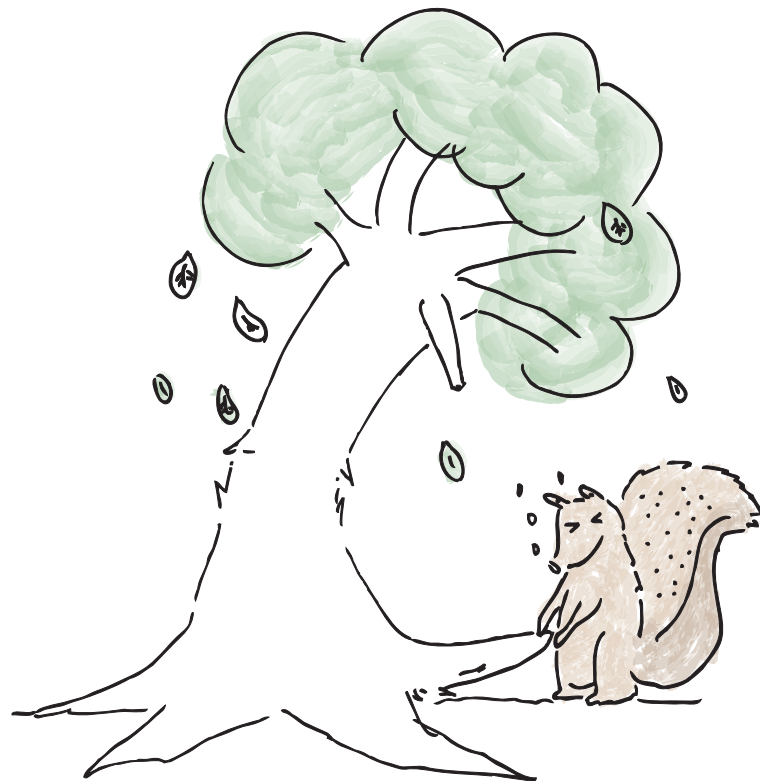
3rd J. T. Dobbins. Effects of undersampling on the proper interpretation of modulation transfer function, noise power spectra, and noise equivalent quanta of digital imaging systems. *Med Phys*, 22(2):171–81, 1995. [3.2.5](#)

- J.A. and Yorkson J. Rowlands. Flat panel detectors for digital radiography. In J. Beutel, H.L. Kundel, and R.L. Van Metter, editors, *Handbook of Medical Imaging*, pages 244 – 248. SPIE, Bellingham, WA, 2000. [3.2.4](#)
- F. Jacobs, E. Sundermann, B. de Sutter, M. Christiaens, and I. Lemahieu. A fast algorithm to calculate the exact radiological path through a pixel or voxel space. *Journal of Computing and Information Technology - CIT*, 6(1):89–94, 1998. [3.3.2](#)
- A. L. Kwan, J. M. Boone, and N. Shah. Evaluation of x-ray scatter properties in a dedicated cone-beam breast ct scanner. *Med Phys*, 32(9):2967–75, 2005. [3.4](#)
- N. D. Prionas, S. Y. Huang, and J. M. Boone. Experimentally determined spectral optimization for dedicated breast computed tomography. *Med Phys*, 38(2):646–55, 2011. [3.3.2](#)
- R.L. Siddon. Fast calculation of the exact radiological path for a three-dimensional ct array. *Med Phys*, 12(2):252–255, 1985. [3.3.2](#)
- J. H. Siewerdsen and D. A. Jaffray. A ghost story: spatio-temporal response characteristics of an indirect-detection flat-panel imager. *Med Phys*, 26(8):1624–41, 1999. [3.4](#)
- J. H. Siewerdsen, L. E. Antonuk, Y. el Mohri, J. Yorkston, W. Huang, J. M. Boudry, and I. A. Cunningham. Empirical and theoretical investigation of the noise performance of indirect detection, active matrix flat-panel imagers (amfpis) for diagnostic radiology. *Med Phys*, 24(1):71–89, 1997. [3.2](#), [3.2.1](#), [3.2.1](#)
- J. H. Siewerdsen, L. E. Antonuk, Y. el Mohri, J. Yorkston, W. Huang, and I. A. Cunningham. Signal, noise power spectrum, and detective quantum efficiency of indirect-detection flat-panel imagers for diagnostic radiology. *Med Phys*, 25(5):614–28, 1998. [3.2](#), [3.2.1](#), [3.2.1](#), [3.2.1](#)

- J. H. Siewerdsen, A. M. Waese, D. J. Moseley, S. Richard, and D. A. Jaffray. Spektr: a computational tool for x-ray spectral analysis and imaging system optimization. *Med Phys*, 31(11):3057–67, 2004. [3.4](#)
- B. R. Whiting, P. Massoumzadeh, O. A. Earl, J. A. O’Sullivan, D. L. Snyder, and J. F. Williamson. Properties of preprocessed sinogram data in x-ray computed tomography. *Med Phys*, 33(9):3290–303, 2006. [3.2.1](#), [3.2.1](#)
- K. Yang, S. Y. Huang, N. J. Packard, and J. M. Boone. Noise variance analysis using a flat panel x-ray detector: a method for additive noise assessment with application to breast ct applications. *Med Phys*, 37(7):3527–37, 2010. [3.2.1](#), [3.2.4](#)

## Chapter 4

# The Optimization of CEDEM Using Breast CT



## 4.1 Motivation

Prior to implementing contrast-enhanced dual energy mammography (CEDEM) in a clinical setting, it is essential to examine the feasibility of CEDEM using breast CT system in the pre-clinical environment. Figure 4.1 gives an overall progression of the CEDEM optimization steps. The image simulation and experimental acquisition are two related steps providing assisting information in optimizing the CEDEM system. With a thorough understanding of breast morphology in Chapter 2, projection images of a realistic breast can be simulated to guide the optimization. Moreover, the experimental acquisition is necessary to validate simulation results. For these steps, the objective of the optimization is to determine the technique factors used to acquire static CEDEM images from a variety of breast compositions and dimensions using breast CT while delivering reasonable radiation dose in a clinical setting. Once the CEDEM technique factors are optimized, the design of the dynamic CEDEM protocol can be determined using a dynamic breast phantom. This chapter will describe the steps in designing the CEDEM optimization and discuss the optimization results.

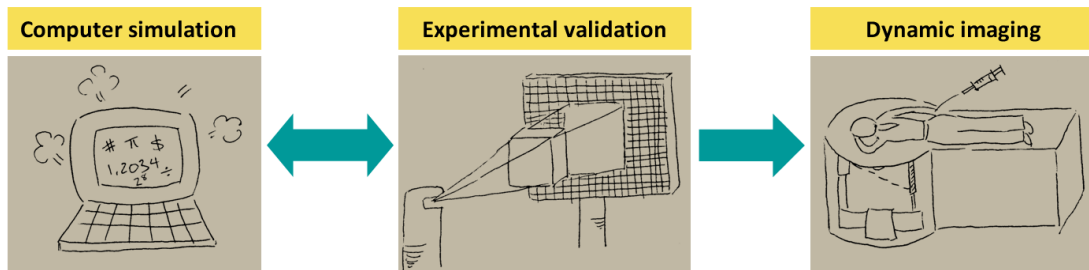


Figure 4.1. A flow diagram of the CEDEM optimization steps is shown.

## 4.2 The Static Breast Phantom

For experimental purpose, static breast phantoms were designed and constructed. The x-ray mass attenuation coefficients of water and polyethylene

were found to closely match that of the glandular and adipose tissues as shown in Figure 4.2. Moreover, Prionas et al. (2011) confirmed that water and polyethylene are reasonable surrogates for glandular tissue and adipose tissue due their similar detector CT signal. Therefore, water and polyethylene were used to mimic breast glandular and adipose tissues in building the static breast phantom. To model the glandular tissue distribution of a real breast, pseudo anatomical structures were constructed by randomly positioning holes of various size on a number of polyethylene slabs (0.3-cm to 1.3-cm thick). To incorporate the ability to construct the breast phantom with a given glandular fraction, the mass of each polyethylene slab (with unique distribution of holes) was measured. The volume glandular fraction was estimated by approximating the total volume of the polyethylene slabs and that of water contained in the breast phantom. A number of polyethylene slabs were inserted in a sealed container filled with water. In addition, diluted iodine-based contrast solution (270 mg/ml iodixanol, Visipaque<sup>TM</sup>) was incorporated to the breast phantom using rectangular cells ( $4.5 \times 1.0 \times 1.0$  cm<sup>3</sup> cuvettes, Ocean Optics, Dunedin, FL.). The iodine-filled cuvettes were mounted into a polyethylene slab in the breast phantom. To avoid the introduction of air bubbles, the breast phantom components were assembled while submerged in a large container of water. The components of the breast phantom are shown in Figure 4.3. Breast phantoms of the realistic range of breast thickness, 8-cm, 10-cm, and 13-cm, were fabricated for the CEDEM study (see Section 2.2.4.3).

The quality of the pseudo anatomical structures in the breast phantom was examined using the anatomical noise power spectrum (ANPS). ANPS is a metric which can characterize the anatomical variability within an image. For projection mammography images, previous studies (Burgess and Judy, 2007; Burgess et al., 2001; Heine and Velthuizen, 2002) have well characterized the ANPS by a power law:  $S(f) = \alpha/f^\beta$ , where  $f$  is the radial spatial frequency.  $\alpha$  and  $\beta$  quantify the magnitude and frequency dependence of the background anatomical noise, respectively. Specifically, the power-law expo-

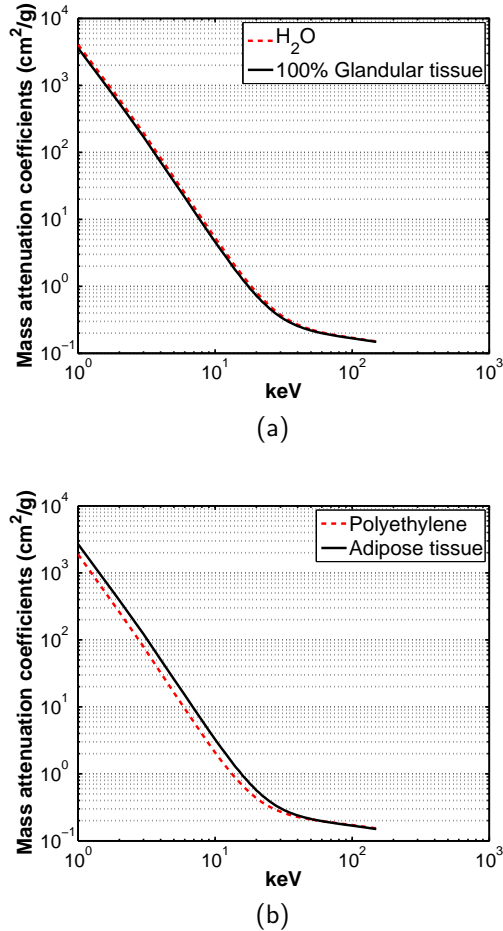


Figure 4.2. The x-ray mass attenuation coefficients is shown as function of x-ray energy (keV) for (a) water vs. glandular tissue and (b) polyethylene vs. adipose tissue.

ment,  $\beta$ , was found to provide reasonable description of the anatomical distribution and its impact on lesion detection. [Burgess et al. \(2001\)](#) found that the average  $\beta$  ( $\pm$  standard deviation) for mammography images is  $2.83 \pm 0.35$ . This metric allows the quantitative comparison of the breast anatomical variability between the mammography images and the bCT projection images of the breast phantom. Therefore, the breast CT projection images of a 8-cm, 40% glandular breast phantom were acquired with x-ray tube peak energy at 80 kV (0.2-mm Cu). The ANPS of the breast phantom projection images was computed using the method described in [Metheany et al. \(2008\)](#). Fig-

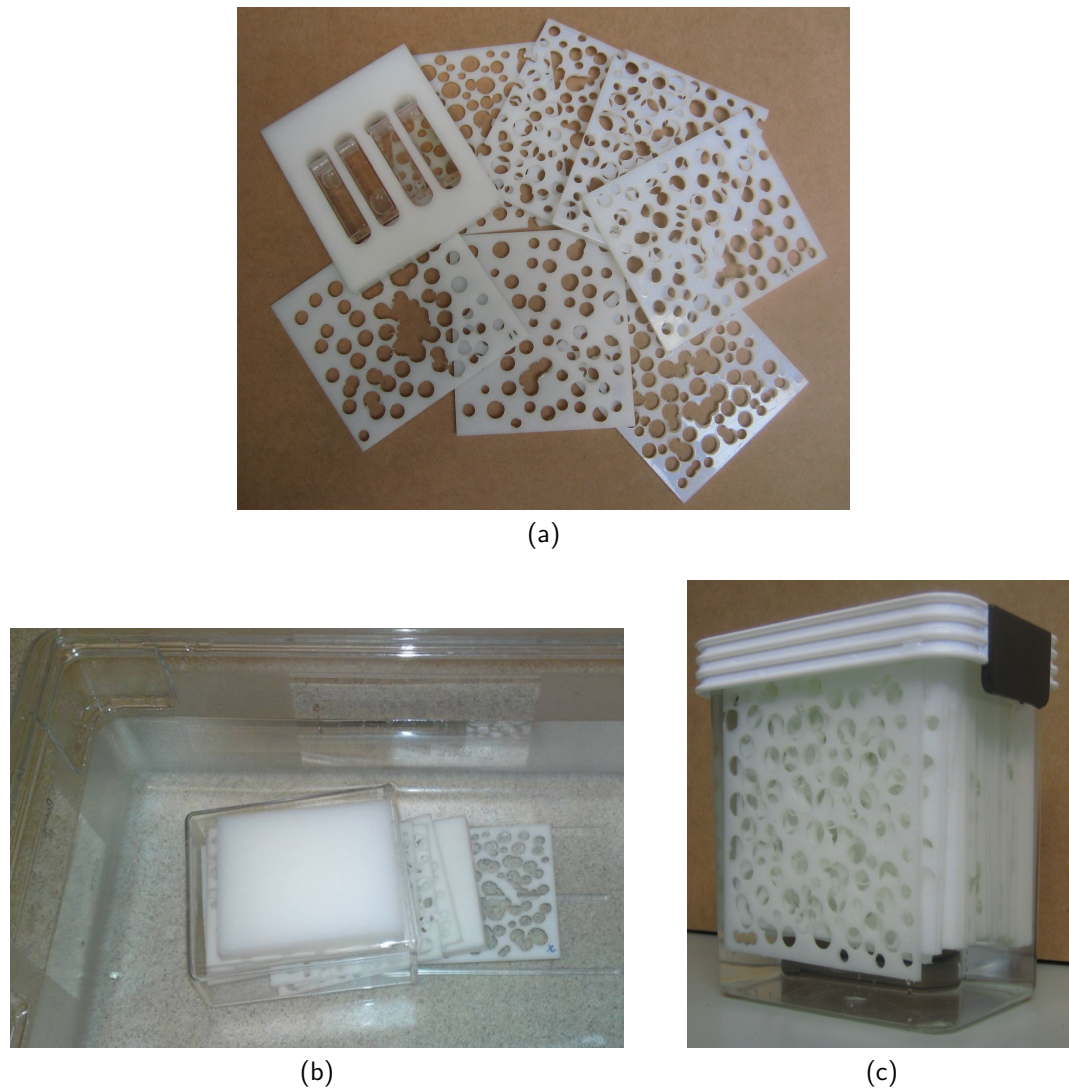


Figure 4.3. (a) The 1/8-inch polyethylene slabs with pseudo anatomical structures are shown. (b) The submersion of the polyethylene slabs when constructing the breast phantom is illustrated. (c) The 8-cm breast phantom with 40% glandular fraction is shown.

Figure 4.4 shows examples of ROIs from a mammography image and that from a breast CT projection image of the breast phantom. Figure 4.5 shows the  $\beta$  value of the projection image with the breast phantom is 3.77. Although the  $\beta$  value calculated from the breast phantom is slightly higher than that from the mammography images, the created anatomical structures in the phantom can closely model the anatomical distribution in a real breast ( $\beta \approx 3$ ). Therefore, the pseudo anatomical structures constructed in the phantoms will allow the pre-clinical study of CEDEM conducted with realistic experimental environment.

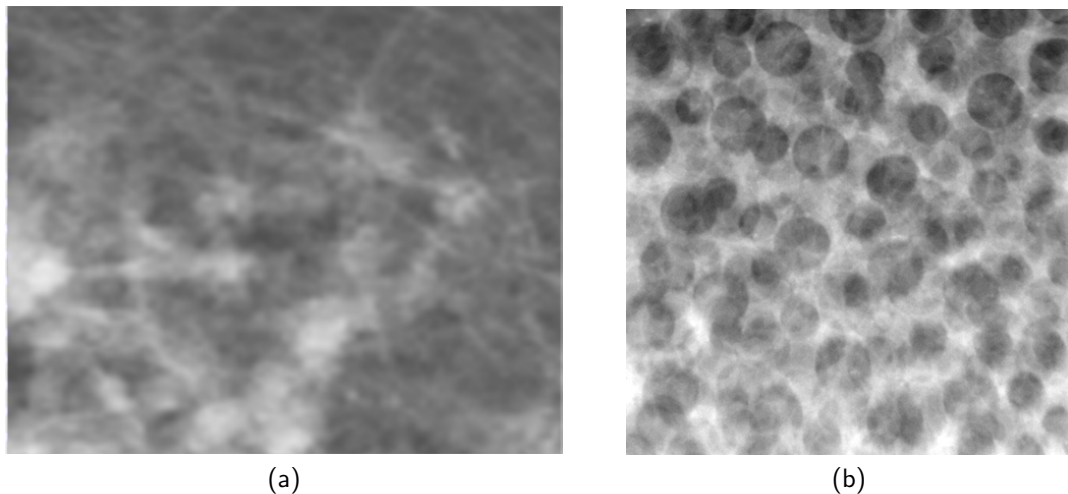


Figure 4.4. The anatomical ROI example from (a) a mammography images and (b) a bCT projection image of a 8-cm, 40% glandular breast phantom.

### 4.3 The Concentration of Iodine in Clinical Setting

The contrast agents are the key component in generating high-quality CEDEM imaging, and hence it is essential to determine the contrast concentration typically seen in a clinical setting. With the ongoing clinical trial of contrast-enhanced breast CT (CE-bCT) at our laboratory, rich data sets

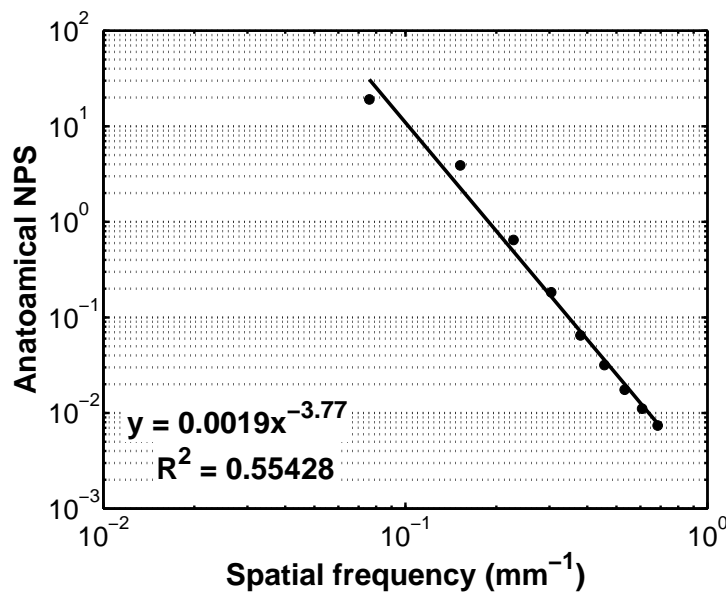


Figure 4.5. The anatomical noise power spectrum of a 8-cm, 40% glandular breast phantom is shown as a function of the spatial frequency. A power-law function was fitted and shown.

of CE-bCT were available to quantify the iodine concentration. Prior to the extracting information from CE-bCT data sets, it is important to establish the relationship between the iodine concentration and image signal as a calibration tool. Thus, the 8-cm, static breast phantom described in Section 4.2 was constructed using the contrast solution with a range of iodine concentration. Breast CT images of the 8-cm breast phantom were acquired and reconstructed with 80-kV x-ray spectrum filtered with 0.2-mm Cu (7 mA). For all available coronal-reconstructed bCT images of the phantom, the mean Hounsfield unit (HU) was computed for each region filled with iodine solution. Figure 4.6 suggests that the iodine concentration is proportional to the mean signal in HU with a 2<sup>nd</sup>-order polynomial. The nonlinear relationship is likely due to beam-hardening effects in the mean signal of the regions with higher iodine concentrations.

The iodine-concentration-to-HU relationship was then used to estimate the iodine concentration in several clinical CE-bCT data sets. For a given

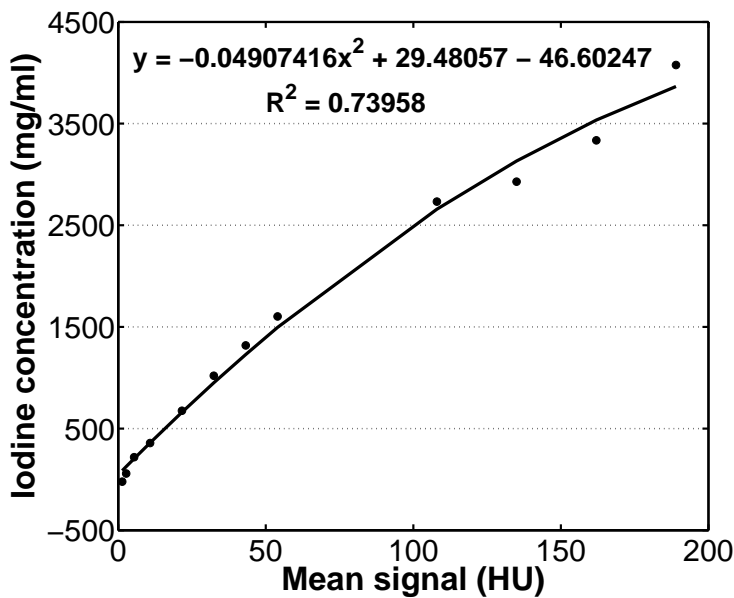


Figure 4.6. The iodine concentration is shown as a function of the mean signal (HU). A 2<sup>nd</sup>-order polynomial fitted to the data is shown ( $R^2 = 0.99202$ ).

woman, the location of the breast lesions (malignant or benign breast cancer types) were manually segmented for all pre-contrast and post-contrast coronal reconstructed bCT images as described in [Prionas et al. \(2010\)](#). The signal difference in the breast cancer regions between the pre-contrast and post-contrast bCT images were computed. The signal difference was thought to closely represent the signal enhancement from the iodine solution injected into the patient's body. Therefore, the iodine concentration was estimated using the iodine-concentration-to-HU relationship found in Figure 4.6 for 52 breast lesions (19 benign lesions and 33 malignant lesions) from 47 clinical CE-bCT data sets. A histogram of the signal enhancement (HU) is illustrated for malignant and benign breast cancer in Figure 4.7. The signal in the malignant lesions enhanced  $50.8 \text{ HU} \pm 5.0$  (standard error), while signal in the benign lesions enhanced  $24.8 \text{ HU} \pm 7.2$ . The estimated iodine concentration corresponding to the signal enhancement is shown in Figure 4.8. The iodine concentration in the malignant lesions is  $1.5 \text{ mg/ml} \pm 0.1$  (standard error), while that in the benign lesions is  $0.9 \text{ mg/ml} \pm 0.2$ . The estimated iodine

concentration from the clinical CE-bCT data sets can guide the design of CE-DEM optimization in the simulation and experimental settings in a realistic manner.

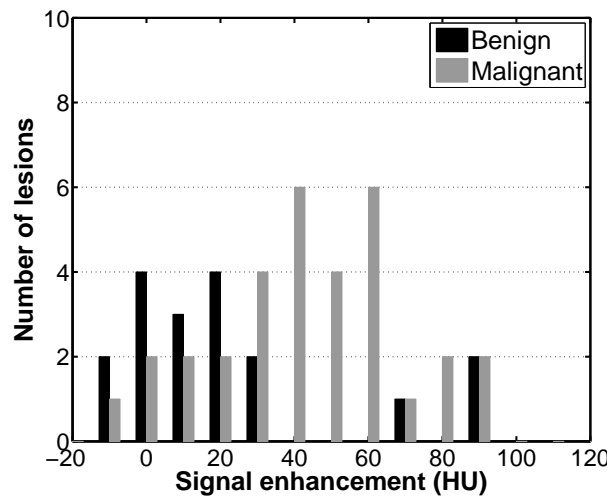


Figure 4.7. A histogram of the signal enhancement (HU) computed from the clinical CE-bCT data sets among 52 breast lesions is shown. The mean signal enhancement ( $\pm$  standard error) in malignant lesions is  $50.8 \text{ HU} \pm 5.0$ , while that in the benign lesions is  $24.8 \text{ HU} \pm 7.2$ .

## 4.4 Dose Calculation

Radiation dose to the patient is one of the main factors to consider when optimizing CEDEM imaging system. To calculate the radiation dose to the fibroglandular tissues in the breast, the glandular dose per fluence  $F(E)$  [ $\mu\text{Gy}/(10^6 \text{ photons/mm}^2)$ ] was generated for each monoenergetic x-ray energy (keV) using previously validated SIERRA Monte Carlo techniques (Boone and V. N. Cooper, 2000; Boone et al., 2000).  $F(E)$  was generated considering the breast CT imaging geometry for the purpose of this study. In relating the glandular dose with a measurable metric, such as air kerma, the air kerma per fluence  $K(E)$  [ $\mu\text{Gy}/(10^6 \text{ photons/mm}^2)$ ] was calculated as the product of energy fluence and mass energy transfer coefficient of air for each monoener-

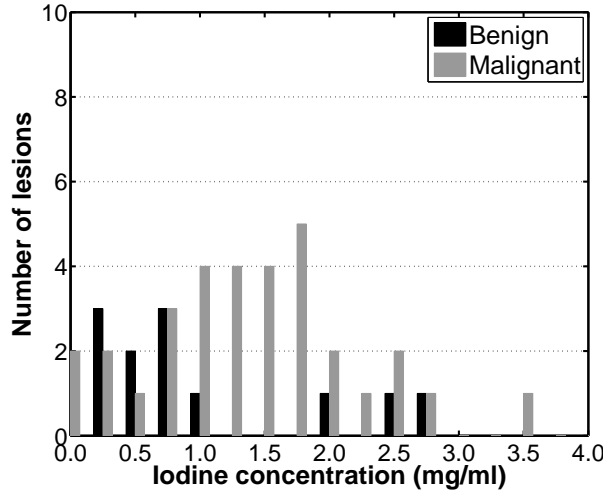


Figure 4.8. A histogram of the iodine concentration (mg/ml) estimated from the clinical CE-bCT data sets among 52 breast lesions is shown. The mean iodine concentration ( $\pm$  standard error) in the malignant lesions is  $1.5 \text{ mg/ml} \pm 0.1$ , and that in the benign lesions is  $0.9 \text{ mg/ml} \pm 0.2$ .

ergetic x-ray energy. For a given x-ray spectrum  $\Phi(E)$  (photons/mm<sup>2</sup>), the polyenergetic normalized glandular dose values  $D_g N_{CT}$  were computed as

$$D_g N_{CT} = \frac{\int_{E=0}^{E=E_{max}} \Phi(E) F(E) dE}{\int_{E=0}^{E=E_{max}} \Phi(E) K(E) dE} \quad (4.1)$$

With the Monte-Carlo determined  $F(E)$  values for a given x-ray technique factor, the mean glandular dose  $D_g$  for a given entrance-skin air kerma  $A$  is calculated by

$$D_g = D_g N_{CT} \times A \quad (4.2)$$

The glandular dose per million photons  $F(E)$  were computed using Monte Carlo techniques for breast thickness (10 cm, 14 cm, and 18 cm) and breast glandular composition (0%, 50%, and 100%) as reported in [Boone et al. \(2004\)](#). Figure 4.9 shows the glandular dose per million photons for 10-cm, 14-cm, and 18-cm breast thickness (glandular fraction of 0%, 50%, and 100%). It

suggests that the glandular dose increases with less dense breasts but decreases with thicker breasts since the glandular dose was normalized by the mass of glandular tissues. Breasts with lower glandular fraction are likely to have lower mass of glandular tissues while thicker breasts tend to have larger mass of glandular tissues. The glandular dose for a given thickness and breast glandular fraction was obtained by linear interpolating using the Monte-Carlo determined  $F(E)$  values shown in Figure 4.9. For a given breast thickness and composition, the  $D_g N_{CT}$  values were calculated using the calibrated TASMIP x-ray spectra (see Section 3.2.3). The mean glandular dose  $D_g$  was then calculated for a set of x-ray technique factors.

For the purpose of CEDEM optimization, it is our goal to maintain the same radiation dose as that of a two-view mammogram during a single or multiple CEDEM acquisition(s). Averaged over four mammography units, Figure 4.10 shows that the mean glandular dose increases as a function of compressed breast thickness to compensate image quality of thicker breasts. Since CEDEM will be implemented without compression, the diameter of an uncompressed breast close to the chest wall  $D_{chestwall}$  was related to the compressed thickness  $T$  using the relationship determined in [Boone et al. \(2001\)](#)

$$D_{chestwall} = 4.96 \times (T)^{1/2} \quad (4.3)$$

to determine the proper mean glandular dose for a given breast diameter and composition. To ensure sufficient detector signal, the x-ray tube current (mA) was set close to its maximum level for each kV/filter combination. To compensate for change in the detector signal when imaging different breast thicknesses, the number of average frames or the acquisition time was adjusted to deliver the desired mean glandular dose for a given set of imaging parameters.

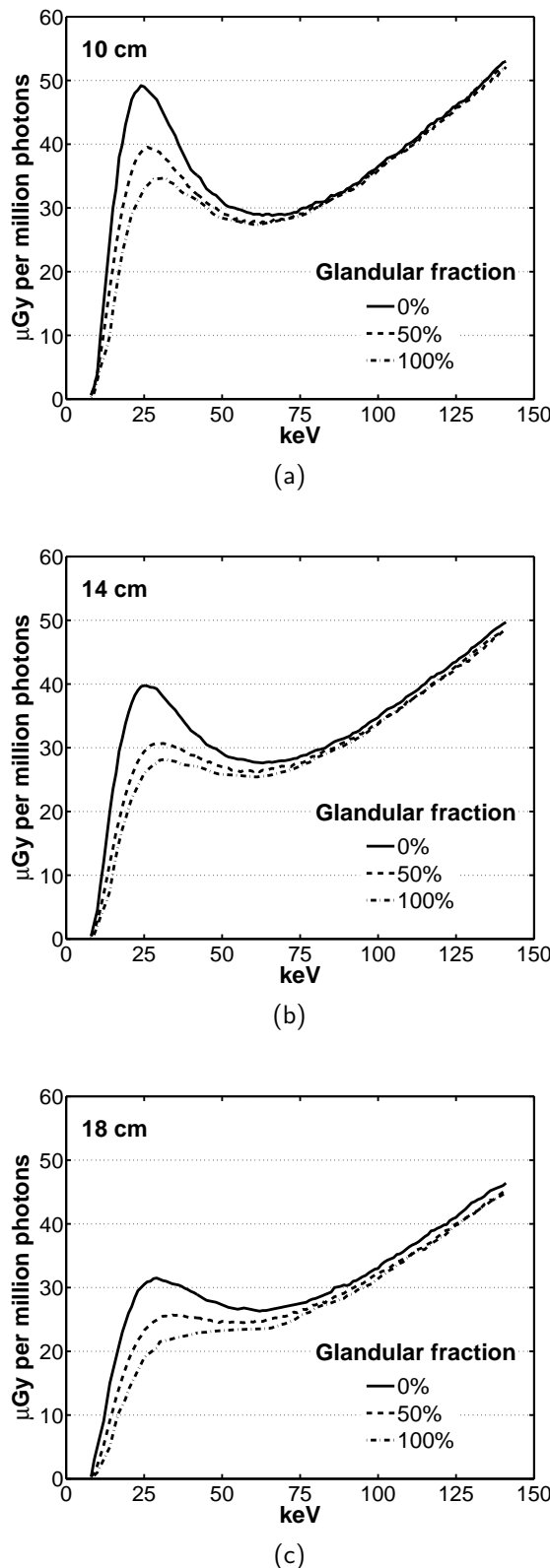


Figure 4.9. The glandular dose per million photons  $F(E)$  are shown as a function of monoenergetic x-ray energy (keV) for 10-cm, 14-cm, and 18-cm breast thickness (0%, 50%, and 100% glandular fraction). The glandular dose data was reported in [Boone et al. \(2004\)](#).

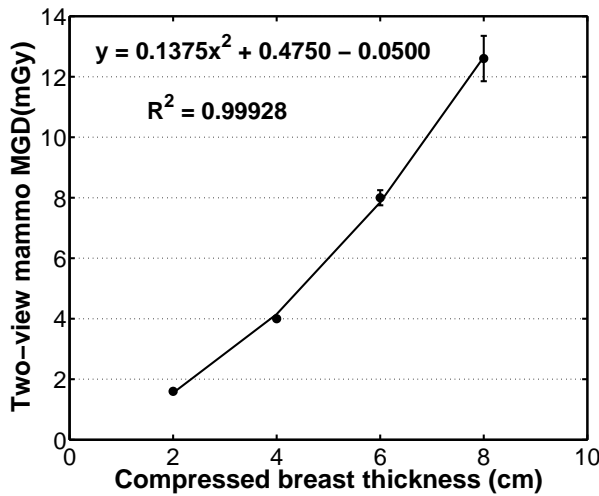


Figure 4.10. The mean glandular dose (MGD) of a two-view mammogram (averaged over four mammography systems) is shown as a function of compressed breast thickness. A 2<sup>nd</sup>-order polynomial was fitted to the data.

## 4.5 The Dynamic Filter Changer

To ensure accurate dual energy processing, fast image acquisition is beneficial to reduce any artifact due to motion. The dynamic filter changer was designed and fabricated to enable fast acquisition of CEDEM images using breast CT system. The filter changer consists of two stacked place holders for mounting any filter in front of the x-ray tube. The motion of the holders is solenoid-controlled to move the holder in the up or down position. Figure 4.11 shows the mechanical drawing (Solidworks® 2009, Concord, MA, courtesy of George Burkett Jr., M.S.) of the filter changer in its up and down position. Figure 4.12 demonstrates the fabricated filter changer as part of the breast CT system.

## 4.6 Initial Static CEDEM Optimization

As discussed in Section 1.4, x-ray tube peak voltage (kV) and filtration are two key components in shaping the appropriate x-ray spectra when perform-

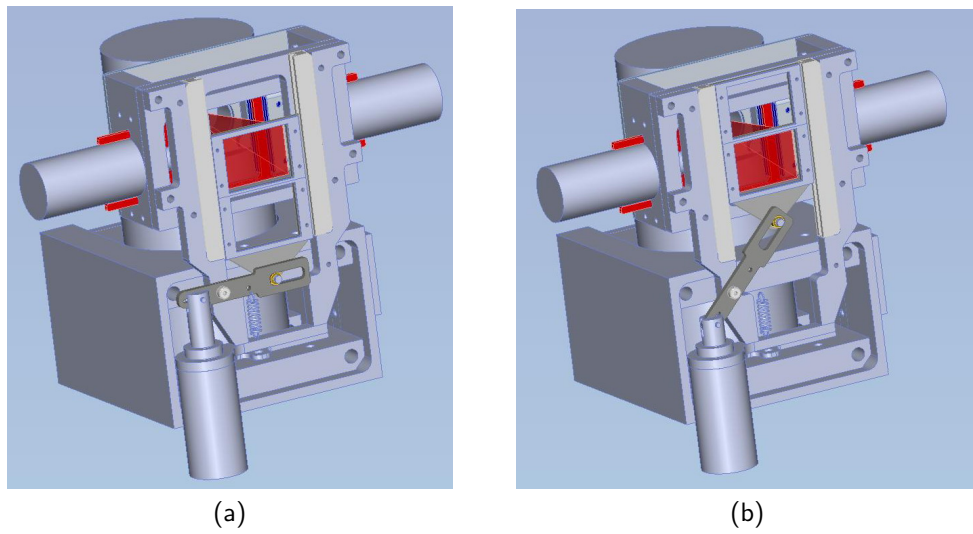


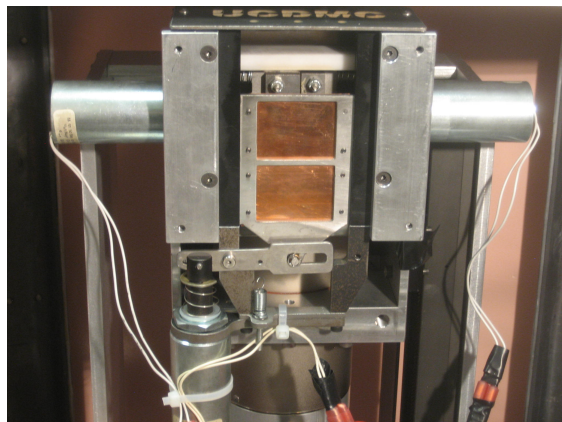
Figure 4.11. The mechanical drawing of the filter changer is shown in (a) the down position and (b) the up position.

ing dual energy imaging. The initial CEDEM optimization was to examine the feasibility of CEDEM using breast CT system by changing both kV and filtration. The initial study focused on determining the optimal combination of kV and filtration to best visualize the contrast agent signal in the CEDEM images. The optimization was performed in computer simulation and in the experimental setting for validation.

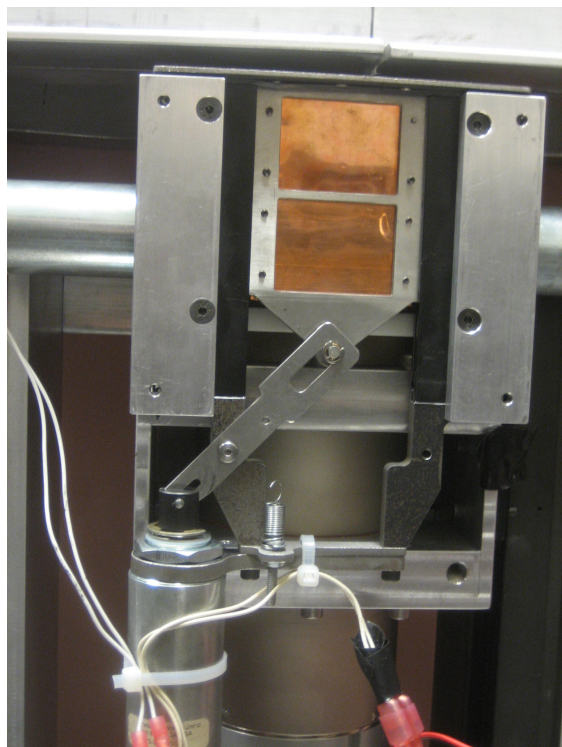
#### 4.6.1 Computer Simulation Method

Since dual energy processing is typically implemented to generate CEDEM images, the ability to manipulate images is useful when performing CEDEM optimization. The purpose of simulating images is to examine the dual energy processing techniques and the image quality of CEDEM images. Dr. D. Zheng initiated this initial computer simulation of the CEDEM system to investigate its feasibility ([Zheng et al., 2007](#)). The numerical simulation was implemented in C (Microsoft VC++ 6.0 SP 5, Redmond, WA) tailored to the imaging geometry of the breast CT system (Bodega).

A mathematical phantom was simulated in the shape of a rectangular



(a)



(b)

Figure 4.12. The fabricated filter changer incorporated onto the breast CT is shown in (a) the down position and (b) the up position.

box. Spheres with different radius were randomly positioned within the simulated phantom mimicking the breast anatomical structures (similar to the design of the static phantom in Section 4.2). Iodine-based contrast solution of different concentration were simulated in the rectangular reservoirs (1-cm thick) inside the phantom. Thus, the breast was modeled with a three-dimensional (3D) voxelized phantom. The x-ray path length  $T_i$  through a material  $i$  in the 3D phantom was approximated by scaling the parallel-beam path length by a factor  $f_{CB}$  based on the ray connecting the x-ray source  $(x_0, y_0)$  and a detector element  $(x, y)$ .

$$f_{CB} = \frac{\sqrt{(x - x_0)^2 + (y - y_0)^2 + SID^2}}{SID} \quad (4.4)$$

where SID is the source-to-detector distance. In this study, the source-to-isocenter distance (SIC) was 51 cm, and SID was 104 cm. Figure 4.13 illustrates the imaging geometry and setup used in this method.

A TASMIP x-ray spectrum  $\Phi(E)$  was generated and calibrated to derive the x-ray spectra considered in this study (see Section 3.2.3). Images can be computed simply by summing the energy fluence of the attenuated x-ray spectrum in each detector element. Given the x-ray linear attenuation coefficients of CsI (the scintillator of the breast CT detector system)  $\mu_{CsI}(E)$  and that of the attenuating material  $i$   $\mu_i(E)$ , the signal of each detector element is described by

$$I_1(x, y) = \sum_{E=0}^{E=E_{max}} \Phi(E) e^{-\sum_i \mu_i T_i} \left( 1 - e^{-\mu_{CsI}(E) T_{CsI}} \right) E \quad (4.5)$$

The Poisson distribution dictates quantum noise in x-ray imaging. Thus, the final detector signal is then given by

$$I_2(x, y) = I_1(x, y) + \tilde{N}_{Poisson} \left( I_1(x, y) \right) \quad (4.6)$$

where  $\tilde{N}_{Poisson}(m)$  is a Poisson-distributed random number with mean  $m$ .

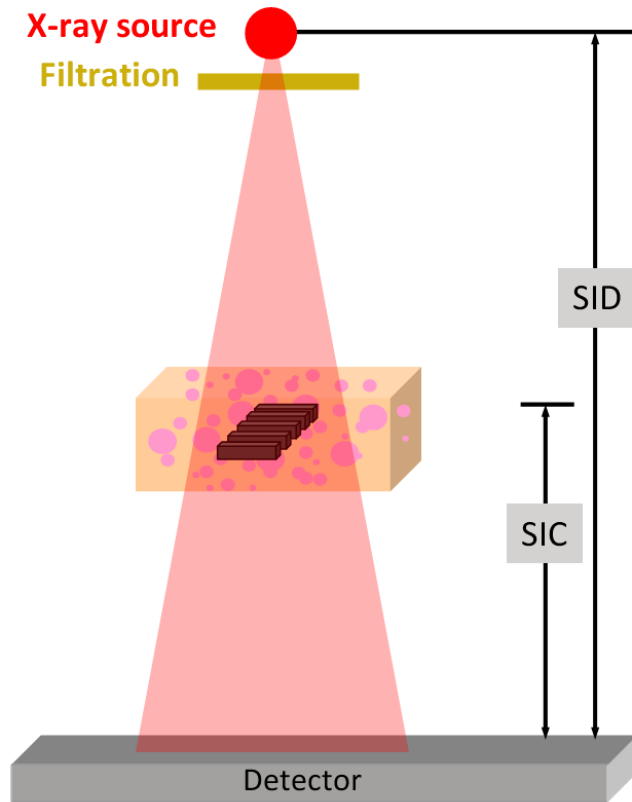


Figure 4.13. The geometry and setup of the imaging environment considered in the initial computer simulation scheme is shown. SIC is the source-to-isocenter distance while SID is the source-to-detector distance of the imaging system.

#### 4.6.2 Image Simulation and Acquisition

For the initial CEDEM optimization, 1.5-mm aluminum (Al) and 1.5-mm Al with additional copper (Cu) filtration were the two filters studied for x-ray spectrum shaping while varying kV. Numerical simulation (described in Section 4.6.1) of a 8-cm breast phantom (glandular fraction of 40%) was performed with 40 kV, 45 kV, ..., 100 kV using the two filters. To evaluate the effectiveness of CEDEM experimentally, breast-equivalent phantoms were fabricated as described in Section 4.2. A 8-cm breast phantom with glandular fraction of 40% was constructed. Projection images of the 8-cm breast phantom placed at the scanner isocenter were acquired using breast CT system while the scanner gantry was stationary (see Figure 4.14). They were

acquired using the x-ray tube peak voltage from 40, 50, . . . , 90 kV filtered with 1.5-mm Al and 1.5-mm Al + 0.3-mm Cu. The  $1 \times 1$  low-gain detector mode was used, capitalizing on the detector's intrinsic resolution. The projection images were offset and flat-field corrected (Kwan et al., 2006). Figure 4.15 shows the computer-simulated and experimental images of the 8-cm breast phantom using 40 kV / 1.5-mm Al. The simulated and experimental images demonstrate the ability to resolve the signal of the anatomical structures and the contrast solution.

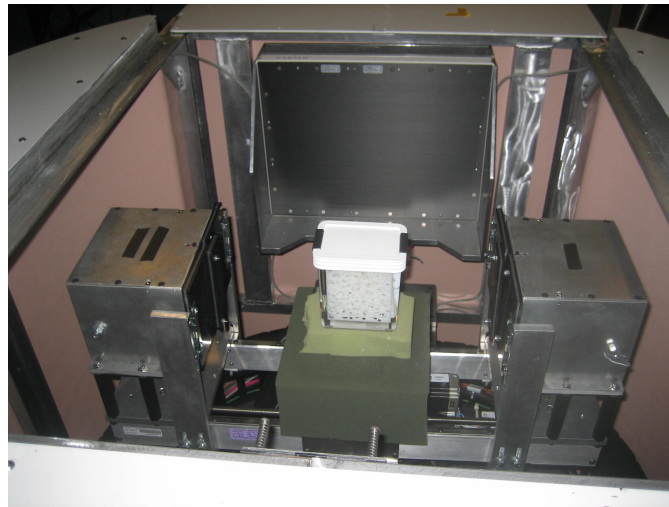


Figure 4.14. The imaging setup of the 8-cm breast phantom using the breast CT system (Bodega) is shown.

### 4.6.3 Optimization Methods and Results

With the acquired low-energy  $I_L(x, y)$  and high-energy images  $I_H(x, y)$ , the dual-energy subtracted images  $I_{DE}(x, y)$  was generated using log weighted subtraction given by

$$I_{DE}(x, y; w_t) = w_t \ln I_L(x, y) - \ln I_H(x, y) \quad (4.7)$$

where  $w_t$  is the weighting factor ranging between 0 and 1. The figure of merit used to determine the  $w_t$  for best suppression of background anatomical

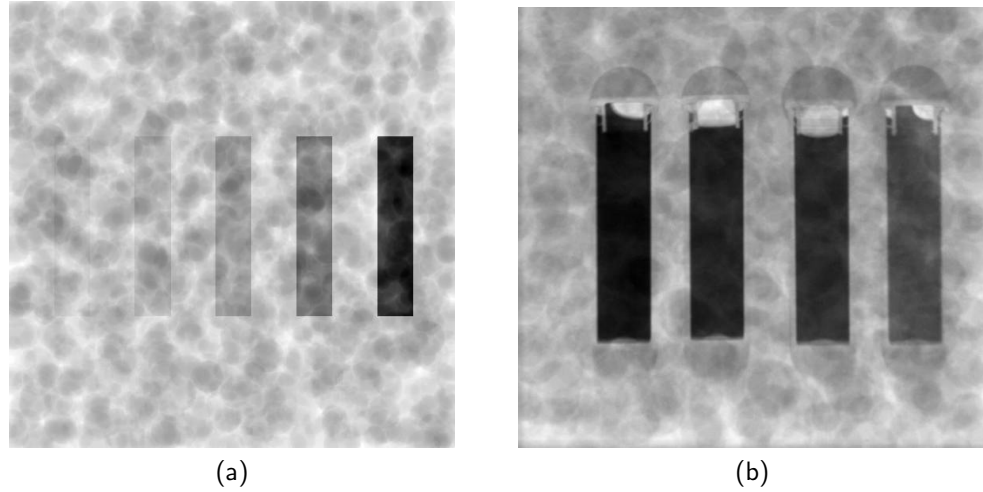


Figure 4.15. The images of a 8-cm, 40% glandular breast phantom are shown using (a) computer simulation and (b) experimental acquisition.

structure is the signal-difference-to-noise ratio (SDNR) defined as

$$SDNR = \frac{|\bar{S}_c - \bar{S}_{bg}|}{\sqrt{\sigma_c^2 + \sigma_{bg}^2}} \quad (4.8)$$

where  $\bar{S}$  and  $\sigma^2$  are the signal mean and variance. The subscript  $c$  denotes the ROI with contrast agent and  $bg$  denotes the ROI with background anatomical structures. The optimal  $w_t$  was determined as the weighting factor that produces the maximum SDNR on the dual-energy subtracted image as

$$w_t^{SDNR} = \max_{w_t} SDNR \left[ I_{DE}(x, y; w_t) \right] \quad (4.9)$$

Figure 4.16 shows the low-energy image (40 kV / 1.5-mm Al), the high-energy image (50 kV / 1.5-mm Al + 0.3-mm Cu), and the corresponding dual-energy subtracted image. The elimination of the background anatomical structures was demonstrated in the dual-energy subtracted image.

The kV-optimization was performed by evaluating the SDNR of the dual-energy subtracted images  $I_{DE}(x, y; w_t^{SDNR})$  for a number of low-energy kV and high-energy kV combinations. The initial kV optimization using computer

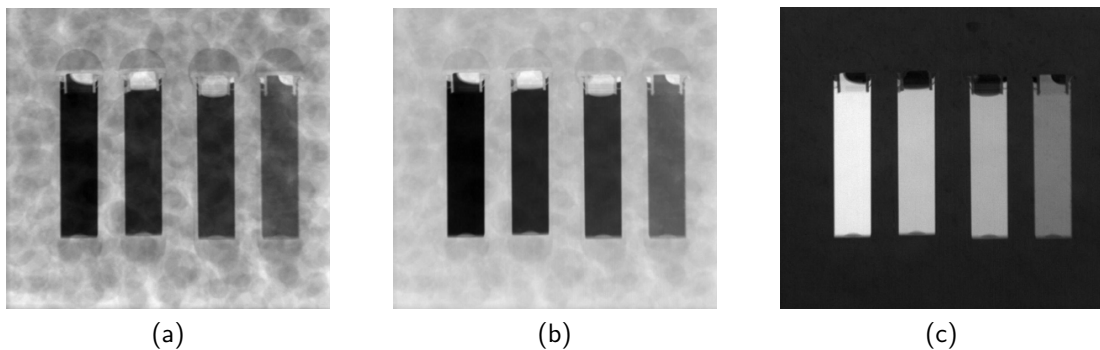


Figure 4.16. The process of log-weighted subtraction is demonstrated. (a) The low-energy image (40 kVp / 1.5-mm Al), (b) the high-energy image (50 kVp / 1.5-mm Al + 0.3-mm Cu), and (c) the dual-energy subtracted image are shown

simulation and experiments is shown in Figure 4.17 using a 8-cm, 40% glandular breast phantom. The *SDNR* was calculated for iodine concentration of 25.6 mg/ml. Both simulation and experiments suggest that the optimal kV combination (low-energy kV / high-energy kV) used with the two filtration (1.5-mm Al and 1.5-mm + 0.3-mm Cu) is 40 kV/50 kV since the optimized SDNR was maximized in this case. Although similar trends were observed in the simulation and experimental data, the magnitude of SDNR was different due to the simplicity of the computer simulation approach.

#### 4.6.4 Optimization Conclusions

The initial kV-optimization reveals that varying kV is not as impacting as varying filtration in shaping x-ray spectra when acquiring dual-energy images with reasonable signal contrast. The small kV difference between the optimal low-energy kV (40 kV) and low-energy kV (50 kV) suggests the next optimization design of only changing filtration (fixing kV) in acquiring the CEDEM images. This dual-energy acquisition approach could potentially produce dual-energy images with comparable signal contrast while reducing image acquisition time. Moreover, the initial optimization suggests the need to develop a computer simulation method that accurately describes the signal

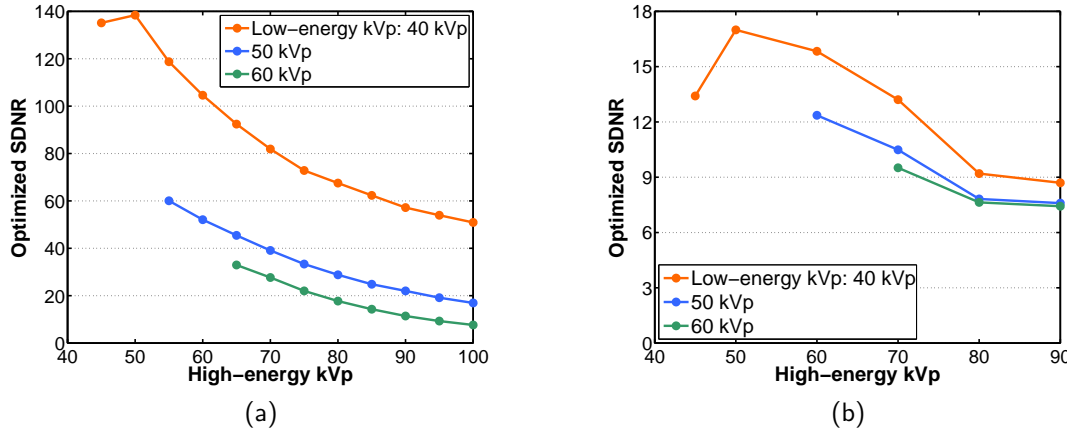


Figure 4.17. The kV-optimization is illustrated using the optimized SDNR (evaluated from the  $I_{DE}(x, y; w_t^{SDNR})$ ) as a function of high-energy kV for 40 kV, 50 kV, and 60 kV as the low-energy kV. The optimization outcome using **(a)** the simulated data and **(b)** the experimental data is shown. SDNR was evaluated for the iodine concentration of 25.6 mg/ml.

and noise transfer of the imaging system. Due to limited x-ray output, this initial study also reveals that  $1 \times 1$  detector mode is not the likely detector mode for acquiring future CEDEM images. Overall, this initial optimization provided useful guidance for the next optimization design in a more realistic manner, considering the CEDEM imaging requirement and system limitations.

## 4.7 Comprehensive Static CEDEM Optimization

The initial CEDEM optimization (Section 4.6) confirms that the x-ray tube peak potential (kV) and filter material are effective in producing CEDEM images. However, the initial study show that kV did not shape the x-ray spectra as effective as the filter selection. The comprehensive static CEDEM optimization focuses on determining the optimal technique factors by fixing the kV and changing the filtration in acquiring CEDEM images. To achieve sufficient x-ray spectra separation, filter materials with K-edge close to io-

dine K-edge (atomic number,  $Z = 53$ , K-edge of 33.2 keV) are good candidates for acquiring low-energy images. Due to readily availability, tin (Sn,  $Z = 50$ ) and copper (Cu,  $Z = 29$ ) are selected as the low-energy and high-energy filter, respectively, in this comprehensive CEDEM optimization. This CEDEM acquisition approach will allow fast CEDEM acquisition by only changing the filtration, which may reduce the effect of patient motion.

#### 4.7.1 Image Simulation and Acquisition

To incorporate the effect of objects, a mathematical breast phantom was simulated as a rectangular box consisting of polyethylene slabs with randomly-positioned holes (similar design in Section 4.6.1). Regions filled with iodinated-contrast agents were included in the mathematical phantom as well. Iodine concentrations of 2.7 mg/ml, 5.4 mg/ml, 10.8 mg/ml, and 21.6 mg/ml were considered. CEDEM images of nine mathematical breast phantoms (combinations of thickness of 8-cm, 10-cm, and 13-cm and volume glandular fraction of 5%, 17%, and 25%) were simulated using the method described in Section 3.2. Low-energy and high-energy images were simulated for x-ray spectra of 40, 50, ..., 100 kV filtered with 0.1-mm Sn and 0.2-mm Cu. For a given kV, x-ray technique factors (mA and detector frame rate) were chosen to ensure sufficient detector signal (operating above the electronic-noise-limited region of the detector). Table 4.1 shows a list of the x-ray technique factors used to simulate low-energy (Sn) and high-energy (Cu) images for each kV.

Physical breast phantoms were constructed as described in Section 4.2. Similar to the simulation setup, nine physical breast phantoms with various combinations of breast thickness and volume glandular fraction were constructed. The physical breast phantoms with 8-cm, 10-cm, and 13-cm thickness are shown in Figure 4.18. Projection images ( $2 \times 2$  low-gain mode) were acquired with the physical breast phantom placed close to the system isocenter. The same x-ray technique factors listed in Table 4.1 were used to acquire low-energy and high-energy images using the breast CT system for comparison with simulation result.

Table 4.1. A list of the x-ray technique factors (kV and mA) are shown in acquiring low-energy (0.1-mm Sn) and high-energy (0.2-mm Cu) images.

<b>kV</b>	<b>0.1-mm Sn</b>		<b>0.2-mm Cu</b>	
	<b>mA</b>	<b>frame rate (fps)</b>	<b>mA</b>	<b>frame rate (fps)</b>
40	18	7.5	23	2.5
50	15	12	19	9.0
60	13	20	13	15
70	12	30	13.5	30
80	8	30	8	30
90	5.5	30	5.5	30
100	4	30	4	30

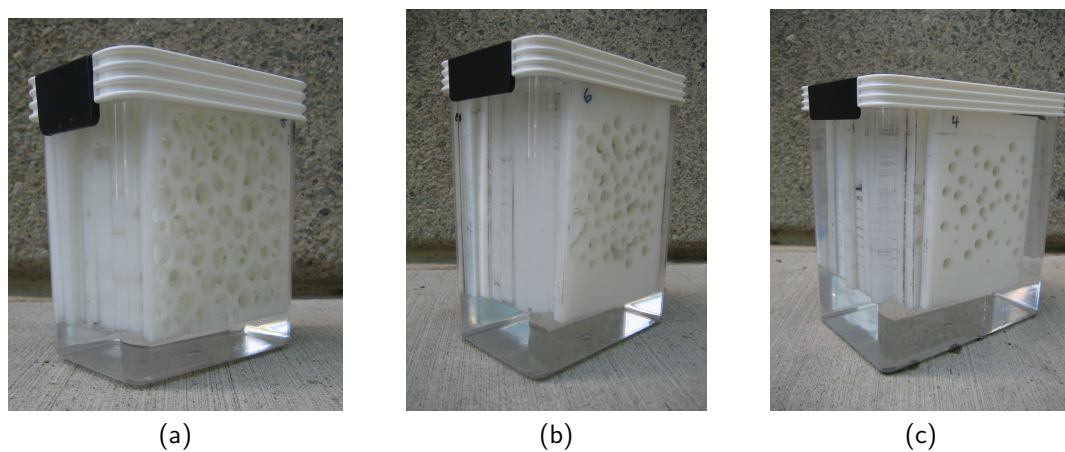


Figure 4.18. The physical breast phantoms are shown with thickness of (a)8-cm, (b)10-cm, and (c)13-cm.

Both simulated and experimentally-acquired images  $I(x, y)$  were flat-fielded and dead-pixel corrected using dark-field images  $I_{dark}(x, y)$  and flood-field images  $I_{flood}(x, y)$  as

$$I_{FF}(x, y) = \frac{I(x, y) - I_{dark}(x, y)}{I_{flood}(x, y) - I_{dark}(x, y)} \quad (4.10)$$

The dark-field and flood-field images were acquired by averaging over 300 projection images ( $2 \times 2$  low-gain mode) using no x-ray output and the chosen x-ray technique factors (mA and fps), respectively. Figure 4.19 shows the simulated and acquired images  $I_{FF}(x, y)$  using 80 kV x-ray spectrum filtered with 0.2-mm Cu with a 8-cm, 10-cm, and 13-cm breast phantom (17%-VGF) respectively. The simulated images show similar image quality as that of the experimentally-acquired images with the object present.

### 4.7.2 Optimization Methods

The goal of the optimization is to determine the x-ray technique factors to generate CEDEM images with the best visualization of the region with iodinated-contrast solution while ensuring the elimination of background anatomical structures. Given the low-energy image  $I_L(x, y)$  and the high-energy image  $I_H(x, y)$ , the CEDEM image  $I_{DE}(x, y)$  was generated using logarithmic-weighted subtraction using Equation (4.7). The objective of the logarithmic-weighted subtraction is to preserve the signal of the contrast agent while suppressing the anatomical structure in the background. The optimal weighting factor is determined based on a number of metrics to robustly implement dual energy subtraction. First, the signal-difference-to-noise ratio (SDNR) was calculated for a given CEDEM image using Equation (4.8), and the  $w_t^{SDNR}$  was determined using Equation (4.9) for  $w_t = 0.0, 0.001, \dots, 1.0$ . Figure 4.20 shows that  $w_t$  can be potentially optimized by maximizing  $SDNR$  or minimizing  $\sigma_{bg}^2$  in the CEDEM images. However,  $SDNR$  and  $\sigma_{bg}^2$  often suggest different optimized  $w_t$  using this approach. In the example of Figure 4.20, the optimized  $w_t$  by maximizing  $SDNR$  is 0.407 while that by minimizing  $\sigma_{bg}^2$  is 0.491.

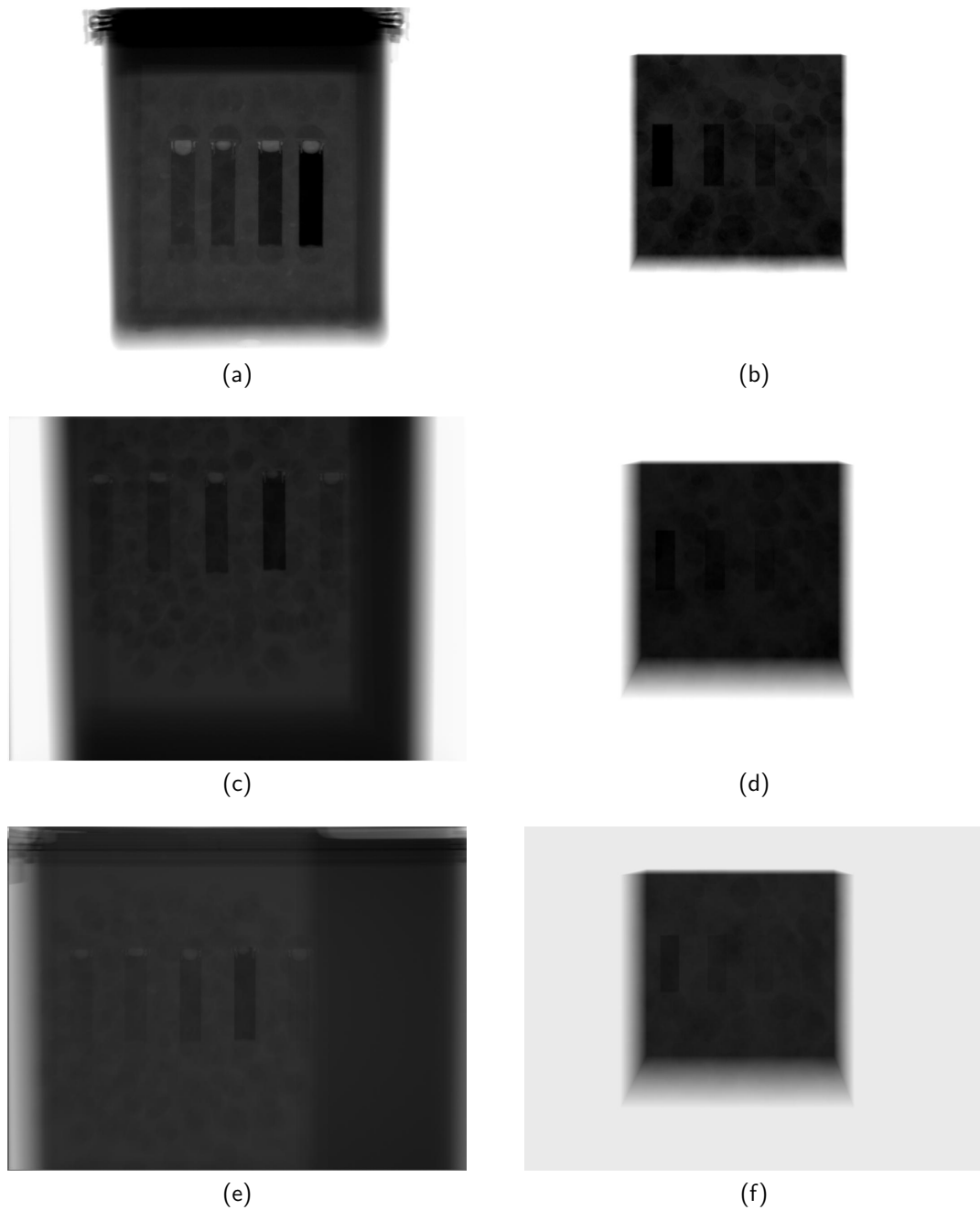


Figure 4.19. The flat-field projection images of a 8-cm breast phantom with 17% volume glandular fraction are shown using (a) experimental acquisitions and (b) computer simulation. (c) and (e) are the experimentally-acquired images for 10-cm and 13-cm breast phantoms with 17%-VGF, respectively. (d) and (f) are the simulated images for 10-cm and 13-cm breast phantoms. The images are shown in logarithmic scale for display purpose.

Figure 4.21 show the CEDEM images using the  $w_t$ 's optimized using  $SDNR$  and  $\sigma_{bg}^2$ . The CEDEM image using  $w_t = 0.407$  (optimized by  $SDNR$ ) appears to have some residual anatomical structure in the background, while the CEDEM image using  $w_t = 0.491$  (optimized by  $\sigma_{bg}^2$ ) successfully suppresses the background structure. As a result,  $SDNR$  was found to be not an ideal metric for successful dual-energy subtraction although it may be a good indication for visualization of the regions of interest. Therefore, minimizing  $\sigma_{bg}^2$  of the CEDEM image was one metric to determine the optimal weighting factor  $w_t^1$  as the following

$$w_t^1 = \min_{w_t} \sigma_{bg}^2 [I_{DE}(x, y; w_t)] \quad (4.11)$$

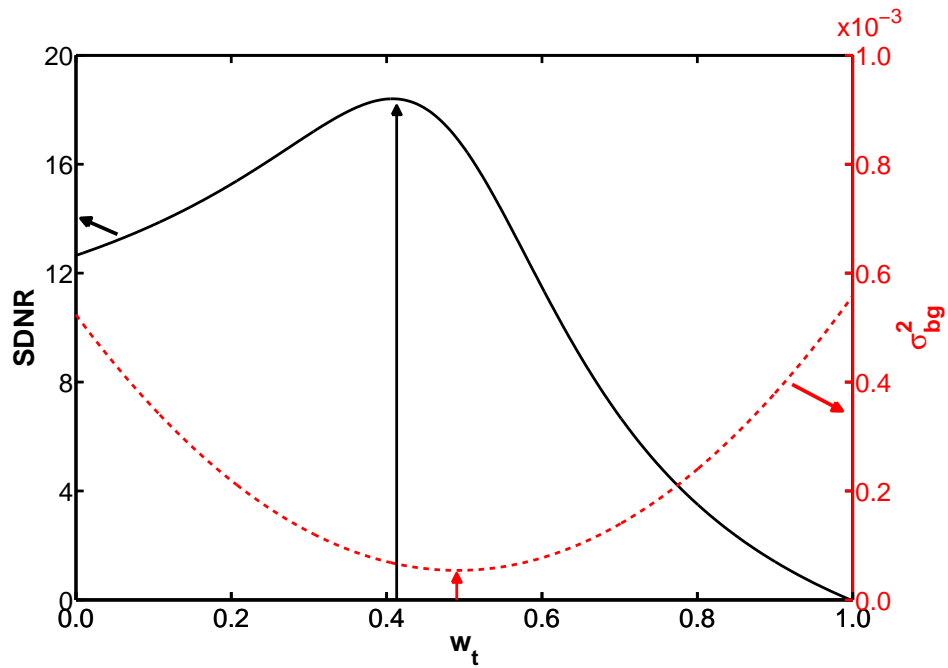


Figure 4.20. The signal-difference-to-noise ratio ( $SDNR$ ) and signal variance in the region of background anatomical structures  $\sigma_{bg}^2$  are shown as a function of dual-energy subtraction weighting factor  $w_t$ . In this example,  $w_t^{SDNR}$  is 0.407 and  $w_t^1$  is 0.491.

In addition to  $\sigma_{bg}^2$ , grey-level-co-occurrence matrix (GLCM) was used as another metric to strengthen the robustness of determining the optimal  $w_t$  for best dual-energy subtraction. GLCM is a method to calculate how often a



Figure 4.21. The CEDEM images of a breast phantom with 8-cm thick and 17% volume glandular fraction are shown using (a)the  $SDNR$ -optimized  $w_t = 0.407$  and (b)the  $\sigma_{bg}^2$ -optimized  $w_t = 0.491$ .

pixel with gray-scale intensity  $i$  occurs horizontally adjacent to a pixel with the value  $j$ . GLCM is useful in order to quantify the distribution of the signal intensity in terms of the degree of correlation, contrast, energy, or homogeneity for a given image. Prior to generating GLCM, the grey-scale image  $I(x, y)$  was scaled to a number of gray-scale levels  $L$  limited by the gray-scale minimum  $I_{min}$  and the gray-scale maximum  $I_{max}$  as

$$I_s(x, y) = \left( \frac{I(x, y) - I_{min}}{I_{max} - I_{min}} \right) (L - 1) \quad (4.12)$$

Lower L (lower than the intrinsic gray-scale level of the image) has similar effect on image noise as that of an average filter. Figure 4.22 shows how the GLCM is calculated for a 4-by-5 scaled image  $I_s(x, y)$ . Element (1, 1) in the GLCM contains the value 1 since there is only one instance where two horizontally adjacent pixels have the value of 1 and 1. Element (5, 7) contains the value of 2 since there are two instances where two horizontally adjacent pixels have the value of 5 and 7. This counting process continues for all elements of  $I_s(x, y)$  to populate all values in the GLCM. The distance between the pixel of interest and its neighbor  $(x_{offset}, y_{offset})$  in generating GLCM is specified in horizontal and vertical directions. In the example of Figure 4.22,

$(x_{offset}, y_{offset}) = (1, 1)$ . For a given image, a number of statistics can be calcu-

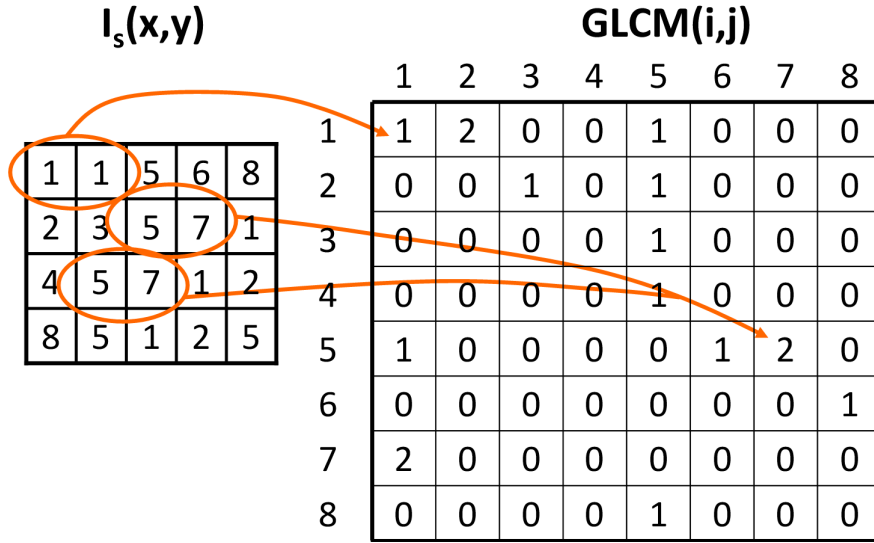


Figure 4.22. The generation of a gray-scale-co-occurrence matrix (GLCM) is demonstrated for a given scaled gray-scale intensity image  $I_s(x, y)$ .

lated from the normalized GLCM  $p(i, j)$  where  $\sum_{i,j} p(i, j) = 1$ . The first statistic quantifies the degree of homogeneity  $H$  of the image defined as

$$H = \sum_{i,j} \frac{p(i, j)}{1 + |i - j|} \quad (4.13)$$

The second statistic measures the degree of contrast  $C$  of the image as

$$C = \sum_{i,j} |i - j|^2 p(i, j) \quad (4.14)$$

$H$  is 1 for a diagonal GLCM where all elements have the same gray-scale intensity as its neighboring pixels.  $C$  is 0 for a constant image.  $H$  and  $C$  were used as additional metrics to determine  $w_t^{Opt}$  for a given CEDEM image. A number of background ROIs with anatomical structures were manually selected for GLCM calculation. For each ROI, Eight GLCM's were generated using  $(x_{offset}, y_{offset}) = (-43, -43), (-43, 0), (-43, 43), (0, -43), (0, 43), (43, -43), (43, 0), (43, -43)$ .  $L = 64$  was used in generating all GLCM's. The mean  $H$   $\bar{H}$

and the mean  $C \bar{C}$  were calculated averaging over all  $H$ 's and  $C$ 's evaluated all GLCM's. The optimal weighting factor  $w_t^2$  was determined by maximizing the degree of homogeneity  $\bar{H}$  for a given CEDEM image

$$w_t^2 = \max_{w_t} \bar{H} \left[ I_{DE}(x, y; w_t) \right] \quad (4.15)$$

Another optimal weighting factor  $w_t^3$  was evaluated by minimizing the degree of contrast  $\bar{C}$  for a CEDEM image as

$$w_t^3 = \max_{w_t} \bar{C} \left[ I_{DE}(x, y; w_t) \right] \quad (4.16)$$

The final optimal weighting factor  $\bar{w}_t$  was then obtained by averaging all  $w_t$ 's determined from Equation (4.11), Equation (4.15), and Equation (4.16). Using the same CEDEM images in Figure 4.20, Figure 4.23 shows that  $\bar{H}$  is maximized and  $\bar{C}$  is minimized at similar values of  $w_t$ . For the example in Figure 4.23,  $w_t^2$  and  $w_t^3$  were found to be 0.477 and 0.522 respectively. The CEDEM images using the  $w_t^2$ ,  $w_t^3$ , and  $\bar{w}_t$  (averaging  $w_t^1 = 0.499$ ,  $w_t^2 = 0.477$ , and  $w_t^3 = 0.522$ ) are shown in Figure 4.24, exhibiting robust dual energy subtraction. Therefore, the three  $w_t$ 's are used to determine the optimal  $w_t$  for robust dual energy subtraction.

The  $w_t$  optimization method using three metrics was found to be effective when implemented with the image that comprised more averaged frames. In another words, averaging more frames in acquisition was found to be more effective in reducing image noise than lowering L when generating the GLCM. Therefore, CEDEM images consisting of more averaged frames, which may result in higher radiation dose, is desirable for robust dual-energy subtraction.

### 4.7.3 kV Optimization

The goal of this optimization is to determine the kV using 0.1-mm Sn/0.2-mm Cu filter combinations to generate CEDEM images with the best SDNR while

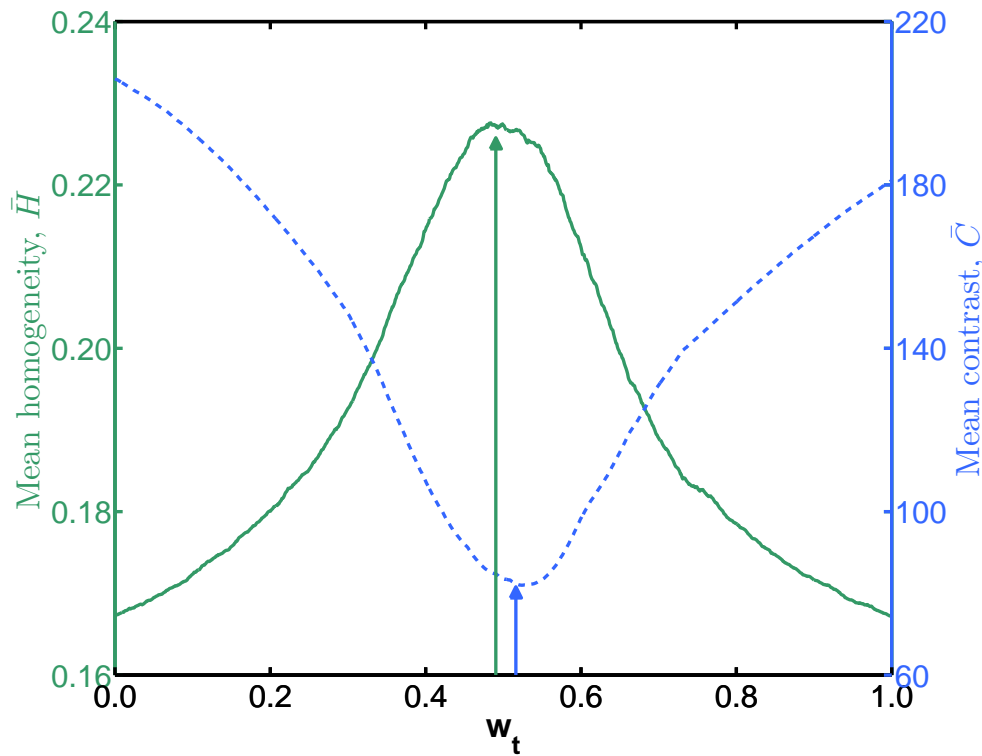


Figure 4.23. The mean degree of homogeneity  $\bar{H}$  and the mean degree of contrast  $\bar{C}$  are displayed as a function of the weighting factor  $w_t$ . In this example,  $w_t^2 = 0.477$  and  $w_t^3 = 0.522$ . These metrics are used to ensure robust dual energy subtraction in generating CEDEM images.

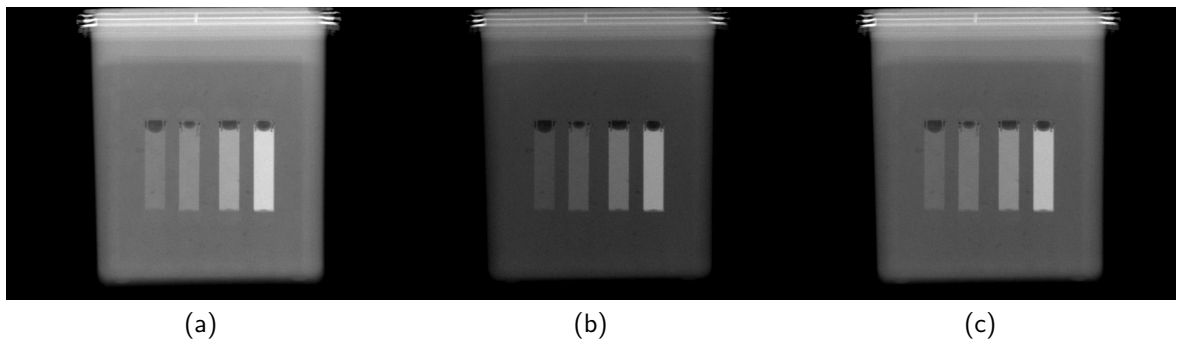


Figure 4.24. The CEDEM images of a breast phantom with 8-cm thick and 17% volume glandular fraction are shown using (a) $w_t^2 = 0.477$ , (b) $w_t^3 = 0.522$ , and (c)  $\bar{w}_t = 0.497$ .

conserving radiation dose to patients efficiently. The optimization was performed using computer-simulated and experimentally-acquired images. To ensure robust dual-energy subtraction as described in Section 4.7.2, higher radiation dose (more averaged frames) was allowed for the first CEDEM image. The subsequent CEDEM images would be acquired with lower radiation dose (fewer averaged frames) for dose conservation during a dynamic CEDEM acquisition protocol. The optimization examines both image quality and dose efficiency in acquiring CEDEM images by varying a number of system and patient parameters. Iodine concentration, breast thickness, breast composition and dose allocation to the low-energy and high-energy images, were examined as a function of kV in acquiring CEDEM images with Sn and Cu. The dose allocation was implemented by varying the mean glandular dose allotted to the Sn-energy images ( $MGD_{Sn}$ ) and Cu-energy images ( $MGD_{Cu}$ ). The dose ratio  $R_d$  is defined as

$$R_d = \frac{MGD_{Sn}}{MGD_{Sn} + MGD_{Cu}} \quad (4.17)$$

To consider the typical range of breast dimension and composition among women, the kV optimization of 9 different breast phantoms were performed in this study. The dimension and volume glandular fraction of the breast phantoms include 8-cm (5%, 17%, and 25% VGF), 10-cm (5%, 17%, and 25% VGF), and 13-cm (5%, 17%, and 25% VGF).

In the kV optimization study, Sn-images and Cu-images that consist of the same number of averaged frames were used to generate CEDEM images ( $R_d = 0.53 - 0.59$ ). For the higher-dose setting, the number of Sn-images and Cu-images to average was determined by allowing only 5 acquired CEDEM images within the two-view mammogram MGD  $MGD_{mammo}$  for a given breast thickness (deliver  $MGD_1$  per CEDEM acquisition). For the lower-dose setting, the number of the acquired CEDEM images given the remaining dose ( $MGD_{mammo} - MGD_1$ ) was calculated such that only one frame of Sn-image and Cu-image are used to generate the CEDEM image. Table 4.2 lists the

Table 4.2. A list of the number of averaged frames used for the high-dose CEDEM acquisition for 8-cm, 10-cm, and 13-cm breast thickness and volume glandular fraction of 5%, 17%, and 25%.

Breast thickness		8 cm			10 cm			13 cm		
kV	VGF	5%	17%	25%	5%	17%	25%	5%	17%	25%
40		1	1	1	3	3	3	7	7	7
50		1	2	2	3	3	3	8	8	8
60		2	2	2	4	4	4	10	10	11
70		2	2	2	5	5	5	12	12	12
80		3	3	3	5	5	5	13	14	14
90		3	3	3	6	6	6	14	15	15
100		3	3	3	6	6	7	16	16	16

number of averaged frames used for high-dose CEDEM images as a function of kV for breast phantoms with various thickness and volume glandular fraction.

#### 4.7.3.1 Mean Glandular Dose

The radiation dose equivalent to two-view mammogram was used as a guideline to regulate the dose delivered in the clinical setting. Using Figure 4.10 with the compressed breast thickness estimated by Equation (4.3), the radiation dose equivalent to two-view mammogram was found to be 1.1 mGy, 2.1 mGy, and 4.9 mGy for the 8-cm, 10-cm, and 13-cm breast, respectively. The mean glandular dose delivered to the nine breast phantoms using the technique factors specified in Table 4.1 was calculated using the method described in Section 4.4. Figure 4.25 shows the mean glandular dose delivered to the breast for 8-cm, 10-cm, and 13-cm (glandular fraction of 5%, 17%, and 25%) as a function of kV. More radiation dose is delivered when using x-ray spectra filtered with 0.1-mm Sn likely due to more lower energy x-rays. The higher radiation dose associated with lower kV's will likely affect the opti-

mization of the practical x-ray technique factors used in acquiring multiple CEDEM images in the clinical setting.

#### 4.7.3.2 Breast Thickness

The kV optimization was performed to examine the effect of breast thickness. Breast thicknesses of 8-cm, 10-cm, and 13-cm were considered for VGF of 25%. The CEDEM images were generated using the appropriate weighting factor  $\bar{w}_t$ .  $\frac{SDNR}{\sqrt{MGD}}$  was then evaluated for the optimized CEDEM images for each breast thickness. Figure 4.26 shows the  $\bar{w}_t$  determined using the simulated and experimentally-acquired images as a function of kV for 8-cm, 10-cm, and 13-cm breast thickness. Similar  $\bar{w}_t$  was found using simulation and experiment data.  $\bar{w}_t$  was found to change slightly with increasing kV for simulation and experiment data. With the same anatomical structure in the background within a breast phantom, the effect of kV on  $\bar{w}_t$  should not change drastically. Figure 4.27 shows the  $\frac{SDNR}{\sqrt{MGD}}$  (for ROIs with iodine concentration of 21.6 mg/ml) and the number of allowable CEDEM images given the  $MGD_{mammo}$  as function of kV for 8-cm, 10-cm, and 13-cm breast phantoms (VGF of 25%). Both simulation and experiments suggest that the kV giving rise to the best  $\frac{SDNR}{\sqrt{MGD}}$  was found to be 50 kV using Sn/Cu filters. As breast thickness increases, the optimized  $\frac{SDNR}{\sqrt{MGD}}$  reduces since thicker objects require more dose for the same SDNR. In addition, higher radiation dose per CEDEM image at 50 kV results in fewer CEDEM images allowed within the  $MGD_{mammo}$  for all 3 breast thicknesses. For an 8-cm breast phantom with 25% VGF, fewer than 6 CEDEM images were allowed when using 40 kV or 50 kV. However, the  $\frac{SDNR}{\sqrt{MGD}}$  at 60 kV is approximately 18, which is slightly below that at 50 kV ( $\frac{SDNR}{\sqrt{MGD}} \simeq 25$ ) but allowing more CEDEM images within the dose limitation. For 10-cm and 13-cm breasts, a similar trade-off between  $\frac{SDNR}{\sqrt{MGD}}$  and the number of allowable CEDEM images was observed as well. To preserve sufficient signal difference between the iodine and background ROIs, 60 kV was thought to be the practical kV using Sn/Cu filters allowing more CEDEM images to be acquired within the dose limitation for all three

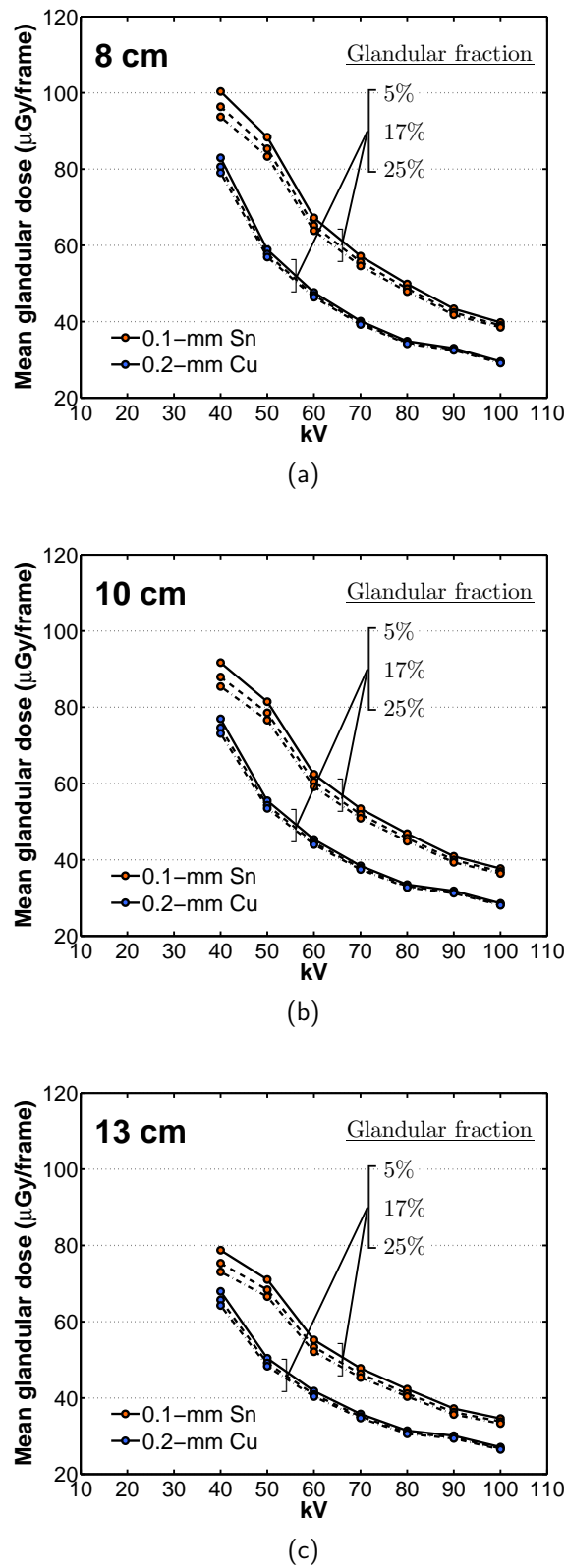


Figure 4.25. The mean glandular dose per frame is shown as a function of kV filtered with 0.1-mm Sn and 0.2-mm Cu for glandular fraction of 5%, 17%, and 25% and breast thickness of (a) 8-cm, (b) 10-cm, and (c) 13-cm.

breast thicknesses.

#### 4.7.3.3 Iodine Concentration

The effect of iodine concentration was examined in the kV optimization. For 8-cm, 10-cm, and 13-cm breast phantoms (VGF of 25%),  $\frac{SDNR}{\sqrt{MGD}}$  evaluated for iodine concentration of 10.8 mg/ml, 5.4 mg/ml, and 2.7 mg/ml was shown as a function of kV in Figure 4.28. 50 kV with Sn/Cu filters was the kV with the best  $\frac{SDNR}{\sqrt{MGD}}$  in CEDEM images. The optimized  $\frac{SDNR}{\sqrt{MGD}}$  was reduced as the iodine concentration decreases since lower iodine concentration is less attenuating. The optimized  $\frac{SDNR}{\sqrt{MGD}}$  also decreases with increasing breast thickness. Trends in simulation and experimental data suggest similar kV optimization results. Discrepancy in  $\frac{SDNR}{\sqrt{MGD}}$  between the simulation and experimental data is likely due to the beam hardening effect from the heavily attenuating materials such as iodine, which was not well characterized in the simulation method. Figure 4.28 suggests that sufficient  $\frac{SDNR}{\sqrt{MGD}}$  was observed for thicker breasts and lower iodine concentration. Although 50 kV produced the best  $\frac{SDNR}{\sqrt{MGD}}$ , 60 kV is a good compromise kV to generate CEDEM images with useful quantitative information.

#### 4.7.3.4 Breast Composition

Breast composition, or the volume glandular fraction, was examined for the kV optimization. For 8-cm breast thickness,  $\frac{SDNR}{\sqrt{MGD}}$  evaluated for iodine concentration of 21.6 mg/ml in the CEDEM images (simulation and experiment data) was presented as a function of kV for VGF of 5% and 17% in Figure 4.29. The number of allowable CEDEM images was shown as well, as a function of kV. Figure 4.30 and Figure 4.31 show the same metrics for 10-cm and 13-cm breast thickness. For 8-cm, 10-cm, and 13-cm breast thickness, volume glandular fraction shows subtle effect on the  $\frac{SDNR}{\sqrt{MGD}}$  for each kV. The kV giving rise to the best  $\frac{SDNR}{\sqrt{MGD}}$  is 50 kV with this result in agreement between simulation and experiment data. Since the mean glandular dose when imaging with 40 kV or 50 kV is higher, 60 kV or higher is more suitable in acquiring multi-

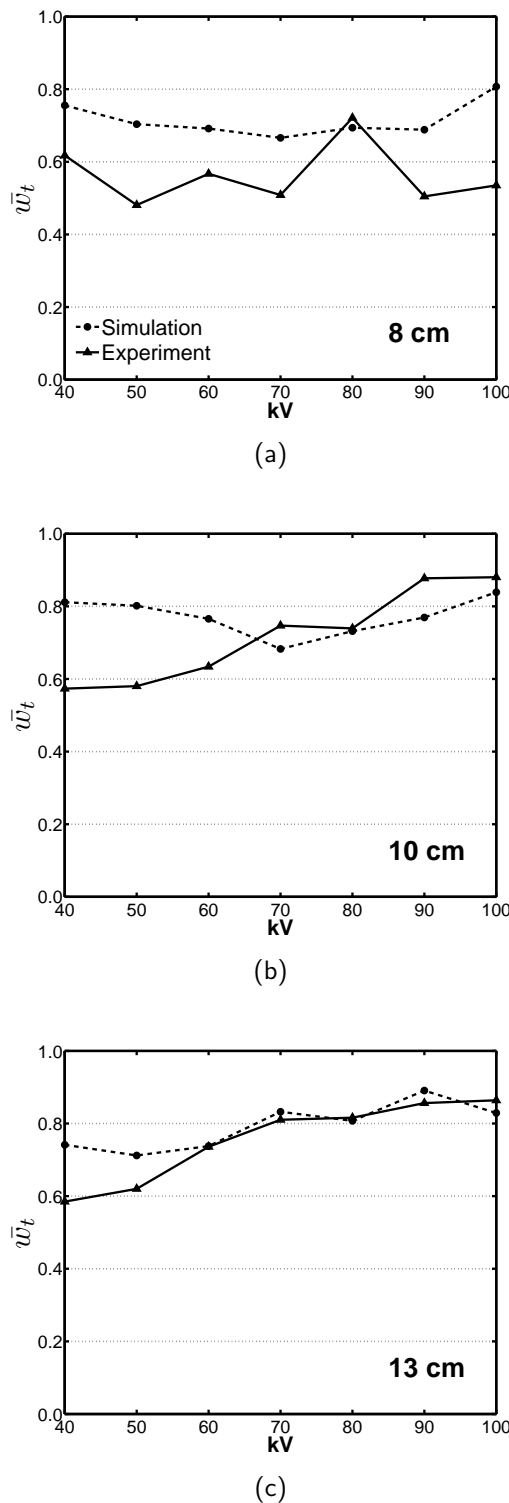


Figure 4.26. The  $\bar{w}_t$  is shown as a function of kV for (a) 8-cm, (b) 10-cm, and (c) 13-cm breast phantom (VGF of 25%).

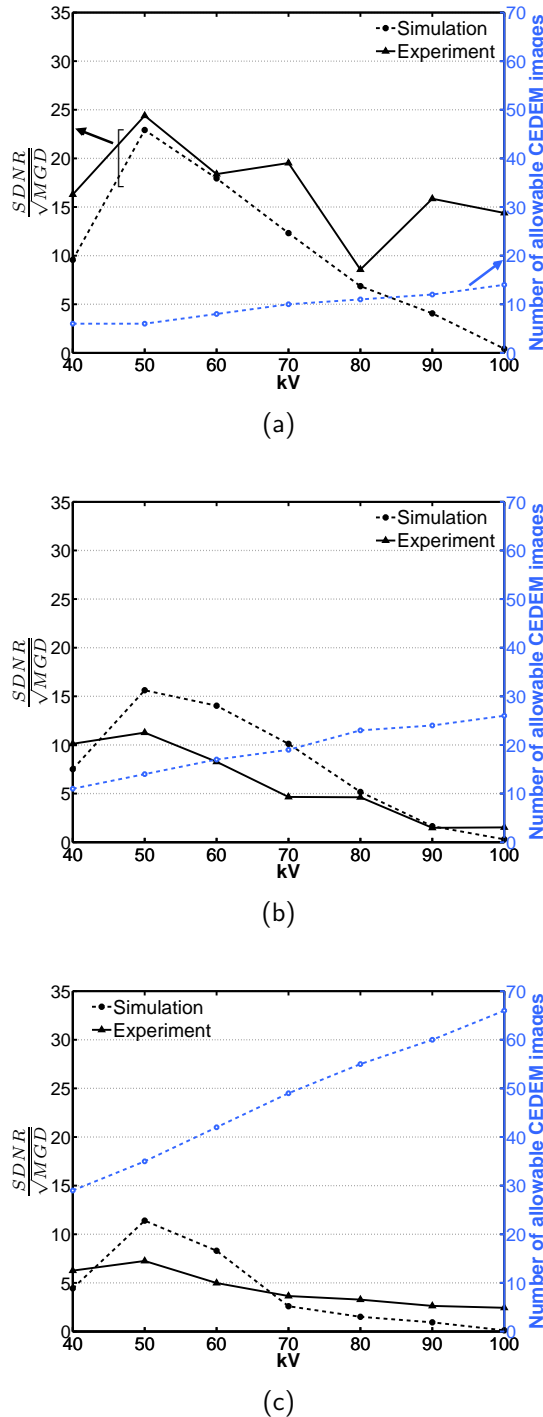


Figure 4.27. The  $\frac{SDNR}{\sqrt{MGD}}$  and the number of allowable CEDEM images given  $MGD_{mammo}$  are illustrated as a function of kV for (a) 8-cm, (b) 10-cm, and (c) 13-cm breast phantoms (VGF of 25%). The  $\frac{SDNR}{\sqrt{MGD}}$  was evaluated for iodine concentration of 21.6 mg/ml.

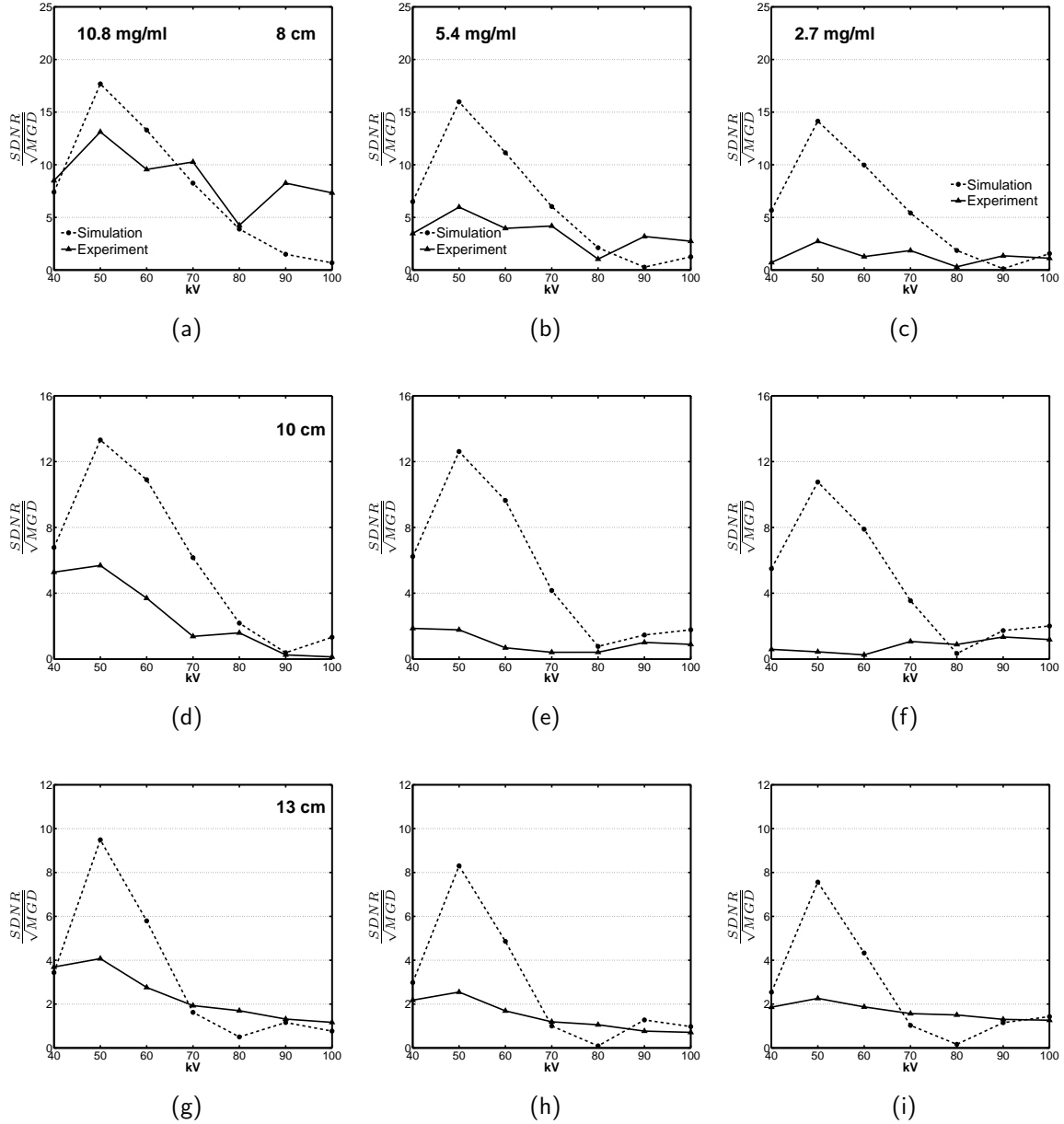


Figure 4.28. The  $\frac{SDNR}{\sqrt{MGD}}$  evaluated for three different iodine concentrations is displayed as a function of kV for three breast thicknesses. (a),(b),(c), (d),(e),(f), and (g),(h),(i) are data for 8-cm, 10-cm, and 13-cm breast thickness (VGF of 25%), respectively. (a),(d),(g), (b),(e),(h), and (c),(f),(i) are data for iodine concentration of 10.8 mg/ml, 5.4 mg/ml, and 2.7 mg/ml. The solid black line represents the experimental result and the dashed black line represents the simulation result.

ple CEDEM images within the allowable mean glandular dose, especially in the case of the 8-cm breast thickness. Therefore, 60 kV is the optimal kV to acquire CEDEM without severely compromising the signal contrast in the CEDEM images.

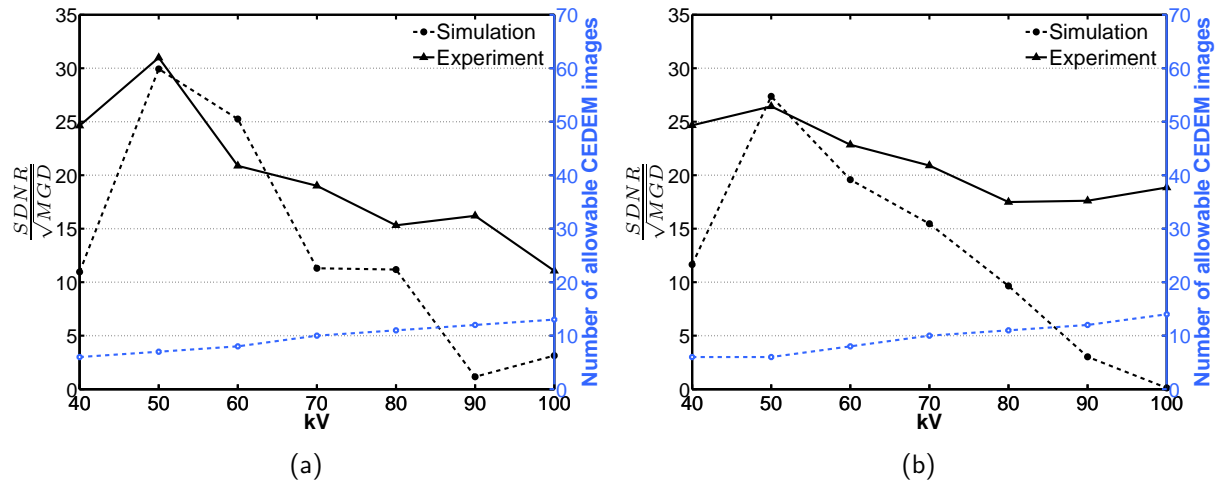


Figure 4.29. The  $\frac{SDNR}{\sqrt{MGD}}$  is shown as a function of kV for 8-cm breast phantom with VGF of (a) 5% and (b) 17%. The  $\frac{SDNR}{\sqrt{MGD}}$  was evaluated for the iodine concentration of 21.6 mg/ml.

#### 4.7.3.5 Dose Allocation

Once 60 kV was found to be optimal and feasible in acquiring CEDEM images, the effect of dose allocation between the Sn-image and Cu-image were examined using 60 kV with Sn/Cu filters. The  $SDNR$  was evaluated for the iodine concentration of 21.6 mg/ml. The dose ratio  $R_d$  defined by Equation (4.17) was used to quantify the proportion of radiation dose when acquiring the low-energy and high-energy images. The dose ratio was varied by changing the number of averaged frames used to generate CEDEM images. For a lower dose ratio, more mean glandular dose is allotted in acquiring Cu-images that consist of more averaged frames, and vice versa. Figure 4.32, Figure 4.33, and Figure 4.34 show the  $\frac{SDNR}{\sqrt{MGD}}$  and number of allowable CE-

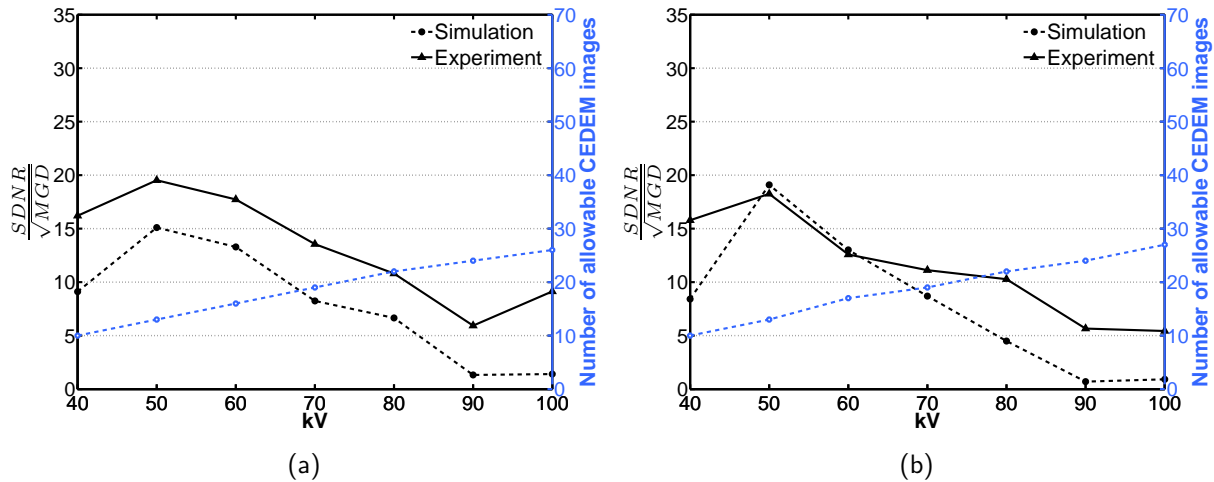


Figure 4.30. The  $\frac{SDNR}{\sqrt{MGD}}$  is shown as a function of kV for 10-cm breast phantom with VGF of (a) 5% and (b) 17%. The  $\frac{SDNR}{\sqrt{MGD}}$  was evaluated for the iodine concentration of 21.6 mg/ml.

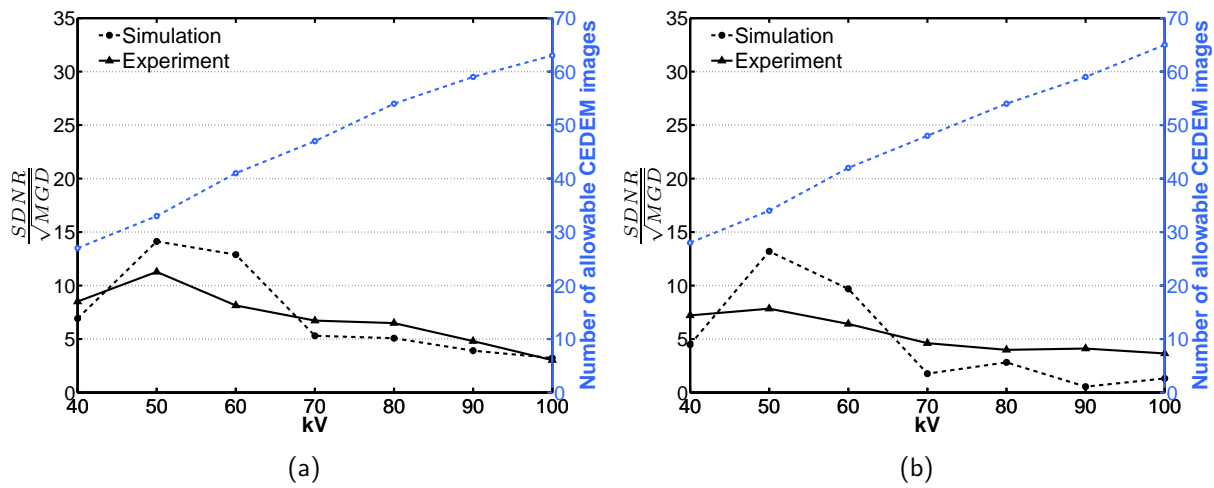


Figure 4.31. The  $\frac{SDNR}{\sqrt{MGD}}$  is shown as a function of kV for 13-cm breast phantom with VGF of (a) 5% and (b) 17%. The  $\frac{SDNR}{\sqrt{MGD}}$  was evaluated for the iodine concentration of 21.6 mg/ml.

DEM images as a function of dose ratio when using 60 kV in acquiring CEDEM images for a 8-cm, 10-cm, and 13-cm breast thickness (VGF of 5%, 17%, and 25%). For all breast thicknesses and VGF's, both simulation and experiment data suggest that the best  $\frac{SDNR}{\sqrt{MGD}}$  was achieved when delivering approximately equivalent dose to Sn-images and Cu-images when acquiring CEDEM images. The number of allowable CEDEM images peaks when allocating approximately equivalent dose to Sn-images and Cu-images. A dose ratio of 0.5 to 0.6 is typically achieved by averaging similar number of frames to acquire Sn-images and Cu-images. For the high-dose CEDEM acquisition, Sn-images and Cu-images that consist of more than two average frames were found favorable to determine the optimized weighting factor for robust dual energy subtraction (also see Section 4.7.2). For the dose ratio lower or higher than 0.5, the Sn-image or the Cu-image requires averaging more frames. Thus, the radiation dose delivered per CEDEM image would increase, which reduces the number of allowable CEDEM images within the dose limitation as shown in Figure 4.32, Figure 4.33, and Figure 4.34. For 8-cm breast phantoms in Figure 4.32, the range of available dose ratio was reduced since the CEDEM acquisition with lower or higher dose ratio requires radiation dose exceeding the allowed mean glandular dose. As a result, when acquiring CEDEM images using 60 kV (Sn/Cu filters), this study suggests that dose ratio of 0.5 to 0.6 is ideal for maintaining the integrity of CEDEM images while adhering to the mean glandular dose of the two-view mammogram.

#### 4.7.4 Optimization Conclusions

A comprehensive investigation of static CEDEM imaging was performed using simulated and experimentally-acquired images considering a number of system and patient parameters, including x-ray technique factors, breast thickness, and breast composition. Adhering to the radiation dose limitation, 60 kV with the dose ratio of 0.5 to 0.6 was found to be optimal in acquiring CEDEM images for breast thickness of 8-cm, 10-cm, 13-cm. Breast composition, or volume glandular fraction, has a more subtle effect on the optimized x-ray

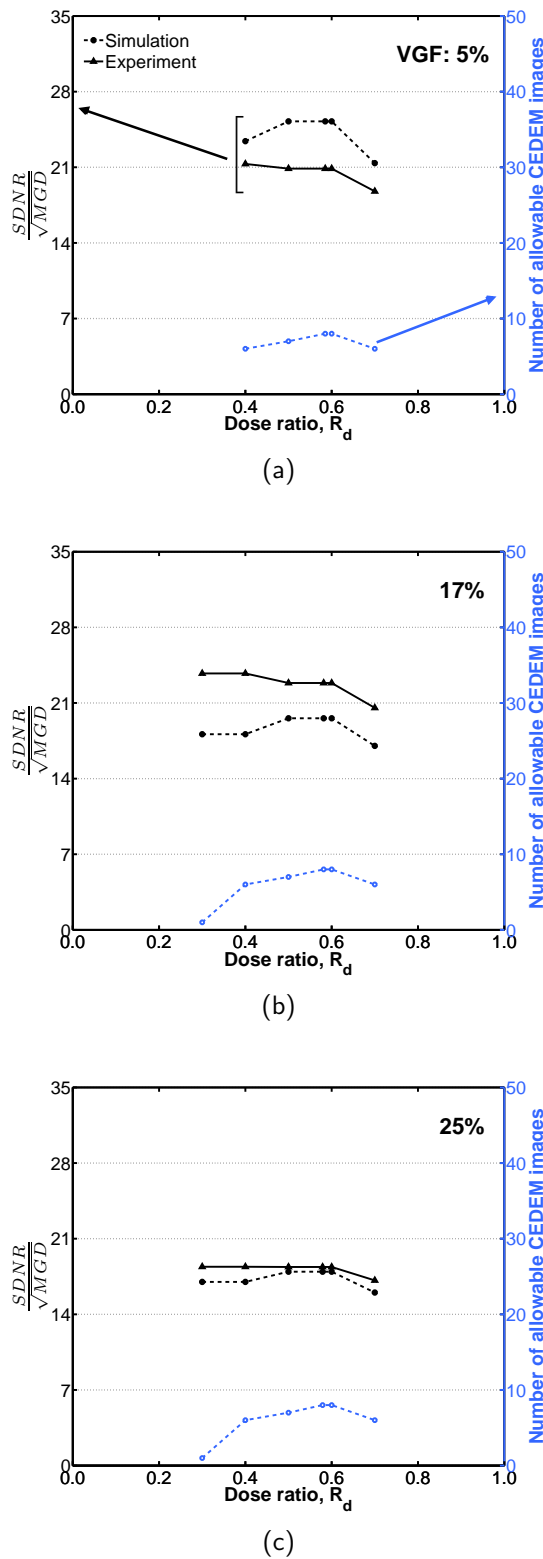


Figure 4.32. The  $\frac{SDNR}{\sqrt{MGD}}$  and the number of allowable CEDEM images given  $MGD_{mammo}$  are displayed as a function of dose ratio for 8-cm breast phantoms (VGF of 5%, 17%, and 25%) acquired with 60 kV. The  $\frac{SDNR}{\sqrt{MGD}}$  was evaluated for the iodine concentration of 21.6 mg/ml.

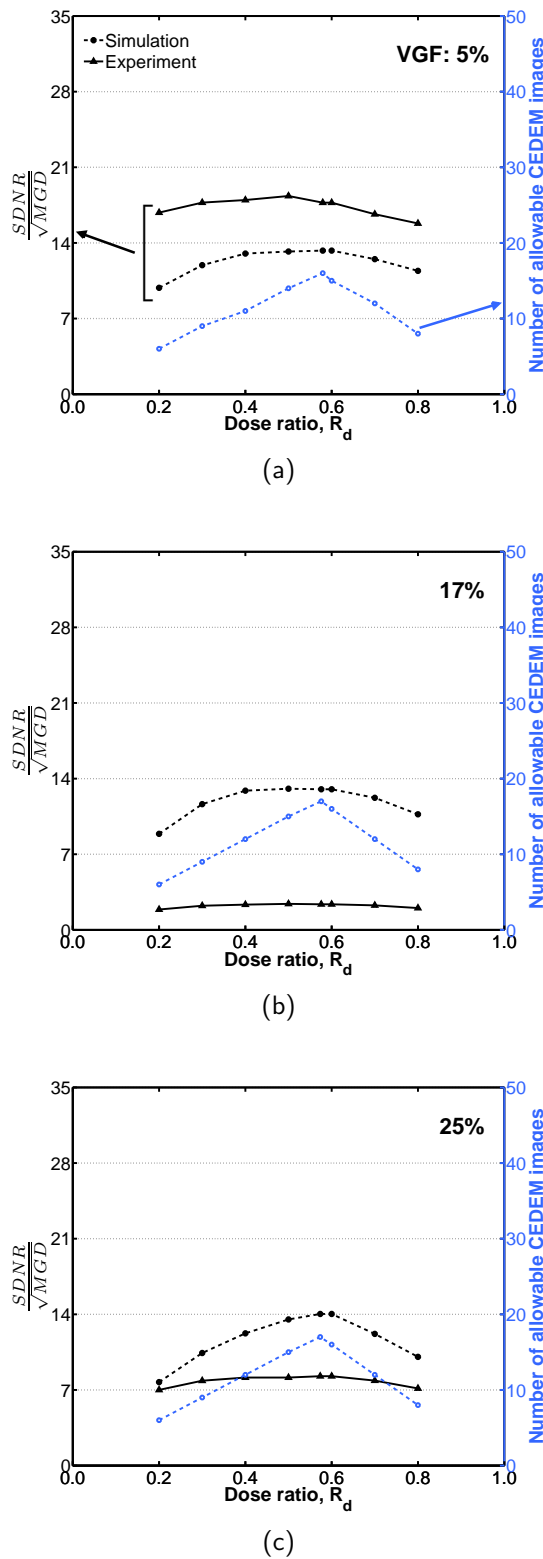


Figure 4.33. The  $\frac{SDNR}{\sqrt{MGD}}$  and the number of allowable CEDEM images given  $MGD_{mammo}$  are displayed as a function of dose ratio for 10-cm breast phantoms (VGF of 5%, 17%, and 25%) acquired with 60 kV. The  $\frac{SDNR}{\sqrt{MGD}}$  was evaluated for the iodine concentration of 21.6 mg/ml.

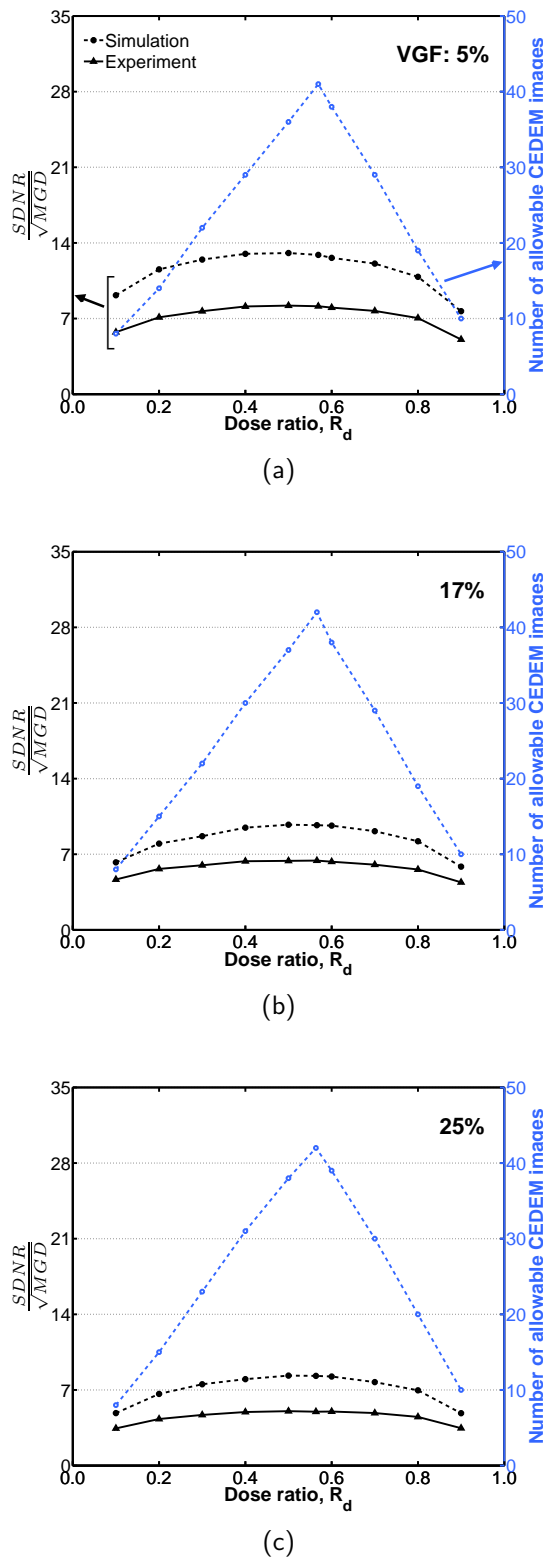


Figure 4.34. The  $\frac{SDNR}{\sqrt{MGD}}$  and the number of allowable CEDEM images given  $MGD_{mammo}$  are displayed as a function of dose ratio for 13-cm breast phantoms (VGF of 5%, 17%, and 25%) acquired with 60 kV. The  $\frac{SDNR}{\sqrt{MGD}}$  was evaluated for the iodine concentration of 21.6 mg/ml.

technique factor. The signal of regions with different iodine concentrations also suggests that similar x-ray technique factors are required to preserve image quality. The dose ratio between the Sn-image and Cu-image in acquiring CEDEM images indicates that equal dose allocation is favorable in generating high-quality CEDEM images exhibiting robust dual energy subtraction. This study confirms that static acquisition using 60 kV (Sn/Cu filters) is feasible to generate CEDEM images with useful quantitative information while delivering radiation dose equivalent to or lower than that of two-view mammogram. The optimized static CEDEM acquisition can be easily adopted for a dynamic acquisition protocol.

## 4.8 The Dynamic CEDEM Imaging

The static CEDEM optimization provide information regarding the effect on signal-difference-to-noise ratio in the CEDEM images when changing a number of system and patient physical parameters. The studies in Section 4.7 show that CEDEM acquisition can produce promising CEDEM images to enhance the signal with iodine contrast agents in a static acquisition using 60 kV with Sn/Cu filters. The goal of this study is to demonstrate the feasibility of acquiring CEDEM images dynamically. The study is also designed to determine the ability of dynamic CEDEM imaging in providing meaningful contrast kinetics curves. Dynamic CEDEM imaging protocols will be designed for a number of patient physical parameters for future clinical trials.

### 4.8.1 The Breast Tumor Flow Chamber

To examine the feasibility of dynamic CEDEM, a dynamic breast phantom was designed and fabricated by a local machine shop. The dynamic breast phantom consists of a static breast phantom (see Section 4.2) and a flow chamber with inlets and outlets. In controlling the fluid kinetics, the flow chamber was characterized by two main flow components, interstitial flow and vascular flow, around the breast tumor site. As described in Section 1.3.1,

the vasculature around the tumor cite tend to be “leaky” compared to that around normal tissues. With appropriate fluid flow and pressure within the tubes, the soaker hose can be made to leak out fluid in a realistic manner. In the flow chamber, soaker hoses were used as a surrogate of the “leaky” or semipermeable vessel associated with the breast tumor. The chamber was filled with plastic balls of different diameters to mimic the flow in the interstitial spaces around the breast tumor site. The flow chamber setup was thought to provide a relatively crude, non-physiological model of the contrast kinetics around the breast tumor cite. Figure 4.35 shows the CAD drawing (Solidworks® 2009, Concord, MA, courtesy of George Burkett Jr., M.S.) of the flow chamber and the fabricated chamber.

For appropriate flow control, computer-controlled pumps and solenoid valves were connected to the chamber inlet and outlet connections, and the pumps and valves were controlled by a data acquisition module (Data Translation®, Inc., Malboro, MA, USA). Solenoid vales were connected to the outlets of the flow chamber to adjust the system’s back pressure. Two peristaltic pumps (Manostat®, Cole-Parmer Instrument Company, Barrington, IL, USA) were used to introduce vascular flow, which is typically rapid. The peristaltic pumps (measured with Tygon® tubing of  $\frac{1}{4}$ " OD,  $\frac{1}{8}$ " ID) are capable of producing flow rates ranging from 0.75 ml/sec to 20.0 ml/sec. Another peristaltic pump (Buchler®) was used to introduce the interstitial flow, typically slower than vascular flow. The peristaltic pump (measured with Tygon® tubing of  $\frac{5}{32}$ " OD,  $\frac{3}{16}$ " ID connected to that of  $\frac{1}{4}$ " OD,  $\frac{1}{8}$ " ID) has much slower flow rates ranging from 0.0042 ml/sec to 0.0420 ml/sec. Figure 4.36 demonstrates the linearity between the “marked” flow rate (manually selected at the pump panel) and the measure flow rate (determined by fluid volume over a fixed period of time) of the pumps used in this study.

#### 4.8.2 The Kinetic Parameters of the Flow Chamber

Knowledge of the contrast kinetic profile were obtained from the clinical dynamic contrast-enhanced MRI (DCE-MRI) data (provided by K.K. Lind-

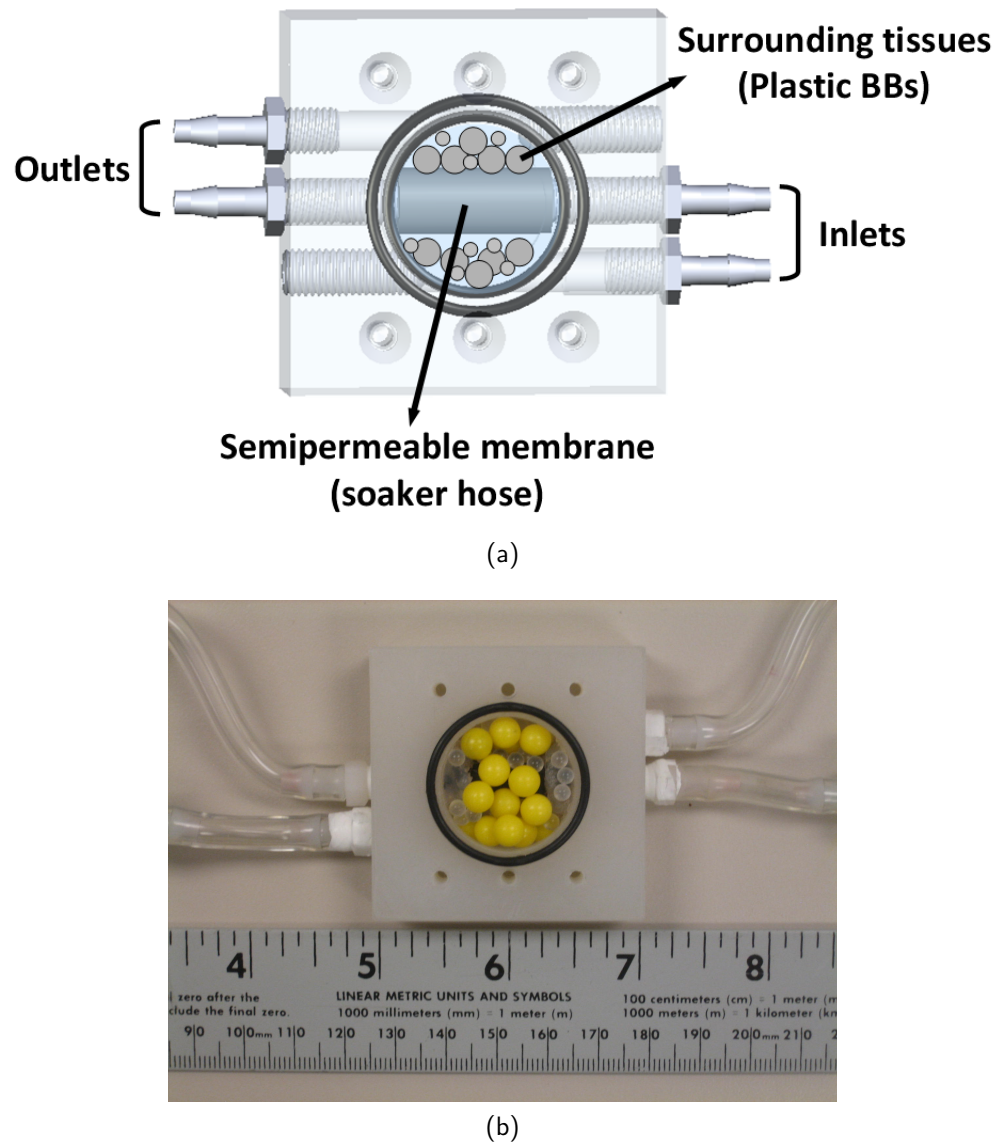


Figure 4.35. (a) The mechanical design of the flow chamber and (b) the fabricated chamber are shown.

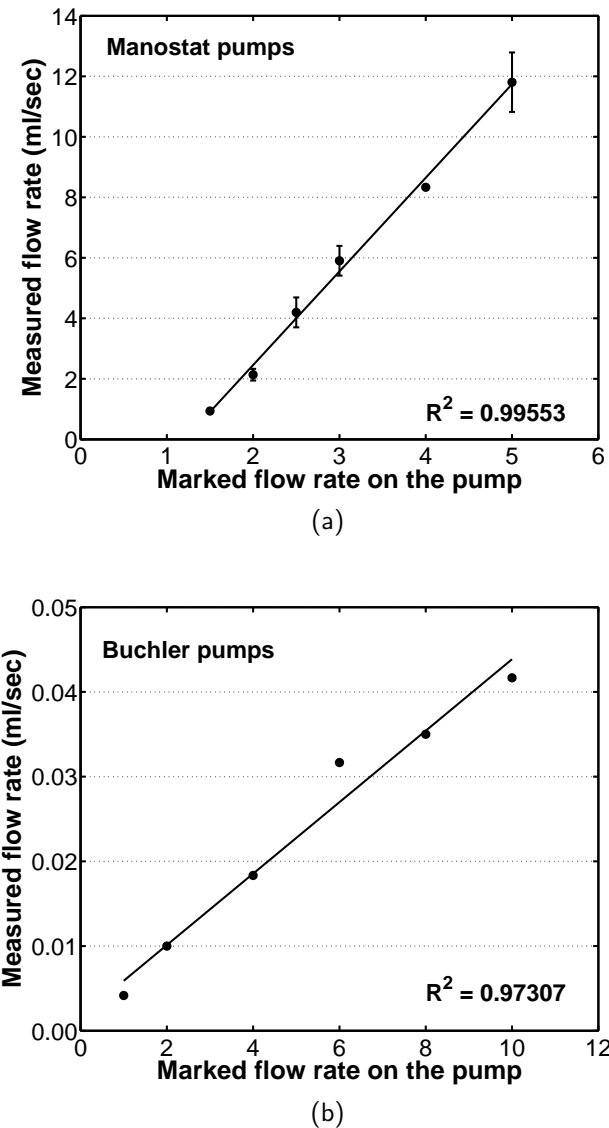


Figure 4.36. The marked flow rate on the pump panel is presented as a function of the flow rate measured using (a) two *Manostat*<sup>®</sup> peristaltic pumps and (b) a *Buchler*<sup>®</sup> peristaltic pump.

fors, M.D.). The MRI  $\frac{1}{T_1}$  rate change has been established to be linearly related to the concentration of contrast agents (Donahue et al., 1994; Jackson et al., 2005; Judd et al., 1995; Rosen et al., 1990), which suggests a non-linear but monotonic relationship between the signal enhancement and the concentration. Therefore, the four-point CED-MRI data was used as a starting point to develop the flow characteristics of the flow chamber of the dynamic breast phantom. Figure 4.37 shows the four-time-point CED-MRI data from patients with four different biopsy-confirmed breast cancer types. The contrast time density curves are all characterized by a rapid initial signal enhancement for the first 1 to 2 minutes, followed by a gradual reduction in signal enhancement for the remaining time. As shown in Figure 4.37, the amount of MRI signal enhancement in the benign lesions is much smaller compared to that of the malignant lesions. Similar trends in signal enhancement were found in the contrast-enhanced breast CT data sets (see Figure 4.7). The rate of signal enhancement was found to depend on the kinetic characteristics of the blood vessels for a given patient.

In order to determine the control setting which produce a given MRI kinetic profile, videos (AVI files) of the flow chamber filled with red-colored water were recorded to reduce the use of x-ray imaging during the optimization phase. X-ray imaging was used once the pump control settings were optimized, as discussed later. Figure 4.38 shows the flow chamber setup diagram with computer control capability. The frames of flow chamber videos were stored and read. The red-colored water was used as the “contrast agent” in the video acquisition since the color red can be easily detected in each RGB frame of the video. The “contrast agent” ROI was segmented using manually-determined global thresholds implemented on the image matrix of the green-color component. The signal within the “contrast agent” ROI was averaged and recorded at each time point for 8 minutes. Figure 4.39 shows a RGB frame of the flow chamber video and the segmented RGB frames using the global thresholds.

There are a number of flow parameters in controlling the flow and pres-

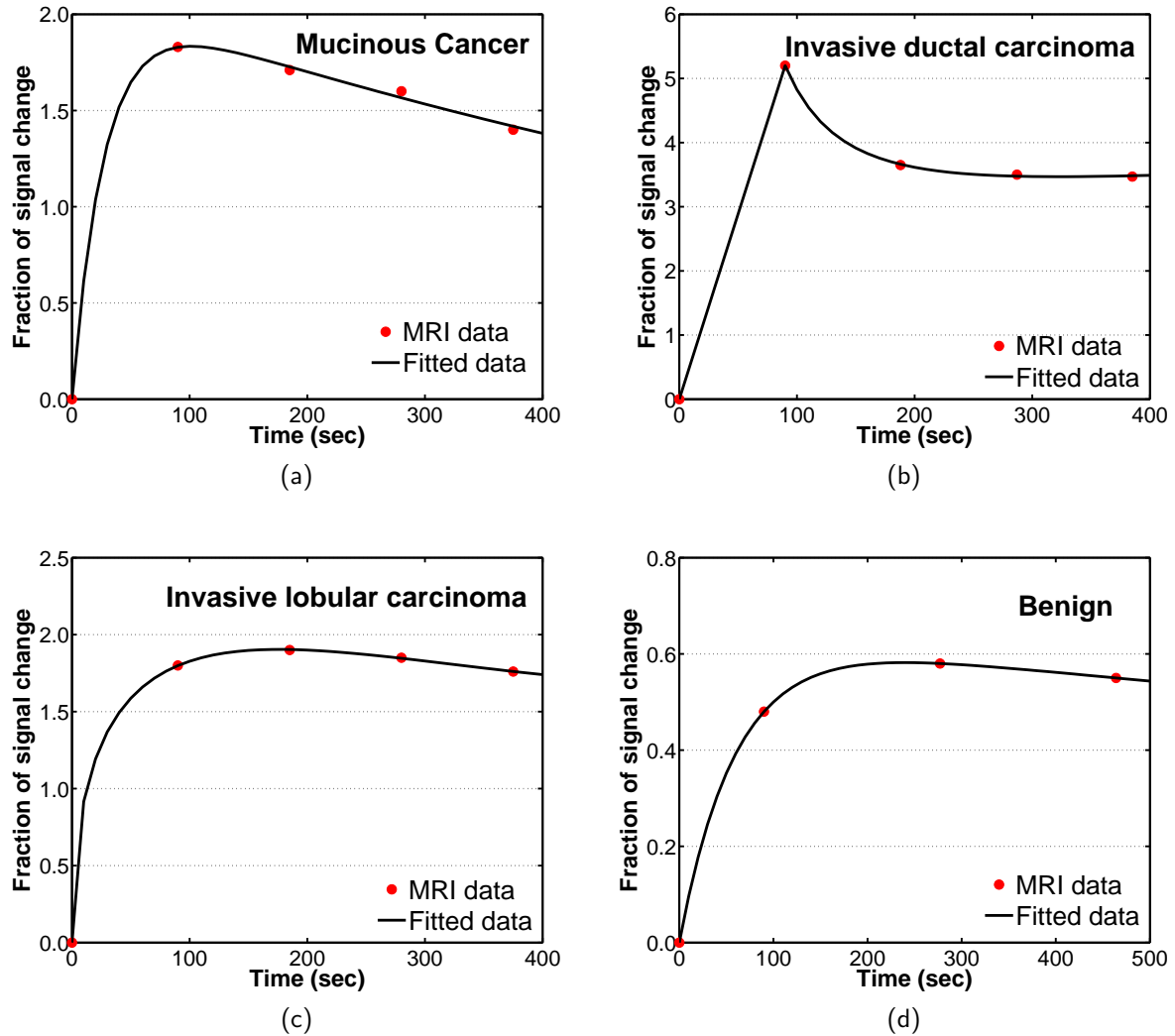


Figure 4.37. The clinical CED-MRI contrast kinetic curves are shown for (a) mucinous cancer, (b) invasive ductal carcinoma, (c) invasive lobular carcinoma, and (d) benign cancer. The fraction of MRI signal change is shown over time in seconds.

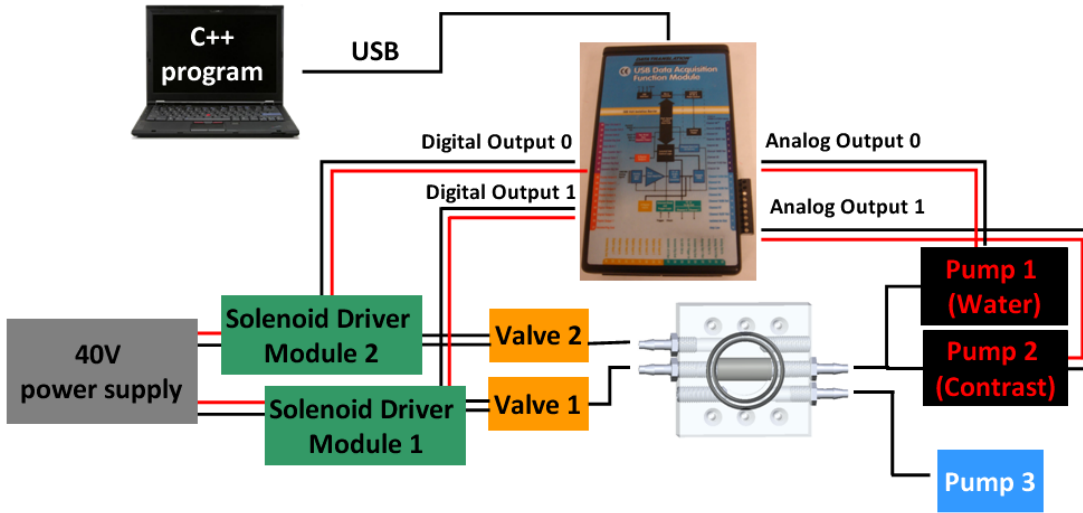


Figure 4.38. The wiring diagram of controlling the flow chamber is illustrated.

sure in the chamber. Figure 4.40 defines the following flow parameters: the flow rate of vascular flow wash-in,  $F_1$ , that of the contrast flow wash-in,  $F_2$ , that of the interstitial wash-out,  $F_3$ , the valve connected to the soaker hose outlet  $V_1$ , the valve connected to the chamber outlet  $V_2$ , the  $V_1$  On/Off duration  $T_1/T_2$ , and the  $V_2$  On/Off duration  $T_3/T_4$ . The flow parameters were determined experimentally using the video recording of the flow chamber as an initial understanding of the fluid dynamics within the chamber. Through trial and error, optimal timing was determined and the empirically-found flow chamber parameters are shown in Figure 4.41. These parameters are capable of generating a contrast kinetic curve consisting of the initial wash-in and subsequent wash-out of the contrast agent. The initial wash-in was controlled by an initial vascular wash-in  $F_1$  followed by the injection of the contrast solution of flow rate  $F_2$ . During this wash-in phase, the interstitial flow rate  $F_3$  was constant at a much lower flow rate. Cycling  $V_1$  between On/Off was used to create back pressure which allowed the contrast solution to leak into the chamber through the soaker hose (the “leaky” vessel). In order to retain the contrast solution in the chamber at the desired rate, a lower frequency cycling of  $V_2$  (longer  $T_4$ ) was used to avoid rapid wash-out of the

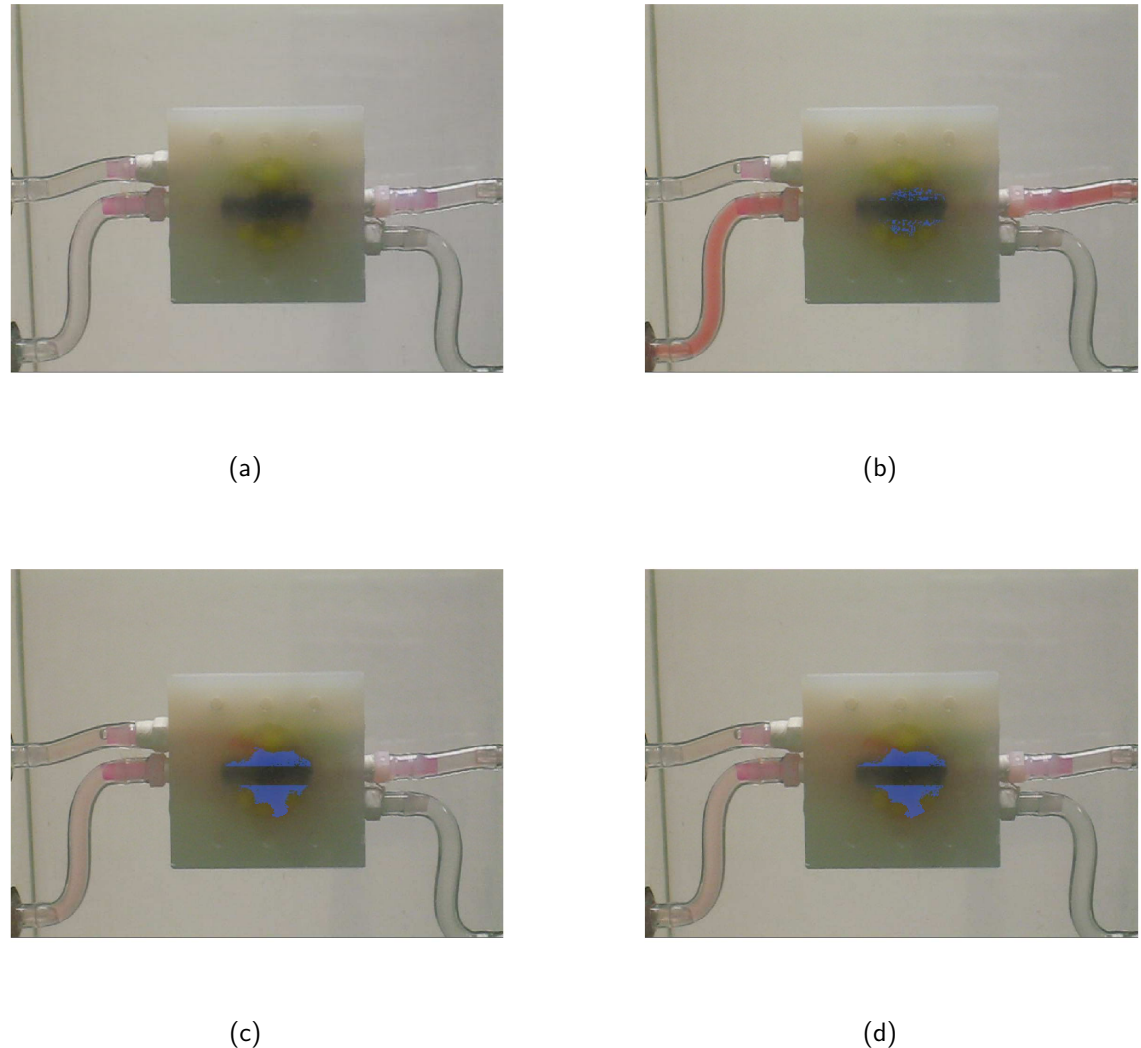


Figure 4.39. **(a)** An example of RGB frame from the flow chamber video is shown. The flow chamber is filled with the red-colored fluid representing the “contrast agent” around the breast tumor site. The segmented RGB frames acquired at **(b)** 33.4 second, **(c)** 233.4 second, and **(d)** 366.7 second since contrast injection are shown. The ROI with blue color indicates the segmented result of the “contrast agent”.

contrast solution. Once the contrast agent is injected into the chamber,  $F_3$  was the main flow parameter which controlled the wash-out of the contrast agent while leaving  $V_1$  shut and  $V_2$  open for the remaining time.  $F_3$  was set to a suitable flow rate to generate a given wash-out profile.

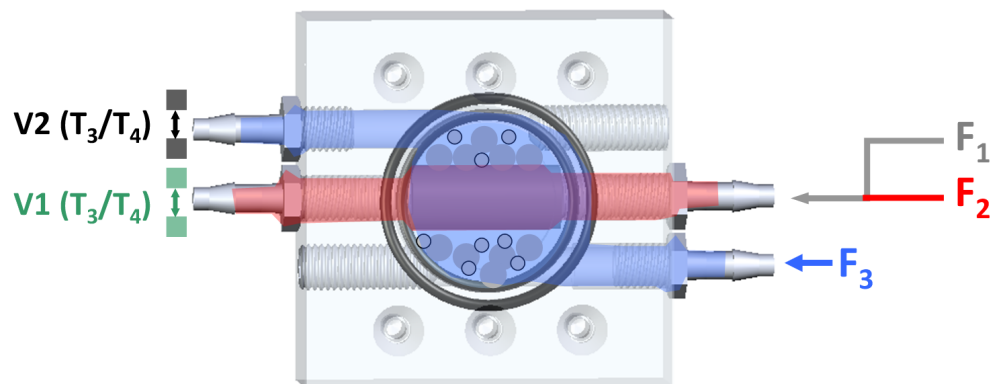


Figure 4.40. A diagram of the flow chamber is illustrated to define the flow parameters.  $F_1$ ,  $F_2$ , and  $F_3$  are the flow rates of the vascular wash-in, the contrast wash-in, and the interstitial wash-out, respectively.

Figure 4.42 shows the normalized signal enhancement as a function of time using the videos of the flow chamber filled with red-colored water. It demonstrates that the flow chamber can generate the high-enhancement and low-enhancement profiles typically seen in breast cancer. Table 4.3 specifies the list of flow parameters used to generate these profiles with slow, medium, and fast wash-out rate. The low-enhancement profile was mainly generated by larger  $T_1$ , where longer time duration of the  $V_1$  opening reduces the pressure within the soaker hose tubing. Thus, less contrast solution leaked into the chamber from the soaker hose. The high-enhancement profile was generated by smaller  $T_1$  which allows larger quantities of contrast to permeate through the soaker hose into the chamber, due to higher tubing pressure. The video recording of the flow chamber in action was found to be useful in optimizing the flow parameters to use for dynamic CEDEM acquisition with the dynamic breast phantom.

Table 4.3. The flow parameters to generate the high-enhancement and low-enhancement kinetic profiles shown in Figure 4.42 are listed.

<b>Contrast kinetic profile</b>	$F_1$ (ml/sec)	$F_2$ (ml/sec)	$F_3$ (ml/sec)	$T_1$ (sec)	$T_2$ (sec)	$T_3$ (sec)	$T_4$ (sec)
<b>High-enhancement Wash-out</b>							
Slow	1.20	1.34	0.0076	0.2	1.5	0.2	25.5
Medium	1.20	1.34	0.0101	0.2	1.5	0.2	25.5
Fast	1.20	1.34	0.0118	0.2	1.5	0.2	25.5
Low-enhancement	1.20	1.34	0.0076	0.8	0.9	0.2	25.5

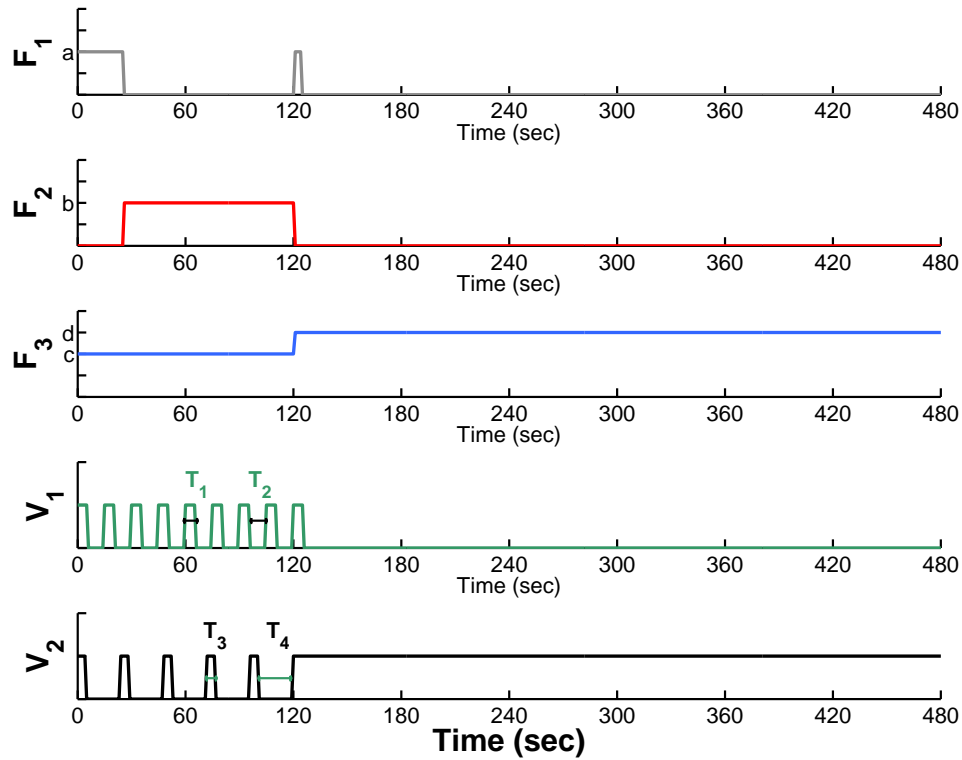


Figure 4.41. The timing diagram of the flow chamber parameters is illustrated.  $F_1$ ,  $F_2$ ,  $F_3$ ,  $V_1$ , and  $V_2$  are defined in Figure 4.40.

### 4.8.3 The Dynamic X-ray CEDEM Acquisition

Once the intricate parameters governing the flow and pressure components of the flow chamber were determined, the dynamic breast phantom was constructed by inserting the flow chamber into a 10-cm thick breast phantom. The dynamic breast phantom was constructed in the same fashion as described in Section 4.2 with an additional flow chamber attached to the phantom container. Figure 4.43 shows the flow chamber attached to the plastic container of 10-cm thickness and the constructed dynamic breast phantom. In order to determine the feasibility of the dynamic CEDEM acquisition, the dynamic breast phantom was imaged by acquiring multiple sequential CEDEM images using the kinetic profiles developed in Section 4.8.2. Placing

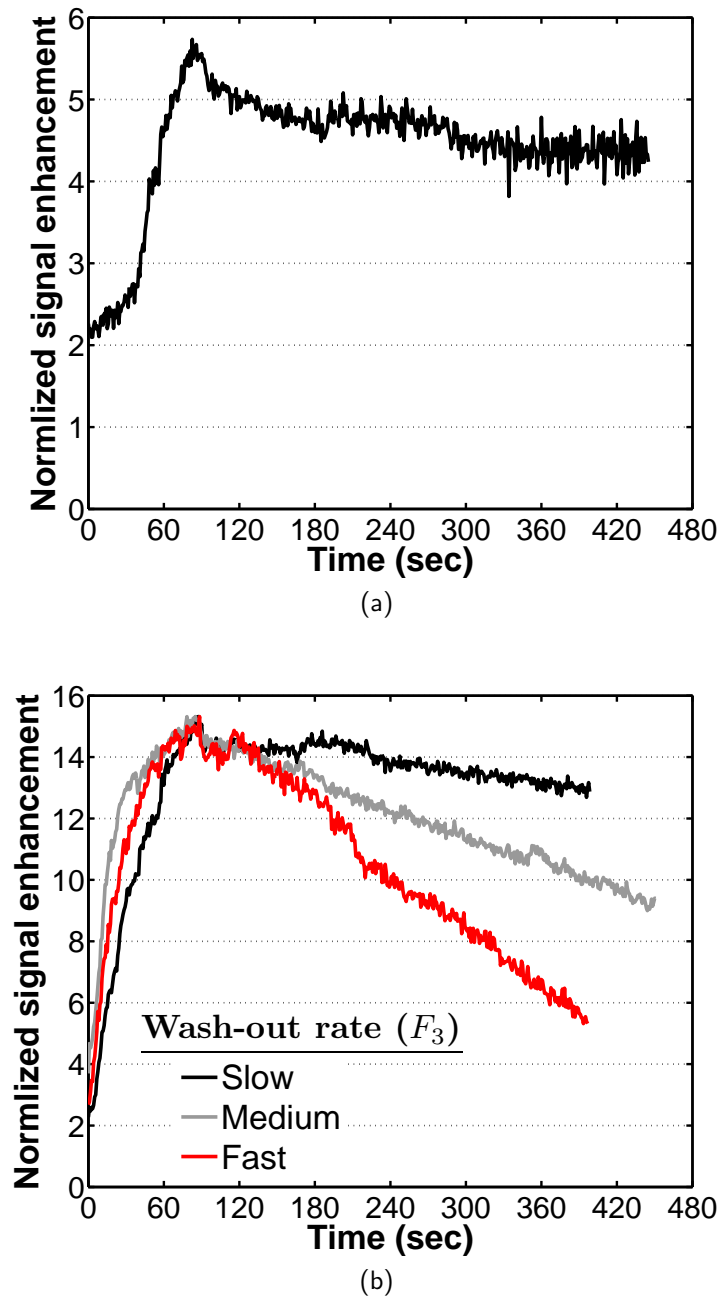


Figure 4.42. The normalized signal enhancement as a function of time is shown as a function of time for (a) low-enhancement contrast kinetic profile and (b) high-enhancement contrast kinetic profile (with slow, medium, and fast wash-out rate).

the dynamic breast phantom close to the system isocenter, projection images filtered with 0.2-mm Sn (12 fps) and 0.2-mm Cu (7.5 fps) were acquired with 55 kV (13 mA) using the breast CT system. Figure 4.44 shows the Sn-image, Cu-image, and the CEDEM image at one time point.

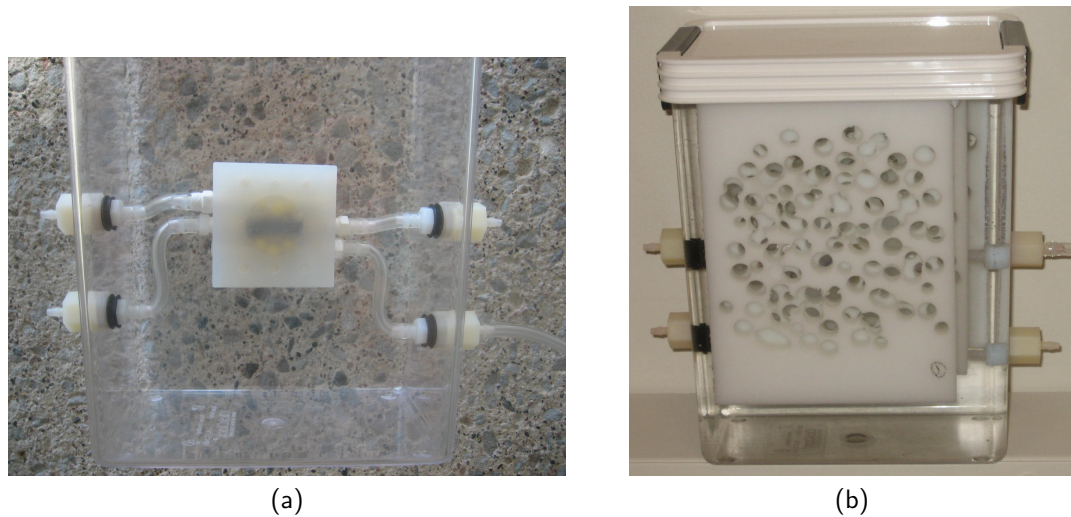


Figure 4.43. (a) The dynamic breast phantom with the flow chamber without the breast slabs and (b) the complete dynamic breast phantom with breasts slabs are shown.

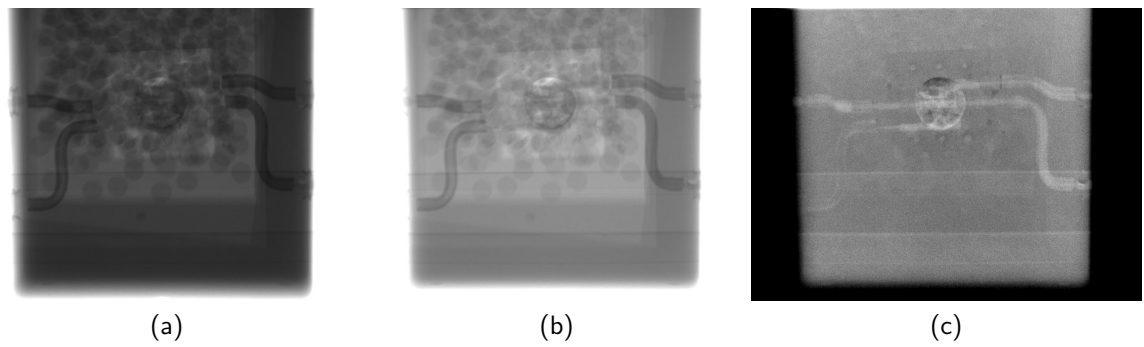


Figure 4.44. (a) The Sn-image, (b) the Cu-image, and (c) the CEDEM image of the dynamic breast phantom are shown. 55 kV (13 mA) was used in acquiring these images with breast CT system.

In order to demonstrate the quantitative capability of dynamic CEDEM imaging, the dynamic breast phantom with a number of contrast kinetic

profiles were imaged for 7-minutes. Twenty-six CEDEM images were acquired and processed to capture each contrast kinetic profiles, and these data were compared to contrast kinetic profile from the clinical CED-MRI data. An Iodine concentration of 12.8 mg/ml was injected into the dynamic breast phantom during the dynamic CEDEM acquisition. The flow parameters of the high-enhancement profile (see Table 4.3) were used to generate kinetic profiles similar to the CED-MRI data for malignant lesions. The wash-out flow rates  $F_3$  (c/d as defined in Figure 4.41) were 0.0101/0.0101 ml/sec, 0.0101/0.0143 ml/sec, 0.0101/0.0169 ml/sec, and 0.0101/0.0228 ml/sec for invasive lobular carcinoma, mucinous cancer, multicentric invasive ductal carcinoma (IDC), and IDC, respectively. Figure 4.45 illustrates the kinetic profiles acquired with the dynamic breast phantom mimicking the CED-MRI kinetic profiles of the four types of malignant breast cancer. The flow parameters of the low-enhancement profile with  $F_3 = 0.0101$  ml/sec were used to generate the kinetic curve similar to that of the benign lesions. Figure 4.46 illustrates the kinetic profiles acquired with the dynamic breast phantom mimicking the CED-MRI kinetic profiles of the benign lesions. Figure 4.45 and Figure 4.46 suggest that the dynamic breast phantom can generate kinetic profiles similar to those from the CED-MRI data of patients with malignant and benign lesions. It also confirms that CEDEM imaging is feasible in capturing the contrast kinetics during a dynamic acquisition with the injection of iodine-based contrast agent. The ability to depict the contrast kinetic profiles from patients with various breast cancer types provides valuable information from the breast CT scanner to aid in diagnoses.

## 4.9 The optimized Dynamic CEDEM protocol

Dynamic CEDEM imaging was shown to be feasible using the breast CT system for quantifying the contrast kinetic curve. Due to radiation dose limitation discussed in Section 4.7.3, the number of temporal frames acquired during a dynamic CEDEM imaging depends on the breast thickness and

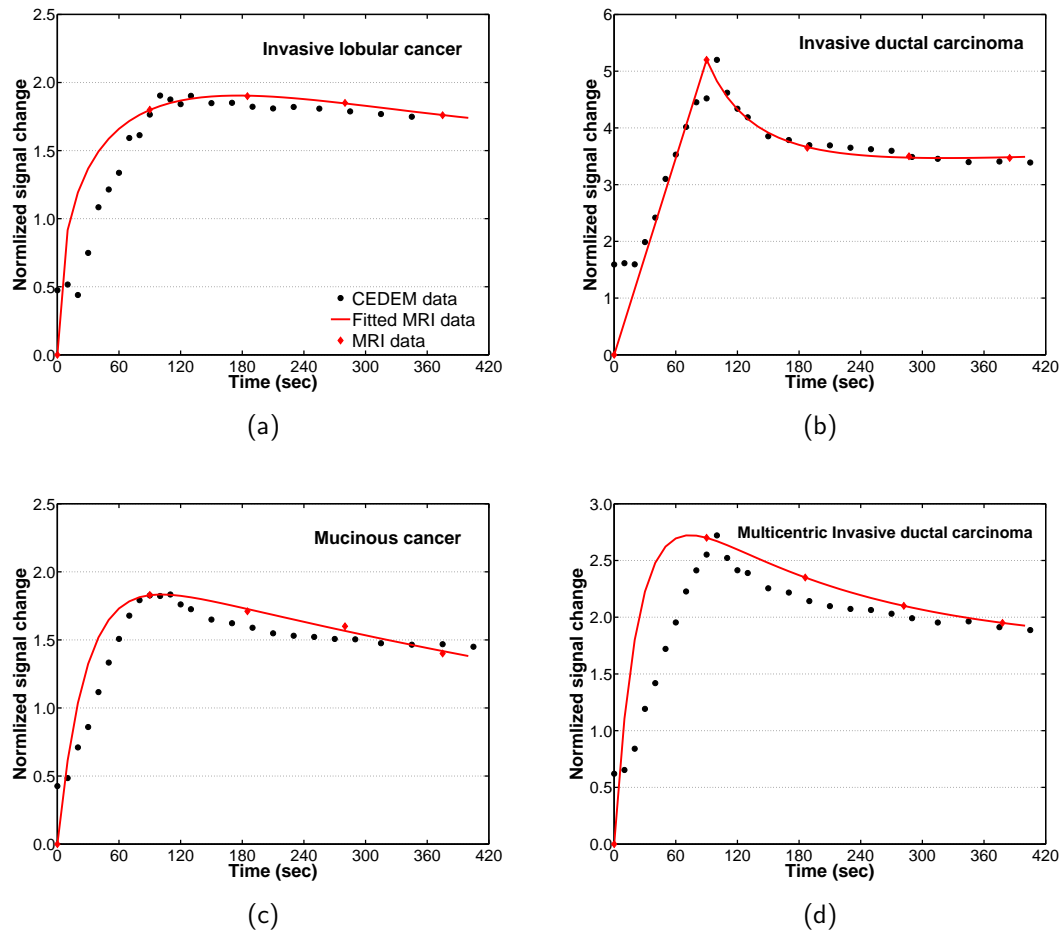


Figure 4.45. The contrast kinetic curves generated from the dynamic CEDEM acquisition are compared to the clinical CED-MRI data of patients with four malignant breast cancer: (a) invasive lobular cancer, (b) invasive ductal carcinoma, (c) mucinous cancer, and (d) multicentric invasive ductal carcinoma.

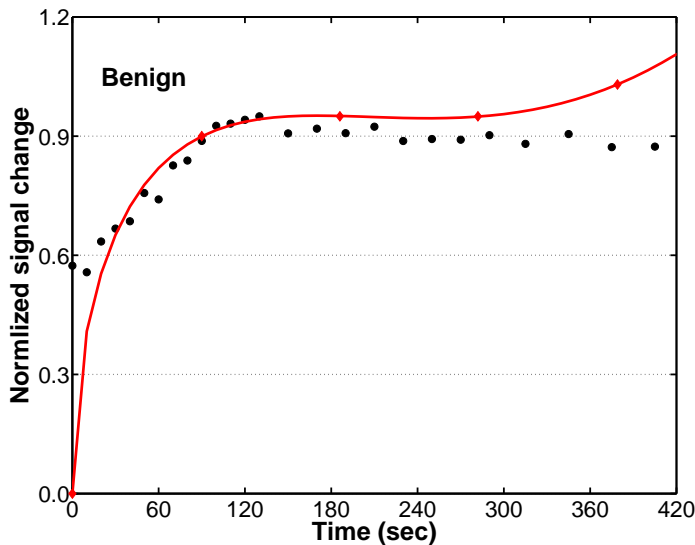


Figure 4.46. The contrast kinetic curves generated from the dynamic CEDEM acquisition is compared to the clinical CED-MRI data of patients with benign breast cancer

breast composition. Using 60 kV with Sn/Cu filters within the dose limitation, Figure 4.32, Figure 4.33, and Figure 4.34 suggest that the number of temporal frames per dynamic CEDEM acquisition are 8, 16, and 40 for 8-cm, 10-cm, and 13-cm breast thickness (respectively) with VGF of 5% to 25%. Figure 4.47 shows an example of the dynamic CEDEM protocol that will be likely implemented in a clinical setting to image an 8-cm breast using a combination of high-dose and low-dose CEDEM acquisition. The first CEDEM image will be acquired with high-dose CEDEM acquisition, allowing more averaged frames to ensure robust dual-energy subtraction. For the remaining time, low-dose CEDEM images (one Sn-image and one Cu-image) will be acquired to effectively use the radiation dose while generating useful functional and quantitative information. The short acquisition time per CEDEM image provides accurate information of the contrast enhancement with minimal effect of patient motion. The study has shown dynamic CEDEM is capable of acquiring fast, low-dose x-ray projection images to characterize the contrast kinetic during a contrast-enhanced imaging protocol.

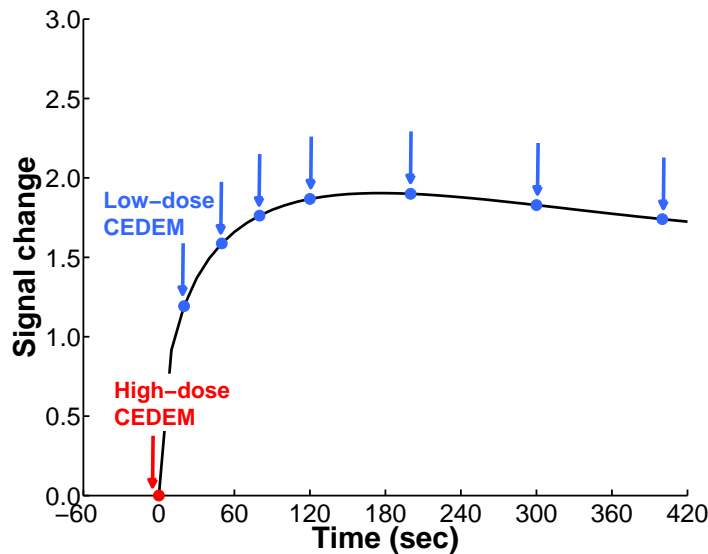


Figure 4.47. An example of the dynamic CEDEM protocol for imaging a 8-cm breast is illustrated with combinations of high-dose and low-dose acquisition. The time between each CEDEM acquisition is varied to effectively characterize the contrast kinetic curve while delivering radiation dose efficiently

## 4.10 References

- J. M. Boone and 3rd V. N. Cooper. Scatter/primary in mammography: Monte carlo validation. *Med Phys*, 27(8):1818–31, 2000. [4.4](#)
- J. M. Boone, K. K. Lindfors, 3rd V. N. Cooper, and J. A. Seibert. Scatter/pri-mary in mammography: comprehensive results. *Med Phys*, 27(10):2408–16, 2000. [4.4](#)
- J. M. Boone, T. R. Nelson, K. K. Lindfors, and J. A. Seibert. Dedicated breast ct: radiation dose and image quality evaluation. *Radiology*, 221(3):657–67, 2001. [4.4](#)
- J. M. Boone, N. Shah, and T. R. Nelson. A comprehensive analysis of dgn(ct) coefficients for pendant-geometry cone-beam breast computed tomography. *Med Phys*, 31(2):226–35, 2004. [4.4](#), [4.9](#)

- A. E. Burgess and P. F. Judy. Signal detection in power-law noise: effect of spectrum exponents. *J Opt Soc Am A Opt Image Sci Vis*, 24(12):B52–60, 2007. **4.2**
- A. E. Burgess, F. L. Jacobson, and P. F. Judy. Human observer detection experiments with mammograms and power-law noise. *Med Phys*, 28(4): 419–37, 2001. **4.2**
- K. M. Donahue, D. Burstein, W. J. Manning, and M. L. Gray. Studies of gd-dtpa relaxivity and proton exchange rates in tissue. *Magn Reson Med*, 32 (1):66–76, 1994. **4.8.2**
- J. J. Heine and R. P. Velthuizen. Spectral analysis of full field digital mammography data. *Med Phys*, 29(5):647–61, 2002. **4.2**
- A. Jackson, D.L. Buckley, and G.J.M. Parker. *Dynamic Contrast-Enhanced Magnetic Resonance Imaging in Oncology*. Medical Radiology (Diagnostic Imaging and Radiation Oncology. Springer, Berlin Heidelberg New York, 2005. **4.8.2**
- R. M. Judd, M. K. Atalay, G. A. Rottman, and E. A. Zerhouni. Effects of myocardial water exchange on t1 enhancement during bolus administration of mr contrast agents. *Magn Reson Med*, 33(2):215–23, 1995. **4.8.2**
- A. L. Kwan, J. A. Seibert, and J. M. Boone. An improved method for flat-field correction of flat panel x-ray detector. *Med Phys*, 33(2):391–3, 2006. **4.6.2**
- K. G. Metheany, C. K. Abbey, N. Packard, and J. M. Boone. Characterizing anatomical variability in breast ct images. *Med Phys*, 35(10):4685–94, 2008. **4.2**
- N. D. Prionas, K. K. Lindfors, S. Ray, S. Y. Huang, L. A. Beckett, W. L. Monsky, and J. M. Boone. Contrast-enhanced dedicated breast ct: initial clinical experience. *Radiology*, 256(3):714–23, 2010. **4.3**

N. D. Prionas, S. Y. Huang, and J. M. Boone. Experimentally determined spectral optimization for dedicated breast computed tomography. *Med Phys*, 38(2):646–55, 2011. [4.2](#)

B. R. Rosen, J. W. Belliveau, J. M. Vevea, and T. J. Brady. Perfusion imaging with nmr contrast agents. *Magn Reson Med*, 14(2):249–65, 1990. [4.8.2](#)

D Zheng, S Huang, H Zhou, and J Boone. *WE-E-L100J-06: Simulation Studies On Contrast Enhanced Dual Energy Mammography*, volume 34. AAPM, 2007. [4.6.1](#)

## Chapter 5

### Summary and Future Work



This dissertation work investigated the feasibility of contrast-enhanced dual energy mammography using breast CT platform to characterize the contrast kinetic curve. In order to understand the object of interest better, Chapter 2 described a comprehensive characterization of breasts using the clinical breast CT data sets at UC Davis. The breast geometry, shape, glandular tissue distribution, and skin thickness were estimated from the breast CT data sets using various imaging processing techniques. The metrics defined in Chapter 2 corrected the common assumptions regarding skin thickness (mean skin thickness of  $\sim 1.5$  mm instead of 4 mm) and the distribution of breast glandular composition (mean VGF of  $\sim 15\%$  instead of 50%). The breast metrics provided useful information regarding the dimension and composition of the breast for the development of CEDEM imaging.

In addition to the breast dimension and composition, the components of the imaging system were examined to better understand their effect in image quality. Part of the CEDEM optimization scheme was to use computer-simulated images to guide and to confirm the experimental acquisitions. Thus, Chapter 3 introduced a semi-empirical simulation approach of energy-integrating x-ray detectors, adopting the theory of cascaded system analysis ([Siewerdsen et al., 1997, 1998](#)). The approach was validated to generate projection images of user-defined objects closely calibrated to the breast CT system. The computer simulation method confirmed the signal and noise transfer theory developed cascaded system analysis with experimentally-determined factors. Instead of the analytical approach, the method incorporated the ability to generate images for applications where image generation of user-defined objects is necessary.

With the comprehensive understanding of the imaging object and the imaging system, Chapter 4 described the CEDEM optimization in two phases. The first phase was the initial effort in determining whether changing filters and kV can shape x-ray spectra optimal for acquiring CEDEM images with the static breast phantom using breast CT system. The initial study found that changing only filter materials (keeping kV constant) was sufficient to

shape x-ray spectra with filter materials best selected for the purpose of imaging with iodine-base contrast solution. Therefore, the readily available tin (Sn) and copper (Cu) were chosen as the optimal filters to create x-ray spectra separation needed for maximizing signal contrast when imaging breasts with iodine-based contrast solution. Using Sn and Cu filters, a comprehensive investigation was performed to determine the optimal x-ray technique factors to acquire high-quality CEDEM images. With agreeing trends between the computer-simulated and experimentally-acquired images, 60 kV with dose ratio of 0.5 to 0.6 was the optimal x-ray technique factor to acquire fast, dose-efficient CEDEM images of 8-cm, 10-cm, and 13-cm thick breasts. The computer simulation approach described in Chapter 3 was shown useful in guiding experiment setup and in confirming experimental results. The number of averaged frames to acquire Sn-images and Cu-images increases with increasing breast thickness to utilize the radiation dose efficiently. Breast composition and iodine concentration did not affect the optimal kV for acquiring CEDEM images. The optimized x-ray technique factors were used to examine the feasibility of the dynamic CEDEM protocol. The dynamic CEDEM images of the dynamic breast phantom with computer-controlled flow parameters demonstrated that dynamic CEDEM imaging is capable of capturing contrast kinetic curve over time. The optimal dynamic protocol consists of one high-dose CEDEM acquisition (Sn-images and Cu-images that consist of multiple average frames) followed by multiple low-dose CEDEM acquisition (one frame of Sn-image and Cu-image). The number of averaged frames used for the first high-dose acquisition and the number of allowable CEDEM temporal acquisitions were subject to change for a given breast thickness and composition. This dynamic CEDEM protocol was thought to provide the best compromise between preserving image integrity with useful quantitative information and delivering radiation dose effectively.

## 5.1 Imaging System Components

The detector mode used for CEDEM acquisition can be investigated with great details for future studies. For each detector element, an analog voltage gain is applied prior to Analog-to-Digital conversion (ADC) of the detected signal. This work has examined the imaging feasibility of CEDEM using the fixed low-gain detector mode. Another detector mode worthy for further investigation is the dynamic-gain detector mode, which is a combination of fixed low-gain and fixed high gain. When operating in dynamic-gain detector mode, the detector element will use a high gain if the signal level is below the preset threshold and vice versa. [Yang et al. \(2010\)](#) found that the additive noise of the fixed low-gain detector mode is a larger fraction of the pixel variance compared to that of the dynamic-gain detector mode. The fractional additive noise was found larger when imaging thicker breasts as well. Thus, the dynamic-gain detector mode may be explored in hope to generate projection images with less effect from the additive noise, especially when imaging thicker objects. The image quality of CEDEM images may be improved, and the dual energy subtraction may be more robust with lower-noise projection images. The dynamic-gain detector mode may result in lower radiation dose per CEDEM acquisition, which increase the number of temporal frames acquired within the dose limitation. The contrast kinetic curve may be sampled at a higher rate to provide more accurately quantitative information.

In addition to exploring different detector mode, a higher x-ray tube rating may be explored to acquire CEDEM images with higher image quality. The x-ray tube rating of the current system is 1000 Watt, which can be limited when acquiring Sn-images where Sn filter attenuates the signal dramatically. In this study, the acquisition frame rate was changed to compensate for the reduction of detected photon counts when imaging with Sn filter. Although reducing the acquisition frame rate and increasing x-ray tube current deliver comparable radiation dose to the patient, it may be more advantageous to acquire Sn-images using an x-ray tube with higher rating instead of reducing

acquisition frame rate to allow faster CEDEM acquisition time. The faster CEDEM acquisition will likely reduce the effect of patient motion, producing more accurate quantitative information of the contrast kinetic over time.

## 5.2 The CEDEM Clinical Study

A clinical trial of the dynamic CEDEM protocol using the optimized x-ray technique factors is the next step to acquire clinical information. The goal of the clinical trial is to determine the change in signal enhancement from the injection of contrast over time among the women with various types of breast cancer. The relationship between the contrast kinetic profile and the physical information of the patient, such as body weight, height, and cardiac output, may be determined. The diagnostic value of the contrast kinetic curves may be quantified as well by examining the contrast kinetic parameters from patients with various types of breast cancer.

The contrast-enhanced breast CT has shown successful in enhancing malignant types of breast cancer as discussed in Section 1.3.3. The timing of contrast injection has been determined by trials and errors during the current CE-bCT clinical trial. The CEDEM clinical trial may be an intermediate step to understand how the contrast kinetics behave with a number of external factors, including the injection flow rate and the contrast injection followed by a saline flush. Moreover, the CE-bCT image procedure for patients with bilateral breast cancer (lesions in both breasts) has not been determined. Therefore, it would be interesting to examine contrast kinetic profiles with different contrast injection procedures, such as the contrast injection with saline flush or the two-bolus contrast injection. Overall, the CEDEM clinical trial will provide valuable information about the realistic contrast dynamics in order to acquire high-quality and clinically-useful breast CT images.

### 5.3 Coda

In conclusion, the imaging parameters in acquiring the contrast-enhanced dual-energy mammography (CEDEM) images were optimized using the breast CT platform. Computer-simulated and experimentally-acquired images support the conclusion that 60 kV with tin and copper filters is the the viable x-ray technique factors to acquire low-dose CEDEM images with visible signal enhancement of iodine-based contrast solution. The optimized CEDEM technique factors for a given breast dimension and composition may be used in a dynamic imaging protocol to quantify the signal enhancement of the contrast solution over time. The dynamic CEDEM acquisition may be a cost-effective, low-dose substitute of CED-MRI in acquiring temporal information of the contrast solution. The contrast kinetic curves may provide a better understanding of how to image patients with contrast agents in detecting breast cancers.

### 5.4 References

- J. H. Siewerdsen, L. E. Antonuk, Y. el Mohri, J. Yorkston, W. Huang, J. M. Boudry, and I. A. Cunningham. Empirical and theoretical investigation of the noise performance of indirect detection, active matrix flat-panel imagers (amfpis) for diagnostic radiology. *Med Phys*, 24(1):71–89, 1997. 5
- J. H. Siewerdsen, L. E. Antonuk, Y. el Mohri, J. Yorkston, W. Huang, and I. A. Cunningham. Signal, noise power spectrum, and detective quantum efficiency of indirect-detection flat-panel imagers for diagnostic radiology. *Med Phys*, 25(5):614–28, 1998. 5
- K. Yang, S. Y. Huang, N. J. Packard, and J. M. Boone. Noise variance analysis using a flat panel x-ray detector: a method for additive noise assessment with application to breast ct applications. *Med Phys*, 37(7):3527–37, 2010. 5.1

## Production Notes

This manuscript was written as a combination of L<sup>A</sup>T<sub>E</sub>X files, and was generated from a L<sup>A</sup>T<sub>E</sub>X class file based on the combination of Harish Bhanderi's CUED template (converted from a4 to letter using the geometry package) and the ucthesis template by Ethan V. Munson. Portable Document Format (PDF) output was made from the L<sup>A</sup>T<sub>E</sub>X source files using pdfL<sup>A</sup>T<sub>E</sub>X with WinEdt 5 using a PC. This dissertation was typeset with 12 point T<sub>E</sub>X Gyre Schola, which is an OpenType font created by the T<sub>E</sub>X Gyre Project, licensed under the GUST Font License for free use. It is based on the New Century Schoolbook, which is a version developed by David Berlow and Matthew Carter of Linotype.

The figures and diagrams were stored generally in JPG, PNG, or PDF formats. The diagrams were primarily drawn in Microsoft Office PowerPoint 2003 ([Microsoft](#)) and Adobe Photoshop and Illustrator CS5 ([Adobe](#)). The figures were plotted with Microsoft Office Excel 2003 ([Microsoft](#)) and MATLAB 7.8.0 (R2009a) ([Mathworks](#)). The images were displayed using ImageJ 1.44d ([ImageJ](#)).

## Appendices

## **Appendix A**

### **Breast CT Forward Projection**

## A.1 Motivation

With the available breast CT data sets, the ability to rotate the breast volume with a given angle is crucial for breast cancer visualization and diagnosis. With the injection of contrast agent, it would be beneficial for physicians and radiologists to target the breast tumors to make appropriate prognosis.

## A.2 Methods and Materials

Forward projection of a computed tomography (CT) reconstructed data set is commonly used to display the three-dimensional capability of the image data set. For a given bCT data set (described in Section 1.2.2), all the coronal-reconstructed images were compiled into a volume. Let  $x$  be the horizontal axis,  $y$  be the verticle axis, and  $z$  be the anterior-posterior image position of a coronal-reconstructed bCT image. The forward projection image of the volume were generated by rotating the volume at an desired angle. To rotate a bCT volume, a rotation matrix with respect to the axis of rotation was applied to the  $x$ ,  $y$ , and  $z$  coordinate of all voxels in the volume. The three-dimensional (3D) rotation matrix with respect to the  $x$ ,  $y$ , and  $z$  axis are defined as the following,

$$\mathbf{R}_x(\theta_x) = \begin{bmatrix} 1 & 0 & 0 \\ 0 & \cos(\theta_x) & -\sin(\theta_x) \\ 0 & \sin(\theta_x) & \cos(\theta_x) \end{bmatrix} \quad (\text{A.1})$$

$$\mathbf{R}_y(\theta_y) = \begin{bmatrix} \cos(\theta_y) & 0 & \sin(\theta_y) \\ 0 & 1 & 0 \\ -\sin(\theta_y) & 0 & \cos(\theta_y) \end{bmatrix} \quad (\text{A.2})$$

$$\mathbf{R}_z(\theta_z) = \begin{bmatrix} \cos(\theta_z) & -\sin(\theta_z) & 0 \\ \sin(\theta_z) & \cos(\theta_z) & 0 \\ 0 & 0 & 1 \end{bmatrix} \quad (\text{A.3})$$

The rotation matrices were used to rotate the volume in any combination of the 3D rotation matrices. For a given angle and a given axis, the 3D volume is thought to rotate with respect to the center of the volume along the given axis of rotation. For a given rotation angle with respect to x, y, and z axis, the resulting rotation matrix is obtained by matrix multiplication of the three rotation matrices,

$$\mathbf{R}(\theta_x, \theta_y, \theta_z) = \mathbf{R}_x(\theta_x)\mathbf{R}_y(\theta_y)\mathbf{R}_z(\theta_z) \quad (\text{A.4})$$

For a voxel position  $(x, y, z)$ , the corresponding position  $(x', y', z')$  of the voxel after rotating the volume is computed as the following,

$$\mathbf{u} = \mathbf{R}(\theta_x, \theta_y, \theta_z)\mathbf{v}$$

where  $\mathbf{u} = \begin{bmatrix} x' \\ y' \\ z' \end{bmatrix}$  and  $\mathbf{v} = \begin{bmatrix} x \\ y \\ z \end{bmatrix}$

(A.5)

For a given bCT data set,  $(x', y', z')$  was computed for all voxel positions  $(x, y, z)$ . Nearest neighbor interpolation and maximum intensity projection (MIP) were used in projecting the 3D volume onto a 2D projection image. MIP method assigns all pixels of the 2D projection image with the signal value of the projected voxel that has the highest signal intensity. In order to generate a 3D-rendered volume, forward projection images of a bCT data set were generated by rotating the volume 360 degrees with respect to z axis. A 15-degree rotation with respect to the x-axis was applied for all the forward projection images for a better visualization of the bCT data set. A movie compiling the forward projection images was created by ImageJ 1.43 with the desired window-and-level display and frame rate.

### **A.3 Results**

Figure A.1 show the forward projection images of a contrast-enhanced bCT data set with roation angles of 0, 60, 120, 180, 240, 300 degree. The 3D rendered images enhanced the conspicuity the mass lesions and calcification in a bCT data set.

### **A.4 Discussion and Summary**

The forward projection images with MIP improve the visualization of bCT data set by providing a good sense of depth within a 3D volume. The approach is optimal with a 3D data set with contrast agent to enhance the conspicuity of breast lesions in a breast. The 3D rendered movie of the forward projection images can help the physicians and radiologists in better detect the breast cancer using a contrast-enhanced bCT imaging protocol. The 3D rendered movie was created by adjusting the window-and-level of the forward projection images subjectively. It would be more accurate to incorporate the physician's and radiologist's diagnosis in generating the 3D rendered movie to avoid the misrepresentation of tissue contrast within a 3D data set.

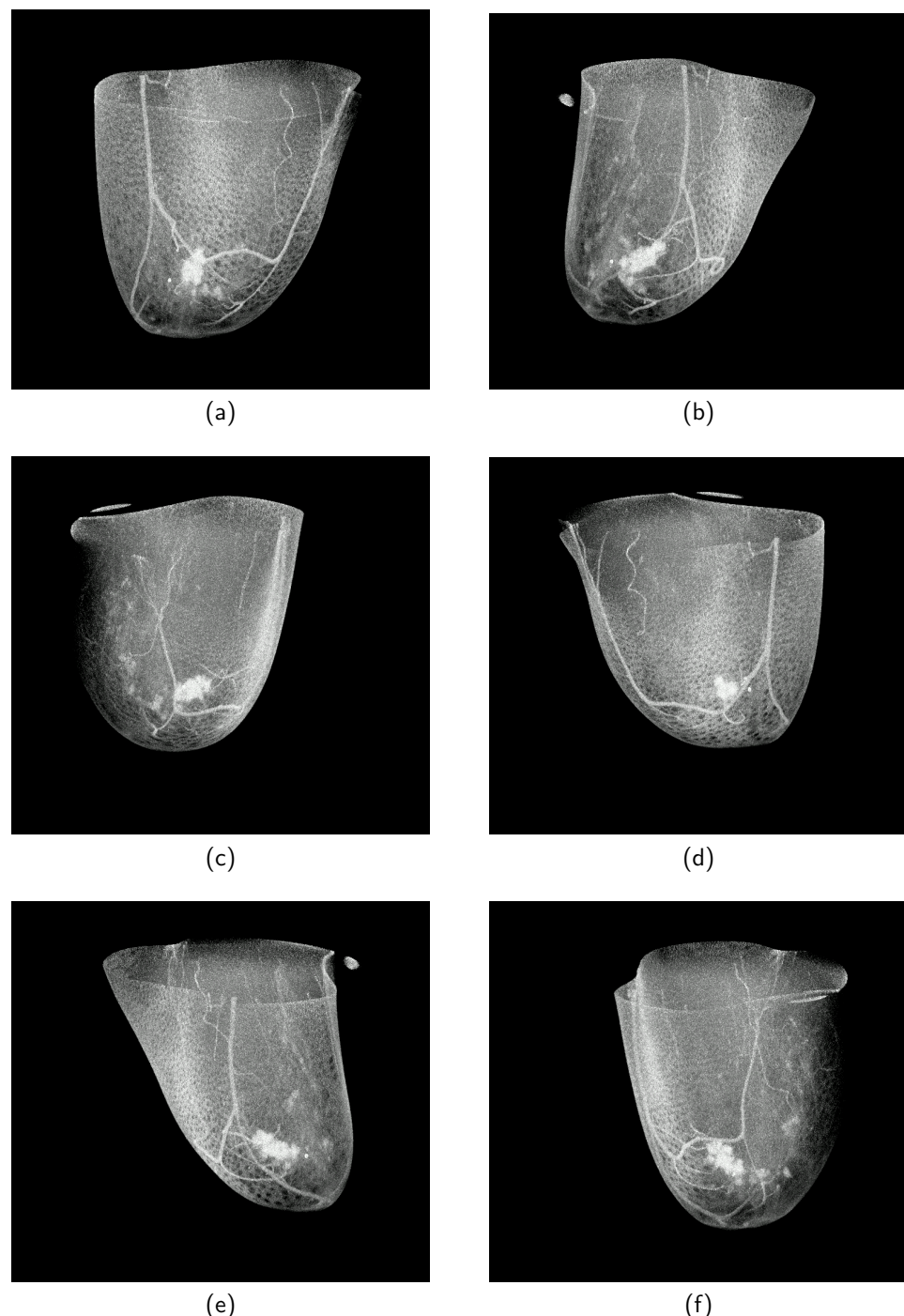


Figure A.1. The forward projection images of a contrast-enhanced bCT data set with  $\theta_x = 15$  and (a)  $\theta_z = 0$  degree, (b)  $\theta_z = 60$  degree, (c)  $\theta_z = 120$  degree, (d)  $\theta_z = 180$  degree, (e)  $\theta_z = 240$  degree, and (f)  $\theta_z = 300$  degree

## **Appendix B**

### **Normalization of the Image Filter**

When applying a image filter to an input signal, the magnitude of signal mean and variance will be changed depending on the design of the filter. In order to maintain the output signal to a desired mean and variance, the filter needs to be normalized to maintain a given variance in the output signal. Let  $f(x)$  be the input discrete function that consists of normally-distributed random numbers with zero-mean and variance  $\sigma_f^2$ . Let the Fourier transform of  $f(x)$  be  $F(u)$ .  $\sigma_f^2$  can be described as

$$\sigma_f^2 = \sum_{u=1}^N F(u)^2 \Delta u \quad (\text{B.1})$$

where  $N$  is the number of elements in  $F(u)$ . Since  $f(x)$  consists of independent, normally-distributed random numbers,  $F(u)$  is a constant  $C$  for all  $u$ 's. Therefore,  $\sigma_f^2$  can be rewritten as

$$\begin{aligned} \sigma_f^2 &= \sum_{u=1}^N C^2 \Delta u \\ &= NC^2 \Delta u \end{aligned} \quad (\text{B.2})$$

Let  $h(x)$  be the image filter and  $H(u)$  be the Fourier transform of  $f(x)$ . The convolution of  $f(x)$  with  $h(x)$  gives rise to the output function  $g(x)$ . The Fourier transform of  $g(x)$  is given as

$$G(u) = F(u)H(u) \quad (\text{B.3})$$

When  $h(x)$  is not normalized prior to convolving with  $f(x)$ , the variance of  $g(x)$  is

$$\begin{aligned}\sigma_g^2 &= \sum_{u=1}^N G(u)^2 \Delta u \\ &= \sum_{u=1}^N F(u)^2 H(u)^2 \Delta u \\ &= C^2 \sum_{u=1}^N H(u)^2 \Delta u\end{aligned}\tag{B.4}$$

It is evident that  $\sigma_g^2$  is modified by a factor when convolving with the filter function that is not normalized properly. In order to maintain the output variance equivalent to the input variance,  $H(u)$  needs to be normalized by a factor  $f_{norm}$  given by

$$\begin{aligned}f_{norm} &= \frac{\sigma_f^2}{\sigma_g^2} \\ &= \frac{NC^2 \Delta u}{C^2 \sum_{u=1}^N H(u)^2 \Delta u} \\ &= \frac{N}{\sum_{u=1}^N H(u)^2}\end{aligned}\tag{B.5}$$

The 1D derivation of  $f_{norm}$  can be extended to a 2D filter function such that

$$f_{norm} = \frac{N_u N_v}{\sum_u^{N_u} \sum_v^{N_v} H(u, v)^2}\tag{B.6}$$

